Finite Element Method using Vector Finite Elements Applied to Eddy Current Problems

Leila Adams

A dissertation submitted to the Department of Electrical Engineering,
University of Cape Town, in fulfilment of the requirements
for the degree of Master of Science in Engineering.

Cape Town, March 2011

Declaration

I know the meaning of plagiarism and declare that all the work in the document, save for that which is properly acknowledged, is my own. This dissertation is being submitted for the degree of Master of Science in Engineering in the University of Cape Town. It has not been submitted before for any degree or examination in any other university.

Signature of Author . . . . . .

Cape Town
8 March 2011

Abstract

Vector fields found in electromagnetics are fundamentally different to vector fields found in other research areas such as structural mechanics. Electromagnetic vector fields possess different physical behaviour patterns and different properties in comparison to the other vector fields and *therein lies the necessity of the development of a finite element which would be able to cater for these differences* . The vector finite element was then developed and used within the finite element method specifically for the approximation of electromagnetic problems .

This dissertation investigates the partial differential equation that governs eddy current behaviour. A finite element algorithm is coded and used to solve this partial differential equation and produce vector field simulations for fundamental eddy current problems. Eddy current phenomena belong to a particular branch of electromagnetic theory, thus the vector field solutions of eddy current problems would possess electromagnetic properties and therefore the vector element proved to be highly desirable choice to use within the implementation of this finite element algorithm.

The dissertation covers research theory concerning the partial differential equation that governs eddy current phenomena and vector finite elements. All the knowledge and concepts gained from this research are then used for the implementation process of a finite element algorithm .

An analytical solution to a simple theoretical eddy current problem was compared to the simulation of the finite element solution of the same eddy current problem. Good physical and behavioural similarities between the simulation and the analytical solution provided proof of the successful implementation of the finite element algorithm and therefore established confidence in the capability of the finite element algorithm to approximate solutions to other eddy current problems. The finite element algorithm was then used on various arbitrary eddy current problems and the simulated vector field solutions were compared to the research theory that was covered in previous chapters and electromagnetic field theory. The analysis shows that the research theory and the field theory is in good agreement with the simulated solutions and thus served as more proof that the implementation of the finite element algorithm was successful.

“The ink of a scholar is mightier that the blood of a martyr.” Prophet Mohammad (P.B.U.H.)

“Seek knowledge from the cradle to the grave.” Prophet Mohammad (P.B.U.H.)

Acknowledgements

I would like to express my thanks to those who assisted me during the course of this research project. In particular:

- to my supervisors Prof. B.D.Reddy and Associate Prof. A.J.Wilkinson for their assistance and help.
- to my family for their support, encouragement and patience during this time.
- to Mr. S. Adams, for some advice regarding the graphical representation of certain vector field results.
- to the University of Cape Town and CERECAM for awarding a Postgraduate Scholarship Bursary.

Contents

List of Figures

List of Tables

List of Symbols

$\vec{B}$ — Magnetic Flux Density
$\vec{D}$ — Displacement Flux Density
$\vec{E}$ — Electric Field Intensity
$\vec{E}_E$ — Induced Electric Field Intensity
$\vec{E}_S$ — Excitation Electric Field Intensity
$\tilde{E}_E$ — Phasor Form of Induced Electric Field Intensity
$\tilde{E}_S$ — Phasor Form of Excitation Electric Field Intensity
$\vec{H}$ — Magnetic Field Intensity
$\vec{H}_E$ — Induced Magnetic Field Intensity
$\vec{H}_S$ — Excitation Magnetic Field Intensity
$\tilde{H}_E$ — Phasor Form of Induced Magnetic Field Intensity
$\tilde{H}_E$ — Phasor Form of Excitation Magnetic Field Intensity
$\vec{J}$ — Current Density
$\vec{J}_E$ — Eddy Currents
β — Attenuation Constant
δ — Skin Depth
ε — Permittivity
λ — Wavelength
μ — Permeability
μ_m — Mobility Constant
ρ_v — Electron Charge Density
σ — Conductivity
ω — Angular Frequency
f — Frequency
$\vec{\nabla}$ — Differential Operator
t — Time

Nomenclature

Finite Element Method—A numerical technique used to solve partial differential equations subject to certain boundary conditions.

Matlab—A scientific programing language used mostly for design and simulation.

Skin Depth—The distance after which the induced electric field or eddy currents has attenuated to approximately 36.8% of it's original value as the field penetrates into a conducting body.

Skin Effect—Relationship shared between the skin depth and the frequency.

Acronyms

BVP—Boundary Value Problem
BC—Boundary Condition
CEM—Computational Electromagnetics
EM—Electromagnetic
FEA-–Finite Element Analysis
FEM—Finite Element Method
FE—Finite Element
PDE—Partial Differential Equation
UCT—University of Cape Town

Chapter 1

Introduction

The finite element method (FEM) is one of the best-known methods for the solution of partial differential equations (PDE's) in applied mathematics and computational mechanics [2]. It is a numerical technique for obtaining an approximate solution to PDE's subject to certain boundary conditions [2, 3]. FEM has been widely used in structural mechanics and thermodynamics since the 1950's approximately [2, 3].

The earliest finite elements called nodal finite elements were used to approximate scalar field problems and the "structural design" of this element had its degrees of freedom (unknown parameters) represent the values of the scalar field at its nodes [7]. The nodal element was used to approximate vector field problems as well [8] but there were slight "structural" modifications made to the element in order to perform this task and this modified element was known as the node-based vector element . The "structural design" of this element has its degrees of freedom representing a cartesian component [2] at each of its nodes.

The first application for electromagnetics (EM) problems was undertaken in the late 1960s [2]. In solving EM problems by the FEM, these node-based vector elements were recognised to *not work very well* [2, 13]. The "structural design" of the node-based vector element makes it impractical and difficult for the element to handle electromagnetic vector field properties and the "structural design" of the element also allowed for "wasteful" computational calculations concerning the degrees of freedom when the element approximated vector fields [13, 3, 2]. In the late 1980's the vector (edge) element was introduced in computational electromagnetics (CEM) [2] and this element avoided and solved many of the problems encountered when solving EM problems [13] in contrast to when node-based vector elements were used.

In 1980, the French mathematician J.C.Nedelec published a paper which investigated the structure of polynomial spaces that the basis functions of a finite element should span in order to reduce the computation of "wasted" degrees of freedom [2]. The "structural design" of the vector element has its degrees of freedom represented as the tangential field component along its edges [8, 2] and this construction allowed for fewer degrees of freedom in contrast to the node-based vector element. J.P.Webb in his paper [13] and J.Jin in his book [3] both state that in vector electromagnetics problems, the curl of the field is often as important as the field itself. The vector element has by construction reduced degrees of freedom that allows for the element to model the curl-space more efficiently as shown by Nedelec [2] thereby approximating curling vector fields more effectively.

Thus, the vector element possesses unique properties which favoured EM behaviour. The dissertation project will focus on the use of this vector element within the FEM to solve a particular branch of EM problems known as eddy current problems [16, 17]. The vector PDE that governs eddy current behaviour is derived using Maxwell's equations and this

PDE is used to solve certain fundamental eddy current configurations.

1.1 Aim and Objective of the Dissertation

The objective of this dissertation is to successfully implement a Finite Element (FE) algorithm that can be used to model a vector PDE that governs eddy current behaviour for certain fundamental theoretical problems. The FE algorithm makes use of the FEM to approximate a solution to the PDE and then uses the vector elements to graphically construct the solution. Investigation into the properties of the vector element was also done to gain a better understanding of how the "structural design" contributes to the function capability of the element to favour EM behaviour in contrast to node-based vector elements.

1.2 Scope and Limitations of the Dissertation

The dissertation covers eddy current problems under investigation that are linear and two-dimensional. This dissertation is a first attempt at research that covers vector finite elements at UCT and therefore a lot of emphasis was placed on the investigation into understanding the properties of the vector elements and on the successful implementation of a FE algorithm which makes use of these vector finite elements. The dissertation therefore approaches the algorithm from a theoretical perspective and thus focuses on implementing the FE algorithm on theoretical eddy current problems and not on real world eddy current problems. The dissertation in this way tries to provide a solid foundation for further research and development into vector finite elements at UCT .

1.2.1 Contents of the Dissertation

In Chapter 2 the PDE that models eddy current behaviour is derived from Maxwell"s equations in differential vector form as well as in phasor form. A brief interpretation of the PDE is given in the last section of this chapter.

Chapter 3 deals with the calculation of analytical solutions of three fundamental eddy current problems. The solution to one of these problems are simulated through the FE algorithm in Chapter 8, where this analytical solution serves the purpose of being a reliable means to test whether the FE algorithm was implemented correctly. Also, the behaviour pattern of the analytical solutions also aids in the interpretation of simulated solutions of the FE algorithm for arbitrary eddy current problems in Chapter 8.

Chapter 4 deals with the theory used to construction a two-dimensional nodal finite element. Derivation of coordinate transformation between two triangular systems and the shape functions are illustrated. The construction of the nodal finite element mainly consists of the use of coordinate transformation and the shape functions. The knowledge of coordinate transformation and shape functions of the nodal finite element are latter incorporated into the construction of the vector finite element.

Chapter 5 begins with some preliminary theory (given in sub-sections 5.1.1, 5.1.2 and 5.1.3) that is needed to explain certain concepts concerning the vector elements. The two-dimensional node-based vector element and two-dimensional vector (edge) element are derived along with their shape functions. The "design structure" of both elements are different and this results in contrasting differences in the functionality and properties of each element when approximating vector fields and EM behaviour. Illustrations and calculations are done as to how the vector element achieves approximating vector fields over

a single element. The vector elements are then used to construct a two-dimensional vector field across a finite element mesh by using an algorithm especially coded for this purpose. Lastly, a short investigation is done to analyse which type of vector fields the vector element is capable and incapable of constructing and a brief overview on the limitations of the vector element that is used for this dissertation is mentioned.

Chapter 6 gives a brief overview of the FEM. A description of each procedure within the FEM is given as well as the derivation of the FE equations and matrices.

Chapter 7 discusses the theory behind the implementation process of the FE algorithm. Concepts, knowledge and findings covered throughout the research found in Chapters 4, 5, 2, 3, 6 and 7 is used in this implementation process.

In Chapter 8 solutions to eddy current problems are simulated where the results of these simulations are analysed. The chapter begins by comparing an analytical solution of a simple fundamental eddy current problem in Chapter 3 to the simulation of the FE solution of the same problem. Simulations of other arbitrary eddy current problems are also done.

Chapter 9 draws a few conclusions and a few recommendations.

Appendix A provides the full derivation of analytical solutions found in Chapter 3.

Chapter 2

Mathematical Model of Eddy Current Behaviour

The model gives a mathematical description by means of a partial differential equation (PDE) of the formation and physical behaviour of eddy currents. Maxwell's equations are used to construct this PDE that governs the eddy current behaviour.

2.1 Differential Vector Form of Maxwell's Equations

The physical behaviour of electromagnetic fields can be adequately summarised mathematically by four differential equations known as Maxwell's equations [5, 10]. Physically these Maxwell's equations describe time-varying electromagnetic fields [5].

Maxwell's equations in differential form are defined as follows [5]:

$$\vec{\nabla} \times \vec{E} = -\frac{\partial \mu \vec{H}}{\partial t} \tag{2.1}$$

$$\vec{\nabla} \times \vec{H} = \sigma \vec{E} + \frac{\partial \varepsilon \vec{E}}{\partial t} \tag{2.2}$$

$$\nabla \cdot \varepsilon \vec{E} = \rho_v \tag{2.3}$$

$$\nabla \cdot \mu \vec{H} = 0 \tag{2.4}$$

where $\vec{E}\left[\frac{\mathrm{V}}{\mathrm{m}}\right]$ is the electric field intensity, $\vec{H}\left[\frac{\mathrm{A}}{\mathrm{m}}\right]$ is the magnetic field intensity, $\mu\left[\frac{\mathrm{H}}{\mathrm{m}}\right]$ is the permeability, $\sigma\left[\frac{\mathrm{S}}{\mathrm{m}}\right]$ is the conductivity, $\varepsilon\left[\frac{\mathrm{F}}{\mathrm{m}}\right]$ is the permittivity, $\rho_v\left[\frac{\mathrm{C}}{m^3}\right]$ is the electron charge density and t symbolises time.

Constitutive relations equations are defined as follows [5]:

$$\vec{D} = \varepsilon \vec{E} \tag{2.5}$$

$$\vec{B} = \mu \vec{H} \tag{2.6}$$

$$\vec{J} = \sigma \vec{E} \tag{2.7}$$

where $\vec{D}\left[\frac{\mathrm{C}}{m^2}\right]$ is the displacement flux density, $\vec{B}[\mathrm{T}]$ is the magnetic flux density and $\vec{J}\left[\frac{\mathrm{A}}{m^2}\right]$ is the current density. The constitutive relations for this dissertation will be represented by linear equations.

Material constants are defined as follows [5]:

$$\mu = \mu_0 \mu_r \tag{2.8}$$

$$\varepsilon = \varepsilon_0 \varepsilon_r \tag{2.9}$$

where $\mu_0 = 4\pi \times 10^{-7}\left[\frac{\mathrm{H}}{\mathrm{m}}\right]$ and $\varepsilon_0 = \frac{1}{36\pi} \times 10^{-9}\left[\frac{\mathrm{F}}{\mathrm{m}}\right]$. The material types specified in this dissertation will posses linear behaviour. The values of the constant terms permeability μ_r, permittivity ε_r and conductivity σ depends on the type of material being modelled [5].

The following vector identity written in terms of the electric field intensity, $\vec{E}$ [5]:

$$\vec{\nabla} \times \vec{\nabla} \times \vec{E} = \vec{\nabla}\left(\vec{\nabla} \cdot \vec{E}\right) - \vec{\nabla}^2 \vec{E} \tag{2.10}$$

will be used in the derivation of the PDE (expressed in differential form) that governs eddy current behaviour. In this dissertation, the focus will be on a on *linear behaved system;* that is, the equations will be considered in their linearised form as well as describe linear behaviour in physical applications.

2.2 Phasor Form of Maxwell's Equations

Time-varying electromagnetic fields are very often either sinusoidal or else periodic in nature [8]. The mathematical handling of sinusoidal functions is made easier by carrying the amplitude and phase information about the sinusoid in the form of a complex number known as a phasor [8]. The primary advantage of using phasors in analysis of time-harmonic systems is the simplification that results in the differentiation and integration with respect to time in mathematical equations [5]. It is important to remember that the use of a phasor can only be applied to a system of mathematical equations when the system under consideration is linear [3, 14].

Maxwell's equations in phasor form are defined as follows [8]:

$$\vec{\nabla} \times \tilde{E} = -j\omega\mu\tilde{H} \tag{2.11}$$

$$\vec{\nabla} \times \tilde{H} = \sigma\tilde{E} + j\omega\varepsilon\tilde{E} \tag{2.12}$$

$$\nabla \cdot \varepsilon\tilde{E} = \rho_v \tag{2.13}$$

$$\nabla \cdot \mu\tilde{H} = 0 \tag{2.14}$$

where in phasor form, $\tilde{E}\left[\frac{\mathrm{v}}{\mathrm{m}}\right]$ is the electric field intensity, $\tilde{H}\left[\frac{\mathrm{A}}{\mathrm{m}}\right]$ is the magnetic field intensity, $\omega\left[\frac{\mathrm{rads}}{\mathrm{s}}\right]$ is the angular frequency and j represents the imaginary number.

Constitutive relations equations in phasor form are defined as follows [8]:

$$\tilde{D} = \varepsilon\tilde{E} \tag{2.15}$$

$$\tilde{B} = \mu \tilde{H} \tag{2.16}$$

$$\tilde{J} = \sigma \tilde{E} \tag{2.17}$$

where in phasor form, $\tilde{D}\left[\frac{\mathrm{C}}{m^2}\right]$ is the displacement flux density, $\tilde{B}[\mathrm{T}]$ is the magnetic flux density and $\tilde{J}\left[\frac{\mathrm{A}}{m^2}\right]$ is the current density. The constitutive relations for this dissertation will be represented by linear equations. The following vector identity written in terms of the electric field intensity in phasor form, $\tilde{E}$ [8]:

$$\vec{\nabla} \times \vec{\nabla} \times \tilde{E} = \vec{\nabla}\left(\vec{\nabla} \cdot \tilde{E}\right) - \vec{\nabla}^2 \tilde{E} \tag{2.18}$$

will be used in the derivation of the PDE (expressed in phasor form) that governs eddy current behaviour.

2.3 Physical Description of the Eddy Current Model

The physical description of the eddy current model is shown pictorially in Figure 2.1.

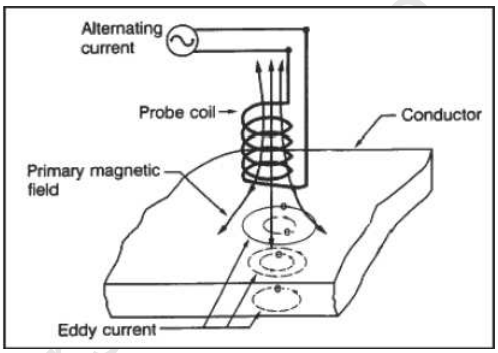

Figure 2.1: Principle Eddy Current Formation within a Conductor
Primary magnetic field induces eddy currents, $\vec{J}_E$ within a conductor.

Eddy Currents, $\vec{J}_E\left[\frac{\mathrm{A}}{m^2}\right]$, are induced electrical currents [10, 19, 16, 17]. A time-varying harmonic magnetic field (primary magnetic field, $\vec{H}_S\left[\frac{\mathrm{A}}{\mathrm{m}}\right]$) develops when a coil is excited by a low frequency sinusoidal current (source current, $\vec{J}_S\left[\frac{\mathrm{A}}{m^2}\right]$) [10, 19, 16, 17] as illustrated in Figure 2.1. The source current $\vec{J}_S$ is modelled by the following equation [10, 19, 16, 17]:

$$\vec{J}_S = \sigma \vec{E}_S \tag{2.19}$$

where σ, represents the conductivity of the coil and $\vec{E}_S\left[\frac{\mathrm{V}}{\mathrm{m}}\right]$ represents the electrical field present within the coil.

Another electrical conductor may come into contact with this time-varying magnetic field, $\vec{H}_S$. The magnetic field, $\vec{H}_S$, then induces eddy currents $\vec{J}_E$, within this conductor [10, 19, 16, 17] as illustrated in Figure 2.1. The eddy currents are modelled by the following equation [10, 19, 16, 17]:

$$\vec{J}_E = \sigma \vec{E}_E \tag{2.20}$$

where σ, represents the conductivity of the electrical conductor that is in contact with the primary magnetic field $\vec{H}_S$, and $\vec{E}_E\left[\frac{\mathrm{V}}{\mathrm{m}}\right]$ represents the electrical field induced by the

primary magnetic field $\vec{H}_S$, within the second conductor [10, 19, 16, 17]. Equation (2.20) can also be written alternatively as [5, 20]:

$$\vec{J}_E = \rho_v \vec{v}_{drift} \tag{2.21}$$

where $\vec{v}_{drift} = \mu_m \vec{E}_E$ and ρ_v, represents the electron charge density. The term $\vec{v}_{drift}$ represents the electron drift velocity [5, 20] within the (secondary) conductor and μ_m, represents the mobility constant of a particular material [5]. Thus:

$$\begin{aligned} \vec{J}_E &= \rho_v \left(\mu_m \vec{E}_E \right) \\ &= (\rho_v \mu_m) \vec{E}_E \end{aligned} \tag{2.22}$$

The conductivity term in Equation (2.20) is given by:

$$\sigma = \rho_v \mu_m \tag{2.23}$$

In conductors, the mobility constant is relatively high due to the chemical atomic bonding structure of a conducting material, known as metallic bonds [20]. The metallic bonds model stipulates the following atomic bonding scheme:

1. conductors (metallic material) have at most one, two, or three valence electrons [20].
2. these valence electrons are not bound to any particular atom within the solid and are more or less free to drift throughout the entire metal [20].
3. these electrons may be thought of belonging to the metal as a whole, or forming a "sea of electrons" or an "electron cloud"[20].
4. the remaining non valence electrons and atomic nuclei form what are called ion cores, which posses a net positive charge equal in magnitude to the total valence electron charge per atom [20]. Figure 2.2 is a schematic illustration of metallic bonding.

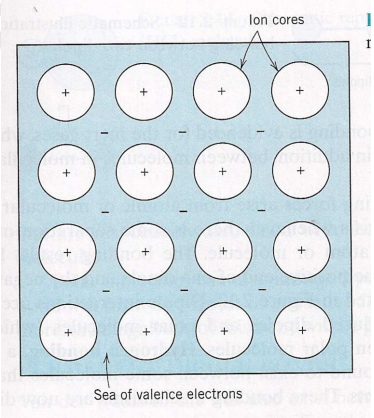

Figure 2.2: Schematic illustration of metallic bonding [20].

The presence of the induced electrical field $\vec{E}_E$, causes a force to be applied to the unbound electrons within the conductor [9]. The movement of these electrons (mobility of the electrons) in response to this applied force, $\vec{E}_E$ gives rise to electrical currents (eddy currents, $\vec{J}_E$) within the conducting material [5, 9] as illustrated in Figure 2.1. These eddy currents create a secondary magnetic field, $\vec{H}_E \left[\frac{\text{A}}{\text{m}} \right]$ that opposes the effect of the applied magnetic field, $\vec{H}_S$ [19, 3]. The induced eddy currents and the creation of secondary magnetic field is known as Lenz's Law [19].

2.3.1 Model Restrictions

The following physical restrictions will be placed on the model for this dissertation:

1. the entire partial differential equation (PDE) that describes eddy current behaviour is formulated in terms of the electric vector field component, $\vec{E_E}$ [16, 17].

2. the model will be assumed to be entirely a *linear system*. Due to the assumption of a linear system, the vector field $\vec{E}_E$ can thus be represented in phasor form $\tilde{E}$ [14, 3].

3. a time-varying harmonic magnetic field, which is the external forced excitation that induces eddy currents within a conductor/material [19].

4. no net free charge density, ρ_v will exists so $\rho_v = 0$ because the total number of carriers (electrons) in a given volume V (of the conductor) equals the number of positively-charged nucleons [8, 10, 5], thus giving the divergence constraint of $\vec{\nabla}.\varepsilon\vec{E} = 0$ for Equation (2.3) [16, 17, 3]. Therefore, term $\vec{\nabla}\left(\vec{\nabla}.\vec{E}\right) = \vec{\nabla}\left(\frac{\rho_v}{\varepsilon}\right)$ in Equation (2.10) is neglected, and Equation (2.10) becomes [8, 10, 5]:

$$\vec{\nabla}\times\vec{\nabla}\times\vec{E} \simeq -\vec{\nabla}^2\vec{E} \tag{2.24}$$

   Similarly, the term $\vec{\nabla}\left(\vec{\nabla}.\tilde{E}\right) = \vec{\nabla}\left(\frac{\rho_v}{\varepsilon}\right)$ in Equation (2.18) is neglected, therefore Equation (2.18) becomes [18]:

$$\vec{\nabla}\times\vec{\nabla}\times\tilde{E} \simeq -\vec{\nabla}^2\tilde{E} \tag{2.25}$$

5. the materials will have a linear behaviour in response to a forced external stimulus [5]. The material constants are written mathematically as in Equations (2.8), (2.9) [5]. The constitutive relations equations are written mathematically as in Equations (2.5), (2.6) and (2.7) in vector form and the Equations (2.15), (2.16) and (2.17) in phasor form respectively [5].

6. rates of time variation is sufficiently slow, the displacement current term, $\varepsilon\frac{\partial\vec{E}}{\partial t}$ in Equation (2.2) is neglected [18, 3]. Thus Equation (2.2) can be approximated as:

$$\vec{\nabla}\times\vec{H} = \sigma\vec{E} \tag{2.26}$$

7. for eddy currents modelled within a conductor the relation $\sigma \gg \omega\varepsilon$ will always hold [8, 10, 5], since conductors posses very high conductivity σ, values and very low dielectric ε, values [5]. This relation causes the term $j\omega\varepsilon\tilde{E}$ in Equation (2.12) to be neglected [16, 17, 5]. Thus the Equation (2.12) can be approximated as [18, 16, 17, 3]:

$$\vec{\nabla}\times\tilde{H} = \sigma\tilde{E} \tag{2.27}$$

2.4 Derivation of the Partial Differential Equation that Governs Eddy Current Behaviour - Differential Vector Form

Derivation of the PDE begins with Equation (2.1) which is stated here again for the readers convenience [5, 16, 17, 3]

$$\vec{\nabla} \times \vec{E_E} = -\frac{\partial \mu \vec{H}}{\partial t}$$

Performing a curl operation on the RHS and LHS of Equation (2.1), gives [5, 16, 17, 3]:

$$\vec{\nabla} \times \vec{\nabla} \times \vec{E_E} = -\frac{\partial}{\partial t}\left(\vec{\nabla} \times \mu \vec{H}\right) \tag{2.28}$$

According to [16, 17, 3] the eddy current model mathematically possesses two magnetic intensity field variables:

$$\vec{H} = \vec{H_E} + \vec{H_S} \tag{2.29}$$

as was also discussed in Section 2.3. Substituting Equation (2.29) into Equation (2.28) and using Equation (2.26) as well, produces:

$$\begin{aligned}
\vec{\nabla} \times \vec{\nabla} \times \vec{E_E} &= -\frac{\partial}{\partial t}\left(\left(\vec{\nabla} \times \mu \vec{H_E}\right) + \left(\vec{\nabla} \times \mu \vec{H_S}\right)\right) \\
&= -\frac{\partial}{\partial t}\left(\vec{\nabla} \times \mu \vec{H_E}\right) - \frac{\partial}{\partial t}\left(\vec{\nabla} \times \mu \vec{H_S}\right) \\
&= -\mu \frac{\partial}{\partial t}\left(\vec{\nabla} \times \vec{H_E}\right) - \mu \frac{\partial}{\partial t}\left(\vec{\nabla} \times \vec{H_S}\right) \\
&= -\mu \frac{\partial}{\partial t}\left(\sigma \vec{E_E}\right) - \mu \frac{\partial}{\partial t}\left(\sigma \vec{E_S}\right) \\
&= -\mu\sigma \frac{\partial}{\partial t}\vec{E_E} - \mu\sigma \frac{\partial}{\partial t}\vec{E_S}
\end{aligned} \tag{2.30}$$

Substituting Equation (2.24) into RHS of Equation (2.30) yields:

$$\begin{aligned}
-\vec{\nabla}^2 \vec{E_E} &= -\mu\sigma \frac{\partial}{\partial t}\vec{E_E} - \mu\sigma \frac{\partial}{\partial t}\vec{E_S} \\
\vec{\nabla}^2 \vec{E_E} - \mu\sigma \frac{\partial}{\partial t}\vec{E_E} &= \mu\sigma \frac{\partial}{\partial t}\vec{E_S}
\end{aligned} \tag{2.31}$$

Equation (2.31) is the general non-homogeneous vector wave equation that represents eddy current behaviour mathematically [6]. It is expected that the solution of Equation (2.31) will yield a vector function of the following general algebraic structure in three-dimensions [6, 15, 4]:

$$\vec{E_E}(x,y,z,t) = U(x,y,z,t)\,\hat{i} + V(x,y,z,t)\,\hat{j} + W(x,y,z,t)\,\hat{k} \tag{2.32}$$

and in two-dimensions [6, 15, 4]:

$$\vec{E_E}(x,y,t) = U(x,y,t)\,\hat{i} + V(x,y,t)\,\hat{j} \tag{2.33}$$

where $\hat{i}$, $\hat{j}$ and $\hat{k}$ are orthogonal unit vectors [6, 15, 4]. The forcing function which is known, is also a vector function and has the following general algebraic structure in three-dimensions:

$$\vec{E_S}(x,y,z,t) = U_S(x,y,z,t)\,\hat{i} + V_S(x,y,z,t)\,\hat{j} + W_S(x,y,z,t)\,\hat{k} \tag{2.34}$$

and in two-dimensions:

$$\vec{E_S}(x,y,t) = U_S(x,y,t)\,\hat{i} + V_S(x,y,t)\,\hat{j} \tag{2.35}$$

Equations (2.32), (2.34) are three-dimensional *vector functions* and Equations (2.33), (2.35) are two-dimensional *vector functions [4, 6]*.

According to Equation (2.31), the term $\vec{E_S}$ acts as the forcing function that induces the electric field, $\vec{E_E}$ in a domain [15, 6, 10]. The presence of the electric field, $\vec{E_E}$ in a conductor causes eddy currents $\vec{J_E}$ to form (refer to section 2.3 for the explanation of how eddy currents are induced in a conductor) [16, 17].

2.5 Derivation of the Partial Differential Equation that Governs Eddy Current Behaviour - Phasor form

Phasor form signifies that the time variable within an equation will be absent, therefore only spatial variables will appear in the equation. Derivation of the PDE in phasor form begins with Equation (2.11). Equation (2.11) is stated here for the readers convenience [18].

$$\vec{\nabla} \times \tilde{E_E} = -j\omega\mu\tilde{H}$$

Similar to Equation (2.29), the magnetic intensity field phasor variable is written as [16, 17, 14]:

$$\tilde{H} = \tilde{H}_E + \tilde{H}_S \tag{2.36}$$

Performing a curl operation the RHS and LHS of Equation (2.11), and at the same time substituting Equation (2.36) into Equation (2.11) produces [16, 17]:

$$\vec{\nabla} \times \vec{\nabla} \times \tilde{E}_E = -j\omega\mu \left(\vec{\nabla} \times \tilde{H}_E\right) - j\omega\mu \left(\vec{\nabla} \times \tilde{H}_S\right) \tag{2.37}$$

Substituting Equation (2.12) into Equation (2.37) produces [16, 17]:

$$\vec{\nabla} \times \vec{\nabla} \times \tilde{E}_E = -j\omega\mu\sigma\tilde{E_E} - j\omega\mu\sigma\tilde{E_S} \tag{2.38}$$

Substituting Equation (2.25) into RHS of Equation (2.38) yields [16, 17]:

$$\begin{aligned} -\vec{\nabla}^2\tilde{E}_E &= -j\omega\mu\sigma\tilde{E_E} - j\omega\mu\sigma\tilde{E_S} \\ \vec{\nabla}^2\tilde{E}_E - j\omega\mu\sigma\tilde{E_E} &= j\omega\mu\sigma\tilde{E_S} \end{aligned} \tag{2.39}$$

Equation (2.39) is the general non-homogeneous vector wave equation in phasor form that represents eddy current behaviour mathematically [16, 17]. It is expected that the solution of Equation (2.39) will yield a vector function of the following general algebraic structure in three-dimensions [6, 15, 4, 5]:

$$\tilde{E_E}(x,y,z) = U(x,y,z)\,\hat{i} + V(x,y,z)\,\hat{j} + W(x,y,z)\,\hat{k} \tag{2.40}$$

and in two-dimensions [6, 15, 4, 5]:

$$\tilde{E_E}(x,y) = U(x,y)\,\hat{i} + V(x,y)\,\hat{j} \tag{2.41}$$

The forcing function which is known, is a vector function and has the following general algebraic structure in three-dimensions:

$$\tilde{E_S}(x,y,z) = U_S(x,y,z)\,\hat{i} + V_S(x,y,z)\,\hat{j} + W_S(x,y,z)\,\hat{k} \tag{2.42}$$

and in two-dimensions:

$$\tilde{E_S}(x,y) = U_S(x,y)\,\hat{i} + V_S(x,y)\,\hat{j} \tag{2.43}$$

[6, 15, 4]. Similar to section 2.4, Equations (2.40) and (2.42) are known as *vector functions* in phasor form [6, 15, 4, 5].

According to Equation (2.39) (the electric field formulation of the eddy current problem in phasor form) the term $\tilde{E_S}$ acts as the forcing function that induces the electric field, $\tilde{E_E}$ in a domain [15, 6, 10]. The presence of the electric field, $\tilde{E_E}$ in a conductor causes eddy currents $\tilde{J_E}$ to form (refer to section 2.3 for the explanation of how eddy currents are induced in a conductor) [16, 17].

2.6 Interpretation of the Mathematical Equations Governing Eddy Current Behaviour

The derivation of the eddy current PDE thus begins with Equations (2.1) and (2.11) as seen in Sections 2.4 and 2.5 respectively.

The physical behaviour of eddy currents induced in a conductor in response to an external forced excitation (a time-varying harmonic magnetic field) is described mathematically by the PDE given by Equation (2.31) in the time domain and Equation (2.39) in the frequency domain respectively. Both Equations (2.31) and (2.39) are able to support problems:

- with source-free region, in this case the PDE is homogeneous and boundary-driven [15].
- that contain the source region, in this case the PDE is inhomogeneous and force-driven [15].

The eddy current PDE is homogeneous and boundary-driven when the geometry of the problem involves the penetration of a time-varying field directly onto the boundary of the domain of a specific problem. When considering boundary-driven problems, the BC can be imposed on the different regions of the domain of the problem [15]. The boundary of the domain can be:

- the material/conductor itself [15].
- small air space which surrounds the material/conductor [15].

The eddy current PDE is inhomogeneous and force-driven when the domain of the problem contains the the source region [15, 6]. The source region is the spatial position within the domain that the magnetic field is prescribed on.

Chapter 3

Analytical Solution of the PDE that Governs Eddy Current Behaviour

Analytical solutions to Equation (2.39) of three fundamental problems were done for the following reasons:

- a FE algorithm was coded to model Equation (2.39) which governs eddy current behaviour. The analytical solution of Section 3.1 will be compared to the FE simulated solution of the same problem, therefore the analytical solutions serves as a reliable means to test whether the algorithm was implemented correctly.
- the behaviour pattern of the analytical solutions may aid in the interpretation of simulated solutions of the FE algorithm for arbitrary eddy current problems which is simulated by the FE program in Chapter 8.
- to gain a better understanding of how the physical behaviour of eddy currents relates to the mathematical equations that govern them.

Producing an analytical solution is achieved by using Equation (2.39). To produce a boundary value problem the RHS of Equation (2.39) is set to zero, the term $j\omega\mu\sigma\tilde{E_S} = 0$. Equation (2.39) becomes [8]:

$$\vec{\nabla}^2\tilde{E_E} - j\omega\mu\sigma\tilde{E_E} = 0 \tag{3.1}$$

Equation (3.1) is homogeneous. This homogeneous Equation (3.1) will be subject to certain boundary conditions that will model certain eddy current situations [8]. Equation (3.1) can be written as:

$$\vec{\nabla}^2\tilde{E_E} - \tilde{k}^2\tilde{E_E} = 0 \tag{3.2}$$

where $\tilde{k}^2 = j\omega\mu\sigma$. Simplification of the term $\tilde{k}$ [8, 10]:

$$\begin{aligned}
\tilde{k} &= \sqrt{j\omega\mu\sigma} \\
&= (j\omega\mu\sigma)^{\frac{1}{2}} \\
&= (\omega\mu\sigma e^{j\frac{\pi}{2}})^{\frac{1}{2}} \\
&= \sqrt{\omega\mu\sigma}e^{j\frac{\pi}{4}} \\
&= \frac{\left(\sqrt{\omega\mu\sigma} + j\sqrt{\omega\mu\sigma}\right)}{\sqrt{2}} \\
&= \sqrt{\omega\mu\sigma}\frac{(1+j)}{\sqrt{2}} \\
&= \frac{\sqrt{\omega\mu\sigma}}{\sqrt{2}}(1+j) \\
&= \sqrt{\frac{\omega\mu\sigma}{2}}(1+j) \\
&= \sqrt{\pi f\mu\sigma}(1+j)
\end{aligned} \tag{3.3}$$

Let $\sqrt{\pi f\mu\sigma} = \beta$, therefore [8, 10]:

$$\tilde{k} = \beta(1+j) \tag{3.4}$$

The wave number $\tilde{k}$ is complex [8, 10].

3.1 PDE Modelled without a Source Region Included in the Domain

In this section, the analytical solution of a simple boundary-driven problem is derived and analysed. The the electric field $\vec{E}_E$, which produces the eddy currents as discussed in Section 2.3, is induced in the conducting body through a uniform time-varying harmonic electric field located at the boundary of the conducting body.

3.1.1 Problem Statement

The aim is to find an analytical solution to Equation (2.39) with a source-free region. The problem is thus boundary-driven as discussed in Section 2.6. The time-varying field:

$$\vec{E}_S(t) = E_{S_0} cos(\omega t)\hat{i} \tag{3.5}$$

where E_{S_0}, is the constant amplitude and ω, is the angular frequency. Equation (3.5) is specified on the boundary of the domain space at position $z = 0$ on the $z - axis$ and this field is polarised in the positive $\hat{i} - direction$ ($x - axis$). The domain of this problem is the $x - z$ plane and is shown in Figure 3.1.

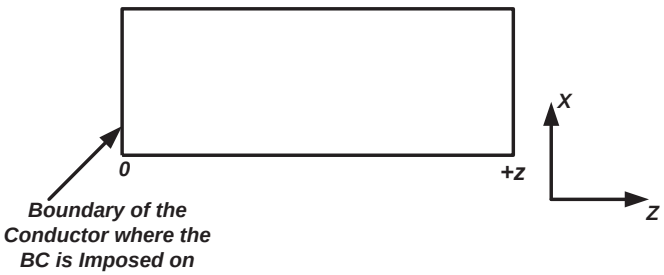

Figure 3.1: Illustration of the Problem Statement of section 3.1.

Convert Equation (3.21) to phasor form [5, 8]:

$$\vec{E}_S(t) = \mathbb{R}e\left(E_{S_0}e^{j\omega t}\right)\hat{i} \tag{3.6}$$

$$\tilde{E_S} = E_{S_0} \tag{3.7}$$

where $\tilde{E_S} = E_{S_0}e^{j\theta}$, but $\theta = 0$. Equation (3.7) will form the boundary condition equation of this problem.

3.1.2 Analytical Solution of Problem

Assume that the, electric vector field component $\tilde{E_E}$ is polarised in the $x-direction$ and travels in the $z-direction$ [8, 3]. Equation (3.2) will take on the following form [8, 3]:

$$\frac{\partial^2\tilde{E_x}}{\partial z^2} - \tilde{k^2}\tilde{E_x} = 0 \tag{3.8}$$

Equation (3.8) is subjected to the following boundary conditions [8]:

$$\tilde{E_x}(0) = E_{S_0} \tag{3.9}$$

$$\tilde{E_x}(\infty) = 0 \tag{3.10}$$

The analytical solution to Equation (3.8) subject to the boundary conditions given by Equations (3.9) and (3.10) is derived to be:

$$\vec{E_x}(z,t) = E_{S_0}e^{-\beta z}\cos(\omega t - \beta z)\,\hat{i} \tag{3.11}$$

where $\beta = \sqrt{\pi f\mu\sigma}$. Please refer to Appendix A for the full derivation of how the solution given by Equation (3.11) was obtained.

Equation (3.11), gives the solution of a spatial propagating *vector wave* $\vec{E_x}$, with an exponential decay in the wave amplitude [5]. The constant β, within the exponential decaying term $e^{-\beta z}$ is also known as the attenuation constant [21, 5]. The phase constant has the same value as the attenuation constant [21, 5].

3.1.3 Skin Depth and Skin Effect Phenomena

The electric field vector wave $\vec{E_x}$, travelling in a conducting media is attenuated by a factor $e^{-\beta z}$ as the wave travels along the direction of propagation (the $z-axis$) , of Equation (3.11) [21]. The attenuation constant $\beta = \sqrt{\pi f\mu\sigma}$ is be written as:

$$\begin{aligned}\delta &= \frac{1}{\beta} \\ &= \frac{1}{\sqrt{\pi f\mu\sigma}}\end{aligned} \tag{3.12}$$

where δ is a constant with dimension in meters $[m]$, this length is called the **skin depth** of the material [5]. The skin depth δ is defined to be the distance after which $\left|\vec{E}_x\right|$, the magnitude of the electric field vector wave $\vec{E}_x$, has decreased to exactly e^{-1} (approximately 36.8%) of it's initial value as the wave penetrates into the domain. For a given medium (eg. $\mu, \sigma = constant$), the skin depth will decrease with increasing frequency, this is known as the **skin effect** [5]. In the particular case of a perfect conductor (or superconductor when $\sigma \to \infty$), the skin depth becomes zero, and it is independent of frequency [5]. The electric and magnetic fields do not penetrate into the medium at all, this is known as the Meissner's effect [19, 9].

The skin depth of a particular material *depends on the frequency* of the electromagnetic wave and on the *conductivity of the material* itself [5]. Eddy currents tend to develop on the outer surfaces of conductors, a phenomenon known as skin effect [17]. The penetration depth is a very important parameter in eddy current phenomenon, and expresses the ability of penetration of the electromagnetic field in conducting bodies [17]. The skin effect has a direct relationship to frequency [17]. The higher the frequency, the smaller the penetration depth [17].

3.1.4 Analysis of Problem

1. Equation (3.11) mathematically describes a spatial propagating sinusoidal wave travelling in the positive $z-direction$ [5] .The electric field is also perpendicular to the direction of the wave propagation and is thus the wave is referred to as a transverse wave [9].

2. The vector wave as it travels along the $z-axis$, decays exponentially (attenuates) in amplitude due to the damping term $e^{-\beta z}$ in the positive $z-direction$ [5, 21]. The decaying exponential term $e^{-\beta z}$, where $\beta = \sqrt{\pi f \mu \sigma}$, controls the attenuation depth of the wave as it travels along the $z-axis$ as described by Equation (3.11), thus the attenuation depth of the wave mathematically depends directly on the variables such as, frequency (f), permittivity (μ) and conductivity (σ) [5, 21]. The attenuation term $e^{-\beta z}$, is directly responsible for the *skin effect* behaviour described in subsection 3.1.3 when the frequency term f is varied [5, 21].

3. The sinusoidal wave originates from the boundary located at coordinate, $z = 0$, due to the excitation boundary condition given by Equation (3.9) [8, 10].

4. The electric field $\vec{E}_x$, exerts a force on the free electrons within the conducting body and thus causes the motion of these electrons [9, 10, 5]. The movement of the electrons produces a current [9, 10, 5] within the conducting body and thus eddy currents $\vec{J}_E$ are formed [19], refer to section 2.3.

The analytical solution, Equation (3.11) is illustrated in Figure 3.2a at a frequency of $f = 5$Hz, time $t = 0$s and Figure 3.2b at a frequency of $f = 0.5$Hz, time $t = 0$s.

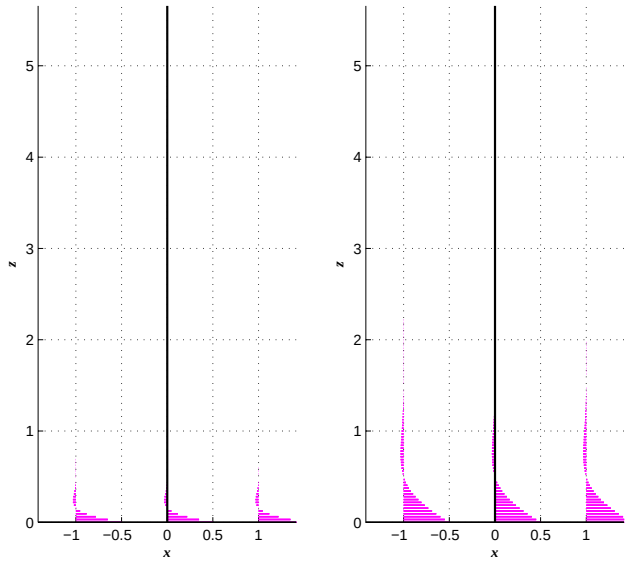

(a) (b)

Figure 3.2: Graphical Solution of Equation (3.11)

Sub-figure 3.2a, simulated at a frequency of $f = 5$Hz. At this frequency, the electric vector wave $\vec{E}_x$ does not propagate far along the $z-axis$. This is an example of skin depth phenomena (refer to subsection 3.1.3). Sub-figure 3.2b, simulated at a frequency of $f = 0.5$Hz. At a lower frequency, the electric vector wave $\vec{E}_x$ propagates further along the $z-axis$ in comparison to the wave in sub-figure 3.2a.

3.2 PDE Modelled with a Source Region Included in the Domain

In this section, the analytical solution of a simple force-driven problem is derived and analysed. The electric field $\vec{E}_E$, which produces the eddy currents, as discussed in Section 2.3 is induced in the conducting body through a uniform time-varying harmonic electric field. The electric field is located at a source/excitation region within the conducting body.

3.2.1 Problem Statement

The aim is to find an analytical solution to Equation (2.39) that contains a source region. An excitation time-varying field:

$$\vec{E}_S(t) = E_{s0}\cos(\omega t)\hat{i} \tag{3.13}$$

is specified on the source region, this field is polarised in the positive $\hat{i}-direction$ ($x-axis$). The domain of this problem is the $x-z$ plane and the location of the source region is at the centre of the domain, at position $z = 0$ as shown in Figure 3.3.

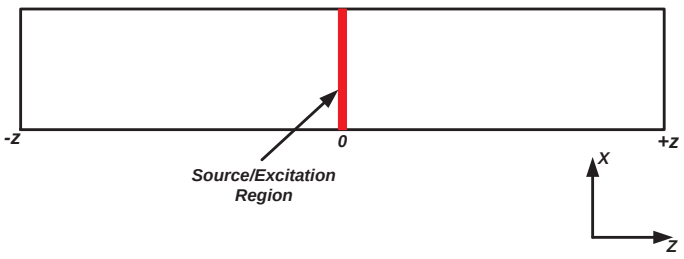

Figure 3.3: Illustration of the Problem Statement of section 3.2.

Convert Equation (3.21) to phasor form:

$$\vec{E}_S(t) = \mathbb{R}e\left(E_{s0}e^{j\omega t}\right)\hat{i} \tag{3.14}$$

$$\tilde{E} = E_{s0} \tag{3.15}$$

where $\tilde{E} = E_{s0}e^{j\theta}$, but $\theta = 0$. Equation (3.15) will form the boundary condition equation of this problem.

3.2.2 Analytical Solution of Problem

Assume that the, $\tilde{E_E}$-field is polarised in the $\hat{i} - direction$ and travels in the $\hat{k} - direction$ ($z - axis$). Equation (3.2) will take on the following form [8, 3]:

$$\frac{\partial^2 \tilde{E_x}}{\partial z^2} - \tilde{k}^2\tilde{E_x} = 0 \tag{3.16}$$

Equation (3.16) is subjected to the following forced condition:

$$\tilde{E_x}(0) = E_{s0} \tag{3.17}$$

The analytical solution to Equation (3.16) subject to the boundary condition given by Equation (3.17) is derived to be:

$$\begin{aligned} \vec{E_x}(z,t) &= \begin{cases} \frac{E_{s0}}{2}e^{\beta z}cos(\omega t + \beta z) & for \quad z < 0 \\ \frac{E_{s0}}{2}e^{-\beta z}cos(\omega t - \beta z) & for \quad z \geq 0 \end{cases} \\ &= \frac{E_{s0}}{2}e^{-\beta|z|}cos(\omega t - \beta|z|) \end{aligned} \tag{3.18}$$

where $\beta = \sqrt{\pi f \mu \sigma}$. Please refer to Appendix A for the full derivation of how the solution given by Equation (3.18) was obtained.

Equation (3.18), gives the solution of two propagating waves travelling in opposite directions along the $z - axis$. The waves emerge from a "source point" and decays in amplitude in the directions of wave propagation [5]. The constant β, within the exponential decaying term $e^{-\beta z}$ is also known as the attenuation constant [21, 5]. The phase constant has the same value as the attenuation constant [21, 5].

3.2.3 Analysis of Problem

- Equation (3.18) describes a pair of sinusoidal waves travelling in the positive $z - direction$ and negative $z - direction$ respectively.

- The sinusoidal waves, as they travel are decaying exponentially due to the damping terms $e^{-\beta z}$ in the positive $z-direction$ and $e^{\beta z}$ in the negative $z-direction$ respectively. At the boundaries of the domain the following boundary conditions are implicitly implied:

$$\tilde{E_x}(\infty) = 0 \tag{3.19}$$

$$\tilde{E_x}(-\infty) = 0 \tag{3.20}$$

  Both sinusoidal waves originate from a spatial source region located at co-ordinate, $z = 0$.

- The attenuating wave behaviour throughout the domain described by Equation (3.18) was caused by a time-varying electric field $\vec{E_S}(t)$ given by Equation (3.13), located at the source region.

The analytical solution, Equation (3.18) is illustrated in Figure 3.4a at a frequency of $f = 5$Hz, time $t = 0$s and Figure 3.4b at a frequency of $f = 0.5$Hz, time $t = 0$s.

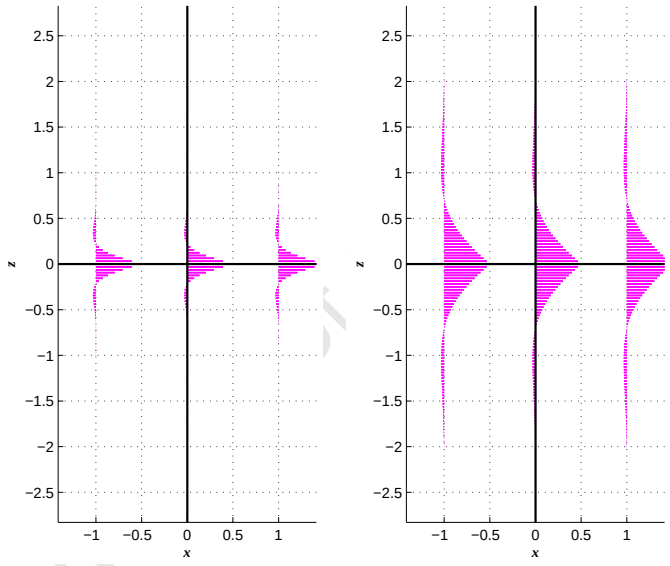

(a) (b)

Figure 3.4: Graphical Solution of Equation (3.11)

Sub-figure 3.4a, simulated at a frequency of $f = 5$Hz. At this frequency, the electric vector wave $\vec{E_x}$ does not propagate far along the positive $z-axis$ and the negative $z-axis$. Sub-figure 3.4b, simulated at a frequency of $f = 0.5$Hz. At a lower frequency, the electric vector wave $\vec{E_x}$ propagates further along the positive $z-axis$ and the negative $z-axis$ in comparison to the wave in sub-figure 3.4a.

3.3 Electric Field Induced within a Conducting Body through a Uniform Time-Varying Harmonic Magnetic Field

In this section, the analytical solution of a boundary-driven problem is derived and analysed. The the electric field $\vec{E_E}$, which produces the eddy currents, as discussed in Section 2.3 is induced in the conducting body through a uniform time-varying harmonic magnetic field located at the boundary of the conducting body.

3.3.1 Problem Statement

The aim is to find an analytical solution to Equation (2.39) with a source-free region, the problem is thus boundary-driven. The time-varying magnetic field:

$$\vec{B}_S(t) = B_0 cos(\omega t)\hat{k} \tag{3.21}$$

is specified on the boundary plane ($x-y$ plane) at the position $z=0$ on the $z-axis$ of the domain space, this field is polarised in the positive $\hat{k}-direction$ ($z-axis$) as shown in Figure 3.5.

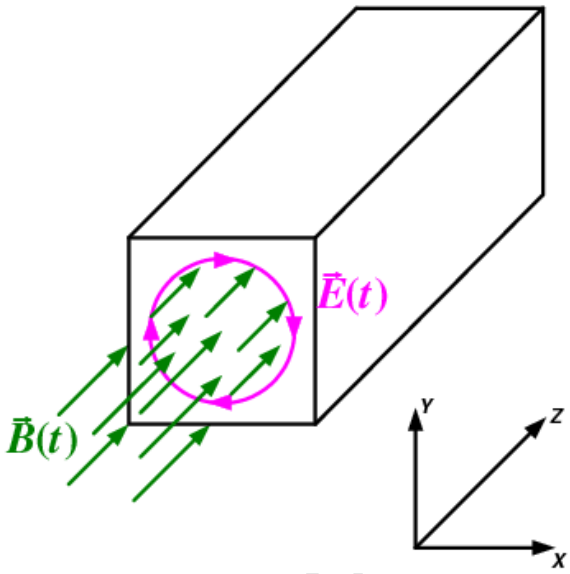

Figure 3.5: Illustration of the Problem Statement of section 3.3.
The magnetic field $\vec{B}(t)$, is uniform over a circular area centred on the origin $(x,y)=(0,0)$, on the surface of the boundary plane ($x-y$ plane).

Convert the time derivative of Equation (3.21) to phasor form:

$$\begin{aligned} \vec{B}_S(t) &= B_0 cos(\omega t)\hat{k} \\ &= \mathbb{R}e\left(B_0 e^{j\omega t}\right) \end{aligned} \tag{3.22}$$

$$\vec{B}_S(t) = \mathbb{R}e\left(B_0 e^{j\omega t}\right) \tag{3.23}$$

$$\begin{aligned} \frac{\partial \vec{B}_S(t)}{\partial t} &= \mathbb{R}e\left(j\omega B_0 e^{j\omega t}\right) \\ -\frac{\partial \vec{B}_S(t)}{\partial t} &= \mathbb{R}e\left(-\tilde{B}_S(\omega)\, e^{j\omega t}\right) \end{aligned} \tag{3.24}$$

$$\tilde{B}_S(\omega) = -j\omega B_0 \tag{3.25}$$

where $\tilde{B}_S(\omega) = -j\omega B_0 e^{j\theta}$, but $\theta = 0$. Applying Equation (2.11) , Faraday's law to Equation (3.25) yields:

$$\begin{aligned} \frac{\partial \tilde{E}_y}{\partial x} - \frac{\partial \tilde{E}_x}{\partial y} &= -j\omega B_0 \\ \frac{\partial \tilde{E}_x}{\partial y} - \frac{\partial \tilde{E}_y}{\partial x} &= j\omega B_0 \\ \frac{\partial\left(\frac{1}{2} y j\omega B_0\right)}{\partial y} - \frac{\partial\left(-\frac{1}{2} x j\omega B_0\right)}{\partial x} &= j\omega B_0 \end{aligned} \tag{3.26}$$

$$\tilde{E_x} = \frac{1}{2} y j\omega B_0 \tag{3.27}$$

$$\tilde{E_y} = -\frac{1}{2} x j\omega B_0 \tag{3.28}$$

Thus, the magnetic field, Equation (3.21) produces a circulating time-varying electric field, given in phasor form as:

$$\begin{aligned} \tilde{E_S} &= \tilde{E_x}\hat{i} + \tilde{E_y}\hat{j} \\ &= \frac{1}{2} y j\omega B_0 \hat{i} + \left(-\frac{1}{2} x j\omega B_0 \hat{j} \right) \\ &= \frac{1}{2} j\omega B_0 \left(y\hat{i} - x\hat{j} \right) \end{aligned} \tag{3.29}$$

This circular/rotational $\tilde{E_S}$-field given by Equation (3.29), is centred about the origin of the boundary plane ($x-y$ plane) and will form the boundary condition equation of this problem.

3.3.2 Analytical Solution of Problem

Assume that the, $\tilde{E_E}$-field is polarised in the $\hat{i} - direction$ and $\hat{j} - direction$ and travels in the $\hat{k} - direction$ ($z - axis$). Equation (3.2):

$$\vec{\nabla}^2 \tilde{E_E} - \tilde{k}^2 \tilde{E_E} = 0$$

will take on the following forms when decomposed into its vector components:

$$\frac{\partial^2 \tilde{E_x}}{\partial z^2} - \tilde{k}^2 \tilde{E_x} = 0 \tag{3.30}$$

in the $\hat{i} - direction$ and

$$\frac{\partial^2 \tilde{E_y}}{\partial z^2} - \tilde{k}^2 \tilde{E_y} = 0 \tag{3.31}$$

in the $\hat{j} - direction$.

Vector Component in $\hat{i} - direction$. Beginning with Equation (3.30):

$$\frac{\partial^2 \tilde{E_x}}{\partial z^2} - \tilde{k}^2 \tilde{E_x} = 0$$

in the $\hat{i} - direction$ and. Equation (3.30) is subjected to the following boundary conditions:

$$\tilde{E_x}(0) = \frac{1}{2} y j\omega B_0 \tag{3.32}$$

$$\tilde{E_x}(\infty) = 0 \tag{3.33}$$

The analytical solution to Equation (3.30) subject to the boundary conditions given by Equations (3.32) and (3.33) is derived to be:

$$\begin{aligned} E_x(z,t) &= \frac{1}{2} y j\omega B_0 e^{-\beta z} \left[cos(\omega t - \beta z) - j sin(\omega t - \beta z) \right] \\ &= -\frac{1}{2} y\omega B_0 e^{-\beta z} sin(\omega t - \beta z) \end{aligned} \tag{3.34}$$

where $\beta = \sqrt{\omega\mu\sigma}$.

Vector Component in $\hat{j}-direction$. Beginning with Equation (3.31):

$$\frac{\partial^2 \tilde{E}_y}{\partial z^2} - \tilde{k^2}\tilde{E}_y = 0$$

in the $\hat{j}-direction$. Equation (3.31) is subjected to the following boundary conditions:

$$\tilde{E}_y(0) = E_{s0} \tag{3.35}$$

$$\tilde{E}_y(\infty) = 0 \tag{3.36}$$

The analytical solution to Equation (3.30) subject to the boundary conditions given by Equations (3.35) and (3.36) is derived to be:

$$\begin{aligned} E_y(z,t) &= -\frac{1}{2}xj\omega B_0 e^{-\beta z}\left[cos(\omega t-\beta z) - jsin(\omega t-\beta z)\right] \\ &= \frac{1}{2}x\omega B_0 e^{-\beta z} sin(\omega t-\beta z) \end{aligned} \tag{3.37}$$

where $\beta = \sqrt{\omega\mu\sigma}$. The full solution of the problem is obtained by adding together the solutions of Equations (3.34) and (3.37), this gives:

$$\begin{aligned} \vec{E}_E(x,y,z,t) &= E_x(y,z,t)\,\hat{i} + E_y(x,z,t)\,\hat{j} \\ &= -\frac{1}{2}y\omega B_0 e^{-\beta z} sin(\omega t-\beta z)\,\hat{i} + \frac{1}{2}xj\omega B_0 e^{-\beta z} sin(\omega t-\beta z)\,\hat{j} \\ &= \left(-\frac{1}{2}y\omega B_0\hat{i} + \frac{1}{2}x\omega B_0\hat{j}\right) e^{-\beta z} sin(\omega t-\beta z) \\ &= \frac{1}{2}\omega B_0\left(-y\hat{i}+x\hat{j}\right) e^{-\beta z} sin(\omega t-\beta z) \end{aligned} \tag{3.38}$$

Please refer to Appendix A for the full derivation of how the solution given by Equation (3.38) was obtained.

3.3.3 Analysis of Problem

1. Equation (3.38) describes a sinusoidal vector wave (having $\hat{i}-directed$ and $\hat{j}-directed$ vector components) travelling in the positive $z-direction$. The vector wave, as it travels along the $z-axis$, decays exponentially (attenuates) due to the damping terms $e^{-\beta z}$in the positive $z-direction$. The wave originates from the boundary located at co-ordinate, $z=0$, due to the excitation boundary condition (time-varying magnetic field) given by Equation (3.21). The analytical solution, Equation (3.38) is illustrated in Figure 3.6a.

2. Equation (3.38) in phasor form:

$$\tilde{E}_E(x,y,z) = \frac{1}{2}\omega B_0\left(-y\hat{i}+x\hat{j}\right) e^{-\beta z} e^{-j\beta z} \tag{3.39}$$

The $\tilde{E}_E$-field wave Equation (3.39), has an *"anti-clockwise" polarised rotational direction* $\left(-y\hat{i}+x\hat{j}\right)$, that is *opposite* to the time-varying $\tilde{E}_S$-field, given by Equation (3.29), which posses a *"clockwise" polarised rotational direction* $\left(y\hat{i}-x\hat{j}\right)$. The "clockwise" time-varying $\tilde{E}_S$-field was produced by a time-varying magnetic field that was polarised in the positive $\hat{k}-direction$ given by Equation (3.21) (refer to section 3.3.1), here the magnetic field is rewritten for the reader's convenience:

$$\vec{B}_S(t) = B_0 cos(\omega t)\,\hat{k}$$

Equation (3.21) can also be written as:

$$\vec{H}_S(t) = H_0 \mu cos(\omega t)\hat{k} \tag{3.40}$$

where $B_0 = H_0\mu$. The $\tilde{E}_E$-field wave given by Equation (3.39), will produce its own magnetic field $\vec{H}_E$ (refer to section 2.3). The "anti-clockwise" rotation direction of the $\tilde{E}_E$-field wave given by Equation (3.39), suggests according to Faraday's law (refer Equation (3.26)) that this time-varying $\vec{H}_E$-field would be polarised in the negative $\hat{k} - direction$. Equation (3.29) and Equation (3.39), illustrates Lenz's law analytically.

Two simulations of the analytical solution given by Equation (3.38) were simulated at frequencies of $f = 5$Hz and $f = 1$Hz shown in Figure 3.6a and 3.6b respectively.

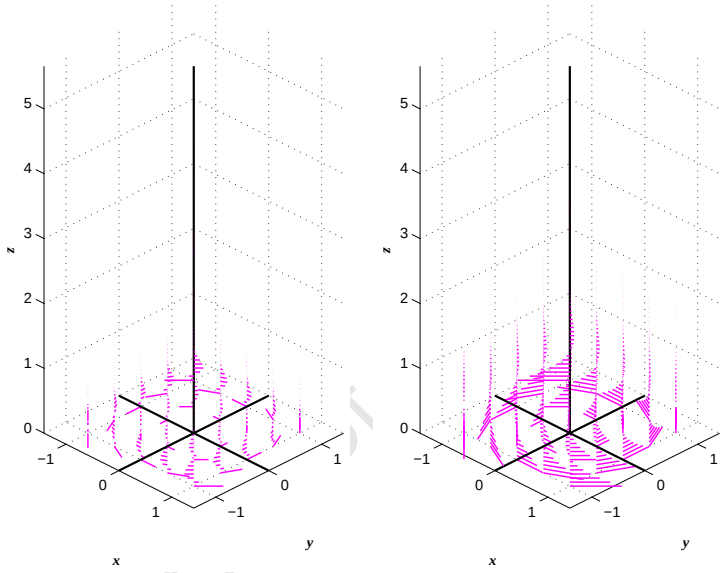

(a) (b)

Figure 3.6: Graphical Solutions of Equation (3.38)

Sub-figure 3.6a, simulated at a frequency of $f = 5$Hz. Single frame picture taken from a movie simulation that runs for approximately 43 seconds. The high frequency value causes the following effects to the vector wave: The wave only travels a short distance along the axis of wave propagation (the $z - axis$) due to an increase in attenuation strength, refer to sub-section 3.1.3. Wave propagation could be seen because the wavelength λ, is small in comparison to the dimension of the domain along the $z - axis$. Sub-figure 3.6b, simulated at a frequency of $f = 1$Hz. Single frame picture taken from a movie simulation that runs for approximately 43 seconds. The low frequency value causes the following effects to the vector wave: The wave travels a longer distance along the axis of wave propagation (the $z - axis$) in comparison to the wave in Figure 3.6a due to an decrease in attenuation strength, refer to sub-section 3.1.3.

Chapter 4

Nodal Finite Elements

The earliest finite elements were designed to approximate scalar fields [7] and these finite elements are also referred to in this dissertation as scalar finite elements. This chapter explains the theory used in the construction of scalar finite elements.

4.1 Scalar Field

A two-dimensional scalar field can be written algebraically as:

$$F(x,y) = f_0 + f_1 x + f_2 y \tag{4.1}$$

where Equation (4.1) can be classified as a polynomial function of two variables ($F(x,y)$) [4, 6] and also as a linear (first-order) polynomial function [4, 6]. The variables f_0, f_1 and f_2 are the coefficients (which are constants) of the polynomial function [4, 6].

4.2 Simplex Elements

Geometries such as lines in one dimension, triangles in two dimension and tetrahedrons in three dimension are often called simplex elements because they are the simplest possible shapes, with the minimum number of vertices, in two and three dimensions respectively, that is found in space [2, 3]. Any polygon no matter how irregular, can be represented exactly as a union of triangles, and any polyhedron can be represented as a union of tetrahedrons [2]. It is thus reasonable to employ the triangle as the fundamental element shape when subdividing a domain in two dimensions, and to extend a similar treatment to three dimensional domain problems by using tetrahedrons [2].

4.3 Two Dimensional Triangular Scalar Finite Element

In the scope of this dissertation, the scalar finite element is capable of constructing scalar fields of the algebraic form as in Equation (4.1) [7].

4.3.1 Triangular Coordinate Transformation

The coordinates of any point within a unit right angled triangle can be transformed to any point within an arbitrary triangle within the cartesian coordinate system by the use of a

transformation matrix [5]. The transformation matrix is derived as follows:

$$P = \begin{bmatrix} 1 & 1 & 1 \\ x_1 & x_2 & x_3 \\ y_1 & y_2 & y_3 \end{bmatrix} \tag{4.2}$$

and

$$U = \begin{bmatrix} 1 & 1 & 1 \\ u_1 & u_2 & u_3 \\ v_1 & v_2 & v_3 \end{bmatrix} \tag{4.3}$$

where Equation (4.2) is called the coordinate matrix which contains the coordinate points (x_1,y_1), $(x_2,y_2)$and (x_3,y_3) located at the vertices (nodes) of an arbitrary triangular element [5]. Another matrix given by Equation (4.3) called the unit coordinate matrix contains the coordinate points (u_1,v_1), $(u_2,v_2)$and (u_3,v_3) located at the vertices (nodes) of a unit right angled triangle [5]. Equation (4.4) computes the transformation matrix:

$$\begin{aligned} T &= PU^{-1} \\ &= \begin{bmatrix} 1 & 0 & 0 \\ x_2 & x_3-x_2 & x_1-x_2 \\ y_2 & y_3-y_2 & y_1-y_2 \end{bmatrix} \end{aligned} \tag{4.4}$$

Equation (4.5) illustrates how the transformation matrix given by Equation (4.4) is used to transform coordinates located in the unit right angled triangle to coordinates located in an arbitrary triangular element:

$$\begin{bmatrix} 1 \\ x \\ y \end{bmatrix} = \begin{bmatrix} 1 & 0 & 0 \\ x_2 & x_3-x_2 & x_1-x_2 \\ y_2 & y_3-y_2 & y_1-y_2 \end{bmatrix} \begin{bmatrix} 1 \\ u \\ v \end{bmatrix} \tag{4.5}$$

$$= \mathscr{L} \begin{pmatrix} 1 \\ u \\ v \end{pmatrix} \tag{4.6}$$

where RHS of Equation (4.5) is a arbitrary set of coordinates located within an arbitrary triangle of the cartesian coordinate system. The LHS of Equation (4.5) contains the coordinate transformation matrix as well as the known coordinates of the unit right angled triangle. In Equation (4.6) the transformation matrix is symbolised by the linear operator $\mathscr{L}$. The transformation matrix in Equation (4.5) is calculated by using the known cartesian points $(x_1,y_1) = (3,4)$, $(x_2,y_2) = (1,2)$and $(x_3,y_3) = (5,1)$ located at the vertices (nodes) of the arbitrary triangle in sub-figure 4.1b. The transformation of the cartesian points from the unit right angle in sub-figure 4.1a to the arbitrary triangle in sub-figure 4.1b is as follows:

$$\begin{aligned} \mathscr{L}(u_1,v_1) &= \mathscr{L}(0,1) \\ &= (x_1,y_1) \\ &= (3,4) \end{aligned} \tag{4.7}$$

and

$$\begin{aligned} \mathscr{L}(u_2,v_2) &= \mathscr{L}(0,0) \\ &= (x_2,y_2) \\ &= (1,2) \end{aligned} \tag{4.8}$$

and

$$\begin{aligned} \mathscr{L}(u_3,v_3) &= \mathscr{L}(1,0) \\ &= (x_3,y_3) \\ &= (5,1) \end{aligned} \tag{4.9}$$

The operator $\mathscr{L}$, transforms coordinates from one coordinate system, the unit right angled triangle coordinate system, to another coordinate system, an arbitrary triangle.

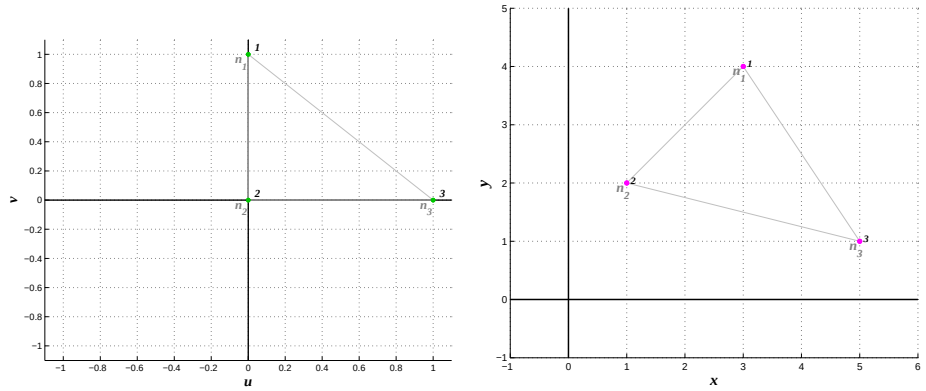

(a) (b)

Figure 4.1: Coordinate Transformation of a Triangle in the Cartesian Coordinate System
Sub-figure 4.1a illustrates the cartesian points $(u_1,v_1) = (0,1)$ is located at node n_1, $(u_2,v_2) = (0,0)$ is located at node n_2 and $(u_3,v_3) = (1,0)$ is located at node n_3 on the unit right angle triangle. Sub-figure 4.1b illustrates that using Equation (4.5) the cartesian points located at the nodes of the unit right angle triangle were transformed to the cartesian points located at the nodes of the arbitrary triangle, where $(x_1,y_1) = (3,4)$ is located at node n_1, $(x_2,y_2) = (1,2)$ is located at node n_2 and $(x_3,y_3) = (5,1)$ is located at node n_3 on the arbitrary triangle. .

The Figure 4.2 illustrates the transformation of a greater number of points from the unit right angle triangle to the arbitrary triangle by using the transformation matrix in Equation (4.5).

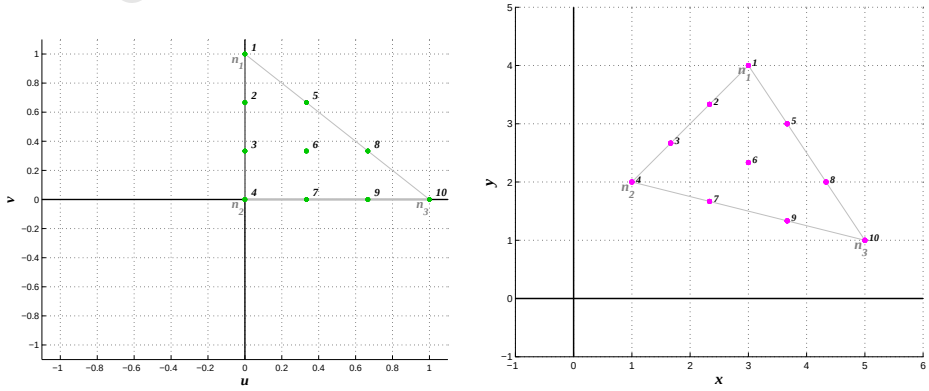

(a) (b)

Figure 4.2: Coordinate Transformation of Multiple Coordinate Points within a Triangle
Sub-figure 4.2a illustrates multiple points that are numbered across the right angle triangle. Sub-figure 4.2b illustrates the transformation of the points in sub-figure 4.2a to the points in the arbitrary triangle. The numbers indicate the transformation position.

4.3.2 Shape Functions

Any linear function, $f^e(x,y)$, within a triangle element can be computed by [2, 5]:

$$f^e(x,y) = a + bx + cy \tag{4.10}$$

$$= \begin{bmatrix} 1 & x & y \end{bmatrix} \begin{bmatrix} a \\ b \\ c \end{bmatrix} \tag{4.11}$$

where coefficients a, b and c have to be known [5]. Equation (4.10) can also be written in the following mathematical form [2, 5]:

$$f^e(x,y) = \lambda_1 f_1 + \lambda_2 f_2 + \lambda_3 f_3 \tag{4.12}$$

$$= \begin{bmatrix} \lambda_1 & \lambda_2 & \lambda_3 \end{bmatrix} \begin{bmatrix} f_1 \\ f_2 \\ f_3 \end{bmatrix} \tag{4.13}$$

where the function values at the nodes $f_1(x_1,y_1) = f_1$, $f_2(x_2,y_2) = f_2$ and $f_3(x_3,y_3) = f_3$ are known [2, 5] and $\lambda_1 = \lambda_1(x,y)$, $\lambda_2 = \lambda_2(x,y)$ and $\lambda_3 = \lambda_3(x,y)$ are linear interpolation functions that span the entire element [1]. A linear interpolation function spanning a triangle must be linear in two orthogonal directions [1]. Since the function values at the nodes are known, Equation (4.10) can be written as a system of linear equations for the three known function values [2, 5]:

$$f_1(x_1,y_1) = a + bx_1 + cy_1 \tag{4.14}$$

$$f_2(x_2,y_2) = a + bx_2 + cy_2 \tag{4.15}$$

$$f_3(x_3,y_3) = a + bx_3 + cy_3 \tag{4.16}$$

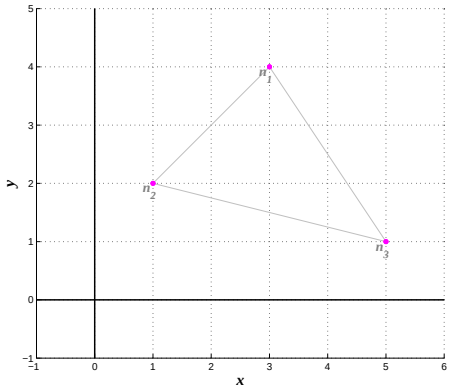

Figure 4.3: Triangle Finite Element

Nodes, n_1 where coordinate (x_1,y_1) is located, n_2 where coordinate (x_2,y_2) is located and n_3 where coordinate (x_3,y_3) is located. The nodes are labelled at the vertices of the triangle.

Equations (4.14), (4.15) and (4.16) are represented in matrix notation [2, 5] as:

$$\begin{bmatrix} f_1 \\ f_2 \\ f_3 \end{bmatrix} = \begin{bmatrix} 1 & x_1 & y_1 \\ 1 & x_2 & y_2 \\ 1 & x_3 & y_3 \end{bmatrix} \begin{bmatrix} a \\ b \\ c \end{bmatrix} \tag{4.17}$$

where the matrix $\begin{bmatrix} 1 & x_1 & y_1 \\ 1 & x_2 & y_2 \\ 1 & x_3 & y_3 \end{bmatrix}$, contains the coordinates located at the nodes of the triangle element as seen in Figure 4.3, these coordinates are known. Calculation of the unknown coefficients $\begin{bmatrix} a \\ b \\ c \end{bmatrix}$, is achieved by [2, 5]:

$$\begin{bmatrix} a \\ b \\ c \end{bmatrix} = \begin{bmatrix} 1 & x_1 & y_1 \\ 1 & x_2 & y_2 \\ 1 & x_3 & y_3 \end{bmatrix}^{-1} \begin{bmatrix} f_1 \\ f_2 \\ f_3 \end{bmatrix} \tag{4.18}$$

but substituting Equation (4.18) into Equation (4.11) gives [2, 5, 3]:

$$f^e(x,y) = \left(\begin{bmatrix} 1 & x & y \end{bmatrix} \begin{bmatrix} 1 & x_1 & y_1 \\ 1 & x_2 & y_2 \\ 1 & x_3 & y_3 \end{bmatrix}^{-1} \right) \begin{bmatrix} f_1 \\ f_2 \\ f_3 \end{bmatrix} \tag{4.19}$$

where

$$\begin{bmatrix} \lambda_1 & \lambda_2 & \lambda_3 \end{bmatrix} = \left(\begin{bmatrix} 1 & x & y \end{bmatrix} \begin{bmatrix} 1 & x_1 & y_1 \\ 1 & x_2 & y_2 \\ 1 & x_3 & y_3 \end{bmatrix}^{-1} \right) \tag{4.20}$$

The interpolation functions are also called shape functions or basis functions [1]. Using MATLAB Symbolic:

$$\begin{bmatrix} 1 & x_1 & y_1 \\ 1 & x_2 & y_2 \\ 1 & x_3 & y_3 \end{bmatrix}^{-1} = \frac{1}{2A_e} \begin{bmatrix} x_2y_3 - x_3y_2 & x_1y_3 - x_3y_1 & x_1y_2 - x_2y_1 \\ y_2 - y_3 & y_3 - y_1 & y_1 - y_2 \\ x_3 - x_2 & x_1 - x_3 & x_2 - x_1 \end{bmatrix} \tag{4.21}$$

$$= \begin{bmatrix} a_1 & a_2 & a_3 \\ b_1 & b_2 & b_3 \\ c_1 & c_2 & c_3 \end{bmatrix} \tag{4.22}$$

where the area of the triangle element is:

$$A_e = \frac{1}{2}(x_2y_3 - x_3y_2 - x_1y_3 + x_1y_2 + y_1x_3 - y_1x_2) \tag{4.23}$$

Equation (4.22) contains the coefficients of the shape functions [3]. Substituting Equation (4.22) into Equation (4.20) gives:

$$\lambda_1(x,y) = a_1 + b_1x + c_1y \tag{4.24}$$
$$\lambda_2(x,y) = a_2 + b_2x + c_2y \tag{4.25}$$
$$\lambda_3(x,y) = a_3 + b_3x + c_3y \tag{4.26}$$

Substituting Equation (4.21) into Equations (4.24), (4.25) and (4.26) gives [5]:

$$\lambda_1(x,y) = \frac{(x_2y_3 - x_3y_2) + (y_2 - y_3)x + (x_3 - x_2)y}{2A_e} \tag{4.27}$$
$$\lambda_2(x,y) = \frac{(y_1x_3 - x_1y_3) + (y_3 - y_1)x + (x_1 - x_3)y}{2A_e} \tag{4.28}$$
$$\lambda_3(x,y) = \frac{(x_1y_2 - y_1x_2) + (y_1 - y_2)x + (x_2 - x_1)y}{2A_e} \tag{4.29}$$

The shape functions have been derived in complete symbolic notation. Equation (4.27), (4.28) and (4.29) shows that the coefficients of the shape functions are constructed from the known coordinates at the nodes of the triangle element in Figure 4.3. Substituting Equation (4.22) into Equation (4.18) produces:

$$\begin{bmatrix} a \\ b \\ c \end{bmatrix} = \begin{bmatrix} a_1 & a_2 & a_3 \\ b_1 & b_2 & b_3 \\ c_1 & c_2 & c_3 \end{bmatrix} \begin{bmatrix} f_1 \\ f_2 \\ f_3 \end{bmatrix} \tag{4.30}$$

Equation (4.30) represents the coefficients of Equations (4.24), (4.25) and (4.26) as a linear combination of the known function values at the nodes $\begin{bmatrix} f_1 \\ f_2 \\ f_3 \end{bmatrix}$, and the coefficients of the shape functions $\begin{bmatrix} a_1 & a_2 & a_3 \\ b_1 & b_2 & b_3 \\ c_1 & c_2 & c_3 \end{bmatrix}$.

Using the above equations a mathematical proof was derived showing that any function value $f^e(x,y)$, within a triangle element can be calculated from a linear combination of the three shape functions given by Equations (4.27), (4.28) and (4.29) and the three known function values $f_1(x_1,y_1) = f_1$, $f_2(x_2,y_2) = f_2$ and $f_3(x_3,y_3) = f_3$ at the nodes of the element:

$$\begin{aligned} f^e(x,y) &= a + bx + cy \\ &= \begin{bmatrix} 1 & x & y \end{bmatrix} \begin{bmatrix} a \\ b \\ c \end{bmatrix} \\ &= \begin{bmatrix} 1 & x & y \end{bmatrix} \left(\begin{bmatrix} a_1 & a_2 & a_3 \\ b_1 & b_2 & b_3 \\ c_1 & c_2 & c_3 \end{bmatrix} \begin{bmatrix} f_1 \\ f_2 \\ f_3 \end{bmatrix} \right) \\ &= \left(\begin{bmatrix} 1 & x & y \end{bmatrix} \begin{bmatrix} a_1 & a_2 & a_3 \\ b_1 & b_2 & b_3 \\ c_1 & c_2 & c_3 \end{bmatrix} \right) \begin{bmatrix} f_1 \\ f_2 \\ f_3 \end{bmatrix} \\ &= \begin{bmatrix} \lambda_1 & \lambda_2 & \lambda_3 \end{bmatrix} \begin{bmatrix} f_1 \\ f_2 \\ f_3 \end{bmatrix} \\ &= \lambda_1 f_1 + \lambda_2 f_2 + \lambda_3 f_3 \end{aligned} \tag{4.31}$$

The end product of Equation (4.31) is written in full notation as:

$$f^e(x,y) = \lambda_1(x,y)\, f_1(x_1,y_1) + \lambda_2(x,y)\, f_2(x_2,y_2) + \lambda_3(x,y)\, f_3(x_3,y_3) \tag{4.32}$$

Equation (4.12) states that the function $f^e(x,y)$, can be calculated at any arbitrary point (x,y), within the triangle element, by the direct summing of the shape functions $\lambda_1(x,y)$, $\lambda_2(x,y)$ and $\lambda_3(x,y)$ of the element along with the known function values $f_1(x_1,y_1)$, $f_2(x_2,y_2)$ and $f_3(x_3,y_3)$ at the nodes of the element.

Visualisation of the Scalar Finite Element and its Corresponding Shape Functions

A small algorithm was coded to visually display a single finite element along with its associated shape functions using the information of sub-sections 4.3.1 and 4.3.2. The

coordinate transformation is calculated according to Equations (4.2), (4.3), (4.4) and (4.5). The shape functions are calculated according to the Equations (4.27), (4.28) and (4.29).

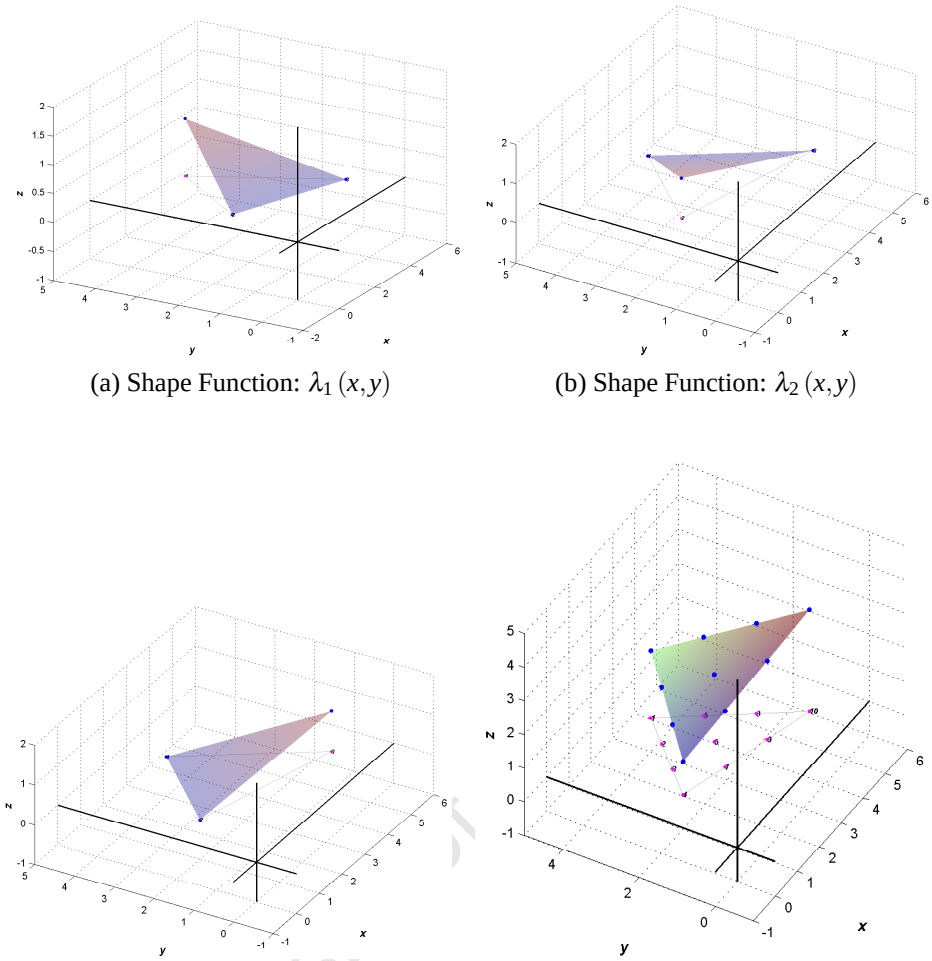

(a) Shape Function: $\lambda_1(x,y)$

(b) Shape Function: $\lambda_2(x,y)$

(c) Shape Function: $\lambda_3(x,y)$

(d) Scalar Field: $f^e(x,y)$

Figure 4.4: Two Dimensional Scalar Finite Element

Figure 4.4d, is a graphical illustration of Equation (4.32). The transparent triangular plate indicates the computed scalar field across the nodal finite element. The blue points located on this transparent triangular plate are the scalar field values $f^e(x,y)$, that are computed through Equation (4.32), using the cartesian points (x,y) within the triangle element of figure 4.3.

Chapter 5

Vector Finite Elements

Vector finite elements were specifically designed to approximate electromagnetic vector fields, also known mathematically as vector functions [2, 3, 7], that obey the Maxwell curl equations [2]. The PDE that models eddy current behaviour is derived from Maxwell's equations in Chapter 2 and the solution to this PDE equation is a vector field (refer to Section 2.5) thus making the vector finite element a highly desirable choice to use within the FE algorithm.

5.1 Preliminary Theory

Some important preliminary theory is provided concerning vectors, vector fields, and EM vector field properties.

5.1.1 Vectors

Any vector can be decomposed into a normal component and tangential component with reference to a certain interface, for example :

$$\vec{E} = E_x\hat{i} + E_y\hat{j} \tag{5.1}$$

where with reference to the y-axis, E_x is the component perpendicular to the y-axis called the normal component and E_y is the component parallel to the y-axis called the tangential component as illustrated in Figure 5.1.

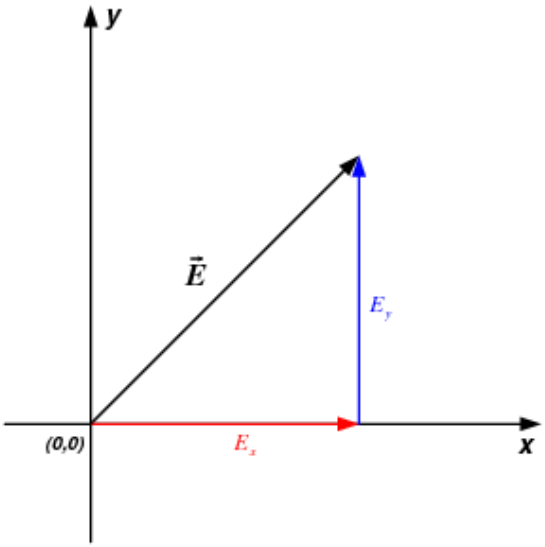

Figure 5.1: Components of a vector

Vector $\vec{E}$, is decomposed into its normal component E_x, and its tangential component E_y. The components E_x and E_y are both constants.

5.1.2 Vector Fields

A two-dimensional vector function can be written in terms of component functions as follows:

$$\vec{E}(x,y) = F(x,y)\,\hat{i} + G(x,y)\,\hat{j} \tag{5.2}$$

where $F(x,y)$ and $G(x,y)$ are the component functions of the vector function $\vec{E}(x,y)$ in the $i-direction$ and $j-direction$ respectively. A typical linear vector field in two dimensions has component functions comprising of linear (first-order) complete polynomial expansion [4, 6, 2]:

$$F(x,y) = f_0 + f_1 x + f_2 y \tag{5.3}$$

where in the $\hat{i}-direction$:

$$G(x,y) = g_0 + g_1 x + g_2 y \tag{5.4}$$

and in the $\hat{j}-direction$. A first-order complete approximation for a two-dimensional function in x and y has three terms [2]. One term is a constant and the other two terms are linear in x and y respectively [2], as seen in Equations (5.3) and (5.4). A complete polynomial expansion can also be referred to as a full-order expansion [13]. These component functions are also known as scalar fields [7].

5.1.2.1 Differential Relations for a Scalar Field

A differential operation can be performed on a scalar field (scalar function) [10, 9, 6]. This differential operation is:

- Gradient of a Scalar Field :

$$\vec{T} = \vec{\nabla} F \tag{5.5}$$

  where F, is a scalar field and $\vec{T}$ is a vector field that is produced when the differential operator $\vec{\nabla}$, "acts upon" F [10].

Gradient of a Scalar Field

This differential relation physically measures the direction of the fastest change of a scalar field in magnitude and direction [10, 9, 6].

5.1.2.2 Differential Relations for Vector Fields

Two important differential operations that can be performed on vector fields [10, 9, 6]. These differential operations are:

- Divergence of a Vector Field :
$$A = \vec{\nabla} \cdot \vec{E} \tag{5.6}$$
where $\vec{E}$, is a vector field and A, is a scalar field that is produced when the differential operator $\vec{\nabla}$, "acts upon" $\vec{E}$ via the dot product [10].

- Curl of a Vector Field :
$$\vec{B} = \vec{\nabla} \times \vec{E} \tag{5.7}$$
where $\vec{E}$, is a vector field and $\vec{B}$, is a vector field that is produced when the differential operator $\vec{\nabla}$, "acts upon" $\vec{E}$ via the cross product [10].

Divergence of a Vector Field

This differential relation physically measures the divergent (spreading out) capability of the vector field $\vec{E}$ (in Equation 5.6), from a point in question or towards a point in question [10, 9, 6]. A divergent vector field can be identified as having a "source point" from where the vector field seems to emerge from or a "sink point" towards where the vector field seems to be heading [10, 9, 6]. A purely divergent vector field has zero curling capability [10, 9, 6] that is:
$$\vec{\nabla} \times \vec{E} = 0 \tag{5.8}$$

Curl of a Vector Field

This differential relation physically measures the rotational (curling) capability of the vector field $\vec{E}$ (in Equation 5.7) around a point in question [10, 9, 6]. A curling vector field can be identified as having no "source point" or "sink point" [10, 9, 6]. A purely rotational vector field has zero divergence capability [10, 9, 6] that is:
$$\vec{\nabla} \cdot \vec{E} = 0 \tag{5.9}$$

5.1.3 Boundary Conditions for Electromagnetic Fields

The boundary conditions are valid for both time-independent and time-dependent electromagnetic fields [5]. In two dimensions and in the cartesian coordinate system, electromagnetic fields can be separated into a component that is parallel to an interface (tangential component) and a component that is perpendicular to an interface (normal component) [5].

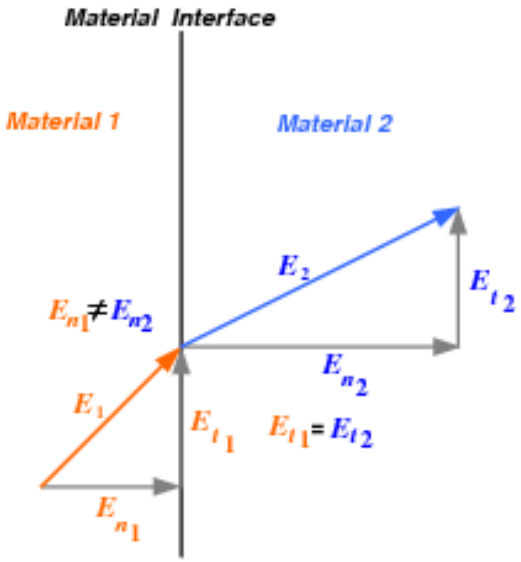

Figure 5.2: Electric Field Deflection Across a Material Interface

The diagram illustrates that the electric field will bend (deflect) as it passes from one medium (material) to another medium, because the tangential components of electric field are continuous and the normal components are discontinuous across the material interface [5, 10]. This bending of electromagnetic waves is called refraction [5, 8].

The tangential components of an electric vector field across a material interface are continuous, that is [5, 8]:

$$\vec{E}_{t1} = \vec{E}_{t2} \tag{5.10}$$

There is a discontinuity between the normal components of an electric vector field across a material interface (different mediums), that is the normal components of an electric vector field across a material interface are not continuous [5, 8]:

$$\vec{E}_{n1} \neq \vec{E}_{n2} \tag{5.11}$$

For example, the normal components of an electric vector field $\vec{E}$, changes abruptly across a dielectric interface because of the dielectric discontinuity [8]:

$$\vec{E}_{n1} = \frac{\varepsilon_2}{\varepsilon_1}\vec{E}_{n2} \tag{5.12}$$

Similarly, the normal components of an electric vector field $\vec{E}$, changes abruptly across a conductor interface because of the conductor discontinuity [8]:

$$\vec{E}_{n1} = \frac{\sigma_2}{\sigma_1}\vec{E}_{n2} \tag{5.13}$$

In electromagnetics, there is a lack of normal continuity of the electric field across different material mediums [7] that is, there is normal discontinuity of the electromagnetic field across different material mediums [8]. Due to the discontinuity of the normal component of Electromagnetic vector fields, *the field vectors will thus change in magnitude and direction across a material interface* [5].

5.2 Two Dimensional Triangular Node-Based Vector Element

To represent a vector field $\vec{E}(x,y)$, with node-based vector elements, the natural approach was to treat the vector field as two coupled scalar fields in two dimensions, E_x in the $\hat{i} - direction$ and E_y in the $\hat{j} - direction$ [7]. The unknown parameters are also called the degrees of freedom and are the two coupled scalar fields located at each node (vertex) of the triangular finite element [7] as illustrated in Figure 5.3.

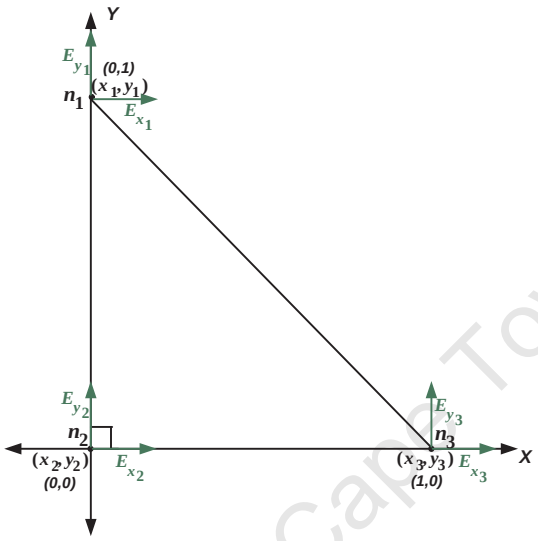

Figure 5.3: Two Dimensional Nodal-Based Vector Element
The scalar fields: E_{x1} and E_{y1} is located at node n_1, E_{x2} and E_{y2} is located at node n_2, E_{x3} and E_{y3} is located at node n_3.

5.2.1 Shape Functions

The shape (basis) functions given by Equations (4.27), (4.28) and (4.29), which are used for the scalar elements are also used for the node-based vector elements . These shape functions are repeated for the readers convenience:

$$\begin{aligned}
\lambda_1 &= \frac{(x_2y_3 - x_3y_2) + (y_2 - y_3)x + (x_3 - x_2)y}{2A_e} \\
\lambda_2 &= \frac{(y_1x_3 - x_1y_3) + (y_3 - y_1)x + (x_1 - x_3)y}{2A_e} \\
\lambda_3 &= \frac{(x_1y_2 - y_1x_2) + (y_1 - y_2)x + (x_2 - x_1)y}{2A_e}
\end{aligned}$$

The algebraic expression of these shape functions can be referred to as complete linear (first-order) polynomials according to sub-section 5.1.2, where this terminology was discussed.

5.2.2 Construction of a Vector Field within a Triangular Node-Based Vector Element

The vector field $\vec{E}_N(x,y)$, across the element can be computed by the following equation [7]:

$$\vec{E}_N(x,y) \simeq \left(E_{x1}\hat{i}+E_{y1}\hat{j}\right)\lambda_1(x,y)+\left(E_{x2}\hat{i}+E_{y2}\hat{j}\right)\lambda_2(x,y)+\left(E_{x3}\hat{i}+E_{y3}\hat{j}\right)\lambda_3(x,y) \tag{5.14}$$

where $\lambda_i(x,y)$ for $i=1:3$ are the nodal shape functions (refer to Equations (4.24), (4.25) and (4.26)) and E_{xi} and E_{yi} for $i=1:3$ are the two coupled scalar fields [7] and $\vec{E}_N(x,y)$ signifies a vector field approximated by a node-based vector element. Equation (4.24), (4.25) and (4.26) is substituted into Equation (5.14). Using MATLAB Symbolic, the complete general symbolic notation of the vector field across the element is:

$$\begin{aligned}
\vec{E}_N(x,y) \simeq & \left(\frac{\left(E_{x1}(x_3-x_2)+E_{x2}(x_1-x_3)+E_{x3}(x_2-x_1)\right)y}{2A_e}\right. \\
& +\frac{\left(E_{x1}(y_2-y_3)+E_{x2}(y_1-y_3)+E_{x3}(y_1-y_2)\right)x}{2A_e} \\
& \left.+\frac{\left(E_{x1}(x_2y_3-x_3y_2)+E_{x2}(y_1x_3-x_1y_3)+E_{x3}(x_1y_2-y_1x_2)\right)}{2A_e}\right)\hat{i}+ \\
& \left(\frac{\left(E_{y1}(x_3-x_2)+E_{y2}(x_1-x_3)+E_{y3}(x_2-x_1)\right)y}{2A_e}\right. \\
& +\frac{\left(E_{y1}(y_2-y_3)+E_{y2}(y_1-y_3)+E_{y3}(y_1-y_2)\right)x}{2A_e} \\
& \left.+\frac{\left(E_{y1}(x_2y_3-x_3y_2)+E_{y2}(y_1x_3-x_1y_3)+E_{y3}(x_1y_2-y_1x_2)\right)}{2A_e}\right)\hat{j}
\end{aligned} \tag{5.15}$$

where the variables (x_1,y_1), (x_2,y_2), (x_3,y_3) are the coordinates at the nodes of the triangle element, A_e is the area of the triangle element given by Equation (4.23), and E_{x1}, E_{x2} , E_{x3}, E_{y1}, E_{y2} and E_{y3} are the coupled scalar fields of the triangle element. Using MATLAB Symbolic to collect all the terms in x, the terms in y and the constant terms in Equation (5.46), it was found that:

The first component function of the field, $\vec{E}_N(x,y)$ takes on the following algebraic structure:

$$F(x,y) = f_0 + f_1x + f_2y \tag{5.16}$$

in the $\hat{i}-direction$. Comparing Equation (5.3) to Equation (5.15), it is found that:

$$f_0 = \frac{\left(E_{x1}(x_2y_3-x_3y_2)+E_{x2}(y_1x_3-x_1y_3)+E_{x3}(x_1y_2-y_1x_2)\right)}{2A_e} \tag{5.17}$$

and

$$f_1 = \frac{\left(E_{x1}(y_2-y_3)+E_{x2}(y_1-y_3)+E_{x3}(y_1-y_2)\right)}{2A_e} \tag{5.18}$$

and

$$f_2 = \frac{\left(E_{x1}(x_3-x_2)+E_{x2}(x_1-x_3)+E_{x3}(x_2-x_1)\right)}{2A_e} \tag{5.19}$$

The second component function of the field , $\vec{E}_N(x,y)$ takes on the following algebraic structure:

$$G(x,y) = g_0 + g_1x + g_2y \tag{5.20}$$

in the $\hat{j}-direction$. Comparing Equation (5.4) to Equation (5.15), it is found that:

$$g_0 = \frac{\left(E_{y1}\left(x_2y_3 - x_3y_2\right) + E_{y2}\left(y_1x_3 - x_1y_3\right) + E_{y3}\left(x_1y_2 - y_1x_2\right)\right)}{2A_e} \tag{5.21}$$

and

$$g_1 = \frac{\left(E_{y1}\left(y_2 - y_3\right) + E_{y2}\left(y_1 - y_3\right) + E_{y3}\left(y_1 - y_2\right)\right)}{2A_e} \tag{5.22}$$

and

$$g_2 = \frac{\left(E_{y1}\left(x_3 - x_2\right) + E_{y2}\left(x_1 - x_3\right) + E_{y3}\left(x_2 - x_1\right)\right)}{2A_e} \tag{5.23}$$

Thus, the vector field has the following general algebraic structure:

$$\vec{E}_N\left(x,y\right) = \left(f_0 + f_1x + f_2y\right)\hat{i} + \left(g_0 + g_1x + g_2y\right)\hat{j} \tag{5.24}$$

where Equation (5.24) is a linear vector field that is, the component functions are complete linear (first-order) polynomials [4, 6, 2] which are similar to Equations (5.3) and (5.4). Thus, the vector field $\vec{E}_N\left(x,y\right)$, takes on the general algebraic structure of Equation (5.2). The element as a whole is considered to be full-order [11]. The node-based vector element supports vector field expansions of the form of Equation (5.24) across a triangular element as derived through Equation (5.15).

5.2.3 Continuity of the Node-based Vector Element

The unknown parameters (degrees of freedom) are the two coupled scalar fields located at each node of the element E_{xi}, for $i = 1:4$, and E_{yj} for $j = 1:4$ [7] as illustrated in Figure 5.4a.

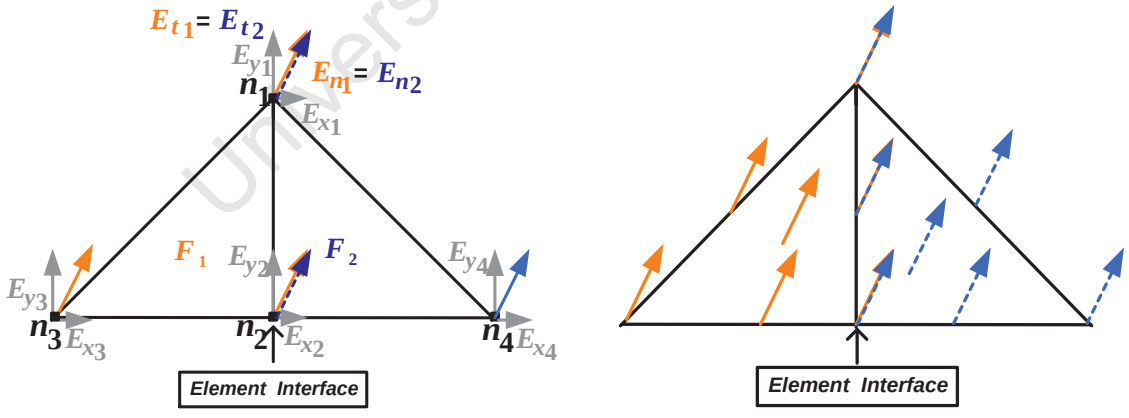

(a) (b)

Figure 5.4: Continuity of the node-based Vector Element Across the Element Interface
Sub-figure 5.4a illustrates that the components E_{xi}, for $i = 1:4$ and E_{yj} for $j = 1:4$ can be viewed as normal and tangential vector components respectively in reference to the element interface. Continuity conditions are placed on these components. Labelling convention: Node numbering n_1, n_2, n_3 and n_4-black, element number one, F_1-red, element number two, F_2-blue. Sub-figure 5.4b illustrates that when continuity conditions are imposed on each cartesian component (normal and tangential) at nodes n_1 and n_2, the result is a vector field that is continuous [7] across both finite elements, thus there is no change in magnitude and direction of the vectors [5] across the element interface.

Figure 5.4a illustrates that the two elements are connected by and share nodes n_1 and n_2. At node n_1, the components E^1_{x1} and E^1_{y1} of the field $\vec{E}^1_N(x,y)$, in element F_1 can be made equal to the components E^2_{x1} and E^2_{y1} of the field $\vec{E}^2_N(x,y)$, in element F_2 by imposing the following continuity condition between the elements:

$$E^1_{x1} = E^2_{x1} \tag{5.25}$$

for component in the $\hat{i} - direction$ and

$$E^1_{y1} = E^2_{y1} \tag{5.26}$$

for component in the $\hat{j} - direction$. The superscript 1 indicates that the components E^1_{x1} and E^1_{y1} and the field $\vec{E}^1_N(x,y)$ all belong to element F_1 and the superscript 2 indicates that the components E^2_{x1} and E^2_{y1} and the field $\vec{E}^2_N(x,y)$ all belong to element F_2. Similarly at node n_2, the same continuity conditions is applied, that is:

$$E^1_{x2} = E^2_{x2} \tag{5.27}$$

for component in the $\hat{i} - direction$ and

$$E^1_{y2} = E^2_{y2} \tag{5.28}$$

for component in the $\hat{j} - direction$. The continuity conditions of Equation (5.25), (5.26), (5.27) and (5.28) forces each cartesian component, normal and tangential, at nodes n_1 and n_2 to be continuous therefore, the entire vector field is continuous [7] across both finite elements and thus there is *no normal discontinuity of this constructed vector field which is a natural property for electromagnetic vector fields [2]. Node-based vector elements impose full-continuity of the vector field across elements* as illustrated in sub-figure 5.4b [7, 13].

Therefore, the use of such elements to solve electromagnetic problems involving changes in material interfaces as discussed in sub-section 5.1.3, where there is a definite discontinuity of the normal part of the vector field as illustrated in Figure 5.2, is not a straightforward task. Certain techniques, which are not in the scope of this dissertation, have been developed to impose tangential continuity and normal discontinuity for node-based vector elements to be used in EM problems [3], but these techniques can be awkward to implement [7].

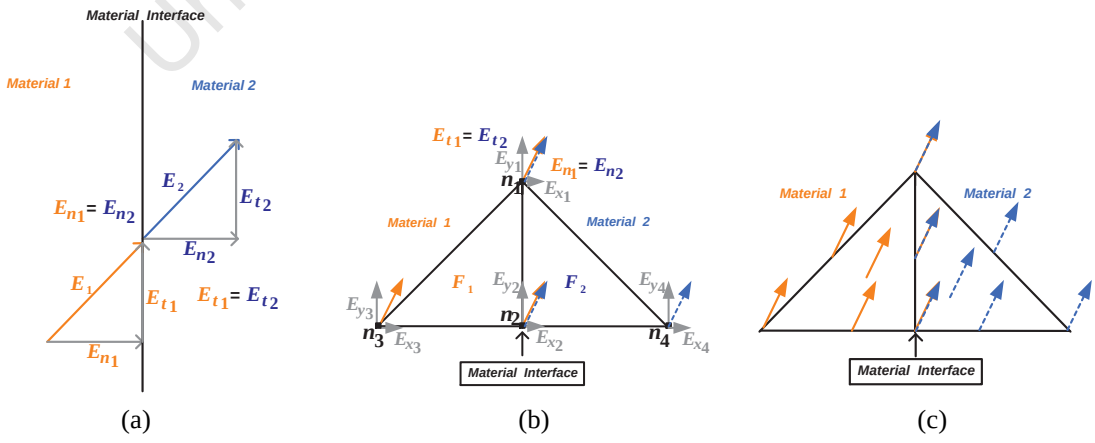

Figure 5.5: Continuity of the node-based Vector Element Across the Material Interface

Sub-figure 5.5a illustrates a vector field will be continuous across an material interface when continuity conditions are placed on both normal and tangential components of this vector field that is, $E^1_n = E^2_n$ and $E^1_t = E^2_t$. Sub-figures 5.5b and 5.5c illustrates how node-based vector elements impose full-continuity of the vector field across material interfaces, thus there is no change in magnitude and direction of the vectors [5] across the material interface .

As a summary to sub-sections 5.2.2 and 5.2.3, these node-based vector elements are both full-order and fully-continuous [11] respectively, where the latter is undesirable for electromagnetic field computations [13]. The "full-order" refers to the component functions possessing complete polynomials expansions as was shown in sub-section 5.1.2 [11, 12].

5.3 Two Dimensional Triangular Vector Element

A two-dimensional vector field $\vec{E}(x,y)$ can be interpolated across a vector element through the use of three shape functions and the edges of the vector element, where the edges are recognised to be the degrees of freedom of the vector finite element, in comparison to the node-based vector element where the coupled scalar fields located at the nodes were the degrees of freedom (refer to Section 5.2)[7]. The edges can be visualised as the "borders" of the vector element that connects the vertices of the element together. Figure 5.6 illustrates a vector finite element consisting of three edges labelled E_{12}, E_{13} and E_{23} and three nodes labelled n_1, n_2 and n_3 [2, 12]. By inspection, the indexing of the edges (shown by their subscripts) can follow the connectivity information of the element, which describes how the edges are connected to the nodes of the element [2, 12]. As illustrated in Figure 5.6:

- Edge E_{12}, is connected to node n_1 and node n_2
- Edge E_{13}, is connected to node n_1 and node n_3
- Edge E_{23}, is connected to node n_2 and node n_3

In the above, E_{ij} is the edge directed from node n_i to node n_j [2, 12]. The edges can also be labelled with the following notation of E_i for $i = 1:3$ [2, 12]. As illustrated in Figure 5.6:

- Edge $E_{12} = E_1$
- Edge $E_{13} = E_2$
- Edge $E_{23} = E_3$

Note that the index i in the notation E_i is different to the index i in the notation E_{ij}.

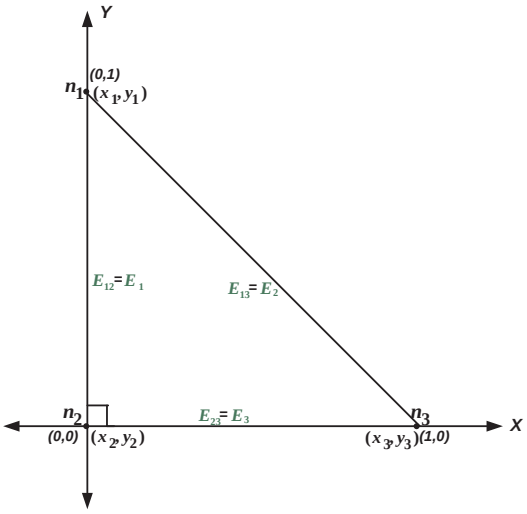

Figure 5.6: Two Dimensional Vector Element

5.3.1 Vector Shape Functions

The vector shape functions of a triangular finite element are defined as follows [2, 3, 7]:

$$\vec{w}_{ij} = \lambda_i \vec{\nabla}\lambda_j - \lambda_j \vec{\nabla}\lambda_i \tag{5.29}$$

There are three such vector functions per triangle [2], which can also be given the following notation of $\vec{N}_i$ for $i = 1:3$. Each shape function $\vec{w}_{ij}$, is associated with an edge E_{ij} directed from n_i to node n_j as follows [2, 12]:

- the edge E_{12}, is associated with the shape function $\vec{w}_{12} = \vec{N}_1$
- the edge E_{13}, is associated with the shape function $\vec{w}_{13} = \vec{N}_2$
- the edge E_{23}, is associated with the shape function $\vec{w}_{23} = \vec{N}_3$

Note that the index i in the notation $\vec{N}_i$ is different to the index i in the notation $\vec{w}_{ij}$. The shape functions used for the nodal finite elements shown in sub-section 4.3.2 are also used to construct the vector shape functions [12, 2]. These shape functions are given by Equations (4.24), (4.25) and (4.26). The gradients of these shape functions are [2, 3]:

$$\vec{\nabla}\lambda_1 = \frac{(y_2 - y_3)}{2A_e}\hat{i} + \frac{(x_3 - x_2)}{2A_e}\hat{j} \tag{5.30}$$

$$\vec{\nabla}\lambda_2 = \frac{(y_3 - y_1)}{2A_e}\hat{i} + \frac{(x_1 - x_3)}{2A_e}\hat{j} \tag{5.31}$$

$$\vec{\nabla}\lambda_3 = \frac{(y_1 - y_2)}{2A_e}\hat{i} + \frac{(x_2 - x_1)}{2A_e}\hat{j} \tag{5.32}$$

for $i, j = 1:3$. The area of the triangular element A_e is given by Equation (4.23) [5].

Using MATLAB Symbolic, the complete symbolic notation of the three vector shape functions for any arbitrary triangle within the cartesian plane was found, using the definition of Equation (5.29):

$$\begin{aligned}
\vec{N}_1 &= \vec{w}_{12} \\
&= \lambda_1\nabla\lambda_2 - \lambda_2\nabla\lambda_1 \\
&= \left(-\frac{1}{4}\frac{(x_2y_3 - x_3y_2 - x_1y_3 + x_1y_2 + y_1x_3 - y_1x_2)y}{A^2} - \frac{1}{4}\frac{(-x_2y_3^2 + x_2y_3y_1 + x_3y_2y_3 + x_1y_3^2 - y_1x_3y_3 - x_1y_3y_2)}{A^2}\right)\hat{i} + \\
&\quad \left(\frac{1}{4}\frac{(x_2y_3 - x_3y_2 - x_1y_3 + x_1y_2 + y_1x_3 - y_1x_2)x}{A^2} + \frac{1}{4}\frac{(-x_2y_3x_3 + x_3^2y_2 - x_3y_2x_1 - y_1x_3^2 + y_1x_3x_2 + x_1y_3x_3)}{A^2}\right)\hat{j} \\
&= \frac{1}{4A^2}\left(-(x_2y_3 - x_3y_2 - x_1y_3 + x_1y_2 + y_1x_3 - y_1x_2)y - (-x_2y_3^2 + x_2y_3y_1 + x_3y_2y_3 + x_1y_3^2 - y_1x_3y_3 - x_1y_3y_2)\right)\hat{i} + \\
&\quad \frac{1}{4A^2}\left((x_2y_3 - x_3y_2 - x_1y_3 + x_1y_2 + y_1x_3 - y_1x_2)x + (-x_2y_3x_3 + x_3^2y_2 - x_3y_2x_1 - y_1x_3^2 + y_1x_3x_2 + x_1y_3x_3)\right)\hat{j}
\end{aligned} \tag{5.33}$$

$$\begin{aligned}
\vec{N}_2 &= \vec{w}_{13} \\
&= \lambda_1\nabla\lambda_3 - \lambda_3\nabla\lambda_1 \\
&= \frac{1}{4A^2}\left((x_2y_3 - x_3y_2 - x_1y_3 + x_1y_2 + y_1x_3 - y_1x_2)y + (-x_2y_3y_2 - x_3y_2y_1 + x_3y_2^2 + x_1y_3y_2 + y_1x_2y_2 - x_1y_2^2)\right)\hat{i} + \\
&\quad \frac{1}{4A^2}\left(-(x_2y_3 - x_3y_2 - x_1y_3 + x_1y_2 + y_1x_3 - y_1x_2)x - (x_2y_3x_1 - x_2^2y_3 + x_3y_2x_2 - y_1x_3x_2 + y_1x_2^2 - x_1y_2x_2)\right)\hat{j}
\end{aligned} \tag{5.34}$$

$$\begin{aligned}
\vec{N}_3 &= \vec{w}_{23} \\
&= \lambda_2\nabla\lambda_3 - \lambda_3\nabla\lambda_2 \\
&= \frac{1}{4A^2}\left(-(x_2y_3 - x_3y_2 - x_1y_3 + x_1y_2 + y_1x_3 - y_1x_2)y - (x_1y_3y_1 - y_1^2x_3 + x_3y_2y_1 - x_2y_3y_1 + y_1^2x_2 - x_1y_2y_1)\right)\hat{i} + \\
&\quad \frac{1}{4A^2}\left((x_2y_3 - x_3y_2 - x_1y_3 + x_1y_2 + y_1x_3 - y_1x_2)x + (x_1^2y_3 - x_2y_3x_1 - y_1x_3x_1 - x_1^2y_2 + y_1x_2x_1 + x_3y_2x_1)\right)\hat{j}
\end{aligned} \tag{5.35}$$

from Equations (5.33), (5.34) and (5.35) it can easily be seen that these shape functions take on the basic algebraic form of:

$$\begin{aligned} \vec{N}_i(x,y) &= N_{xi}\hat{i} + N_{yi}\hat{j} \\ &= (ay+b)\hat{i} + (cx+d)\hat{j} \end{aligned} \tag{5.36}$$

for $i = 1:3$. Substituting the coordinates located at the nodes of the unit right angled triangle of Figure 5.6 into Equations (5.33), (5.34) and (5.35), the vector shape functions for this finite element calculated by MATLAB Symbolic are [2]:

$$\vec{N}_1 = \vec{w}_{12}(x,y) = -y\hat{i} + (x+1)\hat{j} \tag{5.37}$$

$$\vec{N}_2 = \vec{w}_{13}(x,y) = y\hat{i} - x\hat{j} \tag{5.38}$$

$$\vec{N}_3 = \vec{w}_{23}(x,y) = (1-y)\hat{i} + x\hat{j} \tag{5.39}$$

Figure 5.7 displays the vector shape functions given by Equations (5.37), (5.38) and (5.39) on a unit right angle triangle element.

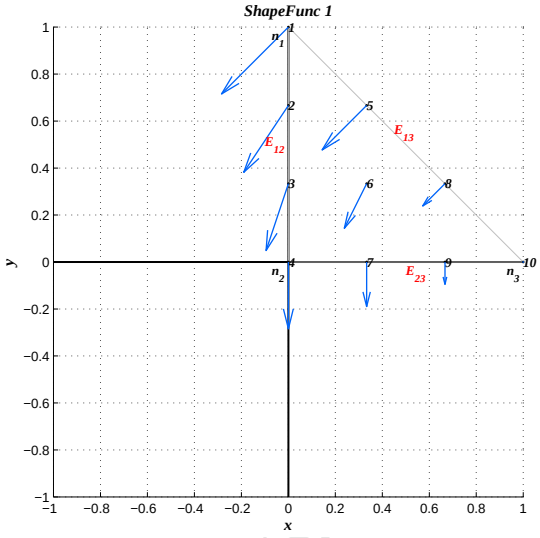

(a) Vector Shape Function: $\vec{N}_1 = \vec{w}_{12}(x,y)$

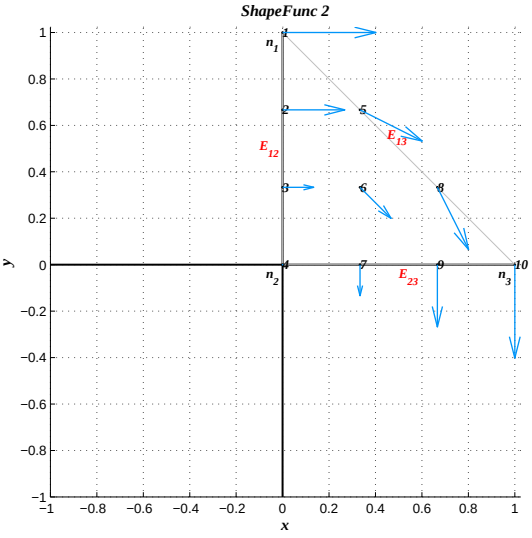

(b) Vector Shape Function: $\vec{N}_2 = \vec{w}_{13}(x,y)$

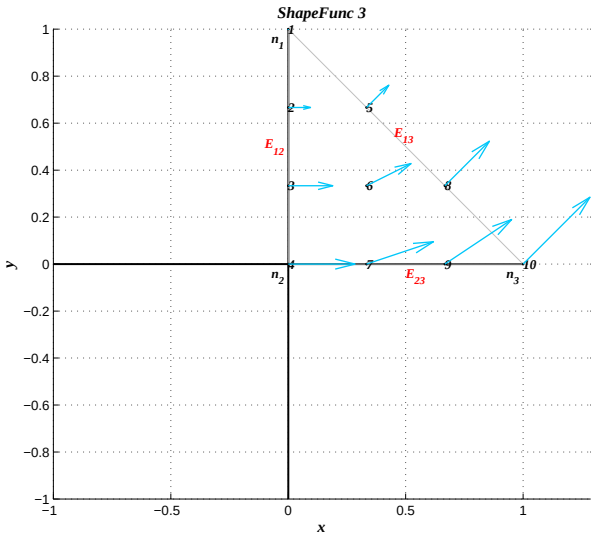

(c) Vector Shape Function: $\vec{N}_3 = \vec{w}_{23}(x,y)$

Figure 5.7: Vector Shape Functions of a Unit Right Angle Triangle

Properties of the Vector Shape Functions

There are some important features that can be noticed concerning the vector shape functions [2]. The shape function, $\vec{N}_3 = \vec{w}_{23}(x,y)$, given by Equation (5.39) is chosen to be analysed.

Visually, along edge E_{12} as seen in Figure 5.7c, the vector function (vector field) given by Equation (5.39) is purely normal that is, only normal components exist and the tangential components are zero in reference to edge E_{12} [2]. These normal components of this vector function also increases linearly from node n_1 to node n_2 along edge E_{12} as illustrated in Figure 5.7c [2]. Similarly along edge E_{13}, the vector function is also purely normal and increases linearly from node n_1 to node n_3 along this edge as illustrated in Figure 5.7c [2]. On edge E_{23} however, the function has both normal and tangential components as illustrated in Figure 5.7c by the vectors located on this edge, therefore these vectors can be separated into both normal components and tangential components, that is:

$$N_{x3} = 1 - y \tag{5.40}$$

is the tangential component function of Equation (5.39) in the $\hat{i} - direction$ with reference to edge E_{23} and

$$N_{y3} = x \tag{5.41}$$

is the normal component function of Equation (5.39) in the $\hat{j} - direction$ with reference to edge E_{23}. Looking carefully at Equation (5.40) it can be seen that along edge E_{23}, all y-coordinates are zero. The tangential component function in the $\hat{i} - direction$ given by Equation (5.40) thus becomes:

$$\left((1-y)\mid_{y=0}\right)\hat{i} = 1\hat{i} \tag{5.42}$$

for $\forall y = 0$ along edge E_{23}, edge E_{23} is located on the $y = 0$ line, see Figure 5.7c. Similarly the normal component function in the $\hat{j} - direction$ given by Equation (5.41) remains:

$$x\hat{j} \tag{5.43}$$

for $\forall y = 0$, but increases linearly in x along edge E_{23} , see Figure 5.7c. Thus along edge E_{23}, the tangential components of shape function $\vec{N}_3 = \vec{w}_{23}(x,y)$, is constant as given by Equation (5.42) and the normal components are linear as given by Equation (5.43). *Vector function $\vec{N}_3 = \vec{w}_{23}(x,y)$, can be described as a function possessing a constant tangential component along edge E_{23} and linear normal component along all other edges (E_{12} and E_{13})* as is clearly seen in Figure 5.7c [2]. The function has a *continuous tangential/linear normal* behaviour abbreviated as CT/LN [2] and due to these properties the "value calculated" for edge E_{23} is the tangential field along edge E_{23} [2]. Analysing the other shape functions $\vec{N}_1 = \vec{w}_{12}(x,y)$ and $\vec{N}_2 = \vec{w}_{13}(x,y)$, the same behaviour pattern will be found along edges E_{12} and E_{13} respectively [2] . Also the "values calculated" for edges E_{12} and E_{13} will represent the tangential field along edges E_{12} and E_{13} respectively [2]. This behaviour pattern directly coincides with the association of a vector shape function with a particular edge as mentioned in sub-section 5.3.1.

Due to this mixed-order behaviour of the shape functions as given by Equations (5.42) and (5.43) [2], the vector element is also known as a CT/LN element or a mixed-order element [2].The curl of the shape functions are calculated as follows:

$$\begin{aligned} \vec{\nabla} \times \vec{N}_i(x,y) &= \left(\frac{\partial N_{yi}}{\partial x} - \frac{\partial N_{xi}}{\partial y}\right)\hat{k} \\ &= (c-a)\hat{k} \end{aligned} \tag{5.44}$$

for $i = 1:3$. The curls of the shape functions are nonzero constants and hence the shape functions and their curls are referred to as being complete to zeroth-order [12].

5.3.2 Construction of a Vector Field within a Triangular Element

The vector field $\vec{E}_V(x,y)$, can be computed at any point of the triangle finite element by directly summing the shape functions within each element along with the edges [2], that is:

$$\vec{E}_V(x,y) \backsimeq E_{12}\vec{w}_{12} + E_{13}\vec{w}_{13} + E_{23}\vec{w}_{23} \tag{5.45}$$

where E_{12}, E_{13} and E_{23} are the edges of the triangular element, $\vec{w}_{12}$, $\vec{w}_{13}$ and $\vec{w}_{23}$ are the vector shape functions [2] and $\vec{E}_V(x,y)$ signifies a vector field approximated by the vector element. Equation (5.33), (5.34) and (5.35) is substituted into Equation (5.45). Using MATLAB Symbolic, the complete general symbolic notation of the vector field $\vec{E}_V(x,y)$ is:

$$\begin{aligned}
\vec{E}_V(x,y) \;=\; & \left(\frac{1}{4A_e}(-E_{12}+E_{13}-E_{23})y\right. \\
& -\frac{(-x_2y_3^2+x_2y_3y_1+x_3y_2y_3+x_1y_3^2-y_1x_3y_3-x_1y_3y_2)E_{12}}{4A_e^2} \\
& +\frac{(-x_2y_3y_2-x_3y_2y_1+x_3y_2^2+x_1y_3y_2+y_1x_2y_2-x_1y_2^2)E_{13}}{4A_e^2} \\
& \left.-\frac{x_1y_3y_1-y_1^2x_3+x_3y_2y_1-x_2y_3y_1+y_1^2x_2-x_1y_2y_1)E_{23}}{4A_e^2}\right)\hat{i}+ \\
& \left(\frac{1}{4A_e}(E_{12}-E_{13}+E_{23})x..\right. \\
& +\frac{(-x_2y_3x_3+x_3^2y_2-x_3y_2x_1-y_1x_3^2+y_1x_3x_2+x_1y_3x_3)E_{12}}{4A_e^2} \\
& -\frac{(x_2y_3x_1-x_2^2y_3+x_3y_2x_2-y_1x_3x_2+y_1x_2^2-x_1y_2x_2)E_{13}}{4A_e^2} \\
& \left.+\frac{(x_1^2y_3-x_2y_3x_1-y_1x_3x_1-x_1^2y_2+y_1x_2x_1+x_3y_2x_1)E_{23}}{4A_e^2}\right)\hat{j}
\end{aligned} \tag{5.46}$$

where the variables (x_1,y_1), (x_2,y_2), (x_3,y_3) are the coordinates at the nodes of the triangle element, A_e is the area of the triangle element, and E_{12}, E_{13} , E_{23} are the edges of the triangle element. Using MATLAB Symbolic to collect all the terms in x, the terms in y and the constant terms in Equation (5.46), it is found that:

The first component function of the field $\vec{E}_V(x,y)$ has the algebraic structure:

$$F(x,y) = f_0 + f_2 y \tag{5.47}$$

in the $\hat{i}-direction$, where $f_1 = 0$ in relation to Equation (5.3) and comparing Equation (5.3) to Equation (5.46), it is found that:

$$f_2 = \frac{1}{4A_e}(-E_{12}+E_{13}-E_{23}) \tag{5.48}$$

and

$$\begin{aligned}
f_0 \;=\; & ..-\frac{(-x_2y_3^2+x_2y_3y_1+x_3y_2y_3+x_1y_3^2-y_1x_3y_3-x_1y_3y_2)E_{12}}{4A_e^2}.. \\
& ..+\frac{(-x_2y_3y_2-x_3y_2y_1+x_3y_2^2+x_1y_3y_2+y_1x_2y_2-x_1y_2^2)E_{13}}{4A_e^2}.. \\
& ..-\frac{(x_1y_3y_1-y_1^2x_3+x_3y_2y_1-x_2y_3y_1+y_1^2x_2-x_1y_2y_1)E_{23}}{4A_e^2}
\end{aligned} \tag{5.49}$$

The second component function of the field has the algebraic structure:

$$G(x,y) = g_0 + g_1 x \tag{5.50}$$

in the $\hat{j} - direction$, where $g_2 = 0$ in relation to Equation (5.4) and comparing Equation (5.4) to Equation (5.46), it is found that:

$$g_1 = \frac{1}{4A_e}(E_{12} - E_{13} + E_{23}) \tag{5.51}$$

and

$$\begin{aligned} g_0 \quad = \quad & .. + \frac{(-x_2y_3x_3 + x_3^2y_2 - x_3y_2x_1 - y_1x_3^2 + y_1x_3x_2 + x_1y_3x_3)E_{12}}{4A_e^2} .. \\ & .. - \frac{(x_2y_3x_1 - x_2^2y_3 + x_3y_2x_2 - y_1x_3x_2 + y_1x_2^2 - x_1y_2x_2)E_{13}}{4A_e^2} .. \\ & .. + \frac{(x_1^2y_3 - x_2y_3x_1 - y_1x_3x_1 - x_1^2y_2 + y_1x_2x_1 + x_3y_2x_1)E_{23}}{4A_e^2} \end{aligned} \tag{5.52}$$

Thus, the vector field that the vector element is capable of constructing has the following general algebraic structure:

$$\vec{E}_V(x,y) = (f_0 + f_2 y)\,\hat{i} + (g_0 + g_1 x)\,\hat{j} \tag{5.53}$$

The vector element supports vector field expansions of the form of Equation (5.53) across a triangular element, there are however a few exceptions and further explanation will be given in sub-section 5.6.1. The element can be referred to as being complete to zeroth-order [11, 12] due to the shape functions themselves being complete to zeroth-order as shown by Equation (5.44).

5.3.3 Tangential Continuity of the Vector Element

The unknown parameters (degrees of freedom) are the edges E_{ij}, of the triangular vector finite element [7]. Assembling the elements together across a mesh requires the element connectivity information [1, 2, 3]. The element connectivity information is a table that shows the information of how each element within the mesh is connected to one another though the edges E_{ij} of the elements, that is, an edge can be shared by at most two elements [1, 2, 3].

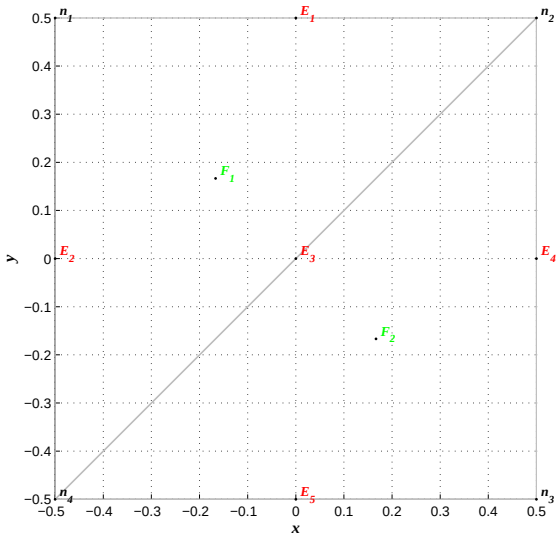

(a)

No.	Faces	Local Edge 1	Local Edge 2	Local Edge 3
1	F_1	E_1	E_2	E_3
2	F_2	E_4	E_3	E_5

(b)

Figure 5.8: Element Inter-Connectivity Information

Sub-figure 5.8a demonstrates that edge E_3, connects elements $F_1$and F_2. Sub-figure 5.8b displays the connectivity data of the vector finite elements generated by MATLAB. This connectivity data is presented in the form of a table called `FaceEdgesData`.

Sub-figure 5.8a illustrates that the two elements are connected by and share edge number E_3. The table referred to in this dissertation as `FaceEdgesData` in sub-figure 5.8b also clearly tabulates this element inter-connectivity information which states the following:

- the column labelled as Faces, contains the global element numbering [2, 12]. The mesh in sub-figure 5.8a contains two elements, element number one, labelled as F_1, and element number two, labelled as F_2.
- the next three columns labelled as Local Edge 1, Local Edge 2 and Local Edge 3, contain the global edge numbering system [2, 12]. Each triangular element is associated with three edges [2, 12]. Element F_1 is associated with edges E_1^1, E_2^1, E_3^1 and element F_2 is associated with edges E_4^2, E_3^2, E_5^2 as illustrated by the table of `FaceEdgesData` in sub-figure 5.8b. The superscript of the edge terms above indicates which element a particular edge belongs to.

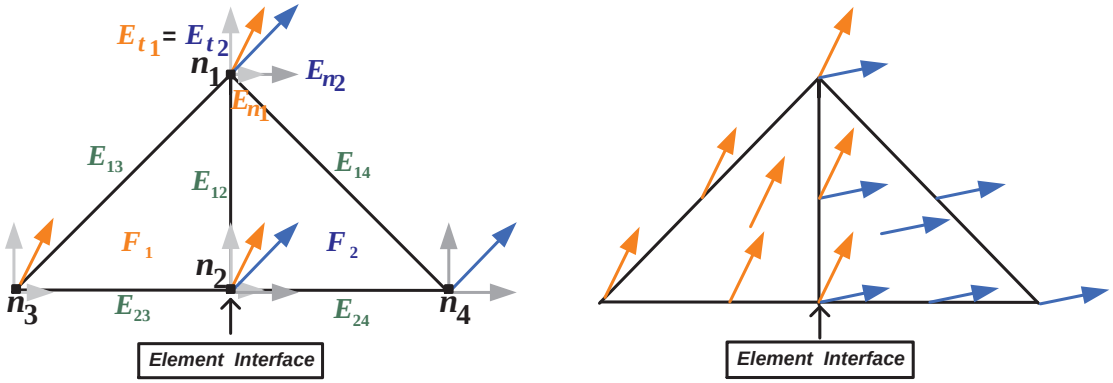

(a) (b)

Figure 5.9: Tangential Continuity and Normal Discontinuity of the Vector Field Across an Element Interface

Sub-figure 5.9a illustrates that the tangential components of the vector field on edge E_{12} is continuous that is $E_t^1 = E_t^2$, and the normal components are discontinuous, that is $E_n^1 \neq E_n^2$. Sub-figure 5.9b illustrates that there is a change in direction and magnitude of the vector field across the element interface (refer to sub-section 5.1.3).

Now, sub-figure 5.9a illustrates that two elements share and are connected by edge numbered E_{12}. The component of the field $\vec{E}^1(x,y)$, in element numbered one, tangent to edge numbered E_{12} can be made equal to the component of the field $\vec{E}^2(x,y)$, in element numbered two, tangent to the same edge numbered E_{12} by imposing the following continuity condition between the elements:

$$E_{12}^1 = E_{12}^2 \tag{5.54}$$

where the superscripts indicates the global finite element numbering system. Equation (5.54) states that edge E_{12}^1 belonging to finite element F_1, is equal to edge E_{12}^2 belonging to finite element F_2. Applying Equation (5.54) to the two element mesh as illustrated in Figure 5.9b, makes the field tangentially continuous across edge E_{12}. The field so constructed is not normally continuous that is, the part of the field perpendicular with reference to the element interface (normal component of vector field) is discontinuous across the element interface because no continuity conditions were placed on the normal components. The vector finite element thus has the ability to impose tangential continuity but not normal continuity on the vector field [7, 11]. Depending on the edge values E_{ij}, chosen for each finite element $F_1$and F_2 and using Equation (5.45) applied to both elements:

$$\vec{E}_V^1(x,y) \backsimeq E_{12}^1\vec{w}_{12}^1 + E_{13}^1\vec{w}_{13}^1 + E_{23}^1\vec{w}_{23}^1 \tag{5.55}$$

and

$$\vec{E}_V^2(x,y) \backsimeq E_{12}^2\vec{w}_{12}^2 + E_{14}^2\vec{w}_{14}^2 + E_{24}^2\vec{w}_{24}^2 \tag{5.56}$$

The vector field $\vec{E}_V(x,y)$, approximated across both elements:

$$\begin{aligned} \vec{E}_V(x,y) &\backsimeq \vec{E}_V^1(x,y) + \vec{E}_V^2(x,y) \\ &= \left(E_{12}^1\vec{w}_{12}^1 + E_{13}^1\vec{w}_{13}^1 + E_{23}^1\vec{w}_{23}^1\right) + \left(E_{12}^2\vec{w}_{12}^2 + E_{14}^2\vec{w}_{14}^2 + E_{24}^2\vec{w}_{24}^2\right) \end{aligned} \tag{5.57}$$

but, according to Equation (5.54),

$$E_{12}^1 = E_{12}^2$$

therefore Equation (5.57) becomes:

$$\vec{E}_V(x,y) = \left(\vec{w}_{12}^1 + \vec{w}_{12}^2\right)E_{12} + \left(E_{13}\vec{w}_{13}^1 + E_{23}\vec{w}_{23}^1\right) + \left(E_{14}\vec{w}_{14}^2 + E_{24}\vec{w}_{24}^2\right) \tag{5.58}$$

where both elements F_1 and F_2 share edge E_{12}, the vector field $\vec{E}_V(x,y)$ will have the ability to change direction and magnitude across the element interface as illustrated by sub-figure 5.9b because the vector element has the ability to interpolate the vector field in such a way that the tangential continuity between the adjacent elements are enforced as shown by the term $\left(\vec{w}_{12}^{1}+\vec{w}_{12}^{2}\right)E_{12}$ in Equation (5.58), while the normal components of the vector field are allowed to be discontinuous [11].

This property makes the vector element very useful for when boundary conditions need to be imposed between different material interfaces [13, 7] as illustrated by Figure 5.10b because the vector field $\vec{E}(x,y)$, physically always changes (direction and intensity/magnitude) across any material interface as shown in Section 5.1.3.

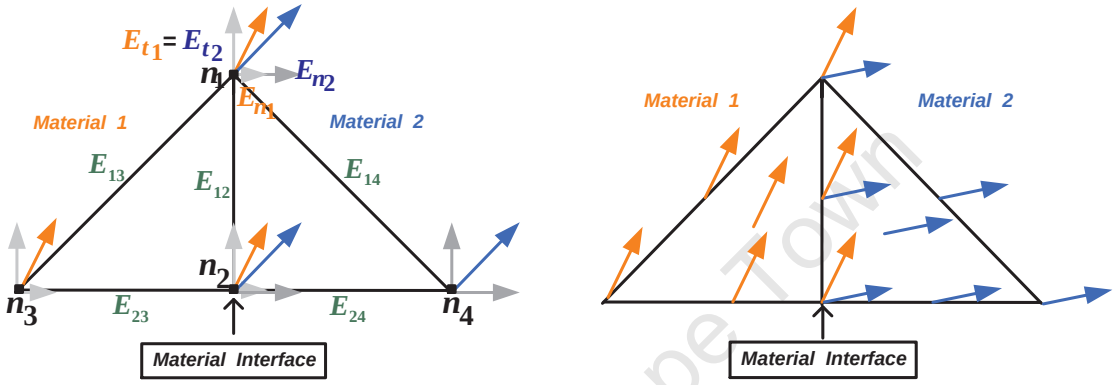

(a) (b)

Figure 5.10: Tangential Continuity and Normal Discontinuity of the Vector Field Across a Material Interface Located Between Two Elements

Sub-figure 5.10b illustrates tangential continuity and normal discontinuity for the vector located on edge E_{12} (which is the material interface between the two elements). Sub-figure 5.10b illustrates how there is a change (in direction and magnitude) of the vector field $\vec{E}_V(x,y)$, across the material interface (each element represents a different material) due to the normal part of the vector field changing abruptly across this interface (normal discontinuity) [7] .

The name CT/LN element used in sub-section 5.3.1 describes the vector element the best, because essentially the construction of the vector field $\vec{E}_V(x,y)$ within the element using the vector shape functions in Equation (5.45) allows the "separation" of the normal and tangential components along the edges of an element, the element is thus able to construct vector fields that are normally discontinuous and tangentially continuous across element boundaries [11, 7] as shown by Figure 5.2.

As a summary to sub-sections 5.3.2 and 5.3.3, these vector elements dropped the "full-order" property and the "fully-continuous" property respectively [13] where the latter is desirable for electromagnetic field computations [7].

5.4 Calculation of a Vector Field Across a Triangular Finite Element

Vector elements only provide a physically meaningful vector field when summed together [2] as given by Equation (5.45). An algorithm was coded to display vector fields across a single finite element. The purpose of this exercise was so to gain a better understanding of how the vector element is able to approximate and display vector fields.

To display certain vector fields would depend on the value of the edges (average tangential field along a particular edge [2]) chosen on a triangular element as given by Equation (5.45). The finite element used is a unit right angled triangle, thus the shape functions are given by Equations (5.37), (5.38) and (5.39).

5.4.1 Construction of a Rotational Field

On a unit right angled triangle the author wished to display the rotational field:

$$\vec{E}\,(x,y) = -y\hat{i} + x\hat{j} \tag{5.59}$$

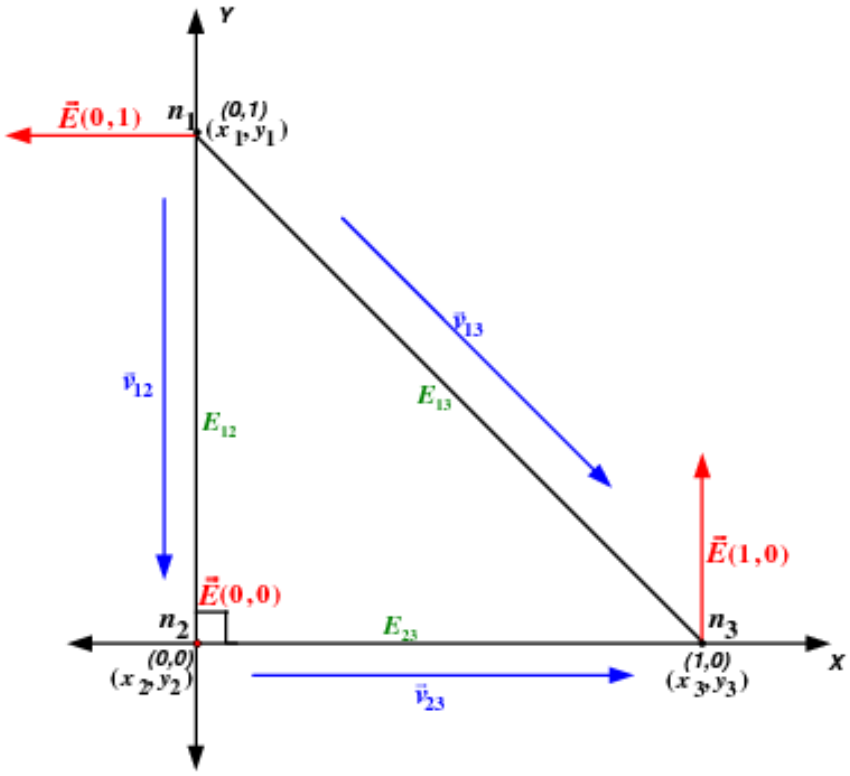

Figure 5.11: Construction of a Rotational Vector Field Across a Element

On each edge of the triangle a local vector $\vec{v}_{ij}$can be calculated. This vector $\vec{v}_{ij}$, is formed by the subtraction of coordinate values as follows [10]:

$$\vec{v}_{ij} = \left(x_j, y_j\right) - \left(x_i, y_i\right) \tag{5.60}$$

these coordinate values are located along an edge E_{ij} on the element (refer to Figure 5.11). Calculation of these vectors $\vec{v}_{ij}$, on the unit triangle using Equation (5.60) are as follows:

$$\vec{v}_{12} = (0,0) - (0,1) = (0,-1) = 0\hat{i} - 1\hat{j} \tag{5.61}$$
$$\vec{v}_{13} = (1,0) - (0,1) = (1,-1) = 1\hat{i} - 1\hat{j} \tag{5.62}$$
$$\vec{v}_{23} = (1,0) - (0,0) = (1,0) = 1\hat{i} + 0\hat{j} \tag{5.63}$$

The lengths of each vector $\left|\vec{v}_{ij}\right|$, on each edge of the triangle can also be calculated where $\left|\vec{v}_{ij}\right| = L_{ij}$ [10], which is the actual length of the edges L_{ij}, of the triangle. Therefore:

$$\left|\vec{v}_{12}\right| = L_{12} = 1 \tag{5.64}$$
$$\left|\vec{v}_{13}\right| = L_{13} = \sqrt{2} \tag{5.65}$$
$$\left|\vec{v}_{23}\right| = L_{23} = 1 \tag{5.66}$$

The unit vectors on each edge of the triangle can be calculated by the well known equation [10]:

$$\hat{e}_{ij} = \frac{\vec{v}_{ij}}{\left|\vec{v}_{ij}\right|} \tag{5.67}$$

Substituting Equations (5.61), (5.62), (5.63), (5.64), (5.65), and (5.66) into Equation (5.67) gives:

$$\hat{e}_{12} = \frac{\vec{v}_{12}}{|\vec{v}_{12}|} = \frac{0\hat{i}-1\hat{j}}{1} \tag{5.68}$$

$$\hat{e}_{13} = \frac{\vec{v}_{13}}{|\vec{v}_{13}|} = \frac{1\hat{i}-1\hat{j}}{\sqrt{2}} \tag{5.69}$$

$$\hat{e}_{23} = \frac{\vec{v}_{23}}{|\vec{v}_{23}|} = \frac{1\hat{i}+0\hat{j}}{1} \tag{5.70}$$

Equation (5.45) approximates a vector field $\vec{E}(x,y)$, across a triangular element [2], therefore substituting Equations (5.37), (5.38) and (5.39) into Equation (5.45) produces:

$$\begin{aligned}
\vec{E}(x,y) &\simeq \vec{E}_V(x,y) \\
&= E_{12}\left(-y\hat{i}+(x+1)\hat{j}\right)+E_{13}\left(y\hat{i}-x\hat{j}\right)+E_{23}\left((1-y)\hat{i}+x\hat{j}\right) \\
&= -E_{12}y\hat{i}+E_{12}(x+1)\hat{j}+E_{13}y\hat{i}-E_{13}x\hat{j}+E_{23}(1-y)\hat{i}+E_{23}x\hat{j} \\
&= \left(-E_{12}y+E_{13}y+E_{23}(1-y)\right)\hat{i}+\left(E_{12}(x+1)-E_{13}x+E_{23}x\right)\hat{j}
\end{aligned} \tag{5.71}$$

To find the tangential component of the field $\vec{E}(x,y)$, along edge E_{13} (refer to Figure 5.11) Equation (5.72) is used [10, 9, 4, 2] :

$$\vec{E}_{tang/E_{13}} = \hat{e}_{13}\cdot\vec{E}(x,y) \tag{5.72}$$

Substituting Equations (5.69) and (5.71) into Equation (5.72) gives:

$$\begin{aligned}
\vec{E}_{tang/E_{13}} &= \left(\frac{1}{\sqrt{2}}\hat{i}-\frac{1}{\sqrt{2}}\hat{j}\right)\cdot\left[\left(-E_{12}y+E_{13}yE_{23}(1-y)\right)\hat{i}+\left(E_{12}(x+1)-E_{13}x+E_{23}x\right)\hat{j}\right] \\
&= \frac{1}{\sqrt{2}}\left(-E_{12}y+E_{13}yE_{23}(1-y)\right)-\frac{1}{\sqrt{2}}\left(E_{12}(x+1)-E_{13}x+E_{23}x\right)
\end{aligned} \tag{5.73}$$

Then substituting cartesian points $x=0$ and $y=1$ at node $n_1=1$ into Equation (5.73):

$$\begin{aligned}
\vec{E}_{tang/E_{13}} &= \hat{e}_{13}\cdot\vec{E}(0,1) \\
&= \frac{1}{\sqrt{2}}(-E_{12}+E_{13}+0)-\left(\frac{1}{\sqrt{2}}-E_{12}+0+0\right) \\
&= \frac{1}{\sqrt{2}}(-E_{12}+E_{13}+E_{12}) \\
&= \frac{E_{13}}{\sqrt{2}}
\end{aligned} \tag{5.74}$$

Following the same procedure as the above, the tangential component of the field $\vec{E}(x,y)$, on edge E_{12} and edge E_{23} are :

$$\vec{E}_{tang/E_{12}} = \frac{E_{12}}{1} \tag{5.75}$$

and

$$\vec{E}_{tang/E_{23}} = \frac{E_{23}}{1} \tag{5.76}$$

respectively.

It can be deduced from Equations (5.74), (5.75) *and* (5.76) *that the edge values* E_{ij}*, of an arbitrary triangle can be calculated by the following well known equation [2, 7]*:

$$\begin{aligned} \vec{E}_{tang/E_{ij}} &= \hat{e}_{ij} \cdot \vec{E}(x,y) \\ &= \frac{E_{ij}}{L_{ij}} \end{aligned} \tag{5.77}$$

where E_{ij} is the edge value, $\vec{E}_{tang/E_{ij}}$ is the tangent vector of the vector field $\vec{E}(x,y)$, located on edge E_{ij} of the triangle and L_{ij} is the length of a particular edge on the triangle. Equation (5.77) states that E_{ij}, controls the tangential field $\vec{E}_{tang/E_{ij}}$, on the local edge of the element numbered by ij [7] and this also makes it simple to constrain the tangential field to a prescribed boundary value [7].

Table 5.1 tabulates the calculation of the vector field $\vec{E}(x,y)$ at each node of the element (refer to Figure 5.11).

Node	Co-ordinate Point	$\vec{E}(x,y) = -y\hat{i} + x\hat{j}$
1	$(x_1,y_1) = (0,1)$	$\vec{E}(0,1) = -1\hat{i} + 0\hat{j}$
2	$(x_2,y_2) = (0,0)$	$\vec{E}(0,0) = 0\hat{i} + 0\hat{j}$
3	$(x_1,y_1) = (1,0)$	$\vec{E}(1,0) = 0\hat{i} + 1\hat{j}$

Table 5.1: Calculation of the Vector Field $\vec{E}(x,y)$ at each Node of the Element

To calculate the tangent vector $\vec{E}_{tang/E_{13}}$ on edge E_{13}, of right-angled triangle Equation (5.77) is used:

$$\begin{aligned} \vec{E}_{tang/E_{13}} &= \hat{e}_{13} \cdot \vec{E}(0,1) \\ &= \left(\frac{1\hat{i} - 1\hat{j}}{\sqrt{2}}\right) \cdot \left(-1\hat{i} + 0\hat{j}\right) \\ &= -\frac{1}{\sqrt{2}} \end{aligned} \tag{5.78}$$

where $L_{13} = \sqrt{2}$ and $E_{13} = -1$. Using Equation (5.77) , it is calculated that:

$$\vec{E}_{tang/E_{12}} = \frac{0}{1} \tag{5.79}$$

where $L_{12} = 1$ and $E_{12} = 0$ and

$$\vec{E}_{tang/E_{23}} = \frac{0}{1} \tag{5.80}$$

where $L_{23} = 1$ and $E_{23} = 0$. Substituting Equations (5.78), (5.79) and (5.80) into Equation (5.71), it is verified that:

$$\begin{aligned} \vec{E}(x,y) &\simeq \vec{E}_V(x,y) \\ &= E_{12}\left(-y\hat{i} + (x+1)\hat{j}\right) + E_{13}\left(y\hat{i} - x\hat{j}\right) + E_{23}\left((1-y)\hat{i} + x\hat{j}\right) \\ &= 0\left(-y\hat{i} + (x+1)\hat{j}\right) + -1\left(y\hat{i} - x\hat{j}\right) + 0\left((1-y)\hat{i} + x\hat{j}\right) \\ &= -y\hat{i} + x\hat{j} \end{aligned}$$

Figure 5.12 displays the vector field $\vec{E}(x,y) = -y\hat{i} + x\hat{j}$ given by Equation (5.59). The shape functions given by Equations (5.37), (5.38) and (5.39) together with the edge value

calculations given by Equations (5.78), (5.79) and (5.80) created the vector field given by Equation (5.59).

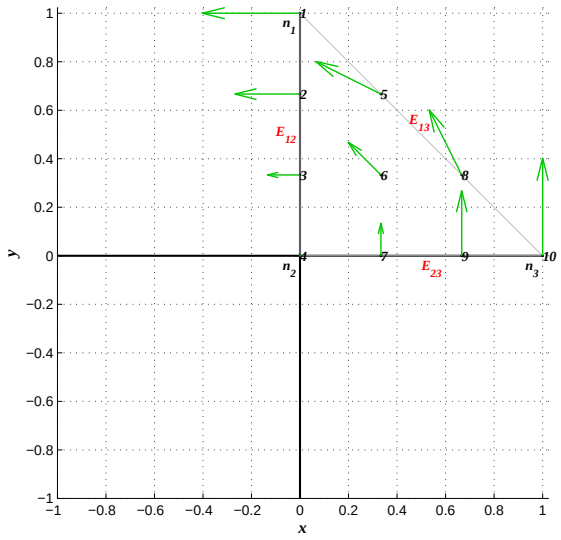

Figure 5.12: Rotational Vector Field Across Element

A rotational vector field $\vec{E}(x,y) = -y\hat{i} + x\hat{j}$, created by the vector element (Note: the `Quiver` function used by MATLAB to display the vector field, has automatically scaled the vectors).

5.4.2 Construction of a Constant Field

On a unit right angle triangle the author wished to display a constant field:

$$\vec{E}(x,y) = 1\hat{i} \tag{5.81}$$

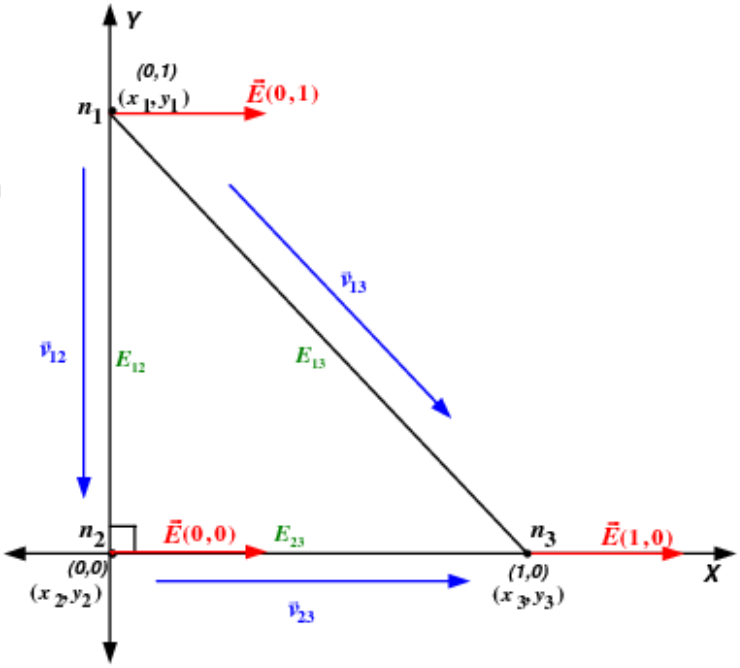

Figure 5.13: Construction of a Constant Vector Field Across a Element

Alternatively Equation (5.77) can be *written in a more convenient way* to calculate the

edges of a triangular finite element. Rearranging Equation (5.77) it is found that:

$$\begin{aligned} E_{ij} &= L_{ij} \quad \left(\vec{E}_{tang/E_{ij}}\right) \\ &= L_{ij} \quad \left(\hat{e}_{ij} \cdot \vec{E}\,(x,y)\right) \\ &= \quad \left(L_{ij}\hat{e}_{ij}\right) \cdot \vec{E}\,(x,y) \\ &= \quad \vec{v}_{ij} \cdot \vec{E}\,(x,y) \end{aligned} \tag{5.82}$$

where $\vec{E}_{tang/E_{ij}} = \hat{e}_{ij} \cdot \vec{E}\,(x,y)$ from Equation (5.77) and $\vec{v}_{ij} = L_{ij}\hat{e}_{ij}$ from Equation (5.67). The vector $\vec{v}_{12}$, $\vec{v}_{13}$ and $\vec{v}_{23}$ has been calculated by Equations (5.61), (5.62) and (5.63) respectively, and the vector field $\vec{E}\,(x,y)$, across the unit triangular element is approximated by Equation (5.71) again.

Table 5.1 tabulates the calculation of the vector field $\vec{E}\,(x,y)$ at each node of the element (refer to Figure 5.13)

Node	Co-ordinate Point	$\vec{E}\,(x,y) = 1\hat{i}$
1	$(x_1,y_1) = (0,1)$	$\vec{E}\,(0,1) = 1\hat{i} + 0\hat{j}$
2	$(x_2,y_2) = (0,0)$	$\vec{E}\,(0,0) = 1\hat{i} + 0\hat{j}$
3	$(x_1,y_1) = (1,0)$	$\vec{E}\,(1,0) = 1\hat{i} + 0\hat{j}$

Table 5.2: Calculation of the Vector Field $\vec{E}\,(x,y)$ at each Node of the Element

To calculate the tangent vector $\vec{E}_{tang/E_{13}}$ on edge E_{13}, of right-angled triangle Equation (5.82) is now used:

$$\begin{aligned} E_{13} &= \vec{v}_{13} \cdot \quad \vec{E}\,(0,1) \\ &= \quad \left(1\hat{i} - 1\hat{j}\right) \cdot \left(1\hat{i} + 0\hat{j}\right) \\ &= \quad 1 \end{aligned} \tag{5.83}$$

Using Equation (5.82) , it is calculated that:

$$E_{12} = 0 \tag{5.84}$$

and

$$E_{23} = 1 \tag{5.85}$$

Substituting Equations (5.83), (5.84) and (5.85) into Equation (5.71), it is verified that:

$$\begin{aligned} \vec{E}\,(x,y) &\simeq \vec{E}_V\,(x,y) \\ &= E_{12}\left(-y\hat{i} + (x+1)\,\hat{j}\right) + E_{13}\left(y\hat{i} - x\hat{j}\right) + E_{23}\left((1-y)\,\hat{i} + x\hat{j}\right) \\ &= 0\left(-y\hat{i} + (x+1)\,\hat{j}\right) + 1\left(y\hat{i} - x\hat{j}\right) + 1\left((1-y)\,\hat{i} + x\hat{j}\right) \\ &= y\hat{i} - x\hat{j} + 1\hat{i} - y\hat{i} + x\hat{j} \\ &= 1\hat{i} \end{aligned}$$

Figure 5.14 displays the vector field $\vec{E}\,(x,y) = 1\hat{i}$ given by Equation (5.81). The the shape functions given by Equations (5.37), (5.38) and (5.39) together with the edge value calculations given by Equations (5.83), (5.84) and (5.85) created the vector field given by Equation (5.81).

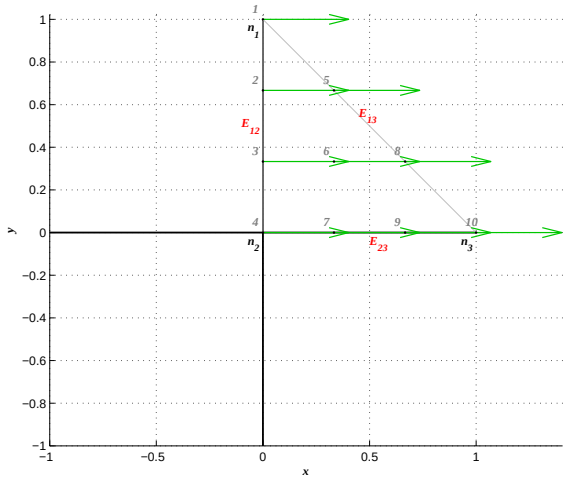

Figure 5.14: Constant Vector Field Across Element

A constant vector field $\vec{E}(x,y) = 1\hat{i}$, created by the vector element (Note: the `Quiver` function used by MATLAB to display the vector field, has automatically scaled the vectors).

It is important to notice that the edges (degrees of freedom) calculated by Equations (5.79), (5.78), (5.80) in Section 5.4.1 and Equations (5.83), (5.84), (5.85) in sub-section 5.4.2 respectively are scalar, but the edges can also be *signed* [2] as demonstrated by Equation (5.78).

5.5 Using Triangular Vector Elements to Create a Two-Dimensional Vector Field across a FE Mesh

Similar to section 5.4, an algorithm was coded to display vector fields across a finite element mesh. The purpose of this exercise was so to use this algorithm as a tool to investigate and at the same time gain a better understanding of the types and properties of vector fields that these vector elements are capable of "constructing" or "building".

5.5.1 Creating a Two-Dimensional Vector Field

The author attempted to simulate a rotational vector field of the form as given by Equation (5.59) (repeated here again for the readers convenience):

$$\vec{E}(x,y) = -y\hat{i} + x\hat{j}$$

across a four element mesh shown by sub-figure 5.16.

The algorithm can display any two-dimensional vector field $\vec{E}(x,y)$ of the form given by Equation (5.53) across a finite element mesh. The algorithm consists of several data processing steps and the knowledge of section 5.4 was incorporated into these steps in order to construct a vector field.

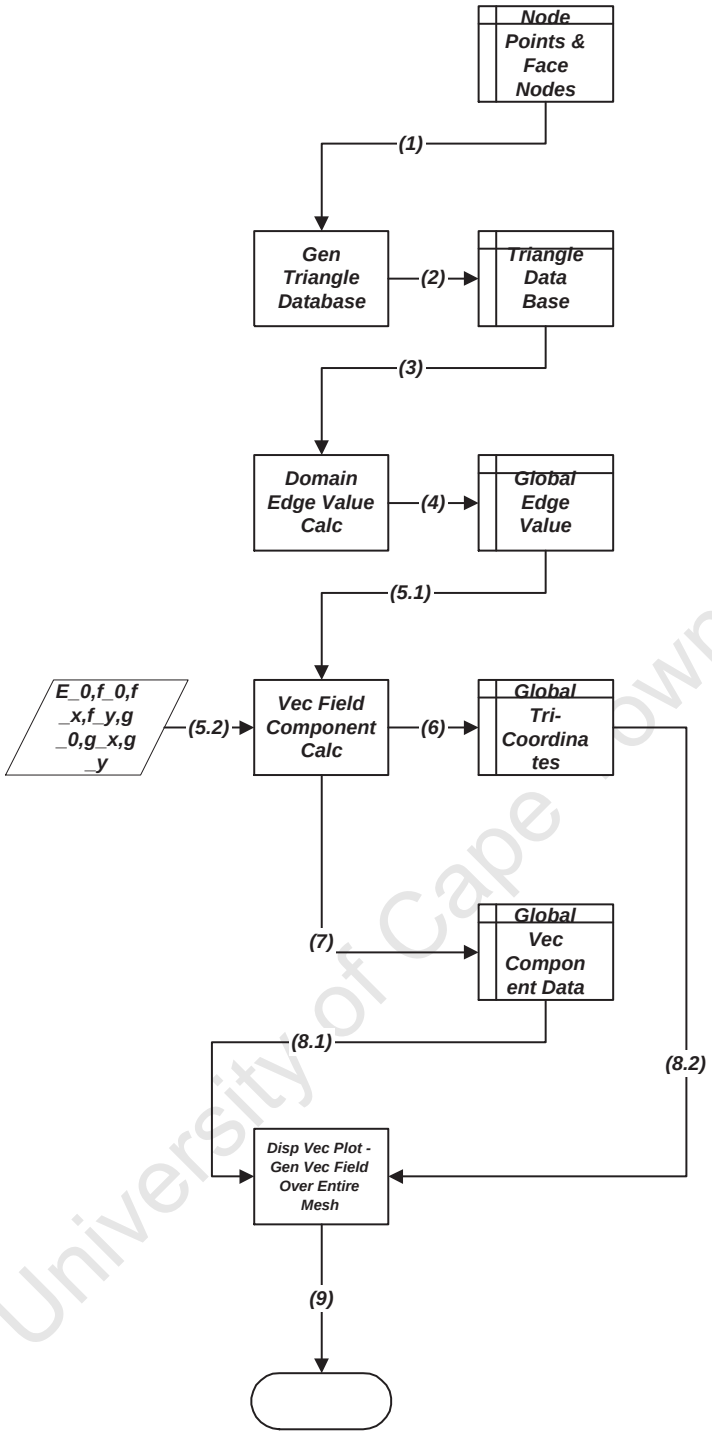

Figure 5.15: Flow Chart Diagram of a Vector Field Simulation

A description with a brief explanation of the process of information flow illustrated in Figure 5.15 is given below:

- Step 1: Data is processed and sorted into useful data structures.
- Step 2: The generated data is collected and stored.
- The stored data information is used in step 3.1 and step 5.2.
- The constants f_0, g_0, f_1, f_2, g_1 and g_2 are used to set the type of vector field that one wishes the vector elements to display according to the Equation (5.2). The

constants are set as $f_0 = 0$, $g_0 = 0$, $f_1 = 0$, $f_2 = -1$, $g_1 = 1$ and $g_2 = 0$ to give Equation (5.59).

- Step 3.1 takes the stored data information together with step 3.2, which takes the constants information to be processed. The edge values of each element within the entire mesh is computed and these edge values are calculated in a similar way to the process shown in sub-sections 5.4.2 and 5.4.1.
- Step 4: The computed edge value information is then stored in a data structure.
- Step 5.2 takes the stored data information together with step 5.1, which takes the edges value information to be processed. The components E_x in the $\hat{i} - direction$ and E_y in the $\hat{j} - direction$ of the vector field $\vec{E}(x,y)$ located at each coordinate (x,y) with in each element of the entire mesh are computed.
- Step 6 and step 7: The vector field component information and associated coordinate information are then stored in data structures.
- Step 8.1 takes the component data information together with step 8.2, which takes the coordinate information to be processed. The component information along with the coordinate information will be used to display the vector field over the entire mesh.
- Step 9: Once the intended vector field is simulated, all computation stops.

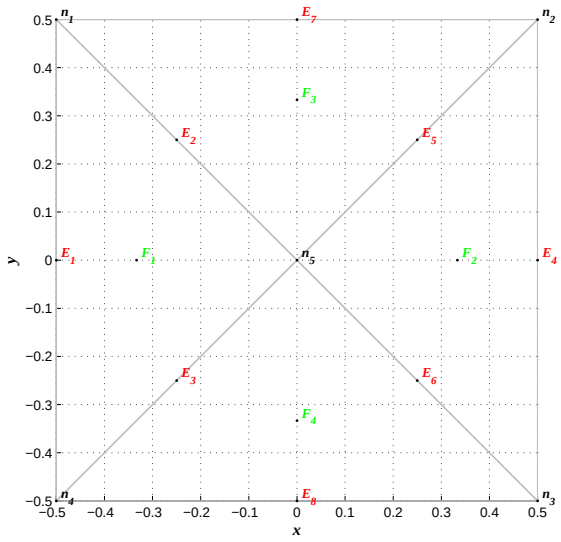

Figure 5.16: Finite Element Mesh

A four element mesh is illustrated. The data is labelled as BLACK-Nodes, RED-Edges and GREEN-Elements.

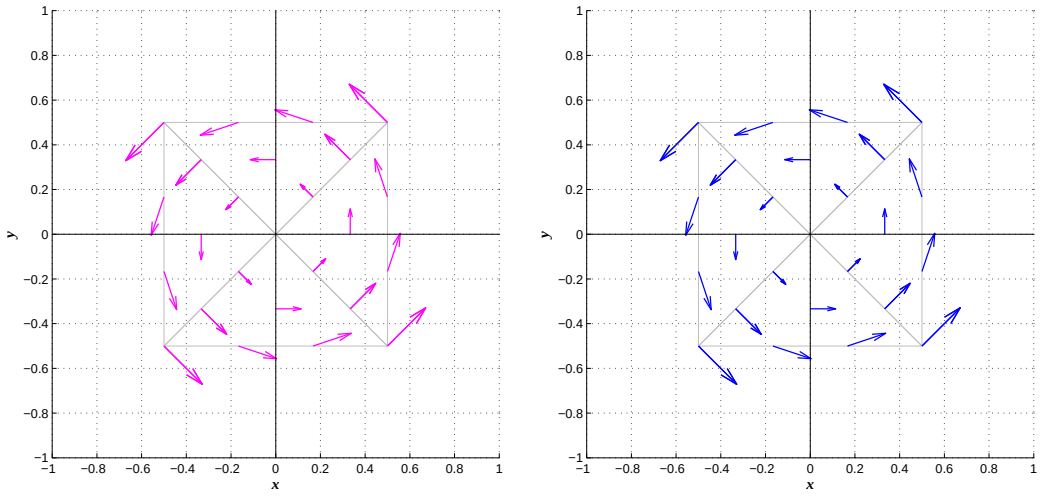

(a) (b)

Figure 5.17: A Rotational Vector Field Built using Four Vector Elements

Sub-figure 5.17a illustrates that Equation (5.45) is applied to each element within the mesh to "build" a vector field, $\vec{E}(x,y) = -y\hat{i} + x\hat{j}$ across the four element mesh. The finite elements are clearly capable of constructing this vector field. In sub-figure 5.17b, the same vector field, $\vec{E}(x,y) = -y\hat{i} + x\hat{j}$ is produced manually by using the MATLAB function MESHGRID and QUIVER.

In sub-figure 5.17a, the vector elements are *clearly capable of constructing* a vector field of the form given by Equation (5.59), across the FE mesh. Edge values are computed to construct the vector field $\vec{E}(x,y) = -y\hat{i} + x\hat{j}$ across each element within the FE mesh by using Equation (5.45) (refer to Section 5.4). Recall from sub-section 5.3.3, that the vector elements are "structurally designed" to be capable of producing vectors that have tangential component continuity but normal component discontinuity across an element interface and tangential component continuity between vectors of different elements (located on an element interface) are enforced through the edge values. However, the edge values computed (to construct the vector field $\vec{E}(x,y) = -y\hat{i} + x\hat{j}$) allowed for a *continuous vector field* to be produced across the FE mesh that is, located on all the element interfaces throughout the FE mesh, there exists tangential component continuity as well as normal component continuity between vectors belonging to different finite elements. Therefore, the vectors situated on the element interfaces (which belong to different finite elements) possess the same magnitudes and directions.

Thus, all the vectors situated on the element interface (grey lines) of each element (within the mesh) *coincide with each other, therefore forming a continuous vector field simulation* on all element interfaces across the FE mesh. In sub-figure 5.17b, the same vector field is plotted manually using the MATLAB function MESHGRID and QUIVER. The vector field simulations of sub-figure 5.17a and sub-figure 5.17b are identical.

The author then attempted to simulate the following vector field:

$$\vec{E}(x,y) = y\hat{i} + x\hat{j} \tag{5.86}$$

across a four element mesh shown by Figure 5.16. The constants are set as $f_0 = 0$, $g_0 = 0$, $f_1 = 0$, $f_2 = 1$, $g_1 = 1$ and $g_2 = 0$ to give Equation (5.86).

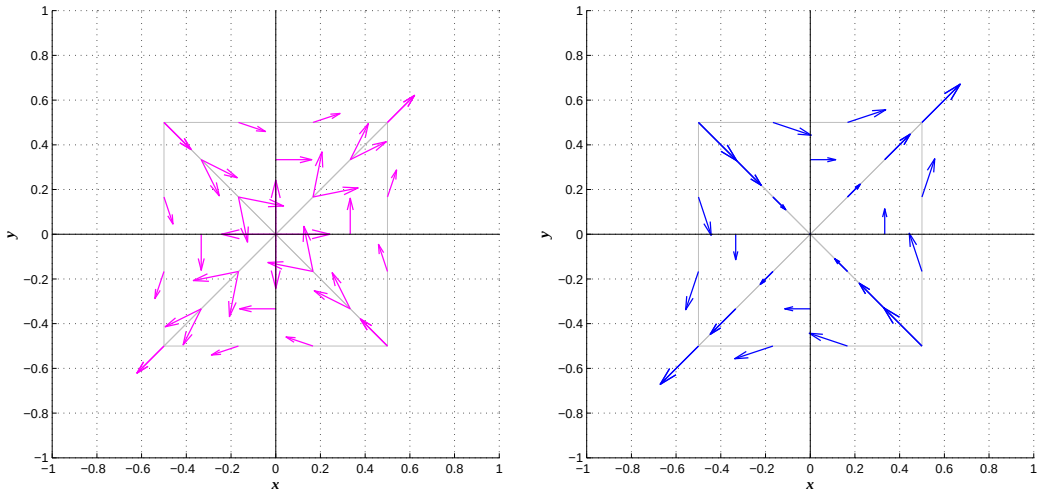

(a) (b)

Figure 5.18: An Arbitrary Vector Field Built using Four Vector Elements

In sub-figure 5.18a, equation (5.45) is applied to each element within the mesh to "build" the vector field, $\vec{E}(x,y) = y\hat{i} + x\hat{j}$ across the four element mesh. The finite elements are clearly incapable of constructing this vector field. In sub-figure 5.18b, the same vector field, $\vec{E}(x,y) = y\hat{i} + x\hat{j}$ is produced manually by using the MATLAB function MESHGRID and QUIVER placed over the same four element mesh of Figure 5.16.

In sub-figure 5.18a, the vector elements *fail to construct* the vector field given by Equation (5.86), across the FE mesh. The edge values computed to produce the vector field $\vec{E}(x,y) = y\hat{i} + x\hat{j}$ (refer to Section 5.4) across the FE mesh, created normal component discontinuity between vectors located on *all element interfaces* belonging to different finite elements of the entire FE mesh and therefore, some of the vectors situated on the element interfaces possess different magnitudes and directions. Thus, a *discontinuous vector field* is produced across the mesh and sub-figure 5.18a clearly shows how the vectors situated on the element interface (grey lines) of each element (within the mesh) *diverge from each other instead of coinciding with each other* as shown in sub-figure 5.17a and so, *a continuous vector field simulation* across the FE mesh could not be constructed. In sub-figure 5.18b, the same vector field (given by Equation (5.86)) is plotted manually using the MATLAB function MESHGRID and QUIVER.

In summary, there are certain vector fields that the vector elements are capable of approximating (as shown by sub-figure 5.17a) and certain vector fields that the vector elements are incapable of approximating (as shown by sub-figure 5.18a). This subject will be further investigated in Section 5.6 and sub-section 5.6.1.

Figure 5.19 shows the FE mesh that will be used for the simulated vector fields of Section 5.6 and sub-section 5.6.1.

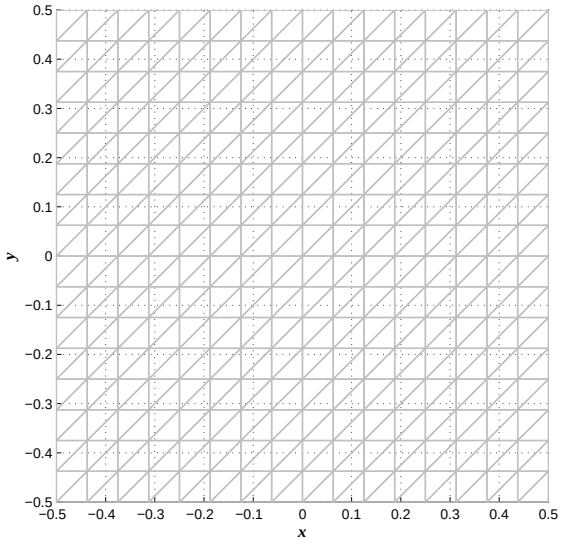

Figure 5.19: Finite Element Mesh
The FE mesh consists of 512 finite elements.

5.6 Properties of the Vector Field Produced by the Vector Element and the Node-based Vector Element

The following properties of the vector field approximated by the vector element and the node-based vector element can be drawn from Sections 5.2 and 5.3:

1. An approximation of a linear vector field $\vec{E}(x,y)$ as given by Equation (5.2), across the node-based vector element is given by Equation (5.14) (repeated here again for the readers convenience):

$$\begin{aligned}\vec{E}_N(x,y) &\simeq \left(E_{x1}\hat{i}+E_{y1}\hat{j}\right)\lambda_1(x,y)+\left(E_{x2}\hat{i}+E_{y2}\hat{j}\right)\lambda_2(x,y)+\left(E_{x3}\hat{i}+E_{y3}\hat{j}\right)\lambda_3(x,y)\\ &= \left(E_{x1}\lambda_1(x,y)+E_{x2}\lambda_2(x,y)+E_{x3}\lambda_3(x,y)\right)\hat{i}+\left(E_{y1}\lambda_1(x,y)+E_{y2}\lambda_2(x,y)+E_{y3}\lambda_3(x,y)\right)\hat{j}\end{aligned}$$

   Here the unknown parameters (degrees of freedom) are associated with the two coupled scalar fields located at each of the three nodes of the element [7], thus giving a total of six unknown parameters for an element E_{x1}, E_{x2} , E_{x3}, E_{y1}, E_{y2} and E_{y3}. An approximation of a linear vector field $\vec{E}(x,y)$ as given by Equation (5.2), across the vector element is given by Equation (5.45) (repeated here again for the readers convenience):

$$\vec{E}_V(x,y) \backsimeq E_{12}\vec{w}_{12}+E_{13}\vec{w}_{13}+E_{23}\vec{w}_{23}$$

   Here there are three unknown parameters (degrees of freedom) associated with the edges of the element E_{12}, E_{13} and E_{23} [7, 2]. The vector element has less degrees of freedom in comparison to the node-based vector element [7], therefore already a huge computational advantage can be concluded when using vector elements because, there will be less degrees of freedom for the FE algorithm to compute for a particular problem [7].

2. J.P.Webb in his paper [11] and J.Jin in his book [12] directly stated that, "in vector electromagnetics, the curl of the field $\nabla \times \vec{E}(x,y)$, is as important as the field itself $\vec{E}(x,y)$" [11, 12]. Therefore, if the vector field is represented by component functions of polynomial of order p, the curl of this vector field will then be represented by a polynomial of degree $p-1$ [11, 12]. The overall accuracy of the solution will then be dominated by this lower degree of $p-1$ [11, 12], therefore the accuracy of the solution will not be affected if the terms (called the gradient terms of order p) that do not contribute to the curl representation are removed while keeping the vector field representation complete to order of $p-1$ [11, 12]. This results in an element with fewer degrees of freedom, but with a better balance in accuracy of representation of the field and its curl [11, 12]. The vector element is the result of applying this idea to an element complete to first-order [11].

   Applying the knowledge of the above paragraph to Equation (5.2) which is a polynomial order (degree) $p=1$, the curl of the vector field $\vec{E}(x,y)$ is:

$$\begin{aligned} \vec{\nabla} \times \vec{E}(x,y) &= \left(\frac{\partial G}{\partial x} - \frac{\partial F}{\partial y}\right)\hat{k} \\ &= \left(\frac{\partial}{\partial x}(g_0 + g_1 x + g_2 y) - \frac{\partial}{\partial y}(f_0 + f_1 x + f_2 y)\right)\hat{k} \\ &= (g_1 - f_2)\,\hat{k} \end{aligned} \tag{5.87}$$

   with polynomial order of $p=0$, the curl is simply a constant with direction. Clearly, the terms $f_1 x$ and $g_2 y$ present in the polynomial expansion (of a linear vector field in two dimensions given by Equation (5.2)) do not contribute to Equation (5.87) and therefore, the terms $f_1 x$ and $g_2 y$ within the polynomial expansion (of Equation (5.2)) "does not affect the curl" of the vector field $\vec{E}(x,y)$ as given by Equation (5.87) [11, 12]. The terms $f_1 x$ and $g_2 y$, are called the gradient terms and are of order $p=1$ [11, 12]. The vector element approximates a vector field of the form as given by Equation (5.53) (repeated here again for the readers convenience):

$$\vec{E}_V(x,y) = (f_0 + f_2 y)\,\hat{i} + (g_0 + g_1 x)\,\hat{j}$$

   The vector element thus "preserves" the terms $f_2 y$ and $g_1 x$ that contribute directly to the curl of the vector field $\vec{E}(x,y)$, given by Equation (5.87) while at the same time "removes" the terms $f_1 x$ and $g_2 y$ that do not have an effect on the curl of the vector field $\vec{E}(x,y)$ given by Equation (5.87) [11, 12]. The divergence of the vector field $\vec{E}(x,y)$ is:

$$\begin{aligned} \vec{\nabla} \cdot \vec{E}(x,y) &= \frac{\partial F}{\partial x} + \frac{\partial G}{\partial y} \\ &= \left(\frac{\partial}{\partial x}(f_0 + f_1 x + f_2 y) - \frac{\partial}{\partial y}(g_0 + g_1 x + g_2 y)\right) \\ &= f_1 + g_2 \end{aligned} \tag{5.88}$$

   The terms $f_1 x$ and $g_2 y$ contributes directly to the divergence of the vector field $\vec{E}(x,y)$, given by Equation (5.88), so the vector element has no divergence since these terms are "removed" [2]. Thus, it is easy to see by mathematical deduction that the vector field represented by Equation (5.53) has no divergence, that is:

$$\begin{aligned} \vec{\nabla} \cdot \vec{E}_V(x,y) &= \frac{\partial}{\partial x}(f_0 + f_2 y) + \frac{\partial}{\partial y}(g_0 + g_1 x) \\ &= 0 \end{aligned} \tag{5.89}$$

and the vector elements are therefore incapable of constructing such a field. The "removal" of the "divergence terms" f_1x and g_2y, makes the vector element incapable of constructing any vector field that possesses a divergence property. This fact is verified graphically in sub-sections 2.1 and 2.2 (refer to sub-section 5.5.1).

2.1 **Divergent Vector Fields**

When the constants are set as $f_0 = 0$, $g_0 = 0$, $f_1 = 1$, $f_2 = 0$ $g_1 = 0$ and $g_2 = 1$, the vector elements failed to represent a purely divergent vector field, of the algebraic form:

$$\vec{E}\,(x,y) = x\hat{i} + y\hat{j} \tag{5.90}$$

The vector elements are not capable of supporting divergent fields as illustrated in Figure 5.20, where the vectors (belonging to different finite elements) situated on the element interfaces (of the FE mesh) "diverge" from each other as explained in sub-section 5.5.1.

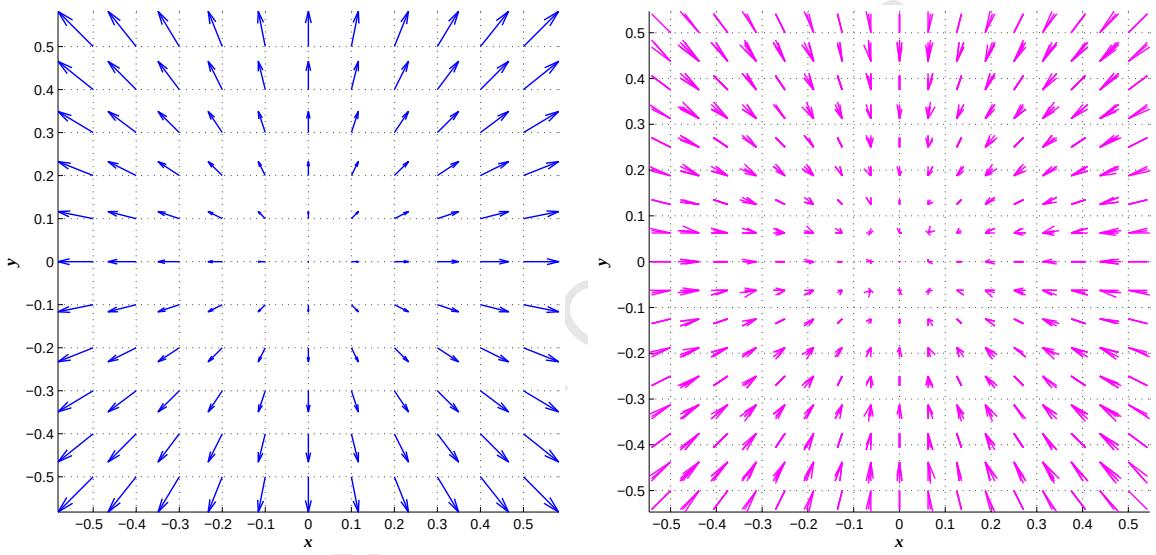

(a) (b)

Figure 5.20: Divergent Vector Field

Sub-figure 5.20a illustrates a purely divergent vector field produced by the MATLAB function `MESHGRID` and using the equation $\vec{E}\,(x,y) = x\hat{i} + y\hat{j}$. This vector field is then plotted with the MATLAB function `QUIVER`. Sub-figure 5.20b illustrates the same vector field ($\vec{E}\,(x,y) = x\hat{i} + y\hat{j}$) which was approximated by using the vector elements. Clearly the vector elements are incapable of constructing the vector field ($\vec{E}\,(x,y) = x\hat{i} + y\hat{j}$) due to there being only "divergent terms" $f_1x = x$ and $g_2y = y$ present within the vector field equation (refer to point number (2) of Section 5.6 and sub-section 5.5.1).

2.2 **Curling and Divergent Vector Fields**

When the constants are set as $f_0 = 0$, $g_0 = 0$, $f_1 = 2$, $f_2 = -3$ $g_1 = 2$ and $g_2 = 3$, the vector elements failed to represent a vector field, of the algebraic form:

$$\vec{E}\,(x,y) = (2x - 3y)\,\hat{i} + (2x + 3y)\,\hat{j} \tag{5.91}$$

The vector elements are not capable of supporting vector fields possessing curling and divergent differential properties as illustrated in Figure 5.21, where the vectors (belonging to different finite elements) situated on the element interfaces (of the FE mesh) "diverge" from each other as explained in sub-section 5.5.1.

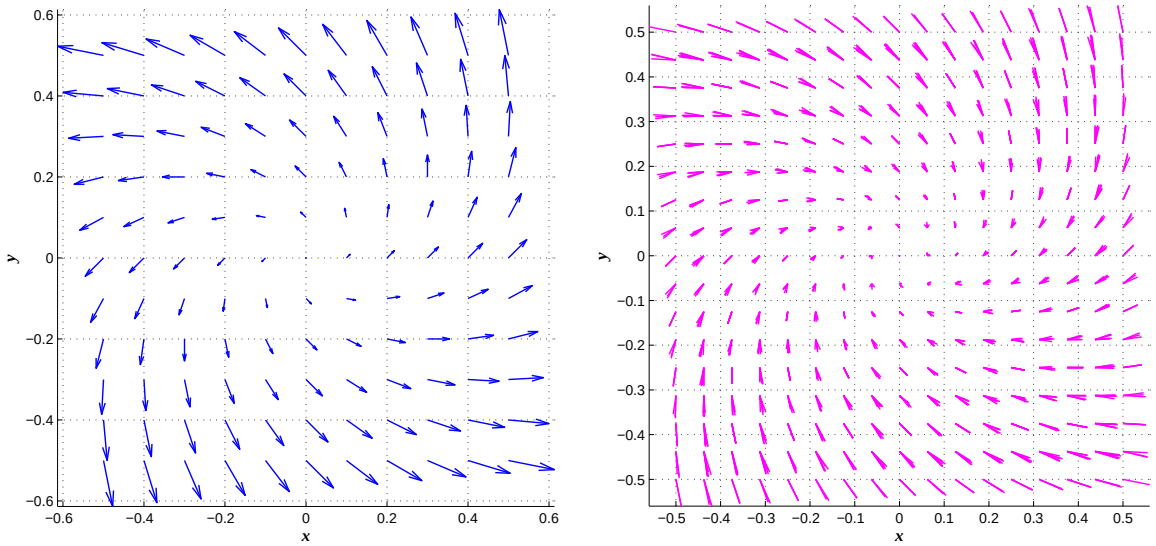

(a) (b)

Figure 5.21: Vector Field having both Curling and Divergent Properties

Sub-figure 5.21a illustrates a vector field possessing curling and divergent properties and is produced by the MATLAB function `MESHGRID` and using the equation $\vec{E}(x,y) = (2x-3y)\hat{i}+(2x+3y)\hat{j}$. This vector field is then plotted with the MATLAB function `QUIVER`. Sub-figure 5.21b illustrates the same vector field ($\vec{E}(x,y) = (2x-3y)\hat{i}+(2x+3y)\hat{j}$) which was approximated by using the vector elements. Clearly the vector elements are incapable of constructing the vector field ($\vec{E}(x,y) = (2x-3y)\hat{i}+(2x+3y)\hat{j}$) due to the "divergent terms" $f_1 x = 2x$ and $g_2 y = 3y$ present within the vector field equation (refer to point number (2) of Section 5.6 sub-section 5.5.1).

3. The node-based vector element approximates a vector field of the form given by Equation (5.24) (repeated here again for the readers convenience):

$$\vec{E}_N(x,y) = (f_0 + f_1 x + f_2 y)\hat{i} + (g_0 + g_1 x + g_2 y)\hat{j}$$

through its three shape functions of complete polynomial expansion and its six associated degrees of freedom given by Equation (5.14). The shape functions and the associated degrees of freedom "preserves" the gradient terms $f_1 x$ and $g_2 y$ within the approximation of the vector field $\vec{E}_N(x,y)$ within the element (as seen by Equation (5.24). Refer to Section 5.2 for the derivation of this equation) and therefore by "design", this element contains "wasted" degrees of freedom because a degree of freedom typically represents a field component at a particular node [2] and *not all field components* for electromagnetic purposes need to be continuous across an inter-element or inter-material boundaries as shown in sub-sections 5.1.3 and 5.3.3 [2, 11, 7]. Therefore, the normal components are the "wasted" degrees of freedom because they together with the nodal shape functions help to "preserve" the terms $f_1 x$ and $g_2 y$ as shown in sub-section 5.2.2 which are not required since they do not contribute to the curl of the vector field $\vec{E}(x,y)$ [11, 12] as given by Equation (5.87).

In comparison, the construction of the vector element is only capable of approximating curling vector fields (as stated above through Equation (5.53)) through its three vector shape functions of mixed-order [12] and the three associated degrees of freedom called edges given by Equation (5.45). The "design" of the vector element has resulted in the use of fewer degrees of freedom (edges) [12] that only "preserves" the terms $f_2 y$ and $g_1 x$ which contribute towards the curl of the vector

field (as stated above through Equation (5.87)). Thus, it is easy to see by mathematical deduction that the vector field represented by Equation (5.53) is capable of rotation:

$$\begin{aligned}\vec{\nabla}\times\vec{E}_V(x,y) &= \left(\frac{\partial}{\partial x}(g_0+g_1x)-\frac{\partial}{\partial y}(f_0+f_2y)\right)\hat{k}\\ &= (g_1-f_2)\hat{k} \qquad (5.92)\end{aligned}$$

The vector fields approximated by the vector elements given by Equation (5.53) is subject to a few exceptions as already mentioned in sub-section 5.3.2. Sub-section 5.6.1 will investigate these exceptions.

Equation (5.89) demonstrates that the vector element cannot represent a divergent vector field and Equation (5.92) demonstrates that the vector element is capable of representing rotational/circulating vector fields. The latter property of the vector element make them very useful and attractive to use for electromagnetic field vectors because the electromagnetic field vectors not only obey the Maxwell curl equations, but they are also constrained by the divergence equations [2] (refer to Chapter 2, specifically Section 2.3.1 point number 2).

As a summary, in vector electromagnetics the electromagnetic behaviour is governed by the Maxwell curl equations as shown in Chapters 2 and 3, therefore the curl of the vector field is of importance [11, 12] and not the divergence of the vector field. From a physical view point, the curl of the electric field is the time-rate of change of the magnetic field [13]. It seems that the purpose of the mixed-order/zeroth-order vector element is to *remove* the terms f_1x and g_2y from the polynomial expansion that make up the electric vector field $\vec{E}(x,y)$ given by Equation (5.2), which do not contribute to the magnetic field [13] (which is the curl of the electric field given by Equation (5.87)).

5.6.1 Investigation of the Types of Vector Fields that The Vector Elements are Capable and Incapable of Constructing

The vector element provides a vector field representation given by Equation (5.53) that is complete to order $p = 0$, which is zeroth-order [11, 12]. However, there are certain vector field representations that the vector elements cannot approximate (refer to sub-section 5.5.1) that fall under the general vector field representation given by Equation (5.53). The algorithm presented in Section 5.5 is used to investigate and verify the above statement.

Equation (5.53) allows for sixteen combinations of vector field representations due to the equation containing the four constant variables of f_0, f_2, g_0 and g_1. Of the sixteen combinations of vector fields in Table 5.3, the vector element is unable to approximate the eight combinations of vector fields found in column C , they are able to approximate the four combinations of vector fields found in column B and they are capable of approximating the four combinations of vector fields found in column A when a constrain is applied to the constants f_2 and g_1.

A	B	C		
$f_2 \neq 0$ AND $g_1 \neq 0$	$f_2 = 0$ AND $g_1 = 0$	$f_2 \neq 0$ OR $g_1 \neq 0$		
$\vec{E}_V(x,y) = (f_0 + f_2 y)\hat{i} + (g_0 + g_1 x)\hat{j}$ A1	$\vec{E}(x,y) = f_0\hat{i} + g_0\hat{j}$ B1	$\vec{E}_V(x,y) = (f_0 + f_2 y)\hat{i} + g_0\hat{j}$ $\vec{E}_V(x,y) = f_0\hat{i} + (g_0 + g_1 x)\hat{j}$ C1	$f_0 \neq 0$ AND $g_0 \neq 0$	**1**
$\vec{E}_V(x,y) = f_2 y\hat{i} + g_1 x\hat{j}$ A2	$\vec{E}_V(x,y) = 0$ B2	$\vec{E}_V(x,y) = f_2 y\hat{i}$ $\vec{E}_V(x,y) = g_1 x\hat{j}$ C2	$f_0 = 0$ AND $g_0 = 0$	**2**
$\vec{E}_V(x,y) = (f_0 + f_2 y)\hat{i} + g_1 x\hat{j}$ $\vec{E}_V(x,y) = f_2 y\hat{i} + (g_0 + g_1 x)\hat{j}$ A3	$\vec{E}(x,y) = f_0\hat{i}$ $\vec{E}(x,y) = g_0\hat{j}$ B3	$\vec{E}_V(x,y) = f_0 + f_2 y\hat{i}$ $\vec{E}_V(x,y) = f_2 y\hat{i} + g_0\hat{j}$ $\vec{E}_V(x,y) = f_0\hat{i} + g_1 x\hat{j}$ $\vec{E}_V(x,y) = g_0 + g_1 x\hat{j}$ C3	$f_0 \neq 0$ OR $g_0 \neq 0$	**3**

Table 5.3: Table of Vector Field Representations

Vector Field Approximations of Column B

The vector elements are capable of approximating constant vector fields, of the algebraic form as seen in block B1 and block B3 of Table 5.3. These fields were simulated and displayed in Figure 5.22.

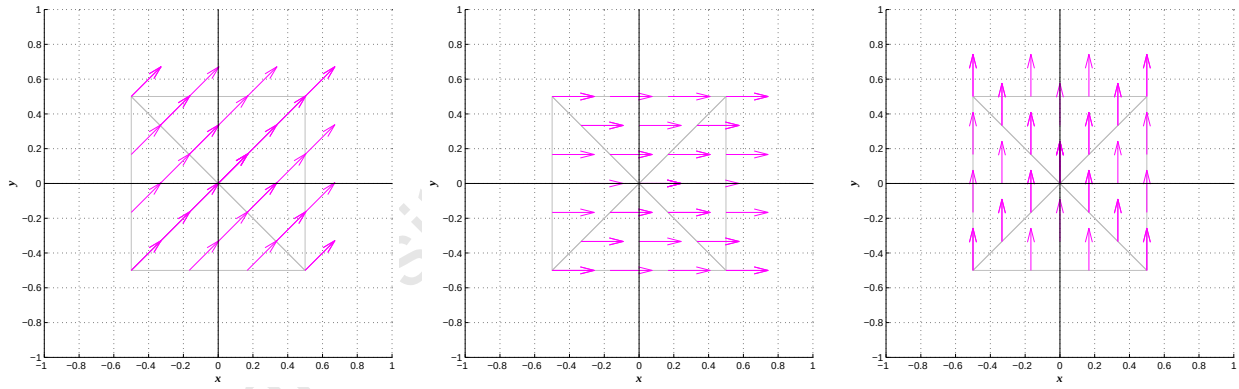

(a) (b) (c)

Figure 5.22: Vector Field Representation of Blocks B1 and B3 of Table 5.3

Sub-figure 5.22a illustrates the vector field $\vec{E}(x,y) = f_0\hat{i} + g_0\hat{j}$. The constant are set as $f_1 = 0$, $f_2 = 0$, $g_1 = 0$, $f_0 = 1$, $g_0 = 1$ and $g_2 = 0$. Sub-figure 5.22b illustrates the vector field $\vec{E}(x,y) = f_0\hat{i}$. The constant are set as $f_1 = 0$, $f_2 = 0$, $g_1 = 0$, $f_0 = 1$, $g_0 = 0$ and $g_2 = 0$. Sub-figure 5.22c illustrates the vector field $\vec{E}(x,y) = g_0\hat{j}$. The constant are set as $f_1 = 0$, $f_2 = 0$, $g_1 = 0$, $f_0 = 0$, $g_0 = 1$ and $g_2 = 0$.

When all the constants are set as zero that is, $f_1 = 0$, $f_2 = 0$, $g_1 = 0$, $f_0 = 0$, $g_0 = 0$ and $g_2 = 0$, then the vector elements displays no vector field as given by the equation in block B2 of Table 5.3.

Vector Field Approximations of Column A

The vector elements are well suited to approximating rotational vector fields and are capable of approximating vector fields of the form as given by the equation in block A2 of Table 5.3 if and only if the following constraint is applied:

$$g_1 = -f_2 \tag{5.93}$$

where Equation (5.93) when applied to the equation in block A2 of Table 5.3, produces a uniform rotational vector field. This can be seen in Sub-figure 5.17a which displays the rotational vector field given by Equation (5.59). Consequently if the following constraint is applied to the equation in block A2 of Table 5.3:

$$g_1 \neq -f_2 \tag{5.94}$$

while choosing $g_1 > f_2$ or either $g_1 < f_2$, then a non-uniform rotational field is produced which the vector elements are not capable of approximating as illustrated in Figure 5.23.

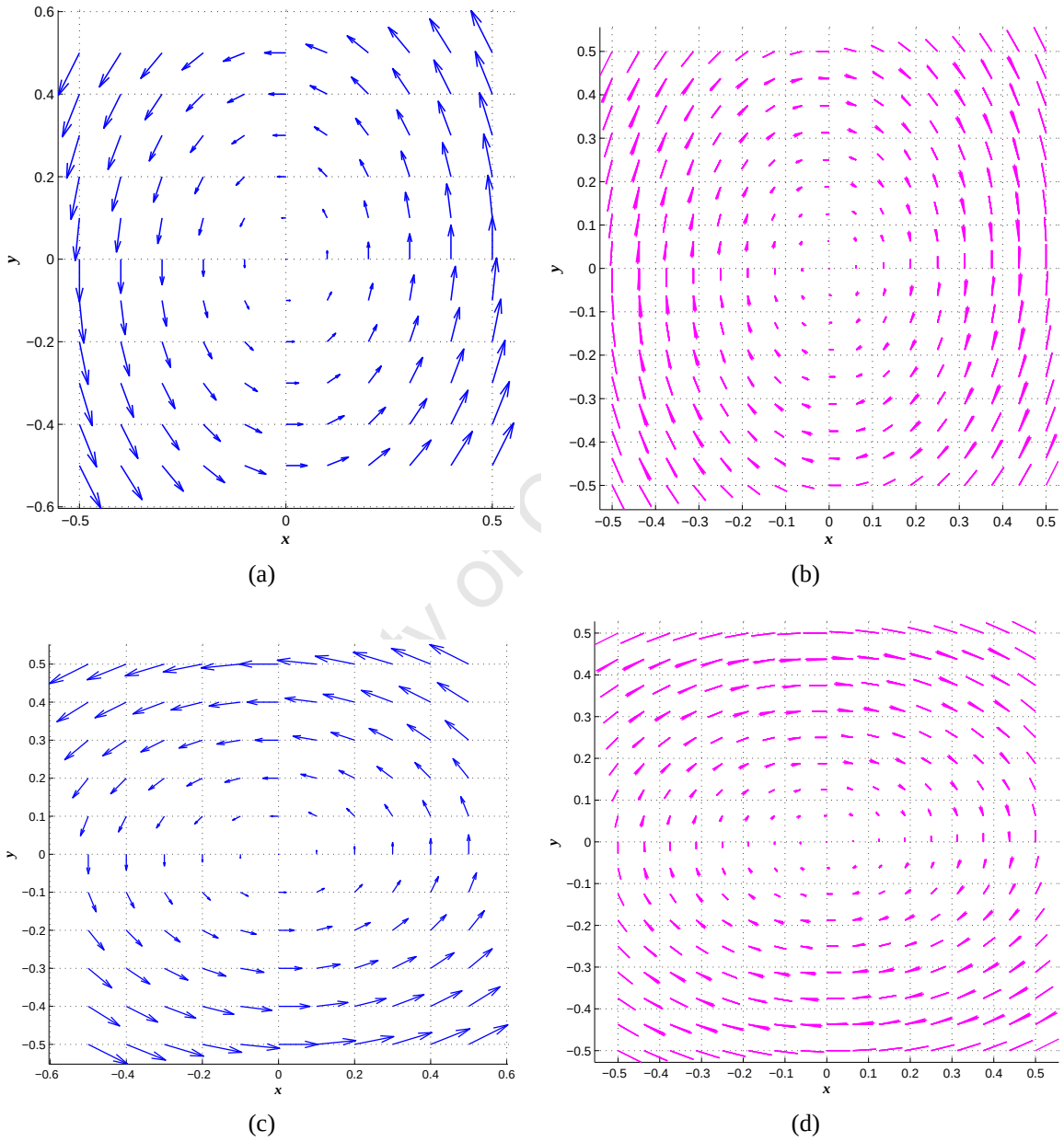

Figure 5.23: Vector Field Representation of Block A2 of Table 5.3

Sub-figure 5.23a illustrates a vector field made by the MATLAB function MESHGRID and using the equation $\vec{E}(x,y) = -2y\hat{i} + 4x\hat{j}$. The vectors are then plotted with the MATLAB function QUIVER. Sub-figure 5.23b illustrates the vector field $\vec{E}(x,y) = f_2 y\hat{i} + g_1 x\hat{j}$ where $g_1 > f_2$. The constants are set as $f_1 = 0$, $f_2 = -2$, $g_1 = 4$, $f_0 = 0$, $g_0 = 0$ and $g_2 = 0$. Sub-figure 5.23c illustrates a vector field made by the MATLAB function MESHGRID and using the equation $\vec{E}(x,y) = -6y\hat{i} + 3x\hat{j}$. The vectors are then plotted with the MATLAB function QUIVER. Sub-figure 5.23d illustrates the vector field $\vec{E}(x,y) = f_2 y\hat{i} + g_1 x\hat{j}$ where $f_2 > g1$. The constants are set as $f_1 = 0$, $f_2 = -6$, $g_1 = 3$, $f_0 = 0$, $g_0 = 0$ and $g_2 = 0$.

Only when Equation (5.93) is applied to the equations located in block A1 and A3, are the vector elements capable of approximating these fields as seen in Figures 5.24, 5.25 and 5.26.

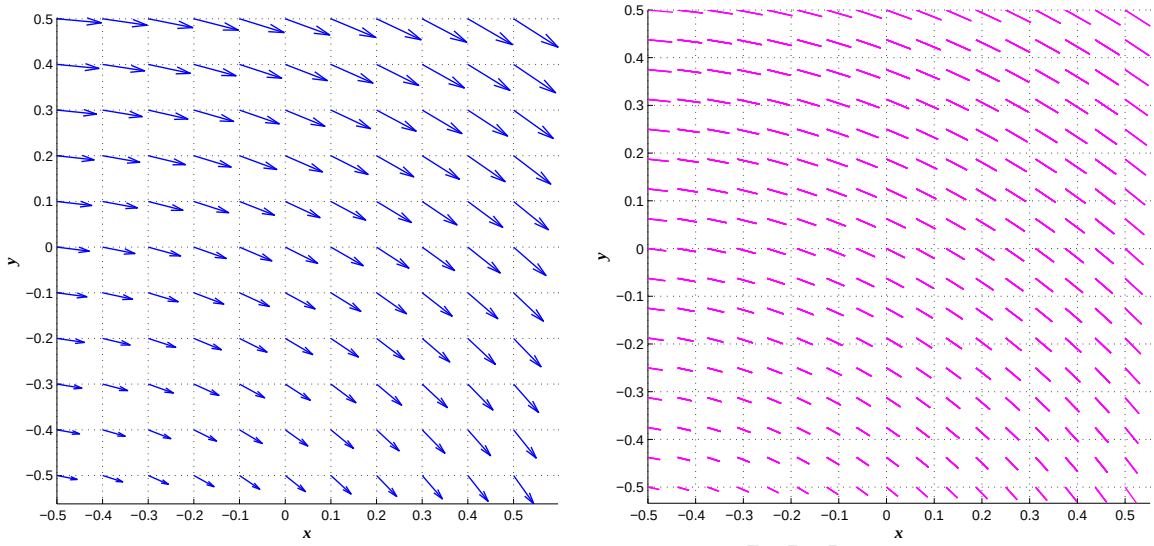

(a) (b)

Figure 5.24: Vector Field Representation of Block A1 of Table 5.3

Sub-figure 5.24a illustrates a vector field made by the MATLAB function MESHGRID and using the equation $\vec{E}(x,y) = (4+3y)\hat{i} - (2+3x)\hat{j}$. The vectors are then plotted with the MATLAB function QUIVER. Sub-figure 5.24b illustrates the vector field $\vec{E}(x,y) = (4+3y)\hat{i} - (2+3x)\hat{j}$ where $g_1 = -f_2$. The constants are set as $f_1 = 0$, $f_2 = 3$, $g_1 = -3$, $f_0 = 4$, $g_0 = -2$ and $g_2 = 0$.

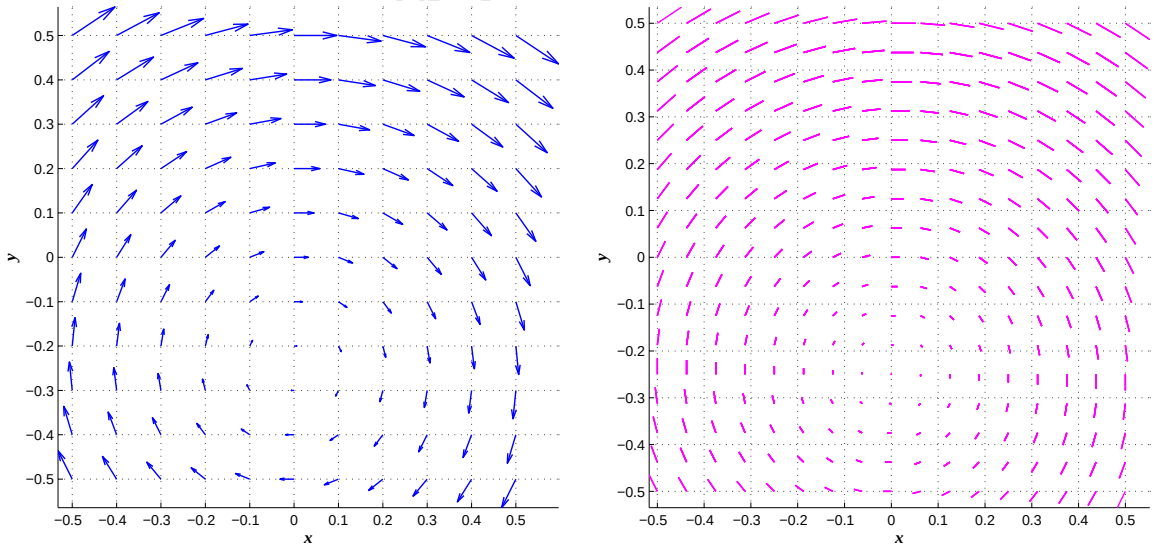

(a) (b)

Figure 5.25: Vector Field Representation of Block A3 of Table 5.3

Sub-figure 5.25a illustrates a vector field made by the MATLAB function MESHGRID and using the equation $\vec{E}(x,y) = \left(\frac{3}{4}+3y\right)\hat{i} - 3x\hat{j}$. The vectors are then plotted with the MATLAB function QUIVER. Sub-figure 5.25b illustrates the vector field $\vec{E}(x,y) = \left(\frac{3}{4}+3y\right)\hat{i} - 3x\hat{j}$ where $g_1 = -f_2$. The constants are set as $f_1 = 0$, $f_2 = 3$, $g_1 = -3$, $f_0 = \frac{3}{4}$, $g_0 = 0$ and $g_2 = 0$.

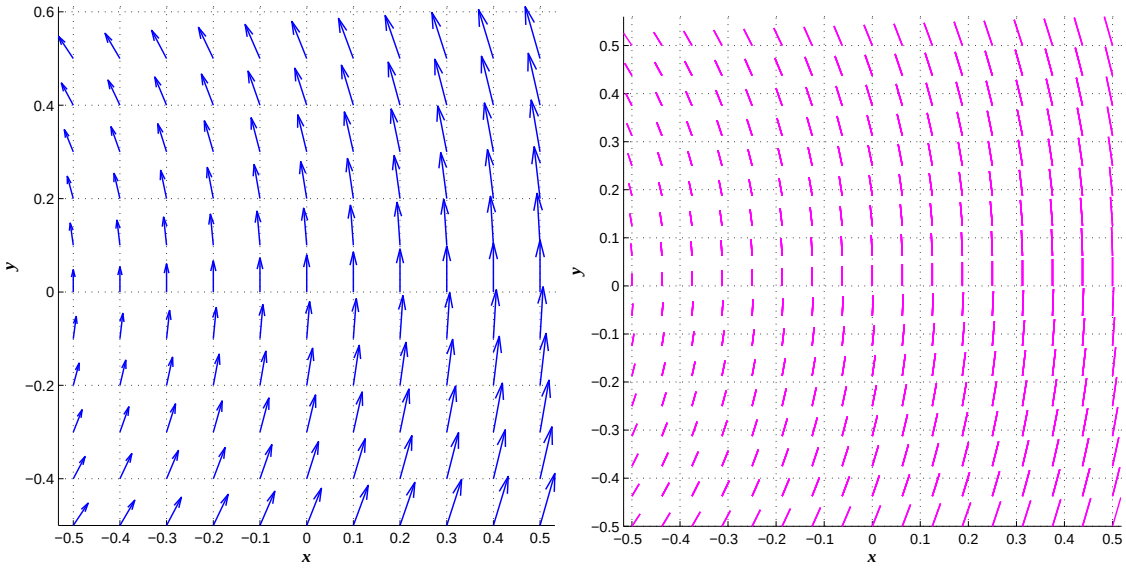

(a) (b)

Figure 5.26: Vector Field Representation of Block A3 of Table 5.3

Sub-figure 5.26a illustrates a vector field made by the MATLAB function MESHGRID and using the equation $\vec{E}(x,y) = -4y\hat{i} + (5+4x)\hat{j}$. The vectors are then plotted with the MATLAB function QUIVER. Sub-figure 5.26b illustrates the vector field $\vec{E}(x,y) = -4y\hat{i} + (5+4x)\hat{j}$ where $g_1 = -f_2$. The constants are set as $f_1 = 0$, $f_2 = -4$, $g_1 = 4$, $f_0 = 0$, $g_0 = 5$ and $g_2 = 0$.

However if, the other constraint of Equation (5.94) is applied to the same equations located in block A1 and A3, then the vector elements are not capable of approximating these fields as seen in Figures 5.27, 5.28 and 5.29.

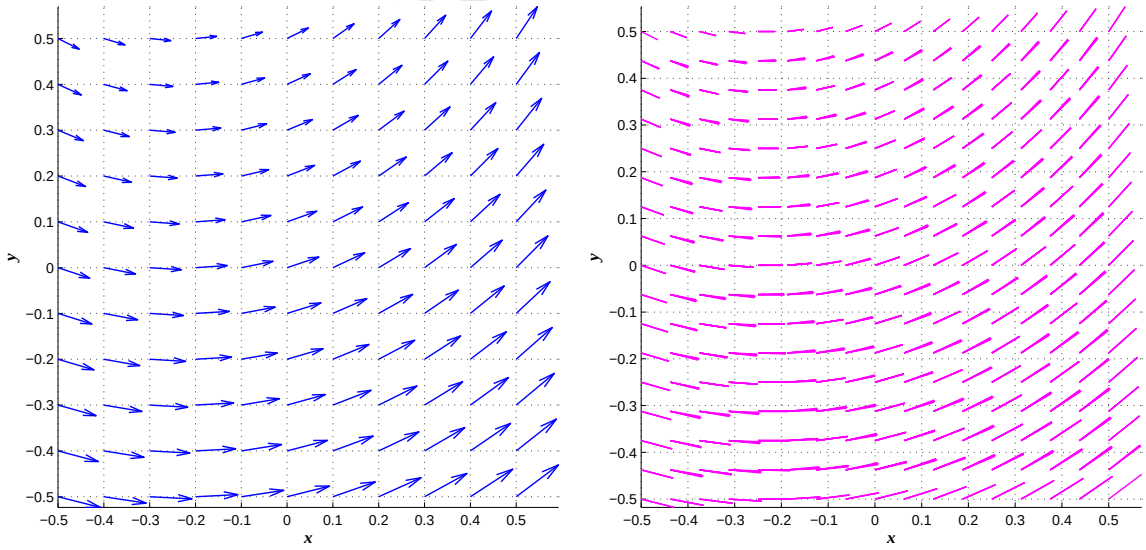

(a) (b)

Figure 5.27: Vector Field Representation of Block A1 of Table 5.3

Sub-figure 5.27a illustrates a vector field made by the MATLAB function MESHGRID and using the equation $\vec{E}(x,y) = (3-2y)\hat{i} + (1+4x)\hat{j}$. The vectors are then plotted with the MATLAB function QUIVER. Sub-figure 5.27b illustrates the vector field $\vec{E}(x,y) = (3-2y)\hat{i} + (1+4x)\hat{j}$ where $g_1 \neq -f_2$. The constants are set as $f_1 = 0$, $f_2 = -2$, $g_1 = 4$, $f_0 = 3$, $g_0 = 1$ and $g_2 = 0$.

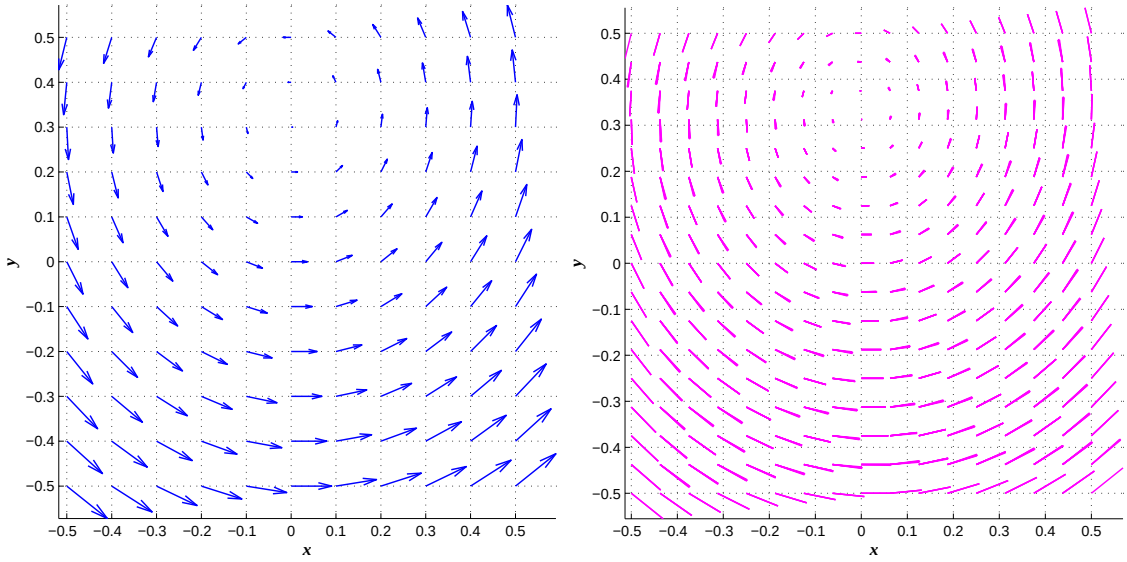

(a) (b)

Figure 5.28: Vector Field Representation of Block A3 of Table 5.3

Sub-figure 5.28a illustrates a vector field made by the MATLAB function MESHGRID and using the equation $\vec{E}(x,y) = (1-3y)\hat{i} + 4x\hat{j}$. The vectors are then plotted with the MATLAB function QUIVER. Sub-figure 5.28b illustrates the vector field $\vec{E}(x,y) = (1-3y)\hat{i} + 4x\hat{j}$ where $g_1 \neq -f_2$. The constants are set as $f_1 = 0$, $f_2 = -3$, $g_1 = 4$, $f_0 = 1$, $g_0 = 0$ and $g_2 = 0$.

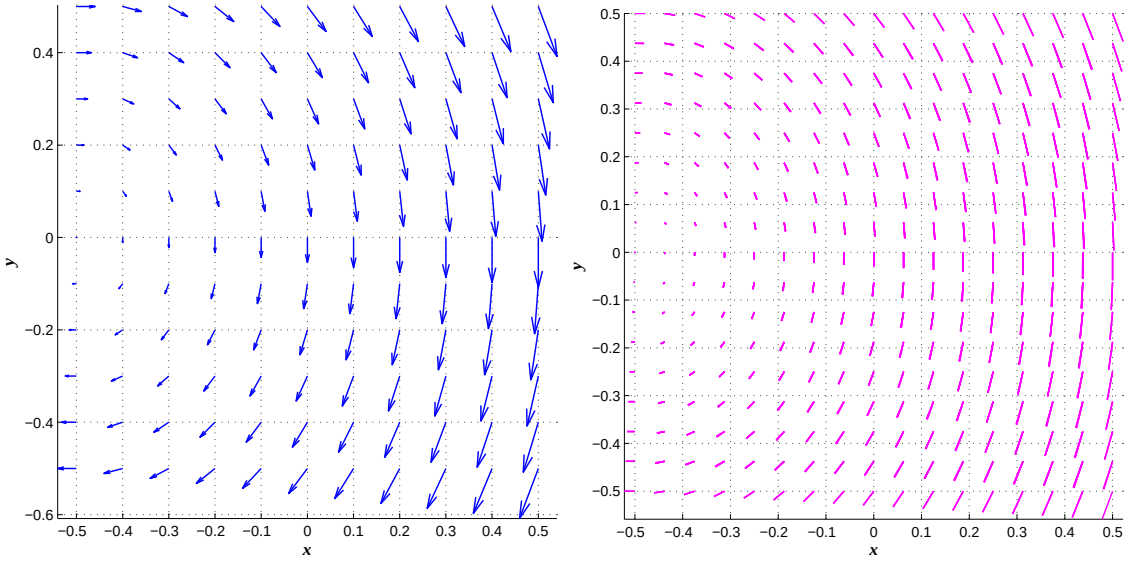

(a) (b)

Figure 5.29: Vector Field Representation of Block A3 of Table 5.3

Sub-figure 5.29a illustrates a vector field made by the MATLAB function MESHGRID and using the equation $\vec{E}(x,y) = 3y\hat{i} - (2+4x)\hat{j}$. The vectors are then plotted with the MATLAB function QUIVER. Sub-figure 5.29b illustrates the vector field $\vec{E}(x,y) = 3y\hat{i} - (2+4x)\hat{j}$ where $g_1 \neq -f_2$. The constants are set as $f_1 = 0$, $f_2 = 3$, $g_1 = -4$, $f_0 = 0$, $g_0 = -2$ and $g_2 = 0$.

Vector Field Approximations of Column C

Equations located in block C1, C2 and C3 all possess a curling differential property, but the vector elements are incapable of approximating these vector fields as seen in Figures

5.31, 5.32, 5.33, 5.34, 5.35 and 5.30.

J.P. Webb stated in his paper [11], that the field interpolation that the vector element provides is not even first-order [11], and therefore linear fields as given by the equations located in block C2 of Table 5.3 cannot be represented by the vector element exactly [11].

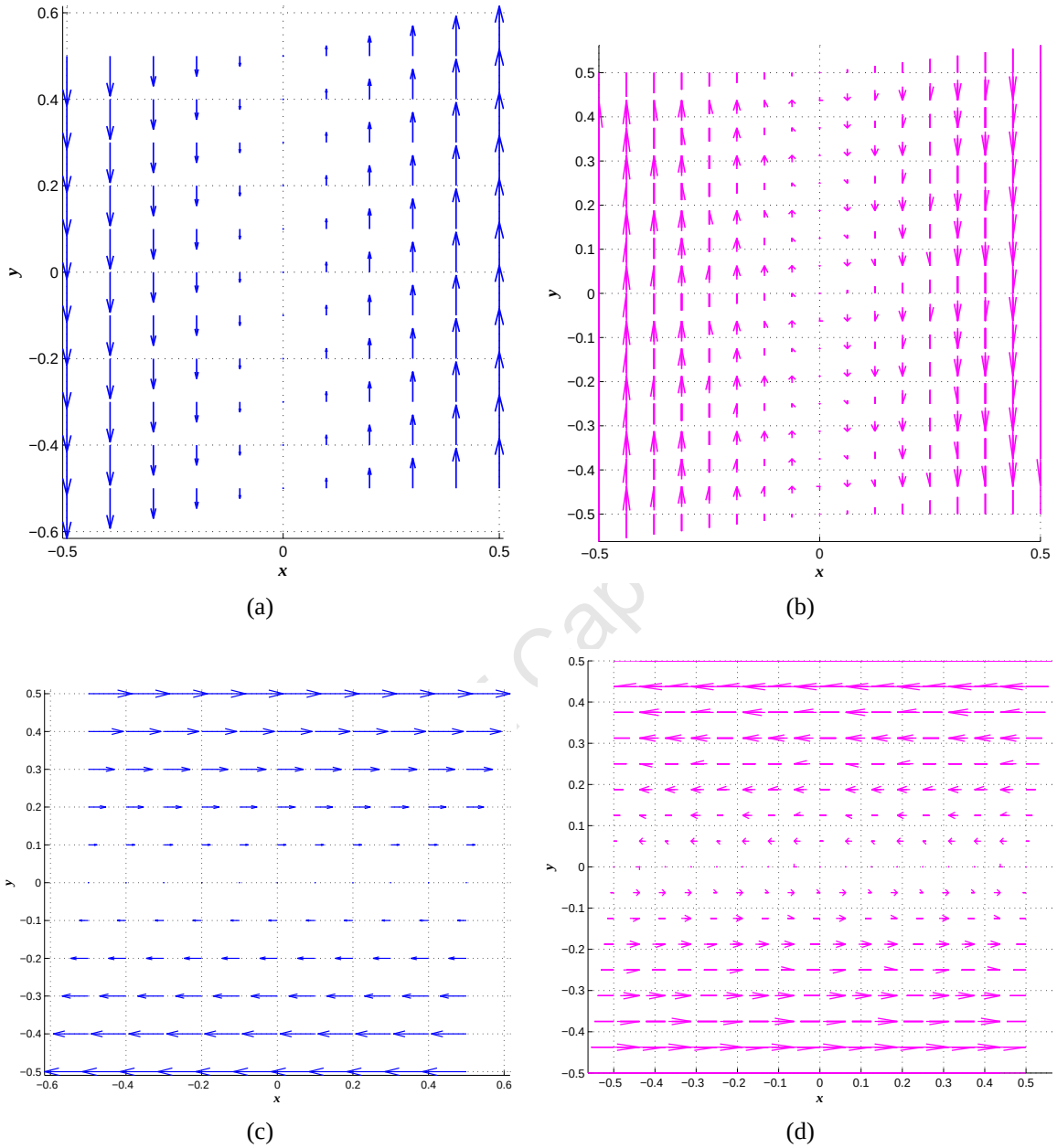

Figure 5.30: Linear Vector Field Representation of Block C2 of Table 5.3

Sub-figure 5.30c illustrates a vector field made by the MATLAB function MESHGRID and using the equation $\vec{E}(x,y) = x\hat{j}$. The vectors are then plotted with the MATLAB function QUIVER. Sub-figure 5.30d illustrates the vector field $\vec{E}(x,y) = x\hat{j}$. The constants are set as $f_1 = 0$, $f_2 = 0$, $g_1 = 1$, $f_0 = 0$, $g_0 = 0$ and $g_2 = 0$. Sub-figure 5.30a illustrates a vector field made by the MATLAB function MESHGRID and using the equation $\vec{E}(x,y) = y\hat{i}$. The vectors are then plotted with the MATLAB function QUIVER. Sub-figure 5.30b illustrates the vector field $\vec{E}(x,y) = y\hat{i}$. The constants are set as $f_1 = 0$, $f_2 = 1$, $g_1 = 0$, $f_0 = 0$, $g_0 = 0$ and $g_2 = 0$.

The above statement of J.P.Webb can be extended to include the variations of linear fields (as seen in blocks C1 and C3) supported by Equation (5.53).

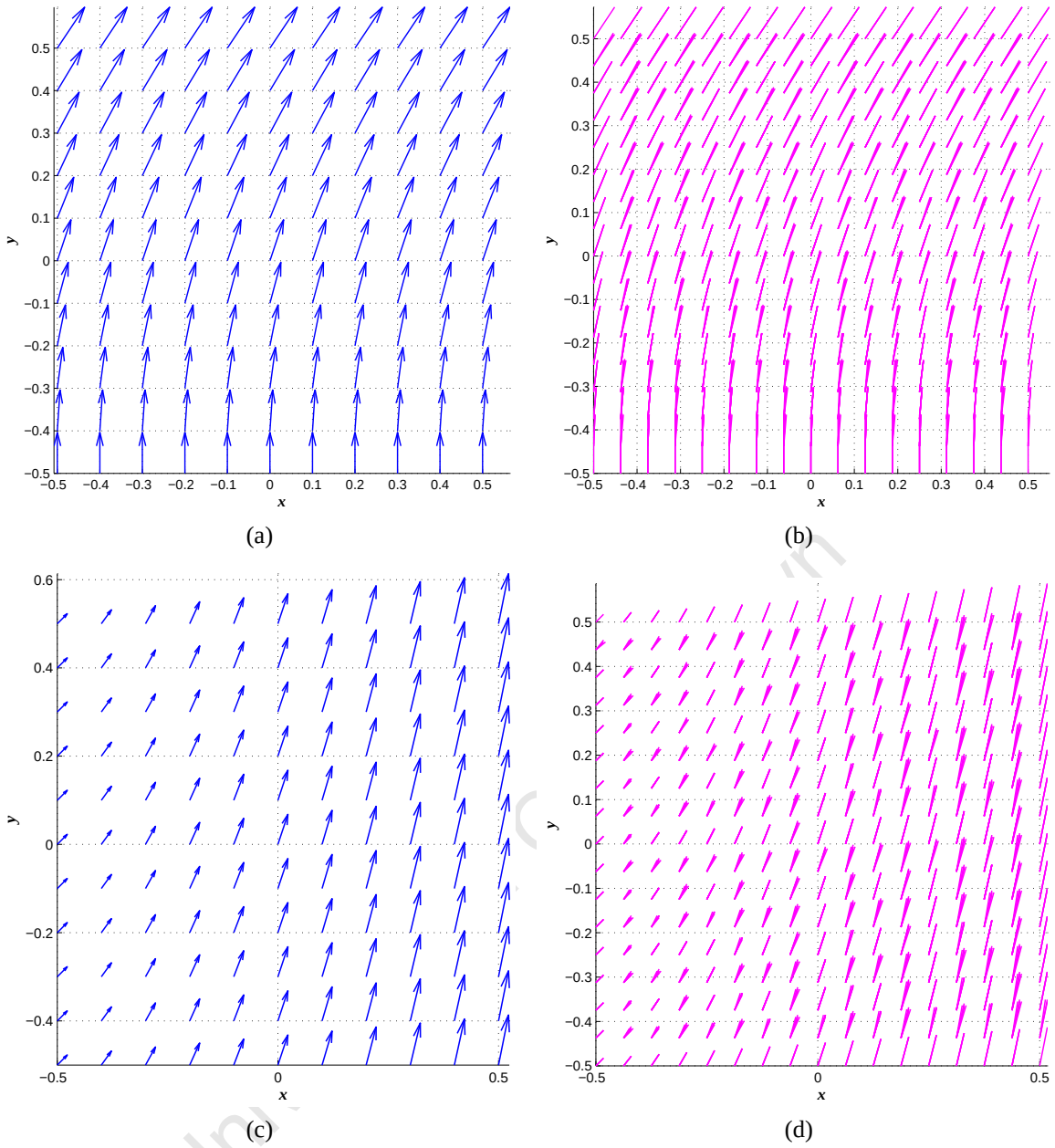

Figure 5.31: Vector Field Representation of Block C1 of Table 5.3

Sub-figure 5.31a illustrates a vector field made by the MATLAB function MESHGRID and using the equation $\vec{E}(x,y) = (1+2y)\hat{i}+3\hat{j}$. The vectors are then plotted with the MATLAB function QUIVER. Sub-figure 5.31b illustrates the vector field $\vec{E}(x,y) = (1+2y)\hat{i}+3\hat{j}$. The constants are set as $f_1 = 0$, $f_2 = 2$, $g_1 = 0$, $f_0 = 1$, $g_0 = 3$ and $g_2 = 0$. Sub-figure 5.31c illustrates a vector field made by the MATLAB function MESHGRID and using the equation $\vec{E}(x,y) = 1\hat{i}+(3+4x)\hat{j}$. The vectors are then plotted with the MATLAB function QUIVER. Sub-figure 5.31d illustrates the vector field $\vec{E}(x,y) = 1\hat{i}+(3+4x)\hat{j}$. The constants are set as $f_1 = 0$, $f_2 = 0$, $g_1 = 4$, $f_0 = 1$, $g_0 = 3$ and $g_2 = 0$.

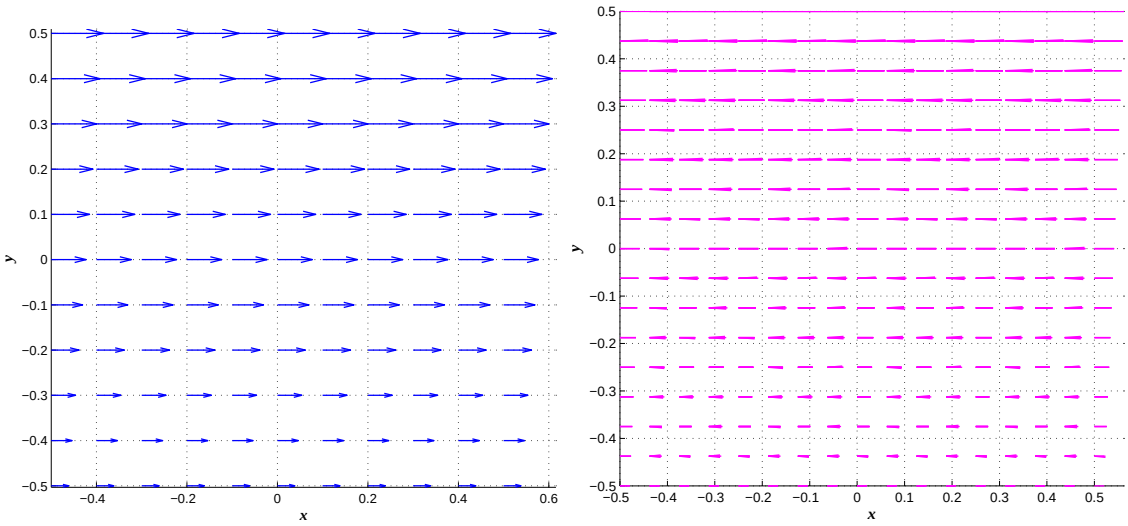

(a) (b)

Figure 5.32: Vector fields of Representation of Block C3 of Table 5.3

Sub-figure 5.32a illustrates a vector field made by the MATLAB function `MESHGRID` and using the equation $\vec{E}(x,y) = (1+y)\hat{i}$. The vectors are then plotted with the MATLAB function `QUIVER`. Sub-figure 5.32b illustrates the vector field $\vec{E}(x,y) = (1+y)\hat{i}$. The constants are set as $f_1 = 0$, $f_2 = 1$, $g_1 = 0$, $f_0 = 1$, $g_0 = 0$ and $g_2 = 0$.

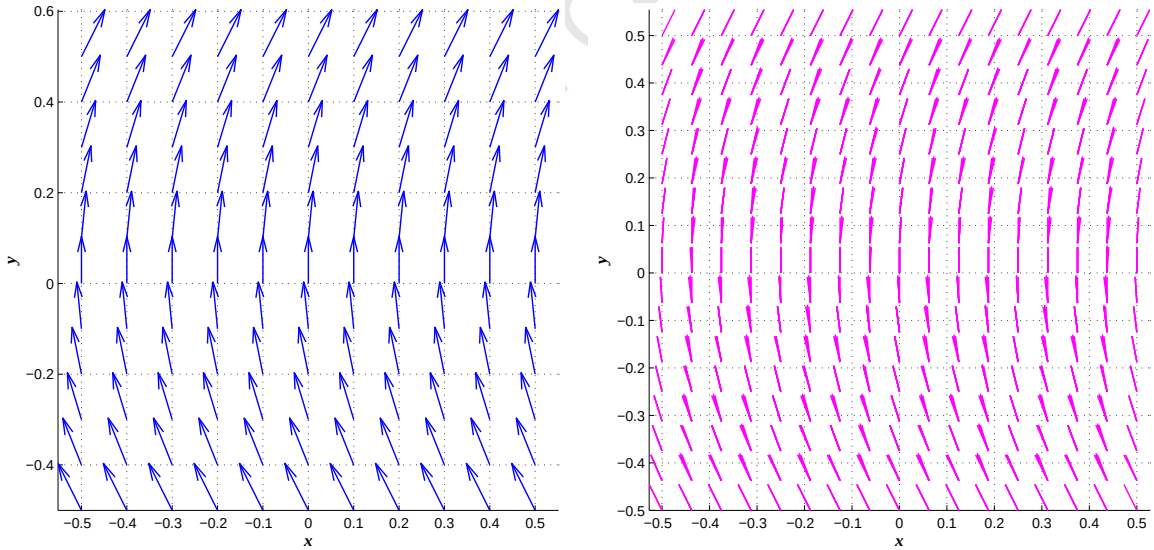

(a) (b)

Figure 5.33: Vector fields of Representation of Block C3 of Table 5.3

Sub-figure 5.33a illustrates a vector field made by the MATLAB function `MESHGRID` and using the equation $\vec{E}(x,y) = y\hat{i} + 1\hat{j}$. The vectors are then plotted with the MATLAB function `QUIVER`. Sub-figure 5.33b illustrates the vector field $\vec{E}(x,y) = y\hat{i} + 1\hat{j}$. The constants are set as $f_1 = 0$, $f_2 = 1$, $g_1 = 1$, $f_0 = 0$, $g_0 = 0$ and $g_2 = 0$.

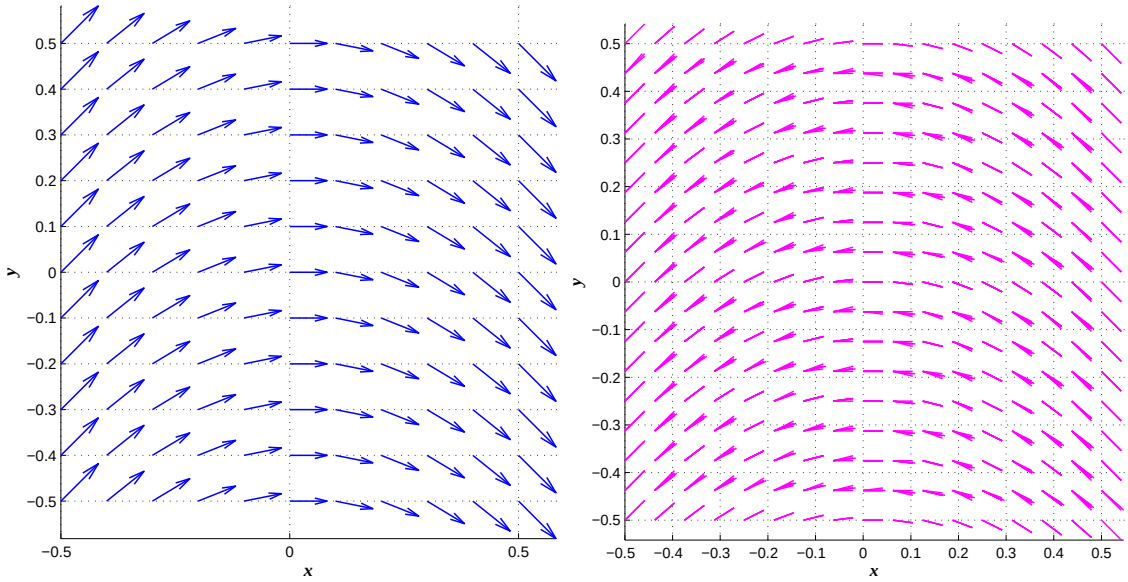

(a) (b)

Figure 5.34: Vector fields of Representation of Block C3 of Table 5.3

Sub-figure 5.33a illustrates a vector field made by the MATLAB function MESHGRID and using the equation $\vec{E}(x,y) = 2\hat{i} - 4x\hat{j}$. The vectors are then plotted with the MATLAB function QUIVER. Sub-figure 5.33b illustrates the vector field $\vec{E}(x,y) = 2\hat{i} - 4x\hat{j}$. The constants are set as $f_1 = 0$, $f_2 = 0$, $g_1 = -4$, $f_0 = 2$, $g_0 = 0$ and $g_2 = 0$.

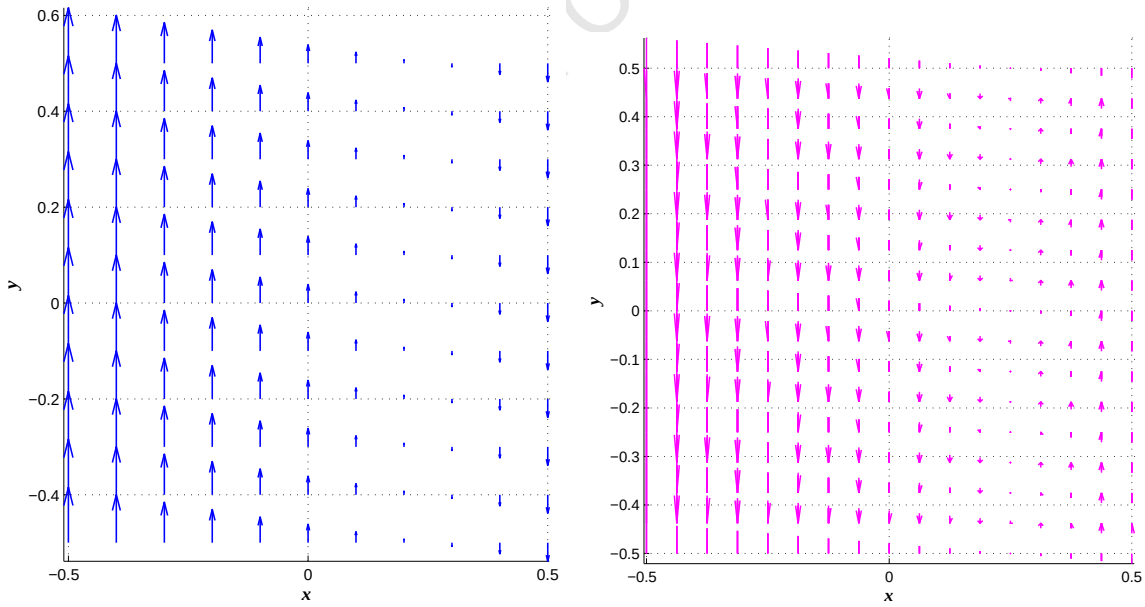

(a) (b)

Figure 5.35: Vector fields of Representation of Block C3 of Table 5.3

Sub-figure 5.35a illustrates a vector field made by the MATLAB function MESHGRID and using the equation $\vec{E}(x,y) = (1-4x)\hat{j}$. The vectors are then plotted with the MATLAB function QUIVER. Sub-figure 5.35b illustrates the vector field $\vec{E}(x,y) = (1-4x)\hat{j}$. The constants are set as $f_1 = 0$, $f_2 = 0$, $g_1 = -4$, $f_0 = 0$, $g_0 = 1$ and $g_2 = 0$.

5.7 Limitations of the Vector Element

The triangular vector elements for this dissertation posses two main limitations which is directly related to how these shape functions were designed mathematically. The limitations are:

1. the element rate of convergence is rather poor [12]; the solution will approach the exact one slowly as the mesh is refined [12]. As in the case of nodal (scalar) elements, a better convergence rate can be achieved using higher-order elements.

2. the element is only capable of approximating simple vector fields as given by Equation (5.53) and is therefore unable to approximate more complex mathematically structured vector fields. Although the element can approximate vector fields such as those given by Equation (5.53), there were however some exceptions that was shown in sub-section 5.6.1.

Higher-order elements falls outside the scope of this dissertation and therefore only a brief overview will be given in the next section.

5.7.1 Higher-Order Vector Elements

There are two competing approaches to higher-order vector elements which are [12, 13]:

- Interpolatory Vector Elements
- Hierarchical Vector Elements

The difference between these elements lies in their construction [12, 13].

Interpolatory Vector Elements

The interpolatory basis functions of these elements are defined on a set of points on the element, such that the basis function vanishes at all points except one [12]. There are advantages associated with these basis functions:

- the functions have good linear independence, thus resulting in a better conditioned matrix system [12].
- they interpolate the tangential component of the vector field, making enforcement of boundary conditions easy [12].
- they have a unified expression which simplifies the implementation of computer codes for the generation of arbitrary-order basis functions [12].

These elements can be used for $h-adaption$ (mesh refinement). Disadvantages of the basis functions:

- the interpolatory basis functions of a given order are all different from those of the lower orders [12]. Hence different order basis functions cannot be used together (in the same mesh), which makes it impossible to implement $p-adaption$ (iterative increase of the element orders in different regions (of the mesh) until the solution is converged to a specified accuracy) [12].

Hierarchical Vector Elements

The basis functions are not defined on a set of points [12]. Higher-order hierarchical basis functions are formed by adding new basis functions to lower-order basis functions [12, 13, 2]. For example, a first-order basis function contain those of the zeroth-order basis functions, and the second-order basis function will in turn contain those of the zeroth-order and first-order basis functions [12], thus a specific higher-order basis function set contains all the lower-order basis functions [2]. This distinct advantage of these basis functions is that they permit the use of different order of basis functions (hence elements) within the same problem, and hence can be used for $p-adaption$ [12].

A good deal of time has been invested in studying the vector element for the following reasons:

- it is important because the vector element is the building block (foundation) of a vector field simulation.
- good knowledge is gained of the properties and limitations of the element.
- the knowledge is needed in order to code an entire finite element (FE) algorithm.

Chapter 6

Finite Element Method

The finite element method (FEM) is a numerical technique used to solve problems that are described mathematically by ordinary differential equations (ODE) and partial differential equations (PDE). [1]. The main idea behind the method is the representation of the domain into smaller sub-domains called finite elements [1]. These finite elements can be represented by [2]:

- lines in one dimension
- triangles in two-dimensions
- tetrahedrons in three-dimensions

The numerical solution (of the ODE or PDE) within a finite element is calculated by using the values computed by FEM at the nodes (when using nodal finite elements) or edges (when using vector finite elements) of the discretized domain, along with the corresponding basis functions associated with the particular finite element [1, 2]. The values of the nodes or edges are obtained after solving a system of linear equations which the FEM sets up [1, 2].

The accuracy of the solution can depend on, among other factors:

- the order of the basis functions, which may be linear, quadratic or higher order [1].
- domain discretization. Increasing the number of elements inside the domain (creating a finner mesh) increases the accuracy of the solution in comparison to a domain discretized by less elements (producing a course mesh) [1].

Finite element analysis (FEA) can handle two different types of problems [2]:

- eigenanalysis (source-free) problems
- deterministic (force driven) problems

Deterministic problems analysed using FEA involve a “source” [2]. Equation (2.31) of Section 2.4 and Equation (2.39) of Section 2.5 respectively describe a deterministic problem, where the “source” can take the form of a boundary condition or the form of an actual source region present within the domain [6, 15]. In the case where the “source” takes the form of a boundary condition, the problem can be classified as boundary-driven, also known as a boundary value problem (BVP) [6, 15]. In the case where the “source” takes the form of actual source region, the problem can be classified as force-driven (refer

to Section 2.6 where these concepts were discussed with reference to Equations (2.31) and (2.39) [6, 15]).

The response of the structure (conductor), to a forced excitation (the source) is described by the solution to Equation (2.31) and Equation (2.39), as discussed in Section 2.6. The FEA is able to compute this solution [2]. The FEM is applied to Equation (2.39) [3, 16, 17].

Summary Outline of FEM

The basic steps involved in the application of FEM are as follows:

1. Create a FE mesh by discretizing the entire domain into sub-domains and the sub-domains are referred to as finite elements [1].
2. Processing of the mesh data information into useful data-structures [2, 12, 3].
3. Obtain a system of linear equations for a single element by applying the Galerkin method to the PDE under investigation [1].
4. Formation of the global matrix system of equations through the assembly of all elements within the domain and incorporation of the boundary conditions (BC's) into this global matrix system [1].
5. Solve the linear system of equations to obtain the unknown edge values of the domain [1].
6. Build the solution vector field (solution to the PDE under investigation) over the entire domain [1].

The dissertation is focused mainly on solving problems over a two-dimensional domain.

6.1 Domain Discretization

The entire domain is divided up into smaller sub-domains, the sub-domains are also called finite elements [1]. The union of all the sub-domains approximately equals the full domain [13].

6.1.1 Two Dimensional Domain Discretization

The domain of a two-dimensional BVP or force-driven problem, usually has an irregular shape, as shown in Figure 6.1(a) [1]. Using the FEM, the first step is to accurately represent the physical domain of the problem by a set of basic shapes called finite elements [1]. The use of a rectangle, for example, as a basic finite element to discretize an irregular domain is certainly the simplest but not the most suitable choice because an assembly of rectangles cannot accurately represent the arbitrary geometrical shape of a domain [1]. In such a case the discretization error is significant, as shown in Figure 6.1(b), although it tends to decrease as the size of the rectangles in the domain becomes smaller [1]. However if a triangle element is used instead as the basic element for the meshing of the two-dimensional domain, the discretization error would be effectively much smaller [1]. This is illustrated graphically in Figure 6.2(a) [1]. A course mesh of an irregular domain

using quadrilateral elements is shown in Figure 6.2(b). Similar to the triangular element, the quadrilateral element results in a smaller discretization error [1].

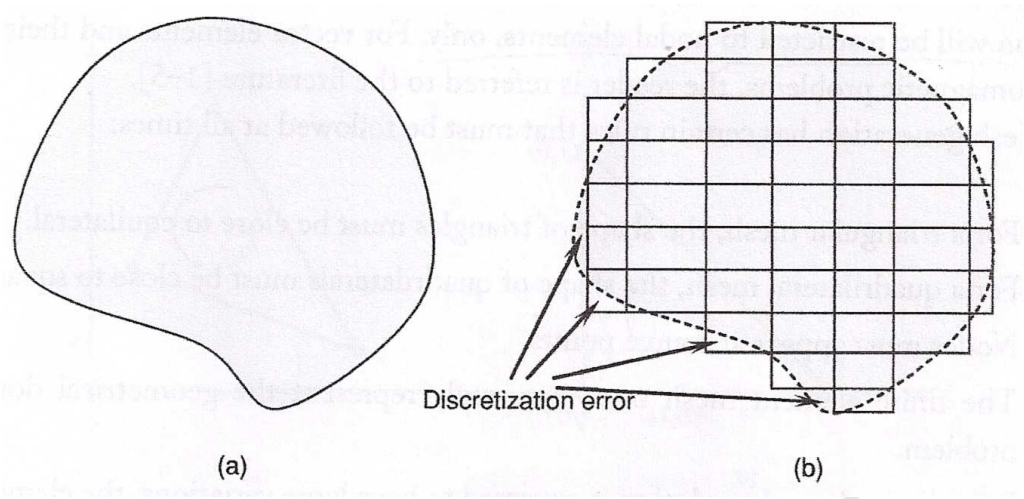

Figure 6.1: Discretization Error using Rectangular Elements [1]
(a)Irregular two dimensional domain. (b)Finite element mesh using rectangular elements.

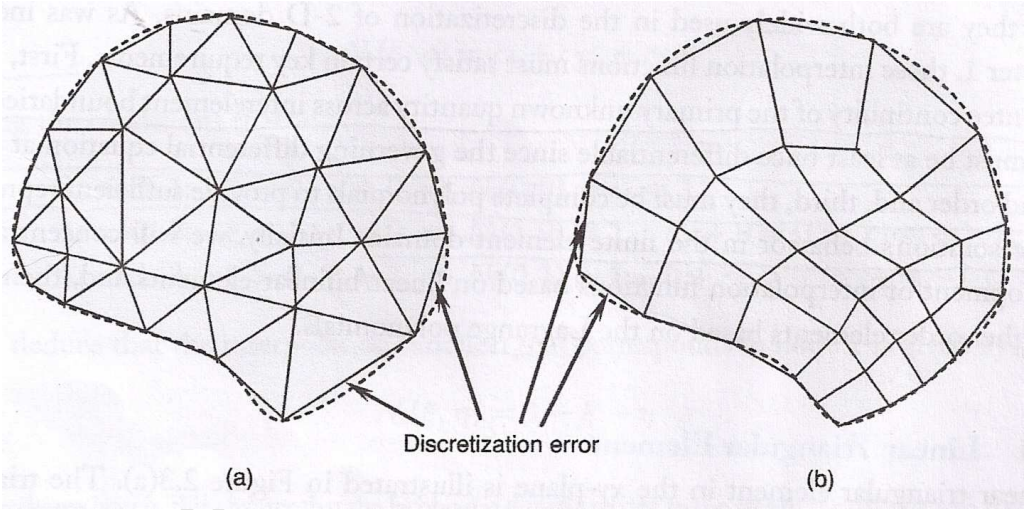

Figure 6.2: Discretization Error using Triangular and Quadrilateral Elements [1]
(a)Finite element mesh using triangular elements. (b)Finite element mesh using quadrilateral elements.

6.2 Data-Structures

The domain is sub-divided into finite elements, thus forming a FE mesh and all finite elements within the entire mesh are connected to one another [1, 5]. The data instructing how the elements are connected to each other through their edges, nodes and coordinates are referred to as the element connectivity information [1, 2]. The element connectivity information is stored in lists which are referred to as data-structures [2, 23].

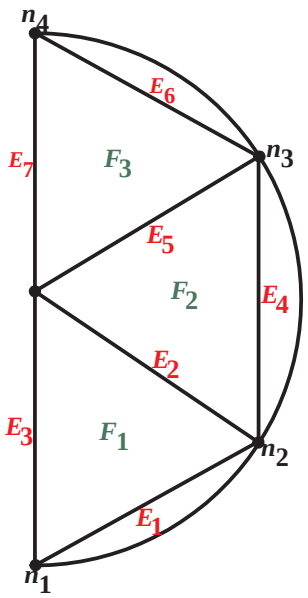

Figure 6.3: A Generic Three Element Mesh

This simple mesh is used to illustrate element connectivity information through Table 6.1 and also the assembly process of the global matrix system in sub-section 6.4.1.

An example of one such data-structure corresponding to the mesh in Figure 6.3 is shown in Table 6.1 and this data-structure contains the element connectivity information instructing how the three elements within the mesh are connected to one another through their edges.

Global Element (Face) No.	Faces	Local Edge 1	Local Edge 2	Local Edge 3
1	F_1	E_1	E_2	E_3
2	F_2	E_4	E_5	E_2
3	F_3	E_6	E_7	E_5

Table 6.1: Connectivity between Elements and Edges

This data-structure is referred to as `FaceEdgesData` in this dissertation. As shown by this table and Figure 6.3, edge E_2 is shared by both element F_1 and element F_2, thus stating that edge E_2 *connects* both element F_1 and element F_2 to each other. Similarly, edge E_5 is shared by both element F_2 and element F_3, thus stating that edge E_5 *connects* both element F_2 and element F_3 to each other.

Table 6.1 shows the following connectivity information of the finite elements in Figure 6.3:

- the column labelled Faces contains the global element numbering of elements within the mesh. The mesh contains three elements labelled as F_1, F_2 and F_3.
- the next three columns labelled as Local Edge 1, Local Edge 2 and Local Edge 3, altogether contains the global edge numbering system of the entire mesh, but the column headings where the edges appear under indicates the local edge numbering system of a particular element.
- row number 1 shows that, element F_1 consists of three edges E_1, E_2 and E_3. Edge E_1 is numbered locally as edge number 1, edge E_2 is numbered locally as edge number 2 and edge E_3 is numbered locally as edge number 3 of element F_1.

- row number 2 shows that, element F_2 consists of three edges E_4, E_5 and E_2. Edge E_4 is numbered locally as edge number 1, edge E_5 is numbered locally as edge number 2 and edge E_2 is numbered locally as edge number 3 of element F_2.
- row number 3 shows that, element F_3 consists of three edges E_6, E_7 and E_5. Edge E_6 is numbered locally as edge number 1, edge E_7 is numbered locally as edge number 2 and edge E_5 is numbered locally as edge number 3 of element F_3.

The arrangement of the element connectivity information within Table 6.1 shows how the *global numbering system of edges within the entire mesh is related to the local numbering system of edges of an individual finite element.*

6.3 Formulation of the System of Linear Equations

There are two methods that are widely used to obtain a system of linear equations also known as finite element equations [2] . The methods are:

- the *variational method*
- the *weighted-residual method*

This dissertation follows the weighted-residual method also known as the Galerkin method [1]. This method begins by forming a residual directly from the PDE [1] given by Equation (2.38) [3, 16, 17]. The element residual is formed by transferring all terms of the Equation (2.38) to the LHS [3]:

$$\vec{\nabla} \times \vec{\nabla} \times \tilde{E_E} - \mu j\omega \tilde{J_s} - \sigma \mu j\omega \tilde{E_E} = r^e \tag{6.1}$$

The residual r^e, is the difference between the approximate solution and the actual solution [1, 2].

6.3.1 Formulation of the Weighted-Integral Equation for a Three-Dimensional Finite Element

The objective is to minimise this element residual in a weighted sense [1]. To achieve this, the residual is multiplied by a vector weighted function $\vec{w}$ and integrated over the domain (which can be three-dimensional or two-dimensional) of a single element [3]. The integral is then set to zero [1]. Equation (6.1) is converted into an weighted-integral equation[1]:

$$\int_v^{(e)} \vec{w} \cdot \left(\vec{\nabla} \times \vec{\nabla} \times \tilde{E_E} + \mu j\omega \tilde{J_s} + \sigma \mu j\omega \tilde{E_E} \right) dV = 0 \tag{6.2}$$

where the integration is done over the volume V, of a three-dimensional finite element and the superscript (e), indicates a single element. Integrating each term of Equation (6.2) gives [16, 17]:

$$\int_v^{(e)} \left[\vec{w} \cdot \left(\vec{\nabla} \times \vec{\nabla} \times \tilde{E_E} \right) \right] dV + \int_v^{(e)} \vec{w} \cdot \left(\sigma \mu j\omega \tilde{E_E} \right) dV = \int_v^{(e)} \vec{w} \cdot \left(-\mu j\omega\sigma \tilde{E_s} \right) dV \tag{6.3}$$

Removing the constants σ, μ, j and ω from the integral in Equation (6.3) produces [16, 17]:

$$\int_v^{(e)} \left[\vec{w} \cdot \left(\vec{\nabla} \times \vec{\nabla} \times \tilde{E_E} \right) \right] dV + \sigma \mu j\omega \int_v^{(e)} \left(\vec{w} \cdot \tilde{E_E} \right) dV = -\sigma \mu j\omega \int_v^{(e)} \left(\vec{w} \cdot \tilde{E_s} \right) dV \tag{6.4}$$

Apply vector integration by parts (based on Green's theorem) to Equation (6.4) [3, 16, 17]:

$$\int_v^{(e)} \left[\left(\vec{\nabla}\times\vec{w}\right)\cdot\left(\vec{\nabla}\times\tilde{E_E}\right)\right] dV - \oint_s^{(e)} \vec{w}\times\left(\vec{\nabla}\times\tilde{E_E}\right)\cdot d\vec{S} + \sigma\mu\, j\omega \int_v^{(e)} \left(\vec{w}\cdot\tilde{E_E}\right) dV = -\sigma\mu\, j\omega \int_v^{(e)} \left(\vec{w}\cdot\tilde{E_s}\right) dV \quad (6.5)$$

According to [16, 17], the flux term $\oint_s^{(e)} \vec{w}\times\left(\vec{\nabla}\times\tilde{E}\right)\cdot d\vec{S} = 0$[1]. Equation (6.5) becomes:

$$\int_v^{(e)} \left[\left(\vec{\nabla}\times\vec{w}\right)\cdot\left(\vec{\nabla}\times\tilde{E_E}\right)\right] dV + \sigma\mu\, j\omega \int_v^{(e)} \left(\vec{w}\cdot\tilde{E_E}\right) dV = -\sigma\mu\, j\omega \int_v^{(e)} \left(\vec{w}\cdot\tilde{E_s}\right) dV \quad (6.6)$$

6.3.2 Formulation of Linear Equations for a Two-Dimensional Finite Element

The two-dimensional weighted-integral equation is similar to Equation (6.6) except that the integration is done over the area of a two-dimensional finite element:

$$\int_A^{(e)} \left[\left(\vec{\nabla}\times\vec{w}\right)\cdot\left(\vec{\nabla}\times\tilde{E_E}\right)\right] dA + \sigma\mu\, j\omega \int_A^{(e)} \left(\vec{w}\cdot\tilde{E_E}\right) dA = -\sigma\mu\, j\omega \int_A^{(e)} \left(\vec{w}\cdot\tilde{E_s}\right) dA \quad (6.7)$$

In the Galerkin method, the vector weighted functions are identical to the interpolation of the shape functions across an element [1] (refer to sub-section 5.3.1). Thus:

$$\vec{w}(x,y) = \vec{N}_i(x,y) \quad (6.8)$$

for $i = 1:3$. There are three shape functions (vector functions) $\vec{N}_i$ for $i = 1:3$ associated with a finite element [2, 3], this concept was illustrated in sub-section 5.3.1. The electric field intensity $\tilde{E_E}$, can be approximated across a triangular element as [16, 17]:

$$\tilde{E}_E^{(e)} = \sum_{j=1}^{3} \tilde{E}_j \vec{N}_j(x,y) \quad (6.9)$$

Substituting Equation (6.8) and Equation (6.9) into Equation (6.7) produces [16, 17]:

$$\int_A^{(e)} \left[\left(\vec{\nabla}\times\vec{N}_i\right)\cdot\left(\vec{\nabla}\times\sum_{j=1}^{3}\tilde{E}_j\vec{N}_j\right)\right] dA + \sigma\mu\, j\omega \int_A^{(e)} \left(\vec{N}_i\cdot\left(\sum_{j=1}^{3}\tilde{E}_j\vec{N}_j\right)\right) dA = -\sigma\mu\, j\omega \int_A^{(e)} \left(\vec{N}_i\cdot\tilde{E_s}\right) dA \quad (6.10)$$

for $i = 1:3$. Applying algebra operations of summation to Equation (6.10) gives [2, 16, 17]:

$$\sum_{i=1}^{3}\sum_{j=1}^{3}\left(\int_A^{(e)}\left[\left(\vec{\nabla}\times\vec{N}_i\right)\cdot\left(\vec{\nabla}\times\vec{N}_j\right)\right] dA\right)\tilde{E}_j + \sum_{i=1}^{3}\sum_{j=1}^{3}\left(\sigma\mu\, j\omega\int_A^{(e)}\left(\vec{N}_i\cdot\vec{N}_j\right) dA\right)\tilde{E}_j = -\sum_{i=1}^{3}\left(\sigma\mu\, j\omega\int_A^{(e)}\left(\vec{N}_i\cdot\tilde{E_s}\right) dA\right) \quad (6.11)$$

[1] This boundary integral term is written as: $\oint_s^{(e)} \vec{w}\times\left(\vec{\nabla}\times\tilde{E}\right)\cdot\vec{n}dS = 0$ where $\vec{n}$ is the normal vector to the boundary of the domain. The terms inside the integral can be reworked using to give the following [16]: $\tilde{E}$ is homogeneous Dirichlet on electric walls $\vec{n}\times\tilde{E} = 0$, non-homogeneous Dirichlet $\vec{n}\times\tilde{E} = \tilde{E}_{in}$ on boundaries where the input field is prescribed and homogeneous Neumann $\vec{n}\times\vec{\nabla}\times\tilde{E} = 0$ on magnetic walls. *Electric walls* refers to boundaries of the domain through which no magnetic flux can penetrate and *Magnetic walls* refers to boundaries of the domain through which no electric flux can penetrate [16].

where it is defined that:

$$M_{ij}^{(e)} = \int_A^{(e)} \left[\left(\vec{\nabla} \times \vec{N}_i \right) \cdot \left(\vec{\nabla} \times \vec{N}_j \right) \right] dA \tag{6.12}$$

and

$$T_{ij}^{(e)} = \int_A^{(e)} \left(\vec{N}_i \cdot \vec{N}_j \right) dA \tag{6.13}$$

and

$$R_i^{(e)} = \int_A^{(e)} \left(\vec{N}_i \cdot \tilde{E}_s \right) dA \tag{6.14}$$

in Equation (6.11). Adding Equation (6.12) and Equation (6.13) together as shown in Equation (6.11) gives [16, 17, 1]:

$$K_{ij}^{(e)} = M_{ij}^{(e)} + \sigma \mu j \omega T_{ij}^{(e)} \tag{6.15}$$

where $K_{ij}^{(e)}$ is referred to as the coefficient matrix [1] and according to Equation (6.11):

$$\begin{aligned} F_i^{(e)} &= \sigma \mu j \omega \left(R_i^{(e)} \right) \\ &= \sigma \mu j \omega \int_A^{(e)} \left(\vec{N}_i \cdot \tilde{E}_s \right) dA \end{aligned} \tag{6.16}$$

where $F_i^{(e)}$ is referred to as the right-hand-side vector. Equations (6.15) and (6.16) are finite element matrices [1, 2, 3]. Equation (2.39) has been discretized, via the Galerkin method, into a system of linear equations [16, 17]:

$$K_{ij}^{(e)} \tilde{E}_i{}^{(e)} = F_i^{(e)} \tag{6.17}$$

where the LHS of Equation (2.39) is represented by the coefficient matrix, $K_{ij}^{(e)}$ for each element in the domain [1]. The RHS of Equation (2.39) is represented by the right-hand-side vector, $F_i^{(e)}$ for certain elements within the domain [1] and $\tilde{E}_i{}^{(e)}$ represents the unknown edge values per element within the FE mesh [2, 12].

6.3.3 Discretization of FE Matrices

Equations (6.12), (6.13) and (6.14) represents the FE matrices that has to be discretized for the implementation process of a FE algorithm. The element coefficient matrix $K_{ij}^{(e)}$ and the element right-hand-side vector $F_i^{(e)}$ were directly derived from the PDE given by Equation (2.38) as shown in Section 6.3 and therefore these matrices contain all the information of the behaviour of the physical system that describes eddy current phenomena [10, 15].

To ensure that the FE matrices are computed as accurately as possible, Equations (6.12), (6.13) and (6.14) were solved analytically as well using MATLAB Symbolic. The discretized matrix equations and the analytical matrix equations were applied to various arbitrary triangular elements, and the solutions obtained from both sources were compared in order to check that the FE matrices were discretized correctly.

6.3.3.1 Local Node and Edge Numbering System of a Vector FE

Section 5.3 introduced the local node and local edge connectivity information of an individual vector finite element which relates how the edges and nodes within the element are connected to each other [2, 12, 1]. *The indexing of the edges E_{ij} shown in sub-section 5.3.1 actually follows a specific local node numbering system applied to each local edge of a triangular finite element [2] and this local node numbering system is based upon a numbering combination sequence found in column B of Table 6.2 [2].*

Order and Repetition	No Order and No Repetition	No Order and Repetition	Order and No Repetition
$(1,1)$	-	$(1,1)$	-
$(2,1)$	-	-	$(2,1)$
$(3,1)$	-	-	$(3,1)$
$(1,2)$	$(1,2)$	$(1,2)$	$(1,2)$
$(2,2)$	-	$(2,2)$	-
$(3,2)$	-	-	$(3,2)$
$(1,3)$	$(1,3)$	$(1,3)$	$(1,3)$
$(2,3)$	$(2,3)$	$(2,3)$	$(2,3)$
$(3,3)$	-	$(3,3)$	-
A	B	C	D

Table 6.2: Table of Numbering Combination Sequences [22]

Using the information of column B, the data-structure containing the information on how the local node numbering system is related to the indexing of each local edge of a finite element is created and shown in Table 6.3 [2].

Local Edge Numbering System	Edge Indexing According to Local Node Numbering System	Local Node No.1 of an Edge	Local Node No.2 of an Edge
E_1	E_{12}	n_1	n_2
E_2	E_{13}	n_1	n_3
E_3	E_{23}	n_2	n_3

Table 6.3: Local Edge and Node Numbering System of a Vector Element

Illustration of the local node numbering system located on each local edge on a triangular vector finite element. The node numbering system of the edges of a single triangular element are as follows: Edge $E_{12} = E_1$, is connected through node n_1 and node n_2. Edge $E_{13} = E_2$, is connected through node n_1 and node n_3. Edge $E_{23} = E_3$, is connected through node n_2 and node n_3. Refer to Figure 5.6 for an illustration of the above [2].

6.3.3.2 Derivation of the Discretized Expression for the FE Matrix Given by Equation (6.12)

To discretize Equation (6.12), the notation of the vector shape functions $\vec{N}_i$ for $i = 1:3$ and $\vec{N}_j$ for $j = 1:3$ is altered slightly as follows:

$$M_{ij}^{(e)} = \int_A^{(e)} \left[\left(\vec{\nabla} \times \vec{w}_{mn} \right) \cdot \left(\vec{\nabla} \times \vec{w}_{kl} \right) \right] dA \tag{6.18}$$

by making use of Equation (5.29), where:

$$\vec{w}_{mn} = \lambda_m \vec{\nabla} \lambda_n - \lambda_n \vec{\nabla} \lambda_m \tag{6.19}$$

and

$$\vec{w}_{kl} = \lambda_k \vec{\nabla} \lambda_l - \lambda_l \vec{\nabla} \lambda_k \tag{6.20}$$

where the subscripts (m,n) in Equation (6.19) and (k,l) in Equation (6.20) follow the same number combination sequence as column B of Table 6.2, thus producing the three vector shape functions $\vec{w}_{12}$, $\vec{w}_{13}$ and $\vec{w}_{23}$ per element [2, 3, 12], as discussed in Section 5.3.1. The notation of the three scalar shape functions is expressed as follows according to Equations (4.24), (4.25) and (4.26) in sub-section 4.3.2:

$$\lambda_m = m_0 + m_1 x + m_2 y \tag{6.21}$$

and

$$\lambda_n = n_0 + n_1 x + n_2 y \tag{6.22}$$

The gradients of Equations (6.21), (6.22) are then:

$$\vec{\nabla} \lambda_m = m_1 \hat{i} + m_2 \hat{j} \tag{6.23}$$

and

$$\vec{\nabla} \lambda_n = n_1 \hat{i} + n_2 \hat{j} \tag{6.24}$$

Substituting Equations (6.21), (6.22), (6.23) and (6.24) into Equation (6.18) gives:

$$\begin{aligned} \vec{w}_{mn} &= m_0 + m_1 x + m_2 y \left(n_1 \hat{i} + n_2 \hat{j} \right) - n_0 + n_1 x + n_2 y \left(m_1 \hat{i} + m_2 \hat{j} \right) \\ &= \left[\left(m_0 + m_1 x + m_2 y \right) n_1 - \left(n_0 + n_1 x + n_2 y \right) m_1 \right] \hat{i} + ... \\ &\quad \left[\left(m_0 + m_1 x + m_2 y \right) n_2 - \left(n_0 + n_1 x + n_2 y \right) m_2 \right] \hat{j} \end{aligned} \tag{6.25}$$

After some algebra manipulation Equation (6.25) becomes:

$$\vec{w}_{mn} = \left[\left(m_0 n_1 - n_0 m_1 \right) + \left(m_2 n_1 - n_2 m_1 \right) y \right] \hat{i} + \left[\left(m_0 n_2 - n_0 m_2 \right) + \left(m_1 n_2 - n_1 m_2 \right) x \right] \hat{j} \tag{6.26}$$

where we let:

$$N_x = \left[\left(m_0 n_1 - n_0 m_1 \right) + \left(m_2 n_1 - n_2 m_1 \right) y \right] \hat{i} \tag{6.27}$$

and

$$N_y = \left[\left(m_0 n_2 - n_0 m_2 \right) + \left(m_1 n_2 - n_1 m_2 \right) x \right] \hat{j} \tag{6.28}$$

Now, to derive the curl of Equation (6.19):

$$\begin{aligned} \vec{\nabla} \times \vec{w}_{mn} &= \left(\frac{\partial N_y}{\partial x} - \frac{\partial N_x}{\partial y} \right) \hat{k} \\ &= \left(\left(m_1 n_2 - n_1 m_2 \right) - \left(m_2 n_1 - n_2 m_1 \right) \right) \hat{k} \\ &= 2 \left(m_1 n_2 - m_2 n_1 \right) \hat{k} \end{aligned} \tag{6.29}$$

Similarly, all the above algebraic processes are applied to Equation (6.20) thus producing:

$$\vec{\nabla} \times \vec{w}_{kl} = 2 \left(k_1 l_2 - k_2 l_1 \right) \hat{k} \tag{6.30}$$

Substituting Equations (6.29) and (6.30) into Equation (6.18) produces:

$$\begin{aligned} M_{ij}^{(e)} &= \int_A^{(e)} \left[\left(2\left(m_1 n_2 - m_2 n_1\right)\hat{k}\right) \cdot \left(2\left(k_1 l_2 - k_2 l_1\right)\hat{k}\right) \right] dA \\ &= 4\left(m_1 n_2 - m_2 n_1\right)\left(k_1 l_2 - k_2 l_1\right)\left(\int_A^{(e)} dA\right) \\ &= 4 \begin{vmatrix} m_1 & m_2 \\ n_1 & n_2 \end{vmatrix} \begin{vmatrix} k_1 & k_2 \\ l_1 & l_2 \end{vmatrix} (A_e) \end{aligned} \tag{6.31}$$

where A_e, is the area of a triangular element given by Equation (4.23). Equation (6.12) has been discretized into its simplest algebraic form.
Equation (6.12) can also be calculated symbolically by the following:

$$\begin{aligned} M_{ij}^{(e)} &= \int_A^{(e)} \left[\left(\vec{\nabla} \times \vec{N}_i\right) \cdot \left(\vec{\nabla} \times \vec{N}_j\right) \right] dA \\ &= \left[\left(\vec{\nabla} \times \vec{N}_i\right) \cdot \left(\vec{\nabla} \times \vec{N}_j\right) \right] \left(\int_A^{(e)} dA\right) \\ &= \left[\left(\vec{\nabla} \times \vec{N}_i\right) \cdot \left(\vec{\nabla} \times \vec{N}_j\right) \right] (A_e) \end{aligned} \tag{6.32}$$

The computational accuracy of Equation (6.31) is verified by symbolically calculating the Equations (5.33), (5.34) and (5.35) directly within Equation (6.32), using MATLAB Symbolic. Both Equations (6.31) and (6.32) produces the same answer to any arbitrary triangular finite element. One such example is illustrated using an element with the following coordinates: $x_1 = -0.5$, $y_1 = 0.5$, $x_2 = 0.5$, $y_2 = 0.5$, $x_3 = -0.5$ and $y_3 = -0.5$. Equation (6.31) produces the result:

$$M_{ij}^{(e)} = \begin{bmatrix} 4 & -4 & 4 \\ -4 & 4 & -4 \\ 4 & -4 & 4 \end{bmatrix} \tag{6.33}$$

and Equation (6.32) produces the result:

$$M_{ij}^{(e)} = \begin{bmatrix} 4 & -4 & 4 \\ -4 & 4 & -4 \\ 4 & -4 & 4 \end{bmatrix} \tag{6.34}$$

where equations (6.33) and (6.34) are identical. The dimension of the FE matrix given by Equation (6.12) is a three-by-three matrix, $M_{ij}^{(e)} = [3 \times 3]$, as shown through Equation (6.34) and Equation (6.33).

6.3.3.3 Derivation of the Discretized Expression for the FEM Matrix Given by Equation (6.13)

To discretize Equation (6.13), the notation of the vector shape functions $\vec{N}_i$ for $i = 1:3$ and $\vec{N}_j$ for $j = 1:3$ is altered slightly as follows:

$$T_{ij}^{(e)} = \int_A^{(e)} \left(\vec{w}_{mn} \cdot \vec{w}_{kl}\right) dA \tag{6.35}$$

Substituting Equations (6.19) and (6.20) into Equation (6.35):

$$\begin{aligned} T_{ij}^{(e)} &= \int_A^{(e)} \left(\vec{w}_{mn} \cdot \vec{w}_{kl}\right) dA \\ &= \int_A^{(e)} \left[\left(\lambda_m \vec{\nabla}\lambda_n - \lambda_n \vec{\nabla}\lambda_m\right) \cdot \left(\lambda_k \vec{\nabla}\lambda_l - \lambda_l \vec{\nabla}\lambda_k\right) \right] dA \end{aligned} \tag{6.36}$$

where the subscripts (m,n) in Equation (6.19) and (k,l) in Equation (6.20) follow the same number combination as column B of Table 6.2, thus producing the three shape functions $\vec{w}_{12}$, $\vec{w}_{13}$ and $\vec{w}_{23}$ per element [2, 3, 12], refer to Section 5.3 where this statement was proved. After some algebra manipulation Equation (6.36) becomes:

$$\begin{aligned} T_{ij}^{(e)} &= \left(\vec{\nabla}\lambda_n \cdot \vec{\nabla}\lambda_l\right) \int_A^{(e)} (\lambda_m \lambda_k)\, dA - \left(\vec{\nabla}\lambda_n \cdot \vec{\nabla}\lambda_k\right) \int_A^{(e)} (\lambda_m \lambda_l)\, dA \ldots \\ &\quad \ldots - \left(\vec{\nabla}\lambda_m \cdot \vec{\nabla}\lambda_l\right) \int_A^{(e)} (\lambda_n \lambda_k)\, dA + \left(\vec{\nabla}\lambda_m \cdot \vec{\nabla}\lambda_k\right) \int_A^{(e)} (\lambda_n \lambda_l)\, dA \end{aligned} \quad (6.37)$$

The integrals in Equation (6.37) can be computed through the generic integration formula for integrals in the simplex coordinate system [2, 1]:

$$\int\int_S \lambda_1^i \lambda_2^j \lambda_3^k dS = \frac{2!i!j!k!}{(2+i+j+k)} A \quad (6.38)$$

Equation (6.13) can also be calculated symbolically by the following:

$$\begin{aligned} T_{ij}^{(e)} &= \int_A^{(e)} \left[\vec{N}_i(x,y) \cdot \vec{N}_j(x,y)\right] dxdy \\ &= \int_0^1 \int_0^{1-u} \left[\left(\vec{N}_i(u,v)\right) \cdot \left(\vec{N}_j(u,v)\right)\right] \left|\frac{\partial x \partial y}{\partial u \partial v}\right| dudv \\ &= \int_0^1 \int_0^{1-u} \left[\left(\vec{N}_i(u,v)\right) \cdot \left(\vec{N}_j(u,v)\right)\right] 2A_e dudv \\ &= 2A_e \int_0^1 \int_0^{1-u} \left[\left(\vec{N}_i(u,v)\right) \cdot \left(\vec{N}_j(u,v)\right)\right] dudv \\ &= 2A_e \int_0^1 \left[\left(\vec{N}_i(u,1-u)\right) \cdot \left(\vec{N}_j(u,1-u)\right)\right] du \end{aligned} \quad (6.39)$$

where $2A_e = \left|\frac{\partial x \partial y}{\partial u \partial v}\right|$ is the Jacobian transformation matrix [1] used when transforming from any arbitrary triangular coordinate system to the unit triangular coordinate system, this concept was discussed in sub-section 4.3.1. The transformation between coordinate systems are done so that Equation (6.13) can be integrated symbolically [1].

The computational accuracy of Equation (6.37) is verified by symbolically calculating the Equation (6.39) directly using MATLAB Symbolic. Both Equations (6.37) and (6.39) produces the same answer to any arbitrary triangular finite element. One such example is illustrated using an element with the following coordinates: $x_1 = -0.5$, $y_1 = 0.5$, $x_2 = 0.5$, $y_2 = 0.5$, $x_3 = -0.5$ and $y_3 = -0.5$. Equation (6.37) produces the result:

$$T_{ij}^{(e)} = \begin{bmatrix} 0.3333 & 0.1667 & 0 \\ 0.1667 & 0.3333 & 0 \\ 0 & 0 & 0.1667 \end{bmatrix} \quad (6.40)$$

and Equation (6.39) produces the result:

$$T_{ij}^{(e)} = \begin{bmatrix} 0.3333 & 0.1667 & 0 \\ 0.1667 & 0.3333 & 0 \\ 0 & 0 & 0.1667 \end{bmatrix} \quad (6.41)$$

Equations (6.40) and (6.41) are identical. The dimension of the FE matrix given by Equation (6.13) is a three-by-three matrix, $T_{ij}^{(e)} = [3 \times 3]$, as shown through Equation (6.41) and Equation (6.40).

6.3.3.4 Derivation of the Discretized Expression for the FEM Matrix Given by Equation (6.16)

To discretize Equation (6.14), the notation of the vector shape functions $\vec{N}_i$ for $i = 1:3$ is altered slightly as follows:

$$R_i^{(e)} = \int_A^{(e)} \left(\vec{w}_{mn} \cdot \tilde{E}_s\right) dA \tag{6.42}$$

The source term $\tilde{E}_s$, has the following general vector algebraic expression, refer to Section 2.5 where the source term $\tilde{E}_s$ in relation to Equation (2.39) was discussed:

$$\tilde{E}_s = F_s(x,y)\hat{i} + G_s(x,y)\hat{j} \tag{6.43}$$

where

$$F_s(x,y) = f_0 + f_1 x + f_2 y \tag{6.44}$$

and

$$G_s(x,y) = g_0 + g_1 x + g_2 y \tag{6.45}$$

Substituting Equations (6.19) and (6.43) into Equation (6.42) produces:

$$R_i^{(e)} = \int_A^{(e)} \left[\left(F_s(x,y)\hat{i} + G_s(x,y)\hat{j}\right) \cdot \left(\lambda_m \vec{\nabla}\lambda_n - \lambda_n \vec{\nabla}\lambda_m\right)\right] dA \tag{6.46}$$

where the subscripts (m,n) in Equation (6.19) follow the same number combination as column B of Table 6.2, thus producing the three shape functions $\vec{w}_{12}$, $\vec{w}_{13}$ and $\vec{w}_{23}$ per element [2, 3, 12], refer to Section 5.3 where this statement was proved.

$$R_i^{(e)} = \int_A^{(e)} \left[\left(F_s\hat{i} + G_s\hat{j}\right) \cdot \left(\lambda_m \left(\vec{\nabla}\lambda_{nx}\hat{i} + \vec{\nabla}\lambda_{ny}\hat{j}\right) - \lambda_n \left(\vec{\nabla}\lambda_{mx}\hat{i} + \vec{\nabla}\lambda_{my}\hat{j}\right)\right)\right] dA \tag{6.47}$$

According to Equations (5.30), (5.31) and (5.32) in sub-section 5.3.1, the notation of the gradients of the scalar shape functions can be expressed as:

$$\vec{\nabla}\lambda_n = \vec{\nabla}\lambda_{nx}\hat{i} + \vec{\nabla}\lambda_{ny}\hat{j} \tag{6.48}$$

and

$$\vec{\nabla}\lambda_m = \vec{\nabla}\lambda_{mx}\hat{i} + \vec{\nabla}\lambda_{my}\hat{j} \tag{6.49}$$

where $\vec{\nabla}\lambda_{nx}$, $\vec{\nabla}\lambda_{ny}$, $\vec{\nabla}\lambda_{mx}$ and $\vec{\nabla}\lambda_{my}$ are constants. Simplifying Equation (6.47) and collecting terms in the $\hat{i} - direction$ and in the $\hat{j} - direction$:

$$\begin{aligned} R_i^{(e)} &= \int_A^{(e)} F_s \left(\lambda_m \vec{\nabla}\lambda_{nx} - \lambda_n \vec{\nabla}\lambda_{mx}\right) dA + \int_A^{(e)} G_s \left(\lambda_m \vec{\nabla}\lambda_{ny} - \lambda_n \vec{\nabla}\lambda_{my}\right) dA \\ &= \vec{\nabla}\lambda_{nx} \int_A^{(e)} (F_s\lambda_m)\, dA - \vec{\nabla}\lambda_{mx} \int_A^{(e)} (F_s\lambda_n)\, dA + \vec{\nabla}\lambda_{ny} \int_A^{(e)} (G_s\lambda_m)\, dA - \vec{\nabla}\lambda_{my} \int_A^{(e)} (G_s\lambda_n)\, dA \end{aligned} \tag{6.50}$$

Substituting Equations (6.48) and (6.49) into Equation (6.50) produces:

$$\begin{aligned} R_i^{(e)} &= \vec{\nabla}\lambda_{nx} \int_A^{(e)} (f_0 + f_1 x + f_2 y)\, \lambda_m dA - \ldots \\ &\quad \vec{\nabla}\lambda_{mx} \int_A^{(e)} (f_0 + f_1 x + f_2 y)\, \lambda_n dA + \ldots \\ &\quad \vec{\nabla}\lambda_{ny} \int_A^{(e)} (g_0 + g_1 x + g_2 y)\, \lambda_m dA - .. \\ &\quad \vec{\nabla}\lambda_{my} \int_A^{(e)} (g_0 + g_1 x + g_2 y)\, \lambda_n dA \end{aligned} \tag{6.51}$$

Simplifying Equation (6.51):

$$\begin{aligned}
R_i^{(e)} &= \vec{\nabla}\lambda_{nx} f_0 \left(\int_A^{(e)} \lambda_m dA \right) + \vec{\nabla}\lambda_{nx} f_1 \left(\int_A^{(e)} x\lambda_m dA \right) + \vec{\nabla}\lambda_{nx} f_2 \left(\int_A^{(e)} y\lambda_m dA \right) - \ldots \\
&= \vec{\nabla}\lambda_{mx} f_0 \left(\int_A^{(e)} \lambda_n dA \right) + \vec{\nabla}\lambda_{mx} f_1 \left(\int_A^{(e)} x\lambda_n dA \right) + \vec{\nabla}\lambda_{mx} f_2 \left(\int_A^{(e)} y\lambda_n dA \right) - \ldots \\
&= \vec{\nabla}\lambda_{ny} g_0 \left(\int_A^{(e)} \lambda_m dA \right) + \vec{\nabla}\lambda_{ny} g_1 \left(\int_A^{(e)} x\lambda_m dA \right) + \vec{\nabla}\lambda_{ny} g_2 \left(\int_A^{(e)} y\lambda_m dA \right) - \ldots \\
&= \vec{\nabla}\lambda_{my} g_0 \left(\int_A^{(e)} \lambda_n dA \right) + \vec{\nabla}\lambda_{my} g_1 \left(\int_A^{(e)} x\lambda_n dA \right) + \vec{\nabla}\lambda_{my} g_2 \left(\int_A^{(e)} y\lambda_n dA \right) \qquad (6.52)
\end{aligned}$$

Equation (6.52) can be expressed in a more convenient way as follows:

$$\begin{aligned}
R_i^{(e)} &= \vec{\nabla}\lambda_{nx} f_0 \left(\int_A^{(e)} \lambda_m dA \right) - \vec{\nabla}\lambda_{mx} f_0 \left(\int_A^{(e)} \lambda_n dA \right) \ldots \\
&\quad \vec{\nabla}\lambda_{nx} f_1 \left(\int_A^{(e)} x\lambda_m dA \right) - \vec{\nabla}\lambda_{mx} f_1 \left(\int_A^{(e)} x\lambda_n dA \right) \ldots \\
&\quad \vec{\nabla}\lambda_{nx} f_2 \left(\int_A^{(e)} y\lambda_m dA \right) - \vec{\nabla}\lambda_{mx} f_2 \left(\int_A^{(e)} y\lambda_n dA \right) \ldots \\
&\quad \vec{\nabla}\lambda_{ny} g_0 \left(\int_A^{(e)} \lambda_m dA \right) - \vec{\nabla}\lambda_{my} g_0 \left(\int_A^{(e)} \lambda_n dA \right) \ldots \\
&\quad \vec{\nabla}\lambda_{ny} g_1 \left(\int_A^{(e)} x\lambda_m dA \right) - \vec{\nabla}\lambda_{my} g_1 \left(\int_A^{(e)} x\lambda_n dA \right) \ldots \\
&\quad \vec{\nabla}\lambda_{ny} g_2 \left(\int_A^{(e)} y\lambda_m dA \right) - \vec{\nabla}\lambda_{my} g_2 \left(\int_A^{(e)} y\lambda_n dA \right) \qquad (6.53)
\end{aligned}$$

Equation (6.53) consists of twelve integrals for each of the three number combinations of subscripts (m,n), thus a total of *thirty-six integrals* has to be computed on each element in the domain that a force-driven excitation is prescribed upon, refer to Sections 2.5, 2.4 and 2.6 where force-driven problems were addressed.

Equation (6.14) can also be calculated symbolically by the following:

$$\begin{aligned}
R_i^{(e)} &= \int_A^{(e)} \tilde{J}_s(x,y)\, \vec{N}_i(x,y)\, dA \\
&= \int_0^1 \int_0^{1-u} \left[\tilde{J}_s(u,v)\, \vec{N}_i(u,v) \right] \left| \frac{\partial x \partial y}{\partial u \partial v} \right| du dv \\
&= \int_0^1 \int_0^{1-u} \left[\tilde{J}_s(u,v)\, \vec{N}_i(u,v) \right] 2A_e du dv \\
&= 2A_e \int_0^1 \int_0^{1-u} \left[\tilde{J}_s(u,v)\, \vec{N}_i(u,v) \right] du dv \\
&= 2A_e \int_0^1 \left[\tilde{J}_s(u,1-u)\, \vec{N}_i(u,1-u) \right] du \qquad (6.54)
\end{aligned}$$

where $2A_e = \left| \frac{\partial x \partial y}{\partial u \partial v} \right|$ is the Jacobian transformation matrix [1] used when transforming from any arbitrary triangular coordinate system to the unit triangular coordinate system. The transformation between coordinate systems are done so that Equation (6.16) can be integrated symbolically [1], refer to sub-section 4.3.1.

The computational accuracy of Equation (6.53) is verified by symbolically calculating the Equation (6.54) directly using MATLAB Symbolic. Both Equations (6.53) and (6.54)

produced the same answer to any arbitrary triangular finite element. One such example is illustrated using an element with the following coordinates: $x_1 = 3, y_1 = 3, x_2 = 1, y_2 = 2$, $x_3 = 5$ and $y_3 = 1$. Equation (6.53) produces the result:

$$R_i^{(e)} = \begin{bmatrix} -2.5927 \\ -14.1217 \\ -5.8411 \end{bmatrix} \tag{6.55}$$

and Equation (6.54) produces the result:

$$R_i^{(e)} = \begin{bmatrix} -2.5927 \\ -14.1217 \\ -5.8411 \end{bmatrix} \tag{6.56}$$

Equations (6.55) and (6.56) are identical. The dimension of the FE matrix given by Equation (6.14) is a three-by-one vector, $R_i^{(e)} = [3 \times 1]$ as shown through Equation (6.56) and Equation (6.55).

6.3.3.5 Finite Element Matrices Dimension

The dimension of Equation (6.12) is a three-by-three matrix, $M_{ij}^{(e)} = [3 \times 3]$ and the dimension of (6.13) is also a three-by-three matrix, $T_{ij}^{(e)} = [3 \times 3]$ as shown in sub-sections 6.3.3.2 and 6.3.3.3 respectively. Equations (6.12) and (6.13) are added together to form Equation (6.15) (refer to Section 6.3) therefore, the coefficient matrix represented by Equation (6.15) will also have a dimension of a three-by-three matrix, $K_{ij}^{(e)} = [3 \times 3]$.

The number of rows and columns of the coefficient matrix, $K_{ij}^{(e)}$ coincides with the number of edges that a triangular vector element possesses (refer to Section (5.3)).

The dimension of Equation (6.14) is a three-by-one vector, $R_i^{(e)} = [3 \times 1]$ (as shown in subsection 6.3.3.4) and according to Equation (6.16) (refer to Section 6.3), the right-hand-side vector represented by Equation (6.16) will also have the dimension of a three-by-one vector, $F_i^{(e)} = [3 \times 1]$.

The number of rows of both the right-hand-side vector $F_i^{(e)}$, coincides with the number of edges that a triangular vector element possesses (refer to Section 5.3).

6.4 Assembly of the Global Matrix System of Equations

Solution of Equation (2.39) (the PDE that governs eddy current behaviour) across a FE mesh, mandates the assembly of all finite elements within the domain based on the element connectivity information [1]. The coefficient matrix $K_{ij}^{(e)}$ and the right-hand-side vector $F_i^{(e)}$ is mapped according to the element connectivity information and added to a global coefficient matrix K_{ij} and a global right-hand-side vector F_i, this forms a global matrix system of equations [1] as follows:

$$K_{ij}\tilde{E}_j = F_i \tag{6.57}$$

where i and j represent the total number of edges within the domain [1]. The process of mapping and adding the entries of each coefficient matrix and right-hand-side vector to the entries of the global coefficient matrix and global right-hand-side vector respectively, is called the *assembly process* [1]. The global matrix system given by Equation (6.57), can be solved to obtain the unknown edge values $\tilde{E}_j$, once the boundary conditions are incorporated into this global system of equations [15, 6].

6.4.1 Implementation of the Assembly Process

An example of the FEM assembly process is shown for a simple three element mesh which is illustrated in Figure 6.3 and in this example, it is assumed that a force-driven function will exist on all the finite elements within this mesh.

The dimension of the element coefficient matrix $K_{ij}^{(e)}$, consists of the number of rows and columns equal to the *number of edges* of a single FE element, as explained in sub-section (6.3.3).5 where $K_{ij}^{(e)} = [3 \times 3]$. The dimension of the global coefficient matrix K_{ij}, consists of the number of rows and columns equal to the *total number of edges* in the finite element domain, denoted as N_{edges}, thus $K_{ij} = \left[N_{edges} \times N_{edges}\right] = [7 \times 7]$ [1, 2, 3].

The dimension of the right-hand-side vector $F_i^{(e)}$, consists of the number of rows equal to the *number of edges* of a single FE element and a single column, as explained in sub-section (6.3.3).5. The dimension of the global right-hand-side vector F_i, consists of the number of rows equal to the *total number of edges* in the finite element domain and a single column, thus $F_i = \left[N_{edges} \times 1\right] = [7 \times 1]$ [1]. The process of assembly begins by looping through all the elements of the domain one-by-one and updating the entries of the global coefficient matrix and the global right-hand-side vector [1] as shown by the pseudo code in Algorithm 6.1.

Algorithm 6.1 Pseudo Code of the Assembly Process of Global Coefficient Matrix and the Global Right-Hand-Side Vector [1]

```
#       initialise the global matrix

K=sparse(Edges,Edges);

F=sparse(Edges,1);

#       loop through the elements

for     e=1:Elements

#       double loop: through the local edges of each element

        for     i=1:3
                for     j=1:3
                        K(E(e,i),E(e,j))=K(E(e,i),E(e,j))+ke(i,j);

                end
                #       logical statement
                if      Element represents a forcing region
                        F(E(e,i))=F(E(e,i))+ fe(i);
                end
        end

end
```

In Algorithm 6.1, *K* denotes the global coefficient matrix, *ke* denotes the element coefficient matrix. The entries of the global coefficient matrix is computed by using the

following equation [1] (which appears in Algorithm 6.1):

$$E(e,i) = E_i \tag{6.58}$$

where e denotes the element number within the mesh, i denotes the local edge number within a finite element and E_i denotes the *global edge number* of the finite element mesh that corresponds to the ith *local edge number* within an element [1]. Equation (6.58) thus *relates the global edge numbering system of the FE mesh to the local edge numbering system of each finite element within the mesh as shown in Section* 6.2, where this information is contained within the data-structure given by Table 6.1. Using Equation (6.58) together with the element connectivity data of Table 6.1 produces the assembly data given by Table 6.4.

Global Element (Face) No.	$E(e,1) = E_i$	$E(e,2) = E_i$	$E(e,3) = E_i$
F_1	$E(1,1) = E_1$	$E(1,2) = E_2$	$E(1,3) = E_3$
F_2	$E(2,1) = E_4$	$E(2,2) = E_5$	$E(2,3) = E_2$
F_3	$E(3,1) = E_6$	$E(3,2) = E_7$	$E(3,3) = E_5$

Table 6.4: Element Connectivity Information used to Construct Global Matrices
Element connectivity information which is used to produce the global matrices through Algorithm 6.1.

The data shown in Table 6.4 is used for the global matrix assembly which is processed through Algorithm 6.1. Algorithm 6.1 produces the following global matrices for the finite element mesh of Figure 6.3:

$$K_{ij} = \begin{bmatrix} K_{11}^{(1)} & K_{12}^{(1)} & K_{13}^{(1)} & 0 & 0 & 0 & 0 \\ K_{21}^{(1)} & \left(K_{22}^{(1)} + K_{33}^{(2)}\right) & K_{23}^{(1)} & K_{31}^{(2)} & K_{32}^{(2)} & 0 & 0 \\ K_{31}^{(1)} & K_{32}^{(1)} & K_{33}^{(1)} & 0 & 0 & 0 & 0 \\ 0 & K_{13}^{(2)} & 0 & K_{14}^{(2)} & K_{12}^{(2)} & 0 & 0 \\ 0 & K_{23}^{(2)} & 0 & K_{21}^{(2)} & \left(K_{22}^{(2)} + K_{33}^{(3)}\right) & K_{31}^{(3)} & K_{32}^{(3)} \\ 0 & 0 & 0 & 0 & K_{13}^{(3)} & K_{11}^{(3)} & K_{12}^{(3)} \\ 0 & 0 & 0 & 0 & K_{23}^{(3)} & K_{21}^{(3)} & K_{22}^{(3)} \end{bmatrix} \tag{6.59}$$

where the global coefficient matrix K_{ij}, contains all the *information of the behaviour of*

the modelled physical system described by the PDE under investigation [6, 15] and

$$F_i = \begin{bmatrix} 0 \\ \left(F_2^{(1)} + F_3^{(2)}\right) \\ 0 \\ F_1^{(2)} \\ \left(F_2^{(2)} + F_3^{(3)}\right) \\ 0 \\ 0 \end{bmatrix} \tag{6.60}$$

where the global right-hand-side vector F_i, contains the *information of an excitation force that the physical system responds towards* [6, 15], also refer to Sections 2.4, 2.5 and 2.6 where the concept of an excitation force of Equation (2.39) was discussed. The superscript present in Equations (6.59) and (6.60) indicates which FE element the element coefficient matrix $K_{ij}^{(e)}$ and the right-hand-side vector $F_i^{(e)}$, belongs to within the FE mesh.
An interesting structural characteristic of the global coefficient matrix given by Equation (6.59) is its sparsity, meaning that the most of its entries are zero [1] and this matrix is square as well [1]. The right-hand-side vector matrix is also sparse as shown by Equation (6.60).

6.5 Solving the Linear System of Equations

The unknown edge values $\tilde{E}_j$, are obtained by solving the global system of linear equations [1], given by Equation (6.57). The term $\tilde{E}_j$, represents the circulations of the electric intensity along the edges of the mesh [16, 17, 1]. There are numerous techniques for solving a linear system of equations such as given by Equation (6.57). In sub-section 7.5.1 a few of these techniques will be briefly addressed.

6.6 Building the Solution Vector Field

Once all the edge values $\tilde{E}_j$, are computed, the electric field intensity $\vec{E_E}^{(e)}$(the superscript (e), indicates a single element), can be calculated across each element in the domain by making use of Equation (6.9) and the element connectivity information [1, 2] (Equation (6.9) is repeated for the readers convenience):

$$\tilde{E_E}^{(e)} = \sum_{i=1}^{3} \tilde{E}_j^{(e)} \vec{N}_j(x,y)$$

The time dependent vector function $\vec{E_E}^{(e)}(x,y,t)$, can be recovered from its phasor representation $\tilde{E_E}^{(e)}$, by multiplying the phasor by $e^{j\omega t}$, and taking the real part of the product (refer to Appendix A) [8, 10, 5]. Thus

$$\vec{E_E}^{(e)}(x,y,t) = \Re\left[\left(\sum_{i=1}^{3} \tilde{E}_i^{(e)} \vec{N}_i(x,y)\right) e^{j\omega t}\right] \tag{6.61}$$

The solution vectors of each element $\vec{E_E}^{(e)}(x,y,t)$, associated with each coordinate point $(x,y)^{(e)}$, within a triangle are computed and collected from all the elements within the

entire domain, thus producing a vector solution $\vec{E_E}(x,y,t)$, across the entire domain along with the associated coordinate points (x,y), on the entire domain. A numerical solution (approximated solution) of Equation (2.38) [1], can then be displayed by plotting the vector information $\vec{E_E}(x,y,t)$, associated with each co-ordinate point (x,y), in the domain. Similarly, to find the solution to the eddy currents $\vec{J_E}$, refer to Section 2.3 for the explanation of the creation of eddy currents within a conductor, Equation (6.61) is multiplied by the conductivity constant σ, giving:

$$\vec{J_E}^{(e)}(x,y,t) = \sigma \vec{E_E}^{(e)}(x,y,t) \tag{6.62}$$

A numerical solution (approximated solution) of eddy currents $\vec{J_E}$ [1], can then be displayed by plotting the vector information $\vec{J_E}(x,y,t)$, associated with each coordinate point (x,y), in the domain.

Chapter 7

Implementation Issues Concerning the FEM

In this chapter, certain issues are addressed concerning the implementation of the FEM.

7.1 Element Connectivity within a FE Mesh

Section 6.1 discussed the division of the domain into triangular finite elements and Section 6.4 presented the assembly process of elements across a mesh. The assembly process requires data information instructing how the elements within the mesh are connected to each other through their edges, nodes and coordinate points [1] and as mentioned in Sections 6.2 and 6.4 this information is referred to as the *element connectivity information* [2, 1]. When coding a FE algorithm, adopting sensible local and global numbering conventions *and then using these numbering conventions* are absolutely essential [2] to maintain the correct element connectivity information. The element connectivity information of the FE mesh is stored in data-structures (as discussed in Section 6.2) and the data-structures contains the *data information relating the global numbering system of the finite elements (also referred to as faces in this dissertation), edges and nodes within the FE mesh to the local numbering system of the edges and nodes of an individual finite element.*

7.1.1 Data Sorting and Handling

The element connectivity information within the FE mesh is sorted and stored into data-structures [1, 2, 23]. These data-structures are accumulated and stored together to create a single "database" referred to in this dissertation as `Triangle Database` as shown in Figure 7.1. Figure 7.2 illustrates a simple two element mesh and the data-structures forming the `Triangle Database` as seen in Figure 7.1 of this mesh are shown below.

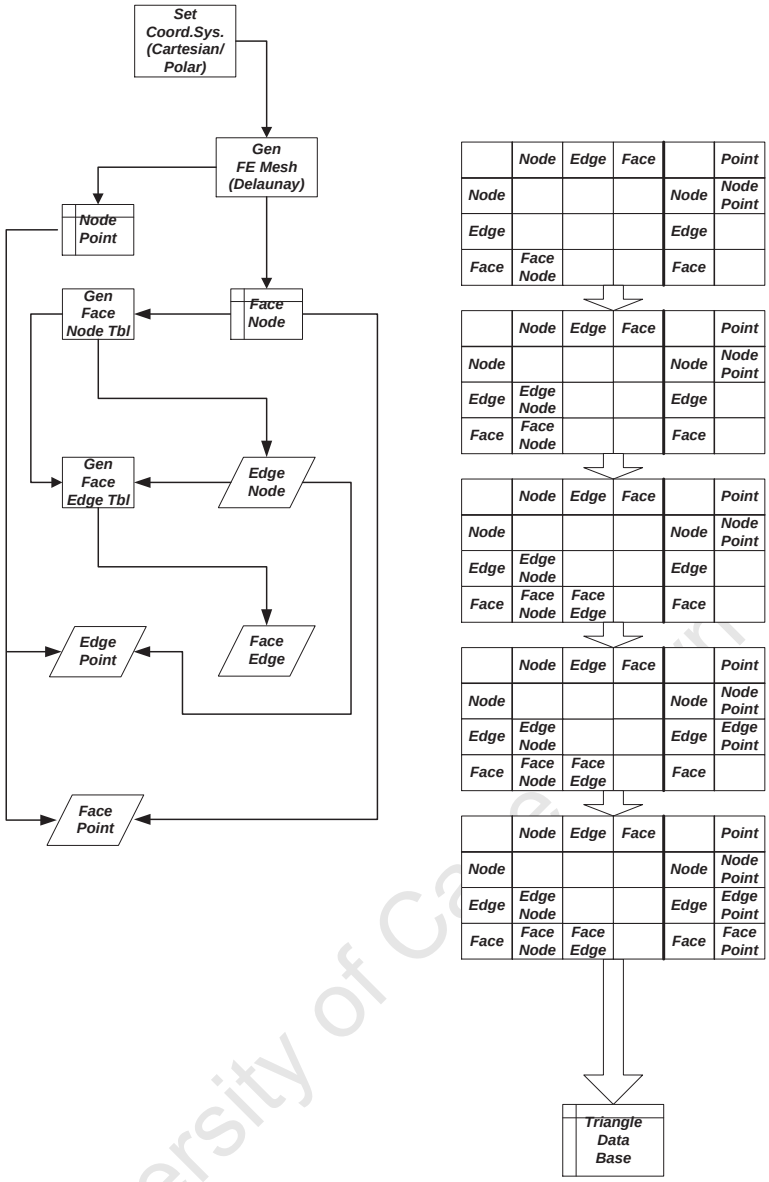

Figure 7.1: Flow Diagram of the Triangle Database Generation

Information flow of how each data-structure is created using data information from the previous set of data-structures.

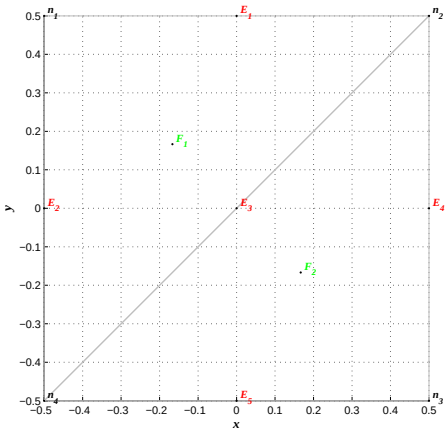

Figure 7.2: Two Element FE Mesh

Summary of Data-Structures that Forms the Database of Connectivity Information of the Finite Element Mesh

Figure 7.1 shows the information flow process of how all data-structures are created from two main sets of data-structures referred to in this dissertation as `NodePointsData` and `FaceNodesData` and for this reason they are also referred to as "parent data-structures". The `NodePointsData` and `FaceNodesData` data-structures for the two element mesh of Figure 7.2 are shown in Tables 7.1 and 7.2 respectively. `FaceNodeData` contains the connectivity information of how each element (F_i for $i = 1:2$) within the mesh is connected to each other through the nodes (n_i for $i = 1:4$) of the elements [1], where a node can be shared by more than one element within a mesh [1]. `NodePointsData` contains the coordinate location information of each node (n_i for $i = 1:4$) within the entire mesh [1].

Global Element (Face) No.	Faces	Local Node No. 1 of a triangular element	Local Node No. 2 of a triangular element	Local Node No. 3 of a triangular element
1	F_1	n_1	n_2	n_4
2	F_2	n_2	n_3	n_4

Table 7.1: Connectivity between Elements and Nodes

Data-structure of connectivity between the elements and nodes of the mesh shown in Figure 7.2. The nodes labelled n_1 , n_2 and n_4 form the vertices of the triangular finite element labelled F_1 and similarly the nodes labelled n_2 , n_3 and n_4 form the vertices of the triangular finite element labelled F_2 [1], refer to Figure 7.2.

Global Node No.	Nodes	Point Coordinate x	Point Coordinate y
1	n_1	-0.5	0.5
2	n_2	0.5	0.5
3	n_3	0.5	-0.5
4	n_4	-0.5	-0.5

Table 7.2: Coordinate Location of the Nodes

Data-structure of the coordinate location of the nodes within the mesh shown in Figure 7.2. Each node is located at a specific coordinate point within the finite element mesh, refer to Figure 7.2.

Data information from `FaceNodeData` in conjunction with data information from Table 6.3 is used to created the data-structure referred to in this dissertation as `EdgeNodesData`. Table 7.3 shows the data-structure `EdgeNodesData` which corresponds to the mesh of Figure7.2. The connectivity information of how each edge (E_i for $i = 1:5$) within the mesh is connected by two nodes (n_i for $i = 1:4$) throughout the mesh is described by `EdgeNodesData` [2, 23].

Global Edge No.	Edges	Local Node1 of an Edge	Local Node2 of an Edge
1	E_1	n_1	n_2
2	E_2	n_1	n_4
3	E_3	n_2	n_4
4	E_4	n_2	n_3
5	E_5	n_3	n_4

Table 7.3: Connectivity between Edges and Nodes

Data-structure of connectivity between edges and nodes of the mesh shown in Figure 7.2. The first column contains the global edge numbering system of the two element mesh shown in Figure 7.2 and the second column labels the edges according to this numbering system . The next two columns labelled as Local Node 1 and Local Node 2 respectively, contain the global node numbering system where each edge is associated with two nodes within the mesh.

Using the node data information which is common to both `EdgeNodesData` and `FaceNodeData`, the data-structure referred to in this dissertation as `FaceEdgesData` is created. This data-structure which is shown by Table 7.4 for the mesh of Figure 7.2 and contains the data information of how each edge is connected to each element (face) within the entire mesh.

Global Element (Face) No.	Faces	Local Edge 1	Local Edge 2	Local Edge 3
1	F_1	E_1	E_2	E_3
2	F_2	E_4	E_3	E_5

Table 7.4: Connectivity between Elements and Edges

Data-structure of connectivity between elements (faces) and edges of the mesh shown in Figure 7.2. The first column contains the global element numbering system of the two element mesh shown in Figure 7.2 and the second column labels the elements according to this numbering system . The next three columns labelled as Local Edge 1, Local Edge 2 and Local Edge 3 contains the global edge numbering system where each element is associated with three edges within the mesh.

The final data-structure as shown in Figure 7.1 referred to in this dissertation as `FacePointsData` is created by using data information from `FaceNodeData` and `NodePointsData`. Here the data information describing how the cartesian points are connected in order to form the elements (faces) of the FE mesh is stored. Table 7.5 illustrates the data-structure `FacePointsData` which corresponds to the mesh of Figure 7.2.

Global Element (Face) No.	Faces	Local Point Coor-dinate x_1	Local Point Coor-dinate y_1	Local Point Coor-dinate x_2	Local Point Coor-dinate y_2	Local Point Coor-dinate x_3	Local Point Coor-dinate y_3
1	F_1	-0.5	0.5	0.5	0.5	-0.5	-0.5
2	F_2	0.5	0.5	0.5	-0.5	-0.5	-0.5

Table 7.5: Connectivity between Elements and Cartesian Points

Data-structure of connectivity between elements (faces) and cartesian points of the mesh shown in Figure 7.2. The first column contains the global element numbering system of the two element mesh shown in Figure 7.2 and the second column labels the elements according to this numbering system . The next six columns contains the coordinate points (x_i, y_i) for $i = 1:3$ associated with each element within the mesh.

7.1.2 Boundary Element Data Information

Once all the data-structures shown in Section 7.1.1 is established, there is now enough information available that can be used to compute the separation of elements located on the boundary of the domain, referred to as *boundary elements*, from the rest of the elements of the domain which are referred to as or *non-boundary elements*. A "database" is then constructed consisting of boundary element and non-boundary element information as shown in Figure 7.3.

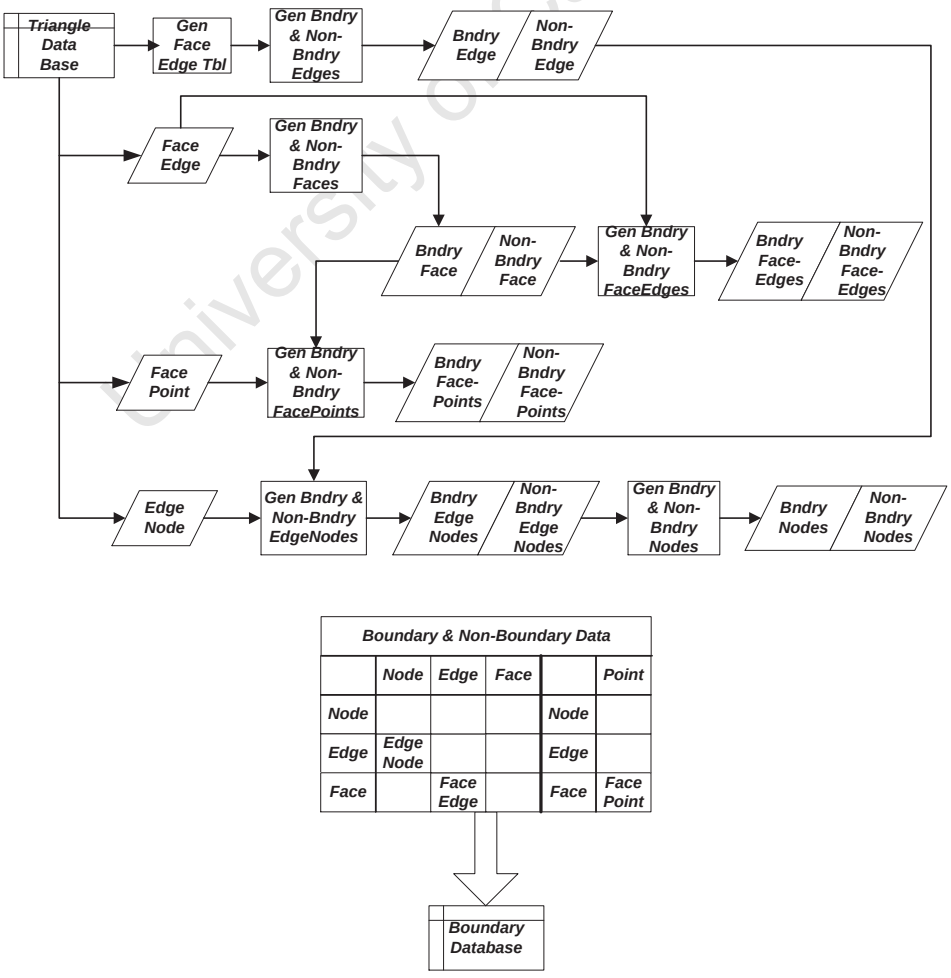

Figure 7.3: Flow Diagram of the Generation of the Boundary Database

Figure 7.2 illustrates a simple two element mesh and the data-structures forming the `Boundary Database` as seen in Figure 7.3 of this mesh are shown below.

Summary of the Data-Structures that Form the Database of Connectivity Information of Elements Located on the Boundary of The Finite Element Mesh

Information from the `Triangle Database` is used to generate the data-structures referred to in this dissertation as `BoundaryEdgesData` and `Non-BoundaryEdgesData` and these data-structures are shown in Table 7.6. The criteria used for separating boundary edges and non-boundary edges is as follows, the edges located in the interior of the domain are *shared by at most two finite elements*, where as edges located on the boundary of the domain *only belong to one finite element* [1].

Global Edge No.	Boundary Edges	Non-Boundary Edges
1	E_1	-
2	E_2	-
3	-	E_3
4	E_4	-
5	E_5	-

Table 7.6: Boundary and Non-boundary Edges

Data-structure of boundary and non-boundary edges of the mesh shown in Figure 7.2. The edge labelled E_3, is shared by both finite element F_1 and F_2 and the other edges, E_1, E_2, E_4 and E_5 are not shared by both finite elements as seen in Figure 7.2.

The data-structure `FaceEdgesData` is used to generate the data-structures referred to in this dissertation as `BoundaryFacesData` and `Non-BoundaryFacesData` and these data-structures are shown in Table 7.7. The criteria used for separating boundary elements and non-boundary element is as follows, when a finite element is located in the interior of the domain, this element will share one of its edges with another finite element whereas, if the element is located on the boundary of the domain, one or two (at most) of its edges will not be shared with another finite element [1].

Global Element (Face) No.	Boundary Faces	Non-Boundary Faces
1	F_1	-
2	F_2	-

Table 7.7: Boundary and Non-boundary Elements

Data-structure of boundary and non-boundary elements (faces) of the mesh shown in Figure 7.2. In Figure 7.2, there are no elements located in the interior of the mesh due to both elements being located on the boundary of the mesh.

The data-structure, `FaceEdgesData` together with the data-structures `BoundaryFacesData` and `Non-BoundaryFacesData` are used to construct the data-structures referred to in this dissertation as `BoundaryFaceEdgesData` and `Non-BoundaryFaceEdgesData`. Refer to Figure 7.3 for an illustration of this process. Table 7.8 contains the information of the edges that

are connected to boundary elements of the mesh and Table 7.9 contains the information of the edges that are connected to non-boundary elements of the mesh.

Boundary Element (Face) No.	Faces	Local Edge 1	Local Edge 2	Local Edge 3
1	F_1	E_1	E_2	E_3
2	F_2	E_4	E_3	E_5

Table 7.8: Connectivity between Boundary Elements and Edges
Data-structure of connectivity between boundary elements (faces) and edges of the mesh shown in Figure 7.2.

Non-Boundary Element (Face) No.	Faces	Local Edge 1	Local Edge 2	Local Edge 3
-	-	-	-	-

Table 7.9: Connectivity between Non-Boundary Elements and Edges
Data-structure of connectivity between non-boundary elements (faces) and edges of the mesh shown in Figure 7.2.

The data-structure, `FacePointsData` together with the data-structures, `BoundaryFacesData` and `Non-BoundaryFacesData` are used to construct the data-structures referred to in this dissertation as `BoundaryFacePointsData` and `Non-BoundaryFacePointsData`. Refer to Figure 7.3 for an illustration of this process. Table 7.10 contains the information of the coordinate points that are connected to boundary elements of the mesh and Table 7.11 contains the information of the coordinate points that are connected to non-boundary elements of the mesh.

Boundary Element (Face) No.	Faces	Local Point Coor-dinate x_1	Local Point Coor-dinate y_1	Local Point Coor-dinate x_2	Local Point Coor-dinate y_2	Local Point Coor-dinate x_3	Local Point Coor-dinate x_3
1	F_1	-0.5	0.5	0.5	0.5	-0.5	-0.5
2	F_2	0.5	0.5	0.5	-0.5	-0.5	-0.5

Table 7.10: Connectivity between Boundary Elements and Cartesian Points
Data-structure of connectivity between boundary elements (faces) and cartesian points of the mesh shown in Figure 7.2.

Non-Boundary Element (Face) No.	Faces	Local Point Coor-dinate x_1	Local Point Coor-dinate y_1	Local Point Coor-dinate x_2	Local Point Coor-dinate y_2	Local Point Coor-dinate x_3	Local Point Coor-dinate x_3
-	-	-	-	-	-	-	-

Table 7.11: Connectivity between Non-Boundary Elements and Cartesian Points
Data-structure of connectivity between non-boundary elements (faces) and cartesian points of the mesh shown in Figure 7.2.

The data-structure, `EdgeNodesData` together with the data-structure, `BoundaryEdgesData` and `Non-BoundaryEdgesData` are used to construct the data-structures referred to in this dissertation as `BoundaryEdgeNodesData` and `Non-BoundaryEdgeNodesData`. Refer to Figure 7.3 for an illustration of this process. Table 7.12 contains the information of the nodes that are connected to edges located on the boundary of the mesh and Table 7.13 contains the information of the nodes that are connected to edges located throughout the interior area of the mesh.

Global Edge No.	Boundary Edges	Local Node1	Local Node2
1	E_1	n_1	n_2
2	E_2	n_1	n_4
4	E_4	n_2	n_3
5	E_5	n_3	n_4

Table 7.12: Connectivity between Boundary Edges and Nodes
Data-structure of connectivity between boundary edges and nodes of the mesh shown in Figure 7.2.

Global Edge No.	Non-Boundary Edges	Local Node1	Local Node2
3	E_3	n_2	n_4

Table 7.13: Connectivity between Non-Boundary Edges and Nodes
Data-structure of connectivity between non-boundary edges and nodes of the mesh shown in Figure 7.2.

The data-structure, `EdgeNodesData` is used to construct the data-structures referred to in this dissertation as `BoundaryNodesData` and `Non-BoundaryNodesData` where this process is shown in Figure 7.3. The Table 7.14 contains the information of the nodes that are located on the boundary of the mesh and of the nodes that are located in the interior area of the mesh.

Global Node No.	Boundary Nodes	Non-Boundary Nodes
1	n_1	-
2	n_2	-
3	n_3	-
4	n_4	-

Table 7.14: Boundary and Non-Boundary Nodes

Data-structure of boundary and non-boundary nodes of the mesh shown in Figure 7.2. All the nodes of the two element mesh shown in Figure 7.2 are located on the boundary and therefore there no nodes located in the interior of the mesh.

7.2 Edge Value Calculation

For boundary-driven problems, there is a known vector field located on the boundaries of the domain of a problem and this known vector field forms the BC of the problem, as discussed in Sections 3.1 and 3.3. *To incorporate the BC into the FEM, the value of the edges (called edge values) located on the boundaries of the domain where the BC is specified, must be computed* [16, 17]. Figure 7.4 illustrates the process of how edge values of the edges *located on the boundaries of the domain* subjected to specific BC's are calculated.

Summary of the Procedure Involved in Edge Value Computation:

1. the process block labelled `LocalTriEdgeVecDataCalc` calculates the vectors of elements according to Equation (5.60) and the computed vector is stored as information signified by the data block `EdgeVector`. In Figure 7.4 the computed vectors are associated with the elements located on the boundary of the domain.

2. the data block containing the constants f_0, g_0, f_1 , f_2, g_1 and g_2 is used to set the constant coefficients of the component functions of a known vector field, refer to Section 5.1.2 . In Figure 7.4, the known vector field corresponds to the vector field located on the boundary of the domain and so forms the BC of the problem.

3. the vectors across a vector element are simulated according to Equation (5.2). The process block labelled `LocalEdgeValueVecFieldCalc`, uses the constants along with the computed vectors (given by the data block `EdgeVector`) to calculated the edge values of an element according to Equation (5.82). In Figure 7.4 the edge values located on the boundary of the domain are computed and therefore is referred to as `BoundaryEdgeValue` data.

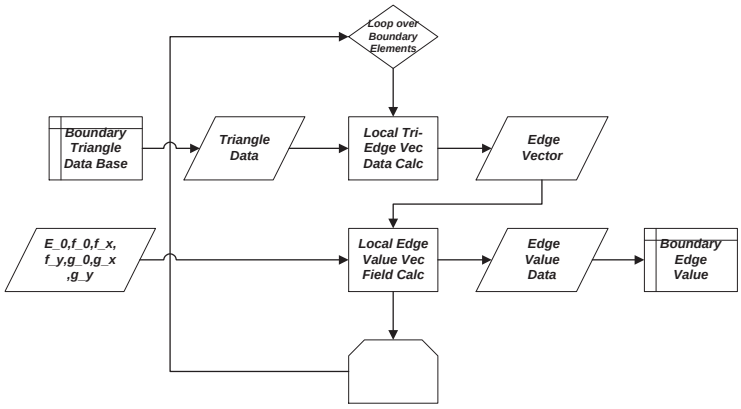

Figure 7.4: Flow Diagram of Boundary Edge Value Computation

7.3 Implementation of the Assembly Process of the Global Matrix System

Equation (2.39) is able to support both boundary-driven and source-driven eddy current problems as previously mentioned in Section 2.6 and the application of either boundary-driven or source-driven problem has a *direct effect on the assembly process of the global matrix system of equations and when applying basic linear algebra to solve this system of equations [1, 15, 6]*.

When considering a force-driven configuration where a *source region exists* within the domain, Equation (6.16) which forms the right-hand-side vector $F_i^{(e)}$, is *only placed on a selected amount of finite elements within the domain that the force function has been prescribed upon [1]*. Suppose that there exists a force-driven function that is imposed only on finite element F_2 of Figure 6.3. The assembly process for a force-driven problem creates the following system of linear equations for the FE mesh shown in Figure 6.3 :

$$\begin{bmatrix} K_{11}^{(1)} & K_{12}^{(1)} & K_{13}^{(1)} & 0 & 0 & 0 & 0 \\ K_{21}^{(1)} & \left(K_{22}^{(1)}+K_{33}^{(2)}\right) & K_{23}^{(1)} & K_{31}^{(2)} & K_{32}^{(2)} & 0 & 0 \\ K_{31}^{(1)} & K_{32}^{(1)} & K_{33}^{(1)} & 0 & 0 & 0 & 0 \\ 0 & K_{13}^{(2)} & 0 & K_{14}^{(2)} & K_{12}^{(2)} & 0 & 0 \\ 0 & K_{23}^{(2)} & 0 & K_{21}^{(2)} & \left(K_{22}^{(2)}+K_{33}^{(3)}\right) & K_{31}^{(3)} & K_{32}^{(3)} \\ 0 & 0 & 0 & 0 & K_{13}^{(3)} & K_{11}^{(3)} & K_{12}^{(3)} \\ 0 & 0 & 0 & 0 & K_{23}^{(3)} & K_{21}^{(3)} & K_{22}^{(3)} \end{bmatrix} \begin{bmatrix} E_1 \\ E_2 \\ E_3 \\ E_4 \\ E_5 \\ E_6 \\ E_7 \end{bmatrix} = \begin{bmatrix} 0 \\ F_3^{(2)} \\ 0 \\ F_1^{(2)} \\ F_2^{(2)} \\ 0 \\ 0 \end{bmatrix} \tag{7.1}$$

Figure 7.5 illustrates the information flow process of the computation of the finite element matrices and of the assembly of the global matrix system for a force-driven problem.

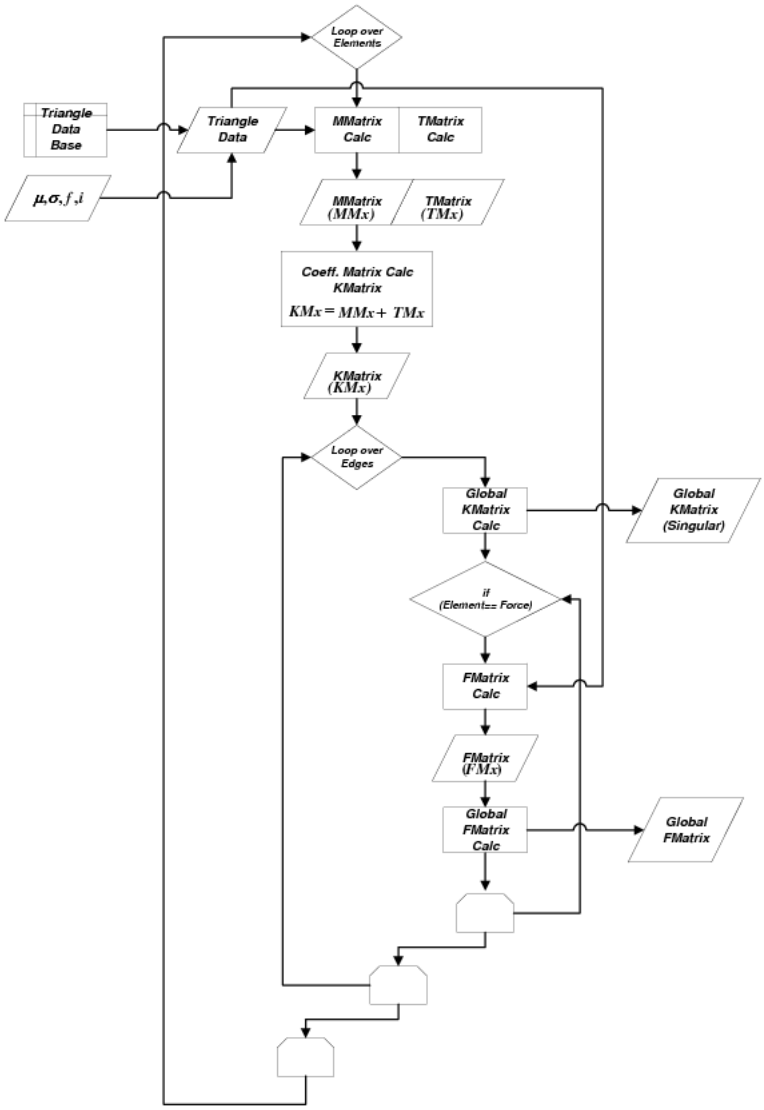

Figure 7.5: Assembly of the Global Matrix System of a Force-driven Configuration
The right-hand-side vector, F_i is computed.

However, when considering a boundary-driven configuration where *no source regions exists* within the entire domain, as stated in Section 2.6, the right-hand-side matrix given by Equation (6.16) then remains zero [15, 6] and there is no computation of the right-hand-side vector $F_i^{(e)}$. The assembly process for a boundary-driven problem creates the following system of linear equations for the FE mesh shown in Figure 6.3:

$$\begin{bmatrix} K_{11}^{(1)} & K_{12}^{(1)} & K_{13}^{(1)} & 0 & 0 & 0 & 0 \\ K_{21}^{(1)} & \left(K_{22}^{(1)}+K_{33}^{(2)}\right) & K_{23}^{(1)} & K_{31}^{(2)} & K_{32}^{(2)} & 0 & 0 \\ K_{31}^{(1)} & K_{32}^{(1)} & K_{33}^{(1)} & 0 & 0 & 0 & 0 \\ 0 & K_{13}^{(2)} & 0 & K_{14}^{(2)} & K_{12}^{(2)} & 0 & 0 \\ 0 & K_{23}^{(2)} & 0 & K_{21}^{(2)} & \left(K_{22}^{(2)}+K_{33}^{(3)}\right) & K_{31}^{(3)} & K_{32}^{(3)} \\ 0 & 0 & 0 & 0 & K_{13}^{(3)} & K_{11}^{(3)} & K_{12}^{(3)} \\ 0 & 0 & 0 & 0 & K_{23}^{(3)} & K_{21}^{(3)} & K_{22}^{(3)} \end{bmatrix} \begin{bmatrix} E_1 \\ E_2 \\ E_3 \\ E_4 \\ E_5 \\ E_6 \\ E_7 \end{bmatrix} = \begin{bmatrix} 0 \\ 0 \\ 0 \\ 0 \\ 0 \\ 0 \\ 0 \end{bmatrix} \tag{7.2}$$

Figure 7.6 illustrates the information flow process of the computation of the finite element matrices and of the assembly of the global matrix system for a boundary-driven problem.

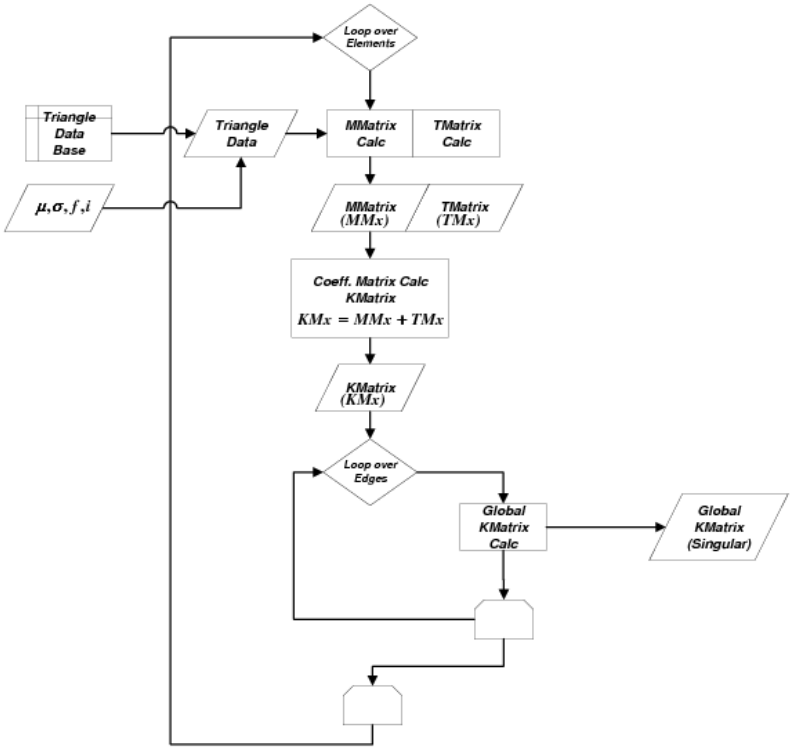

Figure 7.6: Assembly of the Global Matrix System of a Boundary-driven Configuration

There is no computation of the right-hand-side vector $F_i^{(e)}$.

7.4 Applying Linear Algebra to Solve the System of Equations

The application of boundary conditions imposed on both boundary-driven and force-driven problems are considered. The three element mesh of Figure 6.3 is used as an example to demonstrate the resulting system of equations after boundary conditions are imposed on both boundary-driven and force-driven problems.

7.4.1 Application of Boundary Conditions

Prior to imposing BC's, the global matrix system given by Equation (6.57) (which is repeated here again for the readers convenience):

$$K_{ij}\tilde{E}_j = F_i$$

of both boundary-driven and force-driven problems, are *singular* and thus cannot be solved to obtain a unique solution [1, 6, 15]. A *non-singular* matrix system is however obtained after imposing the boundary conditions associated with a given problem [1, 6, 15]. The eddy current configurations that are solved by FEM in this dissertation contain boundary conditions that can be classified as Dirichlet or Essential BC's [16, 17].

The weak formulation of the governing differential equation over the entire finite element domain results in a system of N linear equations with N unknowns [1]. For the FEM using nodal finite elements, the N unknowns correspond to the N nodes of the domain [1] and for the FEM using vector finite elements, the N unknowns corresponds to the N edges of the domain denoted as N_{edges} , as was shown by the example of the FEM assembly process in sub-section 6.4.1.

7.4.1.1 Boundary Driven Configuration

Within a boundary-driven configuration, there exist *no source region* within the domain of the problem [15, 6], as stated in Section 2.6 and sub-section 7.3. Therefore, the entire right-hand-side vector matrix does not exists and thus, the resulting system of linear equations becomes:

$$K_{ij}\tilde{E}_j = 0 \tag{7.3}$$

where

$$F_i = 0 \tag{7.4}$$

The entire global matrix "structure" of the system of linear equations thus looks like Equation (7.2). For a boundary-driven configuration, the edges located on the boundaries of the domain are all known values [16, 17] and the computation of these edge values are subject to the BC's placed on the boundaries of the domain, refer to Section 7.2 where the subject of edge value computation located on the boundary of the domain was discussed.

Suppose that there are boundary conditions imposed on the boundary of the domain of the three element mesh shown in Figure 6.3, which then suggests that the edges values located on the edges, E_1, E_3, E_4, E_6 and E_7 are known (and has been computed as shown in Section 7.2). The values of the interior edges, E_2 and E_5 of the mesh are however unknown and these edge values are solved through the system of linear equations given by Equation (7.2). After imposing the the BC's on Equation (7.2) the resulting system of linear equations is obtained:

$$\begin{bmatrix} \left(K_{22}^{(1)}+K_{33}^{(2)}\right) & K_{23}^{(1)} \\ K_{32}^{(1)} & K_{33}^{(1)} \end{bmatrix} \begin{bmatrix} E_2 \\ E_5 \end{bmatrix} = - \begin{bmatrix} K_{21}^{(1)} & K_{23}^{(1)} & K_{31}^{(2)} & 0 & 0 \\ 0 & 0 & K_{21}^{(2)} & K_{31}^{(3)} & K_{32}^{(3)} \end{bmatrix} \begin{bmatrix} E_1 \\ E_3 \\ E_4 \\ E_6 \\ E_7 \end{bmatrix} \tag{7.5}$$

Equation (7.5) bears the algebraic form of Equation (6.57) and consist of the following matrices:

$$\begin{bmatrix} \left(K_{22}^{(1)}+K_{33}^{(2)}\right) & K_{23}^{(1)} \\ K_{32}^{(1)} & K_{33}^{(1)} \end{bmatrix} \tag{7.6}$$

$$\begin{bmatrix} K_{21}^{(1)} & K_{23}^{(1)} & K_{31}^{(2)} & 0 & 0 \\ 0 & 0 & K_{21}^{(2)} & K_{31}^{(3)} & K_{32}^{(3)} \end{bmatrix} \begin{bmatrix} E_1 \\ E_3 \\ E_4 \\ E_6 \\ E_7 \end{bmatrix} \tag{7.7}$$

$$\begin{bmatrix} E_2 \\ E_5 \end{bmatrix} \tag{7.8}$$

where Equation (7.6) represents the coefficient matrix and the matrix given by Equation (7.7), represents the BC's placed on the system. The book [1] can be referred to for a comprehensive explanation on how Dirichlet boundary conditions are imposed on a system of linear equations. The unknown edge values, E_2 and E_5 can then be computed by solving Equation (7.5) [1, 15, 6].

The BC's as seen in Equation (7.5), actually form the right-hand-side vector of the system of linear equations [15, 6] given by Equation (7.2). The right-hand-side vector is usually associated with a forcing function that causes an excitation force that drives a physical

system which is represented by the coefficient matrix of Equation (7.5), as discussed in sub-section 6.4.1[15, 6].

An analogy can therefore be made when considering the above statement, that is, the imposed BC's has now become the excitation force of a mathematical modelled system and therefore the system can be referred to as *boundary-driven*, refer to Equation (7.5). The computation of the unknown edge values represented by the matrix given by Equation (7.8), represents the response of this physical system towards an external excitation force represented by the right-hand-side matrix of Equation (7.5) [1, 15, 6].

7.4.1.2 Force Driven Configuration

Suppose that there exists a force-driven function that is imposed on finite element F_2 of Figure 6.3 and there are also BC's placed on the edges, E_1, E_3, E_6 and E_7 of Figure 6.3. The resulting system of linear equations are given by Equation (6.57) and the entire global matrix "structure" of the system of linear equations looks like Equation (7.1). After imposing the the BC's on Equation (7.1) the resulting system of linear equations is obtained:

$$\begin{bmatrix} \left(K_{22}^{(1)}+K_{33}^{(2)}\right) & K_{31}^{(2)} & K_{32}^{(2)} \\ K_{13}^{(2)} & K_{14}^{(2)} & K_{12}^{(2)} \\ K_{23}^{(2)} & K_{21}^{(2)} & \left(K_{22}^{(2)}+K_{33}^{(3)}\right) \end{bmatrix} \begin{bmatrix} E_2 \\ E_4 \\ E_5 \end{bmatrix} = \begin{bmatrix} F_3^{(2)} \\ F_1^{(2)} \\ F_2^{(2)} \end{bmatrix} - \begin{bmatrix} K_{21}^{(1)} & K_{23}^{(1)} & 0 & 0 \\ 0 & 0 & K_{31}^{(3)} & K_{32}^{(3)} \end{bmatrix} \begin{bmatrix} E_1 \\ E_3 \\ E_6 \\ E_7 \end{bmatrix} \tag{7.9}$$

Equation (7.9) bears the algebraic form of Equation (6.57) and consist of the following matrices:

$$\begin{bmatrix} \left(K_{22}^{(1)}+K_{33}^{(2)}\right) & K_{31}^{(2)} & K_{32}^{(2)} \\ K_{13}^{(2)} & K_{14}^{(2)} & K_{12}^{(2)} \\ K_{23}^{(2)} & K_{21}^{(2)} & \left(K_{22}^{(2)}+K_{33}^{(3)}\right) \end{bmatrix} \tag{7.10}$$

$$\begin{bmatrix} K_{21}^{(1)} & K_{23}^{(1)} & 0 & 0 \\ 0 & 0 & K_{31}^{(3)} & K_{32}^{(3)} \end{bmatrix} \begin{bmatrix} E_1 \\ E_3 \\ E_6 \\ E_7 \end{bmatrix} \tag{7.11}$$

$$\begin{bmatrix} F_3^{(2)} \\ F_1^{(2)} \\ F_2^{(2)} \end{bmatrix} \tag{7.12}$$

$$\begin{bmatrix} E_2 \\ E_4 \\ E_5 \end{bmatrix} \tag{7.13}$$

where Equation (7.10) represents the coefficient matrix, the matrix given by Equation (7.12) represents the excitation force applied to the system and the matrix given by Equation (7.11) represents the BC's placed on the system. Boundary-driven and force-driven configurations can be classified as deterministic problems as was discussed at the introduction of Chapter 6. The unknown edge values, E_2, E_4 and E_5 given by Equation (7.13) are computed by solving Equation (7.9) [1, 15, 6].

The force-driven function imposed on finite element, F_2, together with the BC's, form the right-hand-side vector of the system of linear equations as clearly seen in Equation (7.9). Equation (7.9) illustrates that the coefficient matrix (which represents or models

the physical system) is *"affected"* by both the force driven function and the BC's, which form the right-hand-side vector of the system of linear equations [15, 6] given by Equation (7.9).

The computation of the unknown edge values represented by the matrix given by Equation (7.13), represents the response of the physical system towards the applied excitation force and the imposed BC's [1, 15, 6].

7.5 Solving the Linear System of Equations

The FEM when applied to boundary-driven problems or force-driven problems results in a set of linear equations that is usually presented in a matrix form [1] as given by Equation (6.57), repeated here again for the readers convenience:

$$K_{ij}\tilde{E}_j = F_i$$

where K_{ij} is the global coefficient matrix [1], $\tilde{E}_j$ is the global vector representing the unknown edge values on the edges of the domain, and F_i is the global right-hand-side vector [1]. The unknown edge values of the edges in the mesh are solved as follows:

$$\tilde{E}_j = K_{ij}/F_i \tag{7.14}$$

where the solution vector $\tilde{E}_j$, is used for the construction of the solution vector field across the domain [1]. In MATLAB the command `sparse` was use to take advantage of the sparsity of the global coefficient matrix, thus preventing unnecessary allocation of computer memory for the zero entries which is a property of the coefficient matrix as shown by Equation (6.59) [1]. The MATLAB command known as matrix-left-division (`mldivide`, "\") was used to solve the the system of linear equations given by Equation (6.57).

Figure 7.7 illustrates the information flow process of the application of BC's placed on the global matrix system and the solution of this system of linear equations for a boundary-driven configuration.

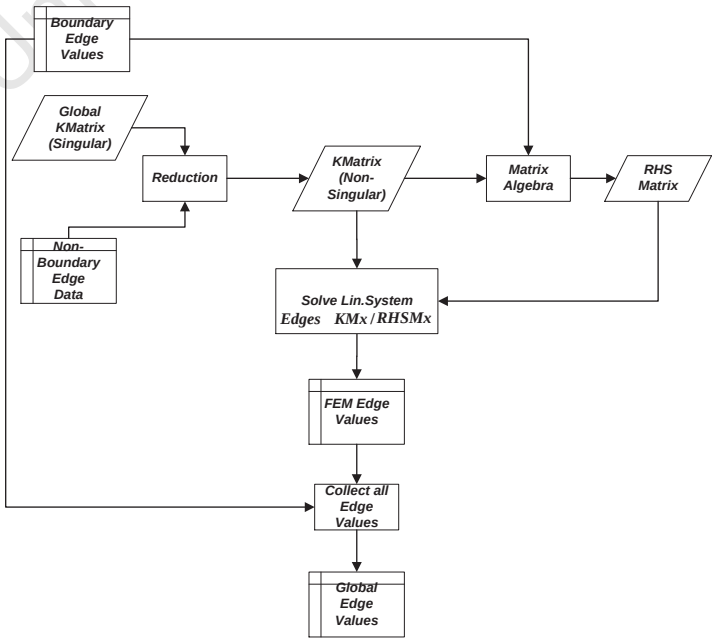

Figure 7.7: Solving the Linear System of Equations for a Boundary-Driven Configuration

Figure 7.8 illustrates the information flow process of the application of an excitation force and BC's placed on the global matrix system and the solution of this system of linear equations for a force-driven configuration.

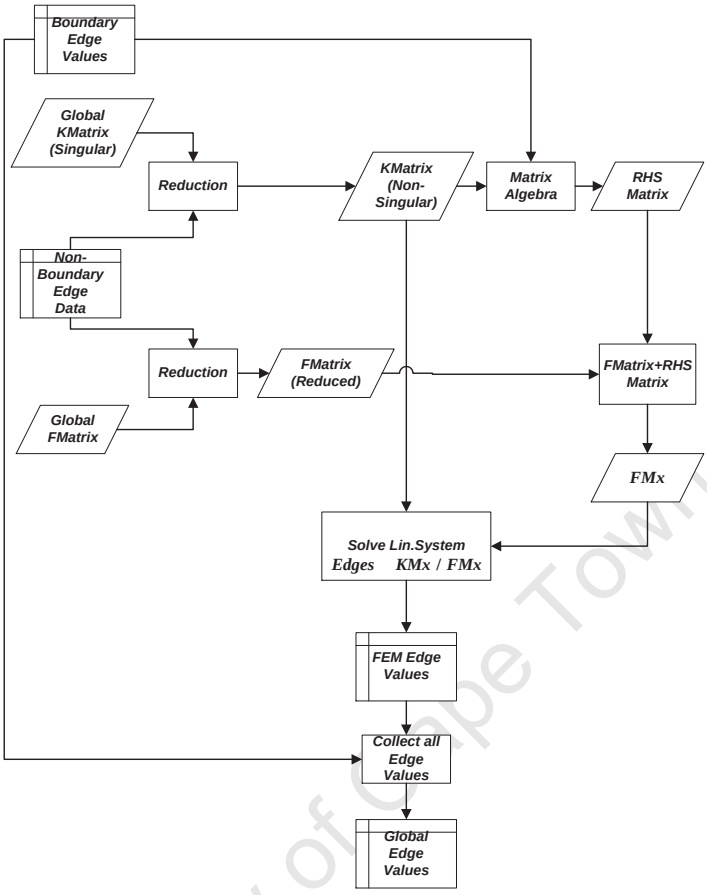

Figure 7.8: Solving the Linear System of Equations for a Force-Driven Configuration

7.5.1 Iterative Techniques for Solving Linear Systems

Iterative techniques for solving linear systems falls outside the scope of this dissertation and therefore only a very brief overview is given. In professional commercial finite element packages, the resulting linear system of equations given by Equation (6.57) is solved using iterative techniques [1]. This type of techniques does not destroy the sparsity of the matrix, and computer memory does not grow out of proportions [1]. Such techniques include conjugate gradient (CG) and bi-conjugate gradient (BiCG) methods combined with a variety of preconditioners and accelerators [1]. Other popular iterative methods that are used in the solution of the global finite element matrix system include the generalised minimal residual (GMRES) method and the quasi-minimal residual (QMR) method [1]. These methods will not be discussed since they can be found in a variety of linear algebra books under the umbrella of *Iterative Methods In Linear Algebra* [1].

7.6 Construction of the Solution Vector Field

Equations (6.9), repeated here again for the readers convenience:

$$\tilde{E}_E^{(e)} = \sum_{j=1}^{3} \tilde{E}_j \vec{N}_j(x,y)$$

states that for each element within the mesh the edges which connects the elements must be known as well as the three shape functions that correspond to each element within the mesh in order to construct the vector field [2, 1]. Figure 7.9 illustrates the information flow process involved in a vector field simulation. The vector components and its associated coordinates are computed as follows:

1. The process block labelled `LocalTriLamdasCalc` calculates scalar shape functions for each element within the mesh according to Equations (4.24), (4.25) and (4.26) associated with each coordinate (x,y) with in the element.

2. The process block labelled `LocalTriShapeFunc` then uses the computed scalar shape functions and associated coordinate information to calculate the vector shape functions of each element according to Equations (5.33), (5.34) and (5.35). Once the vector shape functions has been calculated they are used together with edges information (shown by the data block labelled `GlobalEdgeValues`) according to Equation (6.9) to calculate the components of the solution vector field.

The time dependent vector field $\vec{E_E}^{(e)}(x,y,t)$ across the domain as mentioned in Section 6.6 can be recovered from its phasor representation $\tilde{E_E}^{(e)}$ by using Equation (6.61) and the current density $\vec{J_E}$, which is also referred to as eddy currents [16, 17] within the domain are computed by using Equation (6.62).

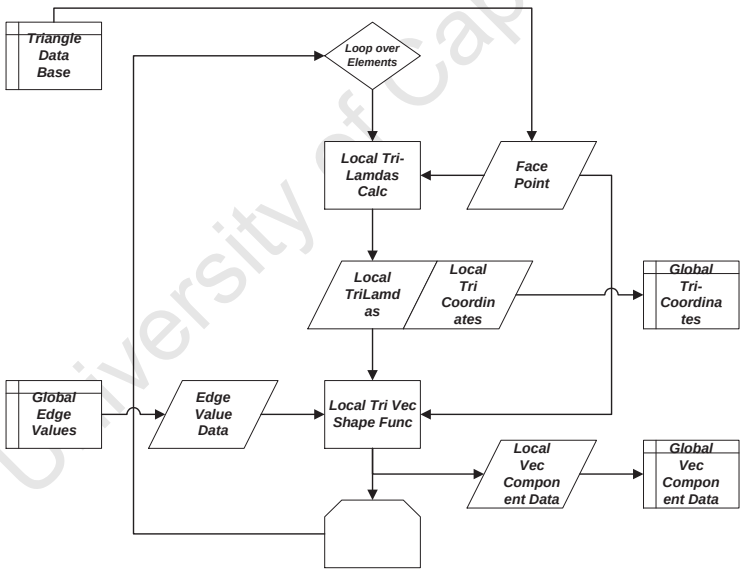

Figure 7.9: Flow Diagram of Global Field Component and Coordinate Data Computation
The global vector component data and together with the associated coordinates data simulates the solution vector field, refer to Section 5.1.2.

7.7 Brief Overview of FE Algorithm

The process of obtaining the finite element solution to Equation (2.39) which governs eddy current behaviour, requires using concepts and information derived from all the previous chapters thus far. There are a number of procedures that are involve in this process and in this section a short explanation of each procedure is given along with an accompanying flow diagram. A brief overview of the process of information flow of the FE algorithm is given below and illustrated graphically in Figure 7.10:

- Step 3:data of the mesh is processed and stored into data-structures containing the element connectivity information.
- Step 4: the collection of these data-structures forms a "database" referred to as `Triangle Database`.
- Step 5: certain data-structures from `Triangle Database` is taken and used to compute the components of the solution vector field.
- Step 6: data from `Triangle Database` is processed and stored into more data-structures that contain element connectivity information concerning the elements located on the boundary of the domain.
  - Step 6.1: the collection of these data-structures forms a database referred to as `Boundary Database`.
  - Step 6.2: data from `Boundary Database` is used to calculate the edge values of the edges located on the boundary of the domain.
  - Step 6.3: f_0, g_0, f_1, f_2, g_1 and g_2 is used to set the constant coefficients of the component functions of the vector field that forms the BC.
  - Step 6.4: the edge values of the edges located on the boundary is collected and stored in a data-structure referred to as `BoundaryEdgeValues`.
  - Step 6.5: the boundary edge values of t `BoundaryEdgeValues` is moved to another data-structure referred to as `GlobalEdgeValues`.
- Step 7: certain data-structures from `Triangle Database` is used in the FEM calculations
  - Step 7.1: the FEM is used to calculate the edge values of edges belonging to elements within the domain according to Equation (2.39). These computed edge values are collected into a data-structure referred to as `FEM EdgeValues`.
  - Step 7.2: the edge values contained in `FEM EdgeValues` is collected along with the edge values contained in `BoundaryEdgeValues` and placed into a data-structure referred to as `GlobalEdgeValues`. `GlobalEdgeValues`, contains all the edge values of the entire mesh.
- Step 8: the edge values contained in `GlobalEdgeValues` is used to compute the vector components of the solution vector field.
- Step 9 and step 10: the vector field components and its associated coordinates for each element within the entire mesh are collected into data-structures referred to as `GlobalTri-Coordinates` and `Global Vec-Component Data` respectively.
- Step 11 and step 12: the vector components are used together with the coordinate information to display the solution vector field.
- Step 13: once the solution vector field has been simulated across the entire domain, all processing stops.

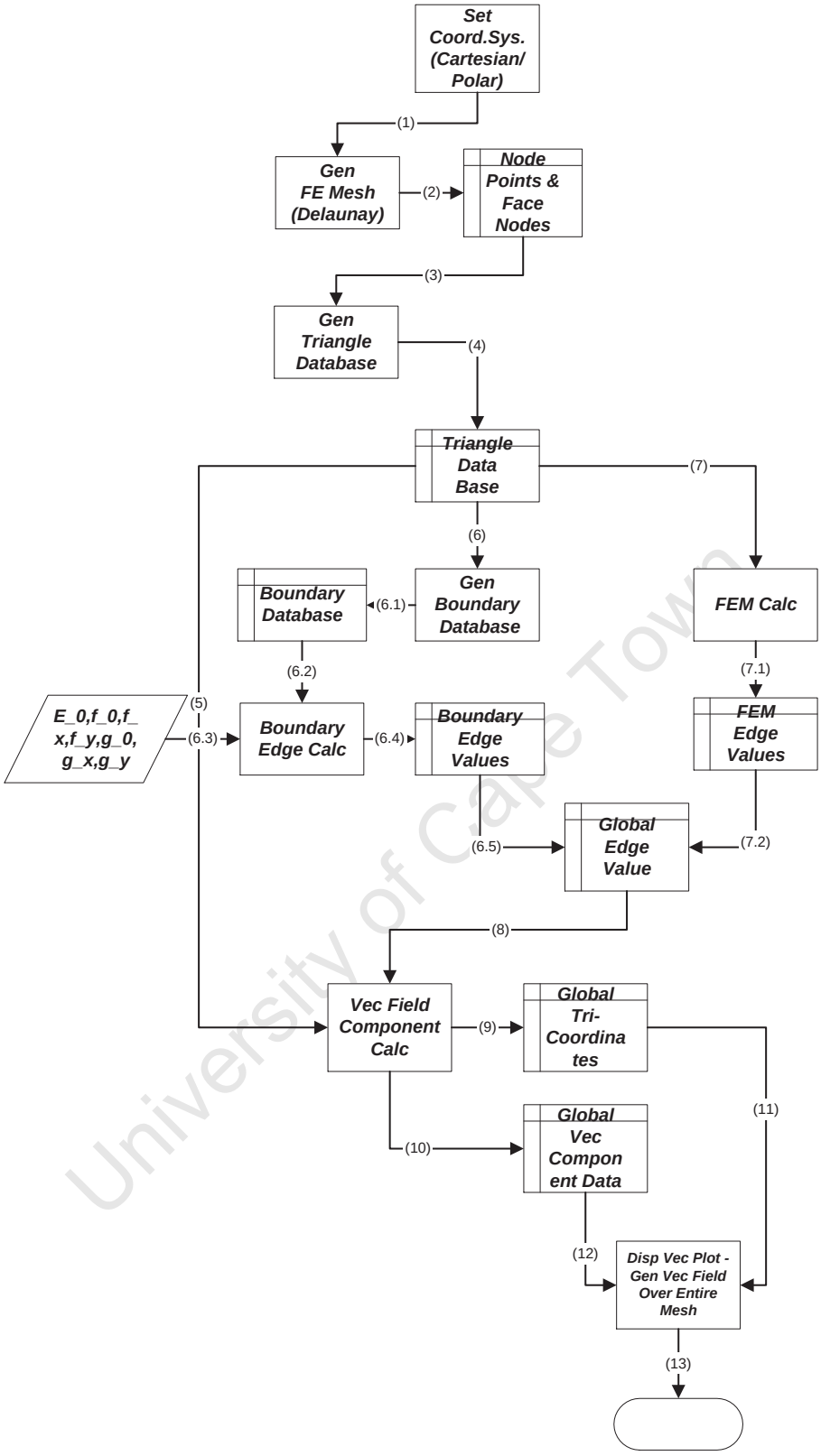

Figure 7.10: General Overview of the Information Flow Process of the FE Algorithm

Chapter 8

FEM Solutions of the PDE that Governs Eddy Current Behaviour

An objective of the dissertation is to develop a FE algorithm that will be able to solve Equation (2.39) which governs eddy current behaviour, for certain fundamental theoretical eddy current configurations (as was stated in Sections 1.1 and 1.2) therefore, *all eddy current configurations under investigation will be of a theoretical nature.* The values of the material constants of conductivity and permittivity used for most of the simulations will be theoretical as well however, there will also be some simulations where realistic values of material constants will be used.

FEM solutions of the eddy current configuration of Section 3.1 were simulated and compared to the analytical solution given by Equation (3.11) (which was derived from the same eddy current configuration of Section 3.1) in order to verify that the FE algorithm was implemented correctly. Once the FE implementation works, it can then be used to generate *visual solutions* to arbitrary eddy current configurations that are either problematic or difficult to solve analytically.

8.1 Finite Element Meshes

Two types of meshes were manually coded for the eddy current configurations investigated in this chapter. The following meshes were created:

- a rectangular mesh in the cartesian coordinate system consisting of (x,y) coordinates.
- a circular mesh in the cartesian coordinate system consisting of (x,y) coordinates.

The procedure for constructing the meshes is given below and illustrated in Figure 7.10:

- Step 1: a coordinate system (cartesian and polar) with coordinate points are created. Coordinates points are manually placed and spaced as equally as possible throughout the domain space, thus ensuring the creation of a finite element mesh that consists of triangular elements that are as equilateral shaped as possible [1]. Equilateral shaped elements are the best suited for the FEM [1].
- Step 2: once the points in the domain are placed, the `Delauney` algorithm of MATLAB is used in order to generate the required mesh.

The finite element meshes generated are shown in Figures 8.1, 8.7, 8.15 and 8.25.

8.2 FEM Solutions of an Analytically Solved Problem

Analytical solutions of sub-section 3.1.2 were compared to the FEM simulated solutions of the same eddy current configuration. This procedure was done as a verification that the FE algorithm is able to compute solutions to Equation (2.39) correctly.

8.2.1 PDE Modelled Without a Source Region Included in the Domain

The problem setup and analytical solution of this particular configuration can be found by referring back to sub-sections 3.1.1 and 3.1.2 respectively. Equation (3.7) which forms the BC of the configuration is set as $E_{S_0} = E_0 = 1\left[\frac{\mathrm{V}}{\mathrm{m}}\right]$ and the dimension of the domain (the conductor) is $0 \leq z \leq 4\mathrm{m}$ on the $z-axis$ and $0 \leq x \leq 0.0175\mathrm{m}$ on the $x-axis$. It is expected that the FE algorithm should be able to model and visually simulate the attenuation behaviour of the propagating wave at different frequencies, since this is a important behaviour effect of an eddy current configuration [19, 16, 17] as shown in sub-sections 3.1.3 and 3.1.4. Figure 8.1 shows the domain of the problem.

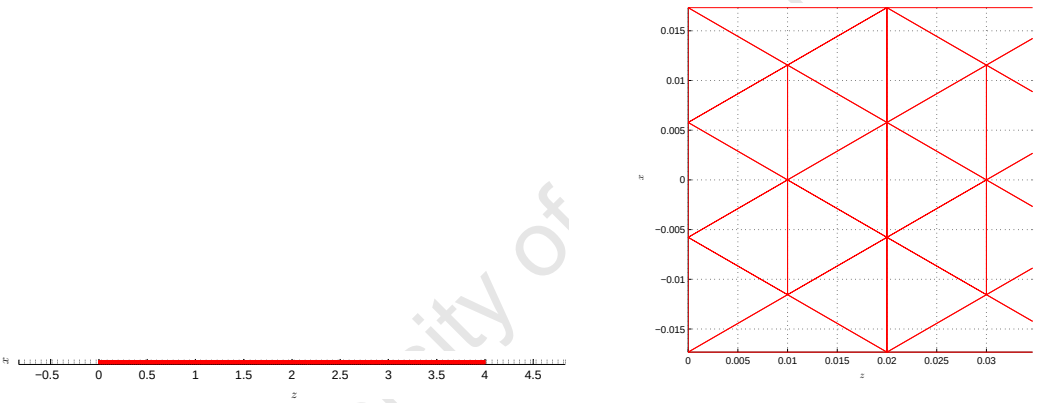

(a) (b)

Figure 8.1: Finite Element Mesh of the Domain

In sub-figure 8.1a, the mesh consists of approximately 2400 triangular elements. The length of the mesh along the $z-axis$ is far greater than the width along the $x-axis$, where the dimension of the domain (the conductor) is $0 \leq z \leq 4\mathrm{m}$ on the $z-axis$ and $0 \leq x \leq 0.0175\mathrm{m}$ on the $x-axis$. In sub-figure 8.1b, a portion of the mesh is enlarged to see the FE grid better.

8.2.2 FEM Simulated Solution

The FE algorithm was used to generate vector field solutions to the problem of Section 3.1. The FE solutions were simulated at a permittivity value of $\mu = 0.25\left[\frac{\mathrm{H}}{\mathrm{m}}\right]$, $t = 0\mathrm{s}$ and a single conductivity value of $\sigma = 4\pi \backsimeq 12.566\ [\frac{S}{m}]$ but at varying frequency values of $f = 1\mathrm{Hz}$, $f = 5\mathrm{Hz}$ and $f = 20\mathrm{Hz}$, in order to illustrate the concept of skin effect behaviour which is an important characteristic found in eddy current configurations [16, 17]. The computational time of the FE algorithm for this problem is 4.699s. FEM simulated solutions of Equation (3.11) at different frequency values are shown in Figures 8.4, 8.3 and 8.2 respectively.

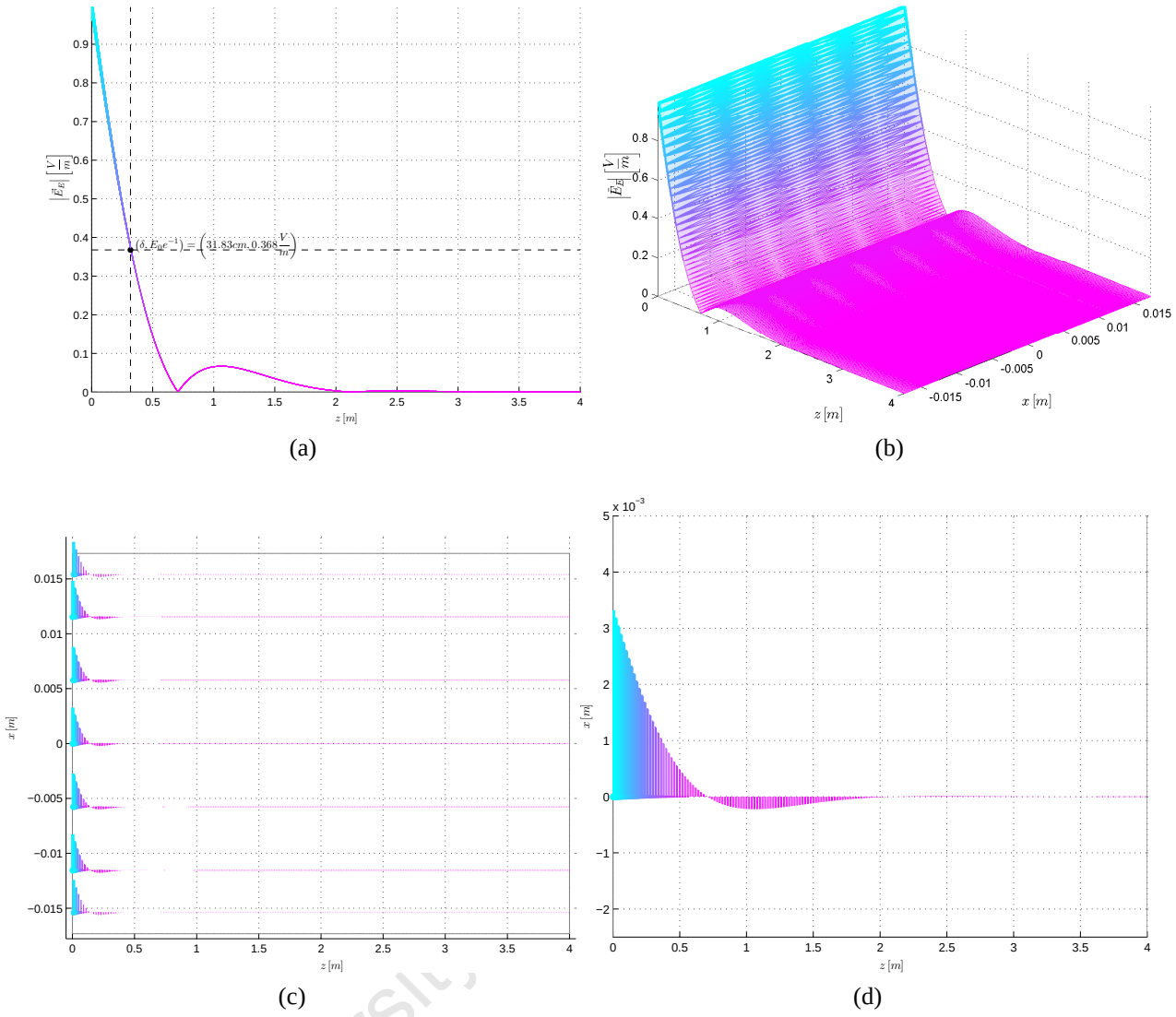

Figure 8.2: Solution Vector Field $\vec{E}_E$ Simulated at a frequency of $f = 1\text{Hz}$

Sub-figure 8.2a, illustrates $\left|\vec{E}_E\right|$, the magnitude of the vector field $\vec{E}_E$, across the axis of wave propagation, the $z-axis$. At a frequency value of $f = 1\text{Hz}$, the vector wave penetrates deeply into the domain in the direction of wave propagation $(z-axis)$. Sub-figure 8.2b, illustrates $\left|\vec{E}_E\right|$, the magnitude of the vector field $\vec{E}_E$, across the entire two-dimensional domain in the form of a meshed graph. Sub-figure 8.2c, illustrates the vector field that would be induced in this domain at a frequency value of $f = 1\text{Hz}$. Sub-figure 8.2d, shows a single vector wave taken from sub-figure 8.2c.

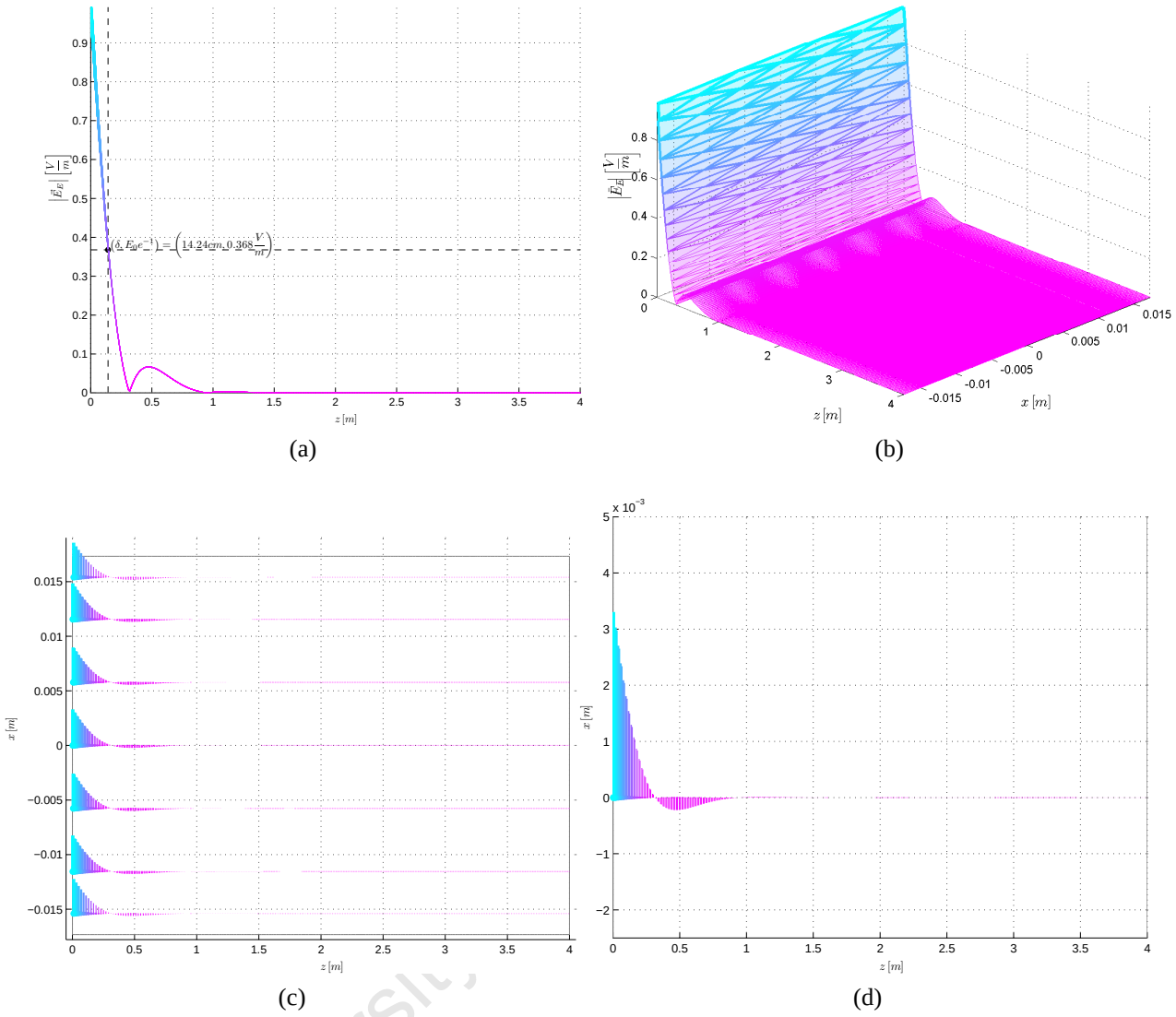

Figure 8.3: Solution Vector Field $\vec{E}_E$ Simulated at a frequency of $f = 5\text{Hz}$

Sub-figure 8.3a, illustrates $\left|\vec{E}_E\right|$, the magnitude of the vector field $\vec{E}_E$, across the axis of wave propagation, the $z-axis$. At a frequency value of $f = 5\text{Hz}$, the attenuation depth of the vector wave is small in the direction of wave propagation $(z-axis)$. Sub-figure 8.3b, illustrates $\left|\vec{E}_E\right|$, the magnitude of the vector field $\vec{E}_E$, across the entire two-dimensional domain in the form of a meshed graph. Sub-figure 8.3c, illustrates the vector field that would be induced in this domain at a frequency value of $f = 5\text{Hz}$. Sub-figure 8.3d, shows a single vector wave taken from sub-figure 8.3c.

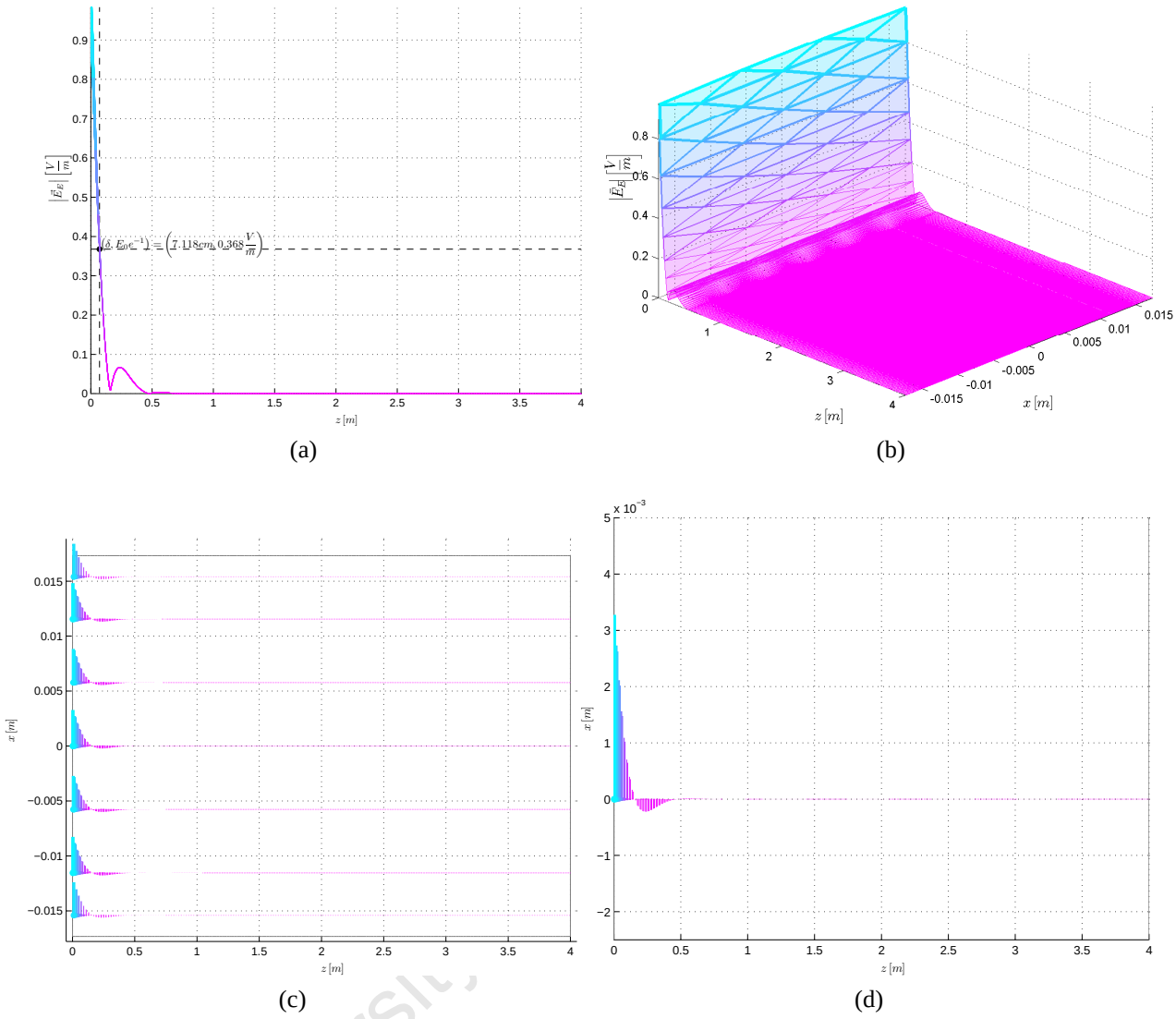

Figure 8.4: Solution Vector Field $\vec{E}_E$ Simulated at a frequency of $f = 20\text{Hz}$

Sub-figure 8.4a, illustrates $\left|\vec{E}_E\right|$, the magnitude of the vector field $\vec{E}_E$, across the axis of wave propagation, the $z-axis$. At a frequency value of $f = 20\text{Hz}$, the skin depth of the vector wave decreases more in the direction of wave propagation ($z-axis$). Sub-figure 8.4b, illustrates $\left|\vec{E}_E\right|$, the magnitude of the vector field $\vec{E}_E$, across the entire two-dimensional domain in the form of a meshed graph. Sub-figure 8.4c, illustrates the vector field that would be induced in this domain at a frequency value of $f = 20\text{Hz}$. Sub-figure 8.4d, shows a single vector wave taken from sub-figure 8.4c.

The following observations were made concerning figures 8.2, 8.3 and 8.4:

- there exists a definite wave propagation along the $z-axis$ of the domain, where the wave originates from the boundary at the position of $z = 0$.
- the vector field $\vec{E}_E$ of the wave is polarised in the $\hat{i}-direction$ which is perpendicular to the direction of wave propagation which is along the $z-axis$, in the $\hat{k}-direction$.
- the vector field $\vec{E}_E$ of the wave also oscillates in the $\hat{i}-direction$ and this is indicated by the changing of direction of the vectors $\vec{E}_E$.
- there is an attenuation of the wave in the direction of wave propagation. The at-

tenuation seems to become stronger as the value of the frequency is set to higher values. Also, the behaviour pattern between the frequency and the attenuation-strength is of an exponential nature.

- in the vector wave solution given by Equation (3.11), it can be observed that the attenuation term $e^{-\beta z}$ dominates the trigonometric term $cos(\omega t - \beta z)$ more and more as the frequency value f, is increased.

- the skin depth (depth of penetration) of the vector field $\vec{E}_E$, decreases as the frequency value f is increased.

8.2.3 Analysis of FEM Generated Solutions

The following analysis of the FEM simulations has been made:

- The FE simulated solutions obeys the mathematical behaviour of the analytical solution given by Equation (3.11) of the eddy current configuration as seen in Figures 8.2, 8.3 and 8.4 respectively. The wave originates from the boundary at the position of $z = 0$, where the BC had been imposed on. This BC is the excitation force which drives the system and thus the problem is classified as boundary-driven, as discussed in Section 2.6 and sub-sections 3.1.2, 3.1.4. The vector field represented by Equation (3.11) consists of three functions:

  - a constant vector field E_{S_0}, polarised in the positive $\hat{i} - direction$.
  - an exponential decaying function, $e^{-\beta z}$ where $\beta = \sqrt{\pi f \mu \sigma}$ which is the cause of the attenuation behaviour present in the vector wave. This function is controlled by the frequency value, f.
  - a trigonometric function $cos(\omega t - \beta z)$, that controls the behaviour of the propagating wave. The term $\beta = \sqrt{\pi f \mu \sigma}$ is the phase constant of the wave.

  The physical behaviour of the vector wave across the domain can be described as non-linear, due to the exponential term $e^{-\beta z}$, and harmonic due to the trigonometric term $cos(\omega t - \beta z)$ present within the analytical solution.

- The solution vector wave can be classified as a transverse wave, because the vector field $\vec{E}_E$ of the wave is polarised in the $\hat{i} - direction$ which is perpendicular to the propagation of the wave which is along the $z - axis$ ($\hat{k} - direction$) of the domain [10, 9].

- Figures 8.2, 8.3 and 8.4 illustrates that as the frequency value f is increased, the attenuation of the solution vector wave increases in strength exponentially along the $z - axis$ (axis of wave propagation) [15, 19] due to the attenuation term $e^{-\beta z}$. The increase in strength of the attenuation term $e^{-\beta z}$ thus causes the decrease in the *skin depth* of the penetrating electric field into the domain, refer to sub-sections 3.1.4 and 3.1.3. This clearly demonstrates the *skin effect* behaviour that is present in conducting bodies [16, 17, 19]. The *relationship present between frequency f and the attenuation strength* can be described as exponential/non-linear:

$$f \sim e^{-\beta z} \tag{8.1}$$

- Besides the analytical solution (in Section 3.1), the author also wished to test the FE solution independently through comparing the calculation of the skin depth value δ, (in Equation (3.12)), with the skin depth δ, found on the $z-axis$ of sub-figures 8.2a, 8.3a and 8.4a. Recall from sub-section 3.1.3, that the skin depth δ, is the distance after which the initial value of $\left|\vec{E}_E\right|$ has decreased by approximately to $e^{-1} = 36.8\%$ when penetrating into the domain, which is the conducting body as shown on the graphs of sub-figures 8.2a, 8.3a and 8.4a. The skin depth value δ, can also be calculated through Equation (3.12) [5, 21], which is repeated here again for the readers convenience:

$$\delta = \frac{1}{\sqrt{\pi f \mu \sigma}}$$

Using Equation (3.12), the following skin depth values has been calculated for this problem with $\mu = 0.25\left[\frac{\mathrm{H}}{\mathrm{m}}\right]$ and $\sigma = 4\pi \backsimeq 12.566\,[\frac{S}{m}]$:

  - at a frequency value of $f = 1\mathrm{Hz}$, $\delta = 31.83\mathrm{cm}$
  - at a frequency value of $f = 5\mathrm{Hz}$, $\delta = 14.24\mathrm{cm}$
  - at a frequency value of $f = 20\mathrm{Hz}$, $\delta = 7.118\mathrm{cm}$

  The skin depth δ, on the graphs of sub-figures 8.2a, 8.3a and 8.4a corresponds to the calculated skin depth values above.

- The vector $\vec{E}_E$, causes eddy currents to form within the domain at the position where the vector wave is present [9, 10, 5, 19], refer to sub-section 3.1.4 and Section 2.3 where an explanation is given concerning how eddy currents are formed within a conducting body.

- To achieve a more accurate approximation of the solution vector field $\vec{E}_E$, given by Equation (3.11), the following factors can be addressed:

  FE Grid Generation

  Grid generation plays an important role as to how good the computation and visualisation of the solution that a FE algorithm will produce [3, 1]. Therefore, the quality of the visual simulated solution depends greatly on the grid generation [3, 1] as follows:

  - the visual solution can be displayed better by adding more triangular elements to the meshed grid, this will allow the FE algorithm to approximate the attenuation of the solution more accurately and a better simulation will be generated [3, 1]. However, such a procedure would increase the computational time of the algorithm extensively [3, 1].
  - to approximate the skin effect more accurately, a possible solution would be to make use of a self-adaptive mesh refinement technique [17]. The application of mesh refinement technique has the result of increasing the density of the elements in the FE mesh of the conducting body, especially near the outer boundary of the domain, where the eddy currents are mainly present due to the skin effect [17]. In this way a eddy current distribution with increased accuracy can be obtained [17]. More grid information (domain coordinates) are needed towards the boundary of the domain (where BC has been imposed), than over the other domain regions in order to be able to accommodate the attenuation (decaying exponential) behaviour of this eddy current problem

with greater accuracy [17]. By placing more coordinates at the regions of the domain where the skin effect is present the generated meshed grid would then posses more triangular elements towards the outer boundary of the domain where BC has been imposed and much less elements towards the other regions of the domain [17]. In this way the number of triangular elements can be kept to a minimum, but a good simulation can still be generated while lowering the computational time of the FE algorithm [17].

Shape Function Limitations

The CT/LN vector element (discussed in sub-section 5.3.1) is used to approximate the solution of Equation (2.39) for the eddy current configuration given in sub-section 3.1.1. The approximated FE solution as shown in sub-section 8.2.2 was verified to obey the mathematical behaviour of the analytical solution of Equation (3.11), as proved in sub-section 8.2.3. Equation (3.11), is repeated here again for the readers convenience:

$$\vec{E}_x(z,t) = E_{s0}e^{-\beta z}cos(\omega t - \beta z)\,\hat{i}$$

The vector shape functions of the CT/LN vector element are constructed from linear polynomials as discussed in Section 5.3. This vector element is able to approximate vector fields of the general algebraic form given in Equation (5.53) repeated here again for the readers convenience:

$$\vec{E}_V(x,y) = (f_0 + f_2 y)\,\hat{i} + (g_0 + g_1 x)\,\hat{j}$$

where the component functions of the vector field $\vec{E}_V(x,y)$, consists of linear polynomials as shown in sub-section 5.1.2 and Section 5.3.

To obtain a more accurate approximation and a better visual simulation, a possible solution would be to use higher-order vector elements [1, 2, 12]. Higher-order vector elements consisting of shape functions constructed from quadratic or higher-order polynomials, as explained in sub-section 5.7.1, which may be better suited to approximating a vector field as given by Equation (3.11). These shape functions of the higher-order vector elements could be more capable of approximating the attenuation term $e^{-\beta z}$ and the trigonometric term $cos(\omega t - \beta z)$ than the linear shape functions used within the CT/LN vector element, thus giving a more sufficient approximation to the attenuation behaviour of the solution vector wave $\vec{E}_E$, in the region of the domain where the skin effect is present.

8.2.3.1 FEM Simulated Solution using Material Constants of Copper

An FE solution was simulated at a frequency of $f = 1$Hz, a conductivity value of $\sigma = 5.8 \times 10^7$ $[\frac{S}{m}]$, $t = 0$s and a permittivity value of $\mu = 4\pi \times 10^{-7}\left[\frac{\mathrm{H}}{\mathrm{m}}\right]$ where $\mu = \mu_0\mu_r = \left(4\pi \times 10^{-7}\right)(0.999994) \simeq \left(4\pi \times 10^{-7}\right)(1) = 4\pi \times 10^{-7}\left[\frac{\mathrm{H}}{\mathrm{m}}\right]$. The simulation is shown in Figure 8.5.

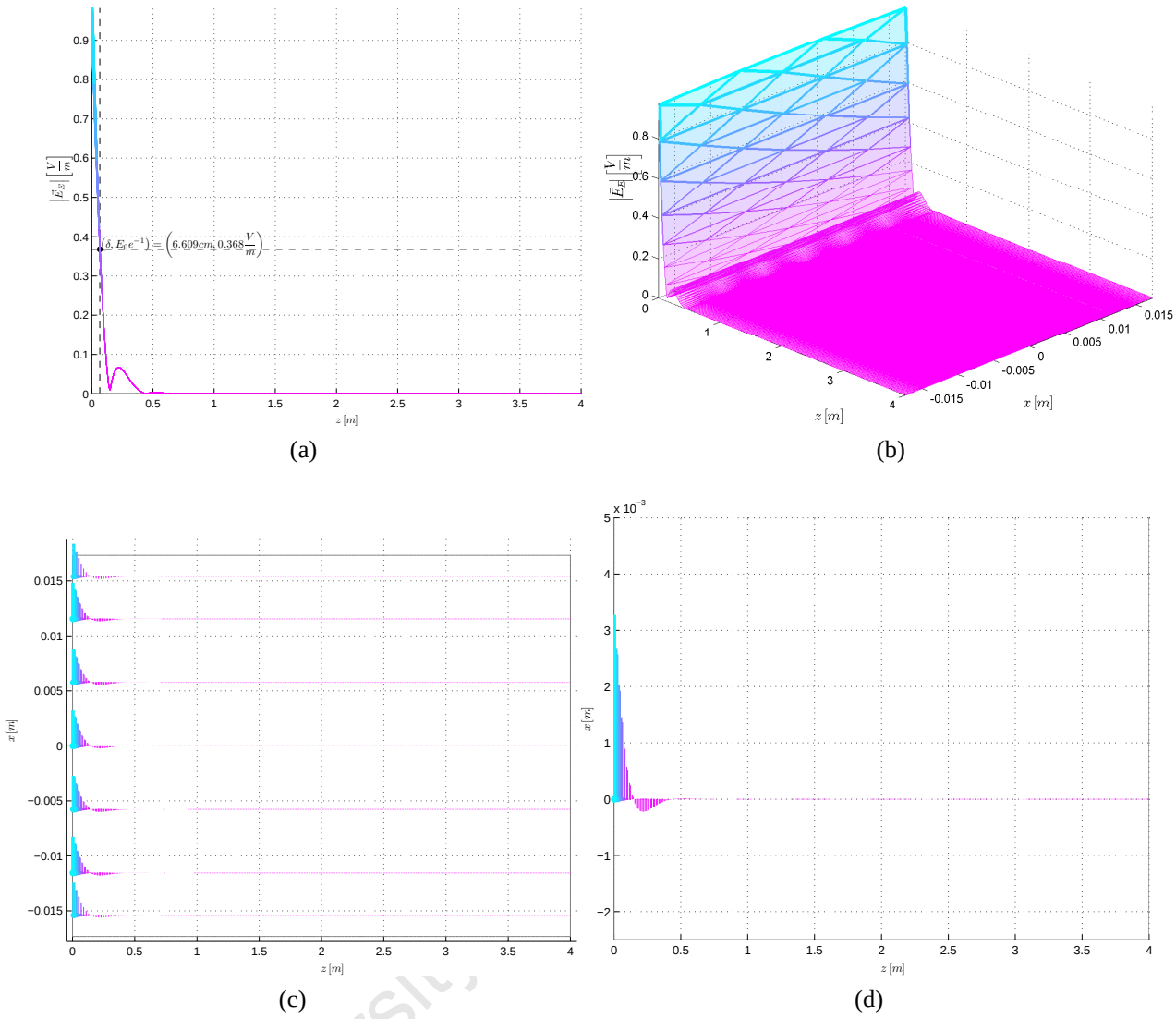

Figure 8.5: Solution Vector Field $\vec{E}_E$ within a Copper Conductor Simulated at a frequency of $f = 1\text{Hz}$

Sub-figure 8.5a, illustrates $\left|\vec{E}_E\right|$, the magnitude of the vector field $\vec{E}_E$, across the axis of wave propagation, the $z-axis$. At a frequency value of $f = 1\text{Hz}$, the skin depth of the solution $\vec{E}_E$, is extremely small due to copper being a very good conductor. Sub-figure 8.5b, illustrates $\left|\vec{E}_E\right|$, the magnitude of the vector field $\vec{E}_E$, across the entire two-dimensional domain in the form of a meshed graph. Sub-figure 8.5c, illustrates the vector field that would be induced in this domain at a frequency value of $f = 1\text{Hz}$. Sub-figure 8.5d, shows a single vector wave taken from sub-figure 8.5c.

Using Equation (3.12), the skin depth value within the copper conductor is calculated to be:

- at a frequency value of $f = 1\text{Hz}$, $\delta = 6.6085\text{cm}$

The skin depth δ, on the graph of sub-figures 8.5a corresponds to the independently calculated skin depth value above. The skin depth of the vector wave solution $\vec{E}_E$, is extremely small within the copper conductor. The high conductivity value possessed by copper of $\sigma = 5.8 \times 10^7\ [\frac{S}{m}]$, causes the attenuation term $e^{-\beta z}$ where $\beta = \sqrt{\pi f \mu \sigma}$ to greatly increase in strength, thus greatly decreasing the penetration depth of the vector wave solution $\vec{E}_E$.

8.2.4 Summary

There is a very good physical and behavioural similarity between the analytical solution and the FE simulated solution. The FE algorithm is able to model and simulate the attenuation behaviour of the propagating wave at different frequencies thereby demonstrating the skin effect phenomena which is an important behaviour effect found in eddy current problems [19, 16, 17]. Also, the skin depth calculations are in correspondence with the simulated solutions. As seen in sub-section 8.2.3.1, the conductivity σ, of a material can also have an influence on the skin depth δ.

The author has been convinced that the FE algorithm is capable of approximating solutions to Equation (2.39) and therefore, the FE algorithm can now be used to generate solutions to arbitrary eddy current configurations that are difficult to solve analytically. Such eddy current configurations will be addressed in subsequent sections to come.

8.3 FEM Solutions of Arbitrary Eddy Current Configurations

The FE algorithm is used to simulate visual solutions to eddy current configurations that are either problematic or difficult to solve analytically and the solutions take the form of the electric vector field intensity $\vec{E}_E$ and the current density $\vec{J}_E$, which are the eddy currents [16, 17] as discussed in Section 2.3.

As stated in Section 2.6, Equation (2.39) which governs eddy current behaviour can support both boundary-driven and force-driven eddy current problems. In this section, three types of eddy current problems will be investigated where, one will be a force-driven problem and the other two will be boundary-driven problems.

8.3.1 FEM Solution of a Boundary-Driven Eddy Current Configuration

This example considers eddy currents $\vec{J}_E$, induced in a solid cylinder made from conducting material. A time-varying harmonic magnetic field which comes into contact with the outer surface of the cylinder, induces an electric field $\vec{E}_E$, within the solid cylinder and this induced electric field then causes eddy currents $\vec{J}_E$, to be produced within the conducting body (refer to Section 2.3).

The geometry of this eddy current configuration is pictured below in sub-figure 8.6a and sub-figure 8.6b illustrates the structure of the domain space of this configuration.

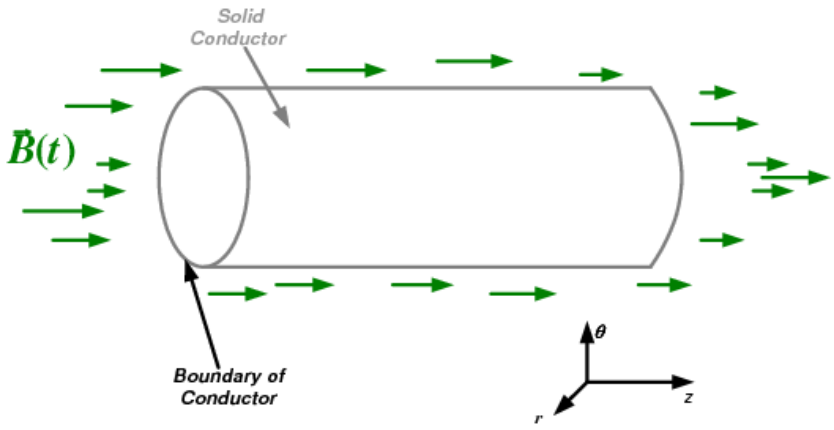

(a)

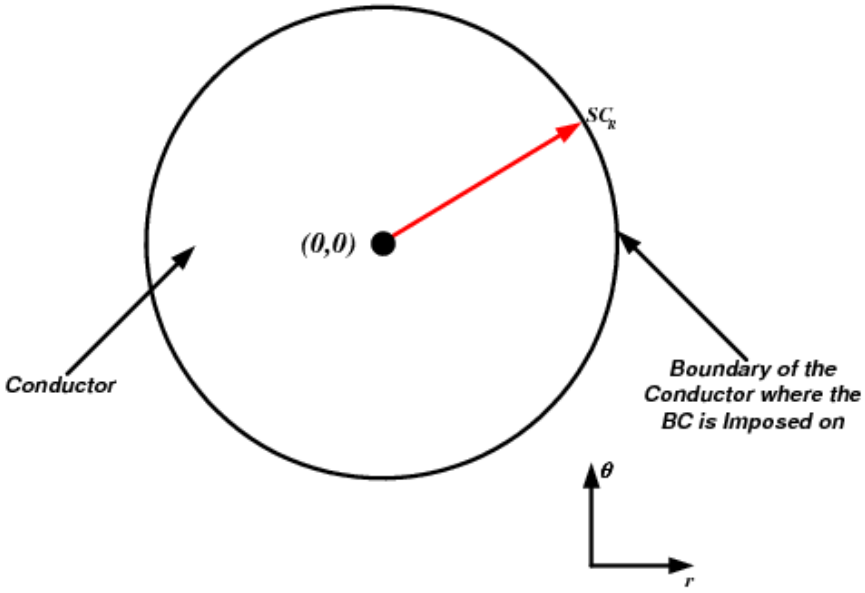

(b)

Figure 8.6: Geometry of the Problem Configuration

Sub-figure 8.6a illustrates the solid cylinder surrounded by a time-varying harmonic magnetic field. In sub-figure 8.6b, the domain consists of: a solid conductor region. SC_R-Radius of the solid cylinder and SC_R forms the boundary of the solid cylinder where the BC will be imposed upon. The polar coordinate system is used for reference due to the circular geometry of the domain.

Problem Setup

The problem involves a solid cylinder made of conducting material, where the outer surface of this solid cylinder comes into contact with a time-varying magnetic field given by Equation (3.21) as illustrated in sub-figure 8.6a. The time-varying magnetic field is repeated here for the readers convenience:

$$\vec{B}(t) = B_0 cos(\omega t)\hat{k}$$

The geometry of the domain space of this problem can be idealised as a two-dimensional planar problem (the circular cross-section of the solid cylinder) where the solution will be simulated on the $r-\theta$ plane as illustrated in sub-figure 8.6b. The dimension of the domain (the conductor) is approximately $0 \leq r \leq 1.8$m on the $r-axis$. The magnetic field according to Faraday's Law creates a circulating/rotating electric field given by Equation

(3.29) in phasor form as shown in sub-section 3.3.1. Equation (3.29) is repeated here for the readers convenience:

$$\tilde{E_S} = \frac{1}{2} j\omega B_0 \left(y\hat{i} - x\hat{j} \right)$$

where $\omega = 2\pi f$. This rotating $\tilde{E_S}$-field of Equation (3.29) forms the BC of this eddy current configuration and is specified on the entire boundary of the domain space as illustrated in sub-figure 8.6b. In this boundary-driven configuration, the region of the domain where the BC is imposed upon, is the circumference/boundary ($r = SC_R = 1.8$m) of the solid cylinder (refer to Section 2.6).

This imposed BC given by Equation (3.29), becomes the excitation force, as explained in sub-section 7.4.1.1, that induces an electric field solution $\vec{E}_E$, within the domain of the solid cylinder $(0 \leq r < SC_R)$. The electric field solution $\vec{E}_E$, then creates eddy currents $\vec{J}_E$, within the conducting regions of the domain. The reader is referred to Section 2.3 for an explanation of the formation of eddy current within a conducting region. Figure 8.7 shows the FE mesh of the problem.

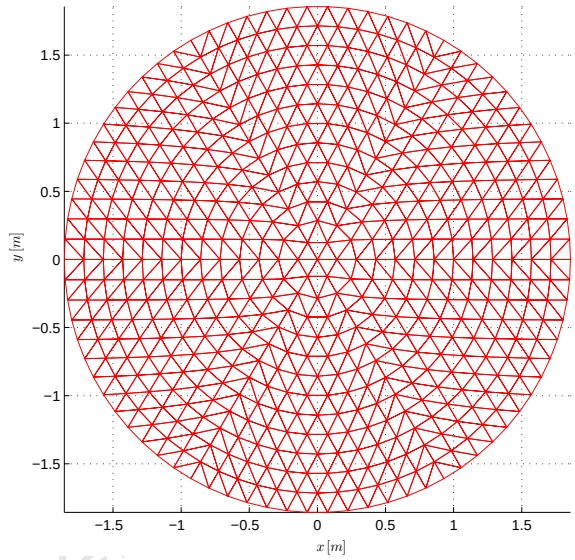

Figure 8.7: Finite Element Mesh of the Domain

The mesh consists of approximately 1014 triangular elements. The entire domain consists of a single material type. RED-conductor region.

Partial Analytical Derivation of this Eddy Current Configuration

Equation (2.40) of Section 2.5 takes on the following form in polar coordinates [6, 15]:

$$\tilde{E_E}(r,\theta,z) = \tilde{F}(r,\theta,z)\,\hat{r} + \tilde{G}(r,\theta,z)\,\hat{\theta} + \tilde{H}(r,\theta,z)\,\hat{z} \tag{8.2}$$

The electric vector field component in phasor form $\tilde{E_E}$, represents a circular wave that is polarised in the $\hat{\theta} - direction$ and travels in the $\hat{r} - direction$. Equation (8.2) thus takes on the following form:

$$\tilde{E_E} = \tilde{G}(r)\,\hat{\theta} \tag{8.3}$$

$$\vec{\nabla}^2 \tilde{G} = \frac{d^2\tilde{G}}{dr^2} + \frac{1}{r}\frac{d\tilde{G}}{dr} \tag{8.4}$$

$$\frac{d^2\tilde{G}}{dr^2} + \frac{1}{r}\frac{d\tilde{G}}{dr} - \tilde{k^2}\tilde{G} = 0 \tag{8.5}$$

The analytical solution of Equation (8.5) involves the calculation of Bessel functions [6, 15].

$$\tilde{G}(r) = c_1 J_0\left(\tilde{k}r\right) + c_2 Y_0\left(\tilde{k}r\right) \tag{8.6}$$

where J_0 and Y_0 are Bessel functions [6, 15].

Due to previous researched knowledge of Section 3.1 and sub-section 8.2.1, it is expected that the following physical traits and behaviour patterns should be found within the simulation of the vector field solution $\vec{E}_E$, of this eddy current configuration across the domain space. The simulated solution should exhibit the following physical traits and behaviour patterns:

- a wave that propagates radially ($r - direction$ of the $r - \theta$plane).
- the polarisation of the vector field $\vec{E}_E$, of the wave should be perpendicular to the direction of wave propagation. The vector field $\vec{E}_E$, should be polarised in the $\theta - direction$ of the $r - \theta$ plane.
- the vector field components of the wave should oscillate in the $\theta - direction$ of the $r - \theta$ plane
- an attenuation of the wave should be in the direction of the wave propagation and this attenuation possesses non-linear behaviour.
- the skin effect phenomena should be present when simulating the solution at different frequencies. The skin effect phenomena is caused by the attenuation of the wave as discussed in sub-sections 3.1.3, 3.1.4 and 8.2.3.

8.3.1.1 FEM Simulated Solutions

The FE algorithm was used to generate vector field solutions to the eddy current configuration of sub-section 8.3.1. The FE solutions were simulated at a permittivity value of $\mu = 0.25\left[\frac{\mathrm{H}}{\mathrm{m}}\right]$, $t = 0$s and a single conductivity value of $\sigma = 4\pi \backsimeq 12.566\ [\frac{S}{m}]$ but at varying frequency values of $f = 0.5$Hz, $f = 1$Hz, $f = 5$Hz, $f = 20$Hz and $f = 50$Hz, in order to illustrate the concept of skin effect behaviour [16, 17]. The computational time of the FE algorithm for this problem is 6.027s. A logarithmic scale was applied to the FEM simulated vector field solutions to reduce the order of magnitude of the range of $\left|\vec{E}_E\right|$and $\left|\vec{J}_E\right|$ to a more suitable range of values. This scaling application provided a visually better simulation of the vector field solutions for the purpose of analysis.

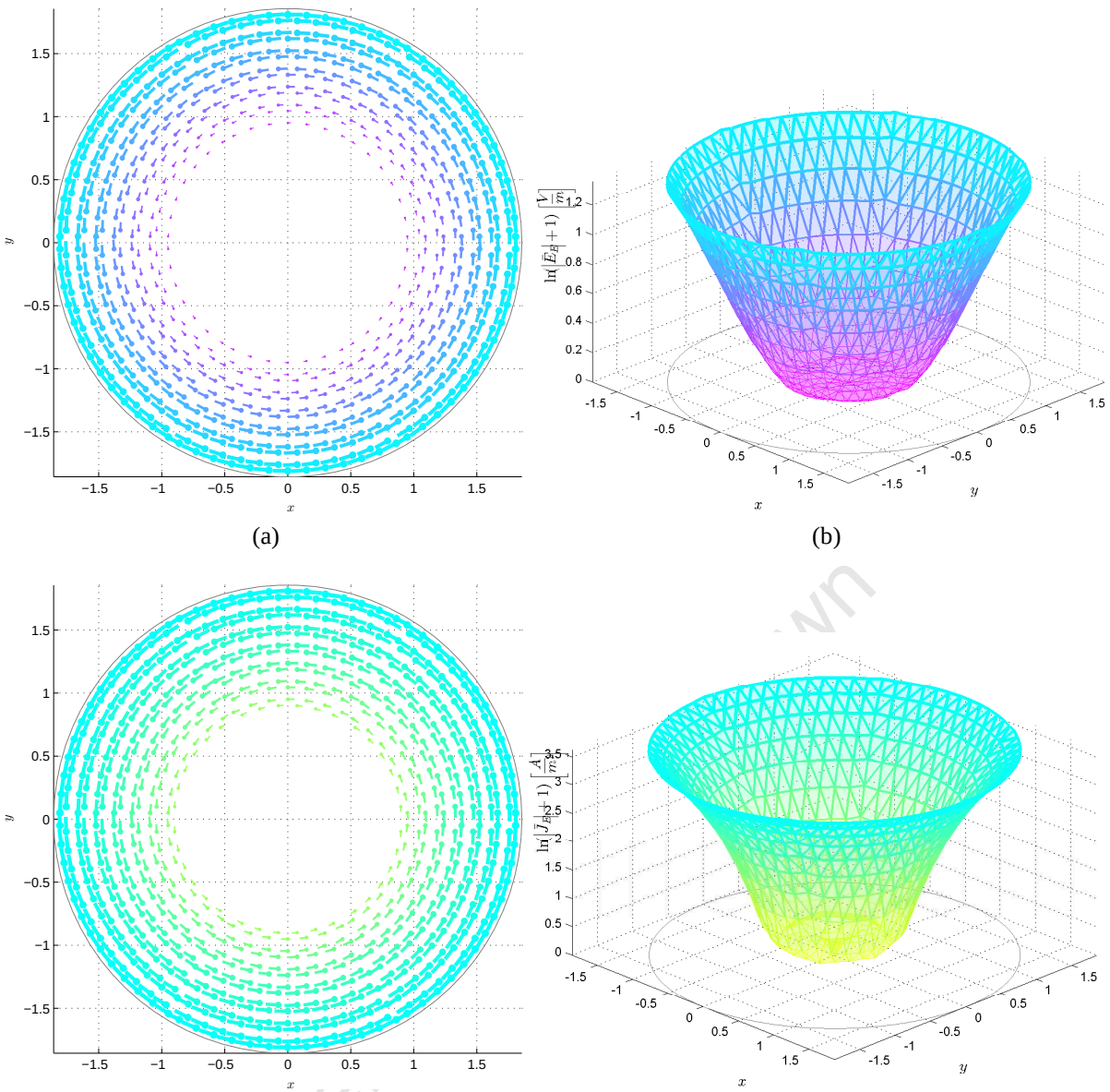

Figure 8.8: Solution Vector Field $\vec{E}_E$ and $\vec{J}_E$ Simulated at a frequency of $f = 0.5$Hz

Sub-figure 8.8a, illustrates the vector field $\vec{E}_E$, that would be induced in this domain at a frequency value of $f = 0.5$Hz. No wave pattern "seems" to be visible because the wavelength of the solution is too large for the dimension of the domain. Sub-figure 8.8b, shows a weak attenuation of the vector field $\vec{E}_E$, along the radial axis towards the centre of the domain. Sub-figure 8.8c, illustrates the eddy currents $\vec{J}_E$, that would be induced in this conductor at a frequency value of $f = 0.5$Hz. No wave pattern "seems" to be visible because the wavelength of the solution is too large for the dimension of the domain. Sub-figure 8.8d, shows a weak attenuation of the vector field $\vec{J}_E$, along the radial axis towards the centre of the domain.

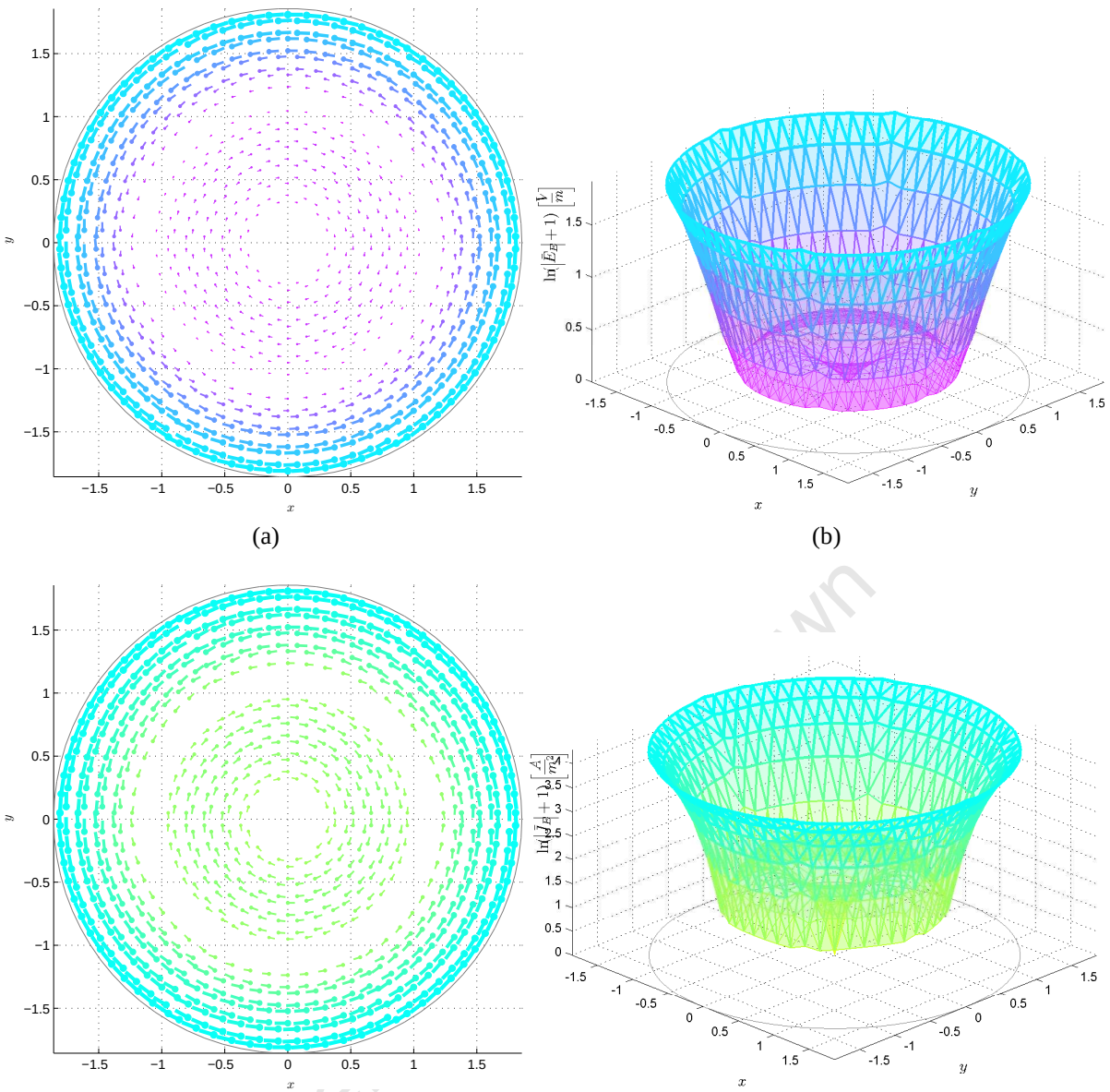

Figure 8.9: Solution Vector Field $\vec{E}_E$ and $\vec{J}_E$ Simulated at a frequency of $f = 1\text{Hz}$

Sub-figure 8.9a, illustrates the vector field $\vec{E}_E$, that would be induced in this domain at a frequency value of $f = 1\text{Hz}$ and a wave pattern of the vector field is clearly visible. Sub-figure 8.9b displays a wave that attenuates along the radial axis towards the centre of the domain. Sub-figure 8.9c, illustrates the eddy currents $\vec{J}_E$, that would be induced in this conductor at a frequency value of $f = 1\text{Hz}$. Sub-figure 8.9d also clearly displays a wave that attenuates along the radial axis towards the centre of the domain.

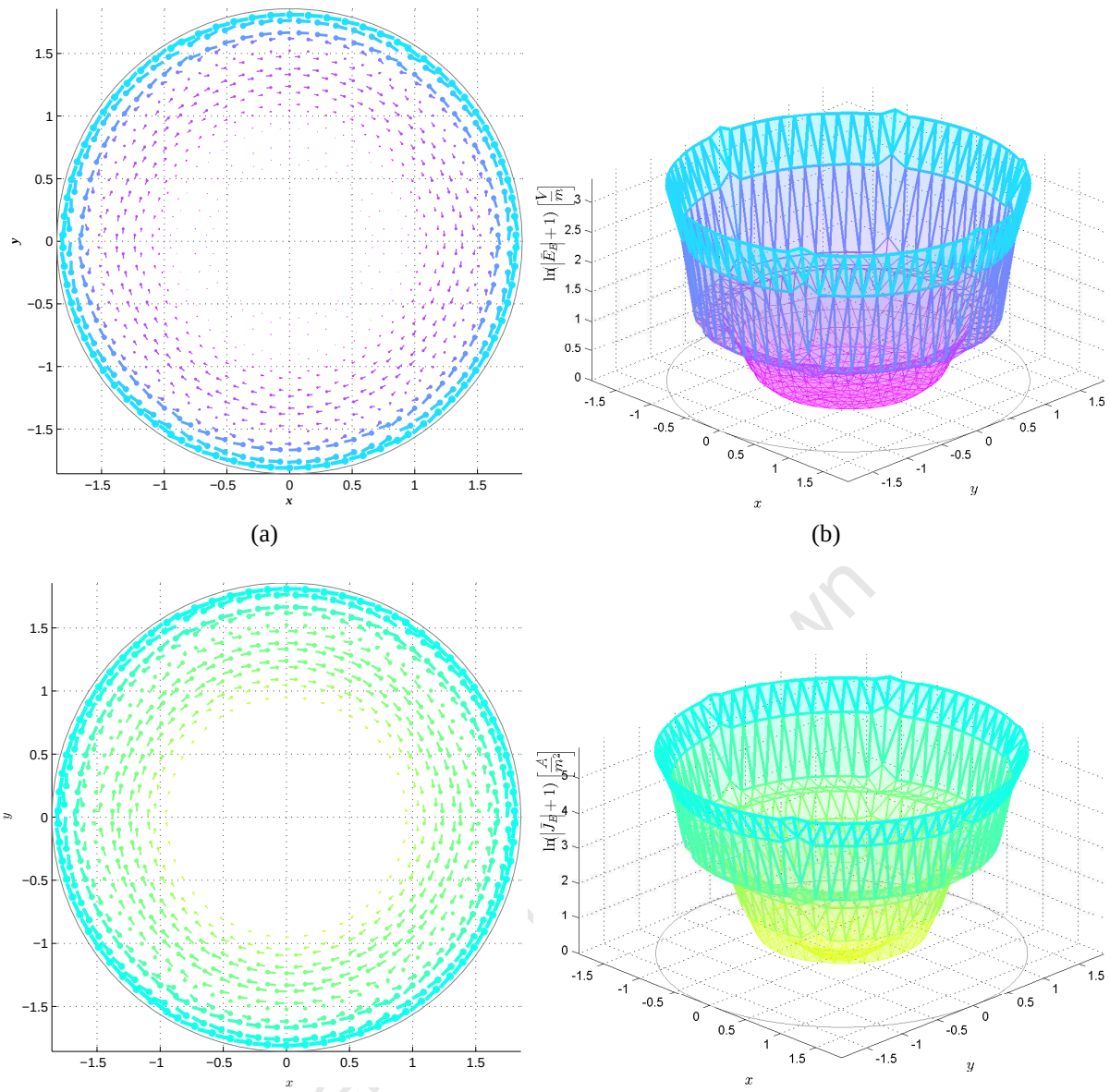

Figure 8.10: Solution Vector Field $\vec{E}_E$ and $\vec{J}_E$ Simulated at a frequency of $f = 5\text{Hz}$

Sub-figure 8.10a, illustrates the vector field $\vec{E}_E$, that would be induced in this domain at a frequency value of $f = 5\text{Hz}$. Penetration of $\vec{E}_E$ into the conductor has become less. Sub-figure 8.10b, shows a stronger attenuation of the vector field $\vec{E}_E$, along the radial axis towards the centre of the domain. Sub-figure 8.10c, illustrates the eddy currents $\vec{J}_E$, that would be induced in this conductor at a frequency value of $f = 5\text{Hz}$. Penetration of $\vec{J}_E$ into the conductor has become less. Sub-figure 8.10d, shows a stronger attenuation of the vector field $\vec{J}_E$, along the radial axis towards the centre of the domain.

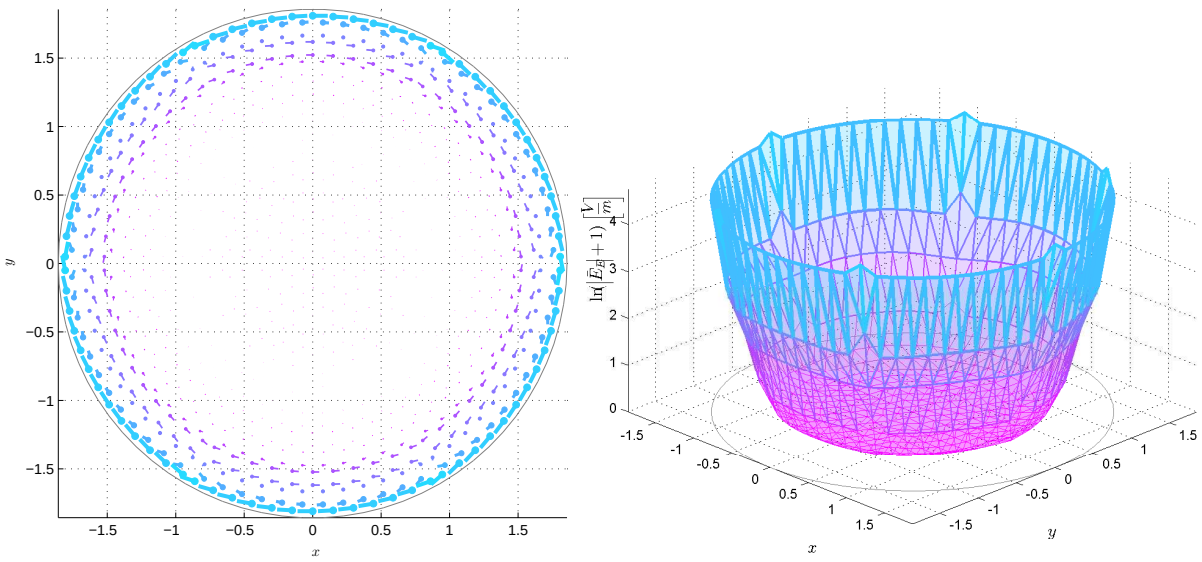

(a) (b)

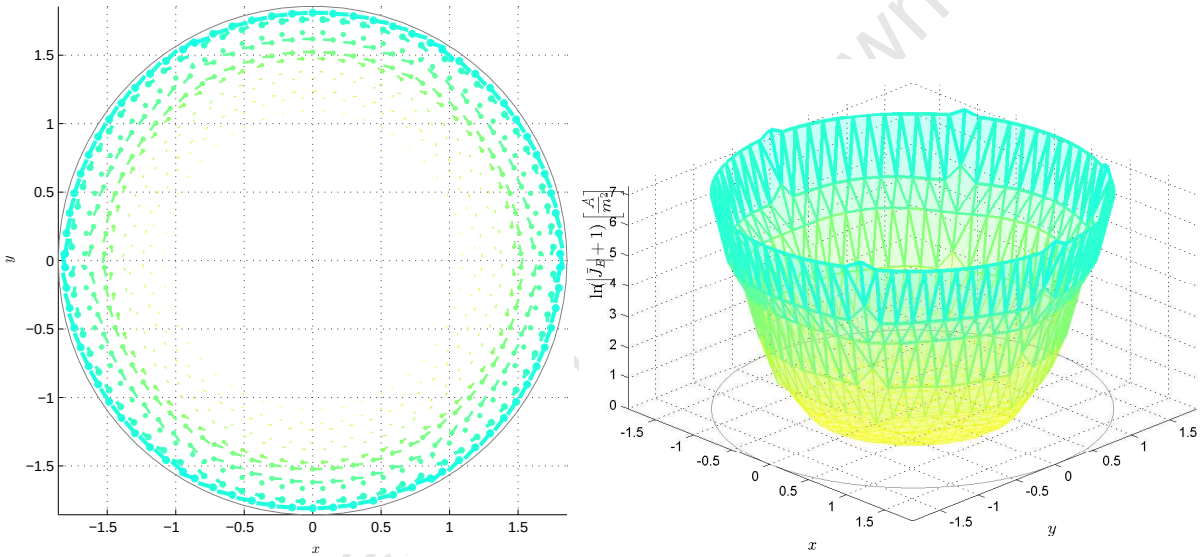

(c) (d)

Figure 8.11: Solution Vector Field $\vec{E}_E$ and $\vec{J}_E$ Simulated at a frequency of $f = 20$Hz

Sub-figure 8.11a, illustrates the vector field $\vec{E}_E$, that would be induced in this domain at a frequency value of $f = 20$Hz. The penetration depth of $\vec{E}_E$ into the conductor is decreasing and the wave pattern is less visible within the vector field due to the increase in attenuation strength the vector field $\vec{E}_E$. Sub-figure 8.11b, shows a sharp attenuation of the vector field $\vec{E}_E$ at this frequency, along the radial axis towards the centre of the domain. Sub-figure 8.11c, illustrates the eddy currents $\vec{J}_E$, that would be induced in this conductor at a frequency value of $f = 20$Hz. The penetration depth of $\vec{J}_E$ into the conductor is decreasing and the wave pattern is less visible within the vector field due to the increase in attenuation strength the vector field $\vec{J}_E$. Sub-figure 8.11d, shows a sharp attenuation of the vector field $\vec{J}_E$ at this frequency, along the radial axis towards the centre of the domain.

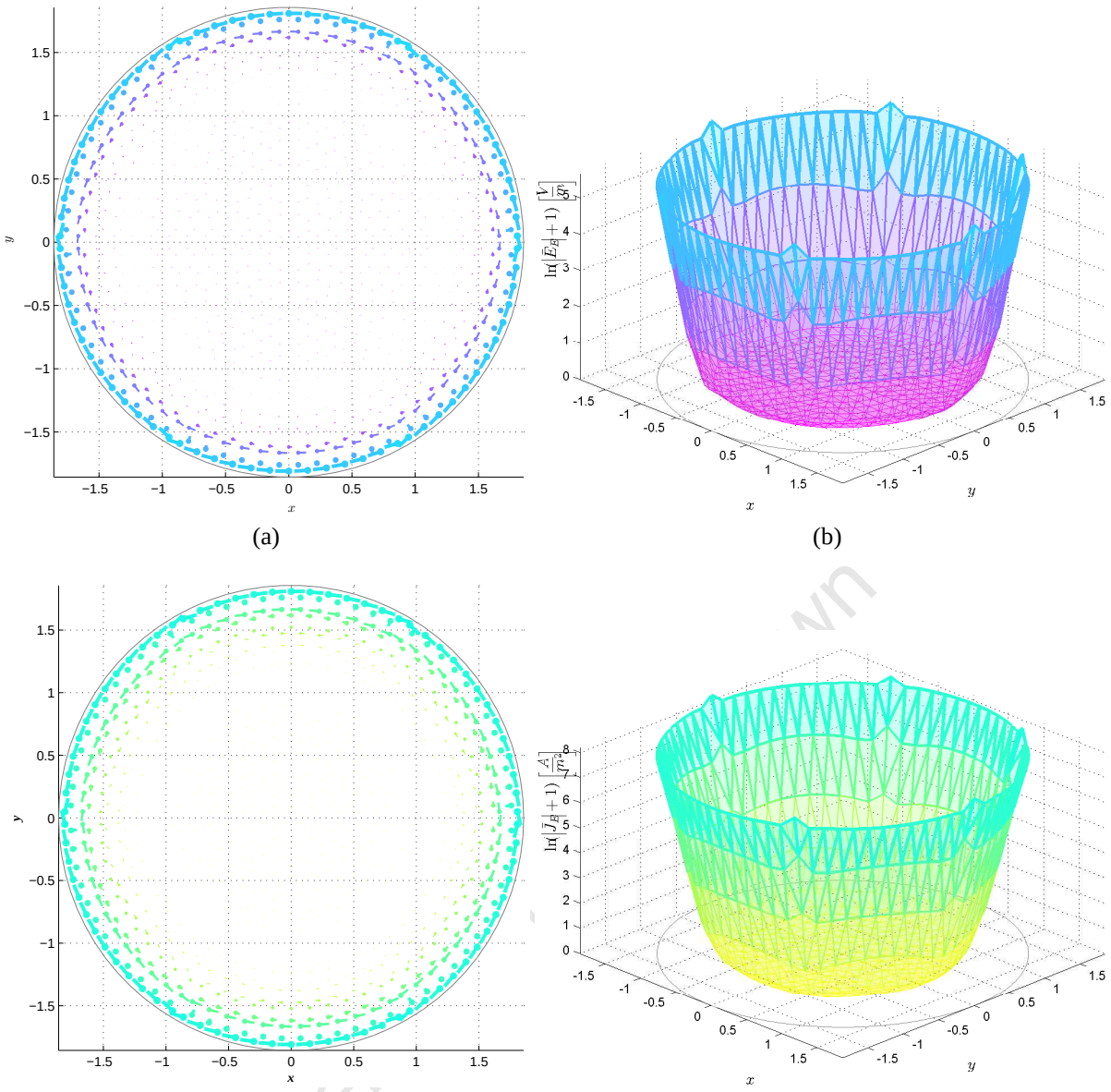

Figure 8.12: Solution Vector Field $\vec{E}_E$ and $\vec{J}_E$ Simulated at a frequency of $f = 50$Hz

Sub-figure 8.12a, illustrates the vector field $\vec{E}_E$, that would be induced in this domain at a frequency value of $f = 50$Hz. The attenuation of the vector field is very strong therefore $\vec{E}_E$ hardly penetrates into the conductor. Sub-figure 8.12b, shows a very sharp attenuation of the vector field $\vec{E}_E$ at this frequency, along the radial axis towards the centre of the domain. Sub-figure 8.12c, illustrates the eddy currents $\vec{J}_E$, that would be induced in this conductor at a frequency value of $f = 50$Hz. The attenuation of the vector field is very strong therefore $\vec{J}_E$ hardly penetrates into the conductor. Sub-figure 8.12d, shows a very sharp attenuation of the vector field $\vec{J}_E$ at this frequency, along the radial axis towards the centre of the domain.

8.3.1.2 Observations of FE Generated Solutions

The following observations were made concerning all the FEM simulations of sub-section 8.3.1.1:

1. A definite wave propagation along the radial direction of the domain in sub-figures 8.9a, 8.10a, 8.11a, 8.12a and sub-figures 8.9c, 8.10c, 8.11c, 8.12c can be seen, where the wave originates from the boundary ($r = SC_r$) and propagates toward the centre of the domain ($r = 0$). In sub-figures 8.8a and 8.8c there "seems" to be no wave propagation.

2. In sub-figures 8.9a, 8.10a, 8.11a, 8.12a and sub-figures 8.9c, 8.10c, 8.11c, 8.12c the vector fields $\vec{E}_E$ and $\vec{J}_E$ is polarised and oscillate in the $\hat{\theta} - direction$, which is perpendicular to the direction of wave propagation which is in the $\hat{r} - direction$ [10, 9].

3. In sub-figures 8.8a, 8.9a, 8.10a, 8.11a, 8.12a and sub-figures 8.8c, 8.9c, 8.10c, 8.11c, 8.12c the following was observed concerning the behaviour of $\vec{E}_E$ and $\vec{J}_E$ in relation to the radius r, of the domain:

   (a) With an increase in frequency f, the vector fields $\vec{E}_E$ and $\vec{J}_E$ appear to penetrate less into the solid conductor region of $0 \leq r < SC_R$.

4. *The meshed graphs of sub-figures 8.8b, 8.9b, 8.10b, 8.11b, 8.12b and sub-figures 8.8d, 8.9d, 8.10d, 8.11d, 8.12d seem to expose certain physical behaviour patterns of the vector fields $\vec{E}_E$ and $\vec{J}_E$ across the domain, more clearly that the vector fields of sub-figures 8.16a, 8.18a, 8.20a, 8.22a and sub-figures 8.17a, 8.19a, 8.21a, 8.23a.* The following was observed concerning the behaviour of $\left|\vec{E}_E\right|$ and $\left|\vec{J}_E\right|$ with relation to the radius r, of the domain:

   (a) Across the solid conductor region located at position $0 \leq r < SC_R$ of the domain, $\left|\vec{E}_E\right|$ and $\left|\vec{J}_E\right|$decays rapidly along the radial axis from position $r = SC_R$, towards the centre of the domain located at $r = 0$.
   (b) The decay of $\left|\vec{E}_E\right|$ and $\left|\vec{J}_E\right|$ across the solid conductor region $0 \leq r < SC_R$ becomes sharper as the frequency f, is increased.

5. In sub-figures 8.8b, 8.9b, 8.10b, 8.11b, 8.12b and sub-figures 8.8d, 8.9d, 8.10d, 8.11d, 8.12d, the meshed graph increases in "height" as the value of the frequency is set higher.

6. The vector field lines becomes "slightly distorted" with an increase in attenuation strength of the solution vector wave as can be seen in sub-figures 8.10a, 8.11a, 8.12a and sub-figures 8.10c, 8.11c, 8.12c.

8.3.1.3 Analysis of FE Generated Solutions

Previous research knowledge of Section 3.1 and sub-section 8.2.3 indicated that the vector fields solutions of $\vec{E}_E$ and $\vec{J}_E$ would attenuate across the solid conductor region $0 \leq r < SC_R$. Such a behaviour pattern of the vector fields solutions is expected because the example investigated in Section 3.1 and 8.2 and including this example was solved using the *same PDE given by Equation* (2.39), which governs the physical behaviour of eddy currents within a conductor and therefore there should be *some similarity in the physical behaviour of the vector field solutions* across their respective domains, although each example contained different BC's and geometry configurations.

The following analysis of the FE simulations has been made according to the observations found in sub-section 8.3.1.2:

1. A wave pattern formation is visible in sub-figures 8.9a, 8.10a, 8.11a, 8.12a and sub-figures 8.9c, 8.10c, 8.11c, 8.12c but not in sub-figures 8.8a and 8.8c. The general relationship shared between the frequency f and the wavelength λ of a wave is inversely proportional, that is :

$$f \backsim \frac{1}{\lambda} \tag{8.7}$$

where the wavelength according to Equation (8.7) becomes shorter as the frequency is increased and similarly the wavelength becomes longer as the frequency is decreased [10, 9]. In all the sub-figures 8.9a, 8.10a, 8.11a, 8.12a, 8.9c, 8.10c, 8.11c, 8.12c, the dimension of the domain is large enough to accommodate the wavelengths λ of these simulated solution vector waves at their set frequency values, but the solution vector wave of sub-figures 8.8a and 8.8c, the wavelength is too large for the dimension of the domain space due to a low frequency value of $f = 0.5\text{Hz}$ and therefore no wave pattern was observed.

2. The solution vector wave can be classified as a transverse wave, because the vector fields $\vec{E}_E$ and $\vec{J}_E$ of the wave is polarised in the $\hat{\theta} - direction$ which is perpendicular to the propagation of the wave which is along the radial direction ($\hat{r} - direction$) of the domain [10, 9] as seen in sub-figures 8.9a, 8.10a, 8.11a, 8.12a and sub-figures 8.9c, 8.10c, 8.11c, 8.12c.

3. According to sub-figures 8.8a, 8.9a, 8.10a, 8.11a, 8.12a and sub-figures 8.8c, 8.9c, 8.10c, 8.11c, 8.12c the following analysis is made concerning the behaviour of $\vec{E}_E$ and $\vec{J}_E$ in relation to the radius r, of the domain:

   (a) The attenuation of the vector fields $\vec{E}_E$ and $\vec{J}_E$ becomes stronger with an increase in frequency f, along the radial axis of the domain from position $r = SC_R$, towards the centre of the domain located at $r = 0$, thus the stronger the attenuation, the less the electric field $\vec{E}_E$ penetrates into the conducting body. As the frequency is increased the electric field $\vec{E}_E$, becomes situated closer and closer towards the boundary of the solid cylinder located at position $r = SC_R$ of the domain as shown in sub-figures 8.8a, 8.9a, 8.10a, 8.11a, 8.12a. This behaviour pattern is a clear indication of skin effect phenomena (refer to sub-section 3.1.3) which is an important characteristic of eddy current problems [16, 17]. The electric field $\vec{E}_E$, causes the motion of the free electrons within the conducting body, so producing an electric current density at the positions where the electric field penetrates the conducting body [10, 9, 19, 20] as seen in sub-figures 8.8c, 8.9c, 8.10c, 8.11c, 8.12c. It is this current density that is referred to as eddy currents, $\vec{J}_E$ [16, 17].

4. According to sub-figures 8.8b, 8.9b, 8.10b, 8.11b, 8.12b and sub-figures 8.8d, 8.9d, 8.10d, 8.11d, 8.12d the following analysis is made concerning the behaviour of $\left|\vec{E}_E\right|$ and $\left|\vec{J}_E\right|$ in relation to the radius r, of the domain:

   (a) $\left|\vec{E}_E\right|$ and $\left|\vec{J}_E\right|$decays rapidly along the radial axis from position $r = SC_R$, towards the centre of the domain located at $r = 0$. The attenuation behaviour could be "described as" an exponential "decaying" function with relation to the $r - axis$ which begins at the boundary of $r = SC_R$ and rapidly decays towards the centre ($r = 0$) of the solid conductor.

   (b) The exponential "decaying" function (attenuation of $\left|\vec{E}_E\right|$ and $\left|\vec{J}_E\right|$) along the radial axis from position $r = SC_R$, towards the centre of the domain located at $r = 0$, becomes steeper as the frequency f is increased, which is another indication of skin effect phenomena (refer to sub-section 3.1.3).

5. The increase in strength of the magnitude of the electric vector field $\left|\vec{E}_E\right|$, present in all meshed graphs of sub-figures 8.8b, 8.9b, 8.10b, 8.11b, 8.12b and sub-figures

8.8d, 8.9d, 8.10d, 8.11d, 8.12d can be attributed to the BC given by Equation (3.29) because, Equation (3.29) increases in magnitude when the frequency value f, is increased.

6. The "distortion" of some of the vectors present in the simulations at high frequency values as seen in sub-figures 8.10a, 8.11a, 8.12a and sub-figures 8.10c, 8.11c, 8.12c could be attributed to FE grid generation and shape function limitations. These factors which may have an affect on the simulations are addressed below.

FEM Grid Generation

Grid generation plays an important role as to how good the computation and visualisation of the solution that the FE algorithm will produce [3, 1]. Therefore, the quality of the visual simulated solution depends greatly on the grid generation [3, 1] as follows.

- the visual solution can also be displayed better by adding more triangular elements to the meshed grid, this could allow the FEM algorithm to approximate the attenuation of the solution more accurately and a better simulation will be generated [3, 1]. This however would increase the computational time of the algorithm extensively [3, 1].

- to avoid the distortion of the vectors within the solution vector field simulated at high frequency values, a possible solution would be to make use of a self-adaptive mesh refinement technique [17]. The application of mesh refinement technique has the result of increasing the density of the elements in the conducting body, especially near the outer boundary of the domain, where the eddy currents are mainly present due to the skin effect (refer to sub-section 3.1.4 and Section 2.3) [17]. In this way an eddy current distribution with increased accuracy can be obtained [17]. More grid information (domain coordinates) are needed towards the radial outer boundary of the domain than towards the inner domain space of the circular disk to accommodate the non-linear attenuation behaviour of this eddy current problem with greater accuracy [17]. By placing more domain coordinates at the radial outer boundary of the domain, the generated meshed grid would then posses more triangular elements towards the outer boundary of the domain and much less elements towards the interior of the circular disk [17]. In this way the number of triangular elements can be kept to a minimum, but a good simulation can still be generated while lowering the computational time of the FE program.

The grid spacings along the $r-axis$ are all of equal length and so does not appropriately accommodate the non-linear attenuation behaviour observed along the $r-axis$ of the simulations found in sub-figures 8.10a, 8.11a, 8.12a and sub-figures 8.10c, 8.11c, 8.12c.

Shape Function Limitations

Similar to what was investigated in sub-section 8.2.3, the choice of vector elements used could have an impact on the accuracy of the solution vector field approximation and on the visualisation of the simulation (refer to sub-section 8.2.3 and Section 5.7) [11, 12, 1] .

The distortion of the vectors within the solution vector field simulated at high frequency values, could demonstrate that the CT/LN vector element *is capable but not well suited* to approximate a vector field as given by Equation (3.11). A possible solution, would be to use higher-order vector elements. Higher-order vector elements consists of shape

functions constructed from quadratic or higher-order polynomials (refer to sub-section 5.7.1). These shape functions of the higher-order vector elements could be more capable of approximating the non-linear attenuation behaviour of the solution vector field than the linear shape functions used within the CT/LN vector element (that was investigated in Sections 5.1.2 and 5.3 respectively), thus giving a more sufficient approximation and a better visual simulation of the attenuation behaviour of the solution vector wave in the region of the domain where the skin effect is present.

8.3.1.4 FEM Simulated Solution using Material Constants of Copper

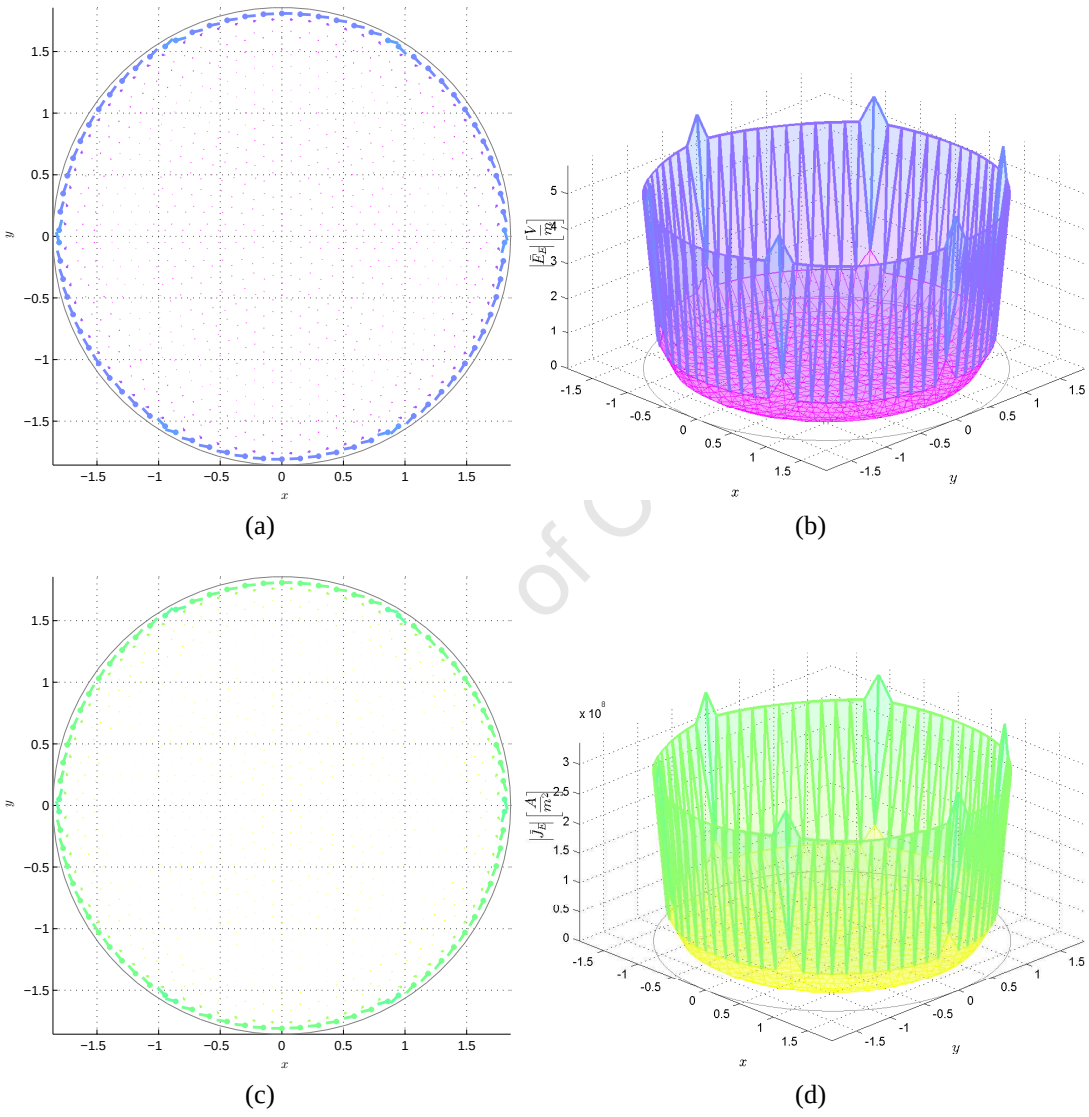

Figure 8.13: Solution Vector Field $\vec{E}_E$ within a Copper Conductor Simulated at a frequency of $f = 1$Hz

Sub-figure 8.13a, illustrates the vector field $\vec{E}_E$, that would be induced in this domain at a frequency value of $f = 1$Hz. The penetration depth of $\vec{E}_E$ into the conductor is extremely small. Sub-figure 8.13b, shows a very sharp attenuation of the vector field $\vec{E}_E$ at this frequency, along the radial axis towards the centre of the domain. Sub-figure 8.13c, illustrates the eddy currents $\vec{J}_E$, that would be induced in this conductor at a frequency value of $f = 1$Hz. These eddy currents are mainly situated on the perimeter of the conducting body. Sub-figure 8.12d, shows a very sharp attenuation of the vector field $\vec{J}_E$ at this frequency, along the radial axis towards the centre of the domain.

The FE solution was simulated at a frequency of $f = 1\text{Hz}$, a conductivity value of $\sigma = 5.8 \times 10^7$ $[\frac{S}{m}]$, $t = 0\text{s}$ and a permittivity value of $\mu = 4\pi \times 10^{-7}\left[\frac{\text{H}}{\text{m}}\right]$ where $\mu = \mu_0\mu_r = \left(4\pi \times 10^{-7}\right)(0.999994) \simeq \left(4\pi \times 10^{-7}\right)(1) = 4\pi \times 10^{-7}\left[\frac{\text{H}}{\text{m}}\right]$. The simulation is shown in Figure 8.13.

The penetration depth (skin depth δ) of the vector wave solutions $\vec{E}_E$ and $\vec{J}_E$, is extremely small within the copper conductor. The high conductivity value possessed by copper of $\sigma = 5.8 \times 10^7$ $[\frac{S}{m}]$ "seems" to increase the attenuation of $\vec{E}_E$ and $\vec{J}_E$. Thus, the electric field $\vec{E}_E$ and the eddy currents $\vec{J}_E$, are mainly present on the perimeter of the conducting body.

8.3.1.5 Summary

The FE algorithm is able to model and simulate:

- the physical behaviour of the electric vector field $\vec{E}_E$, and electric current density/eddy currents $\vec{J}_E$, across the entire domain.
- the attenuation behaviour of the vector fields $\vec{E}_E$ and $\vec{J}_E$ at different frequencies thereby demonstrating the skin effect phenomena, which is an important behaviour effect found in eddy current problems [19, 16, 17].

However, improvements to the accuracy of the solution vector field approximations and the simulations visually could be achieved through the used of higher-order vector elements and a self-adaptive mesh refinement technique. Higher-order vector elements could be more capable of approximating the non-linear attenuation behaviour of the solution vector field in comparison to linear vector elements. The simulations of the analytical solutions of Section 8.2 and the boundary-driven simulations of sub-section 8.3.1, both suggest that the use of a self-adaptive mesh refinement technique would be useful, in that more accurate results and better visual simulations could be obtained, since the mesh would physically be able to accommodate the behaviour of the skin effect phenomena which is always present in eddy current configurations [5, 3, 19].

As seen in sub-section 8.3.1.4, the conductivity σ, of a material can also have an affect on the attenuation of $\vec{E}_E$ and $\vec{J}_E$ and therefore also has an affect on the penetration depth of the vector fields $\vec{E}_E$ and $\vec{J}_E$ into the conducting body.

8.3.2 FEM Solution of a Boundary-Driven Eddy Current Configuration

This example considers eddy currents $\vec{J}_E$, induced in a solid cylinder made from conducting material. A time-varying harmonic magnetic field which exists within an air space region which surrounds the cylinder, induces an electric field $\vec{E}_E$, within the solid cylinder and this induced electric field then causes eddy currents $\vec{J}_E$, to be produced within the conducting body, as explained in Section 2.3.

The geometry of the eddy current configuration is pictured below in sub-figure 8.14a and sub-figure 8.14b illustrates the structure of the domain space of this configuration.

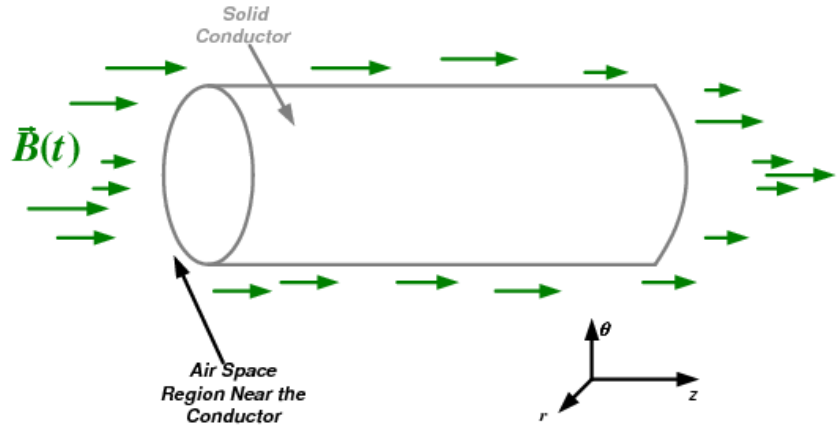

(a)

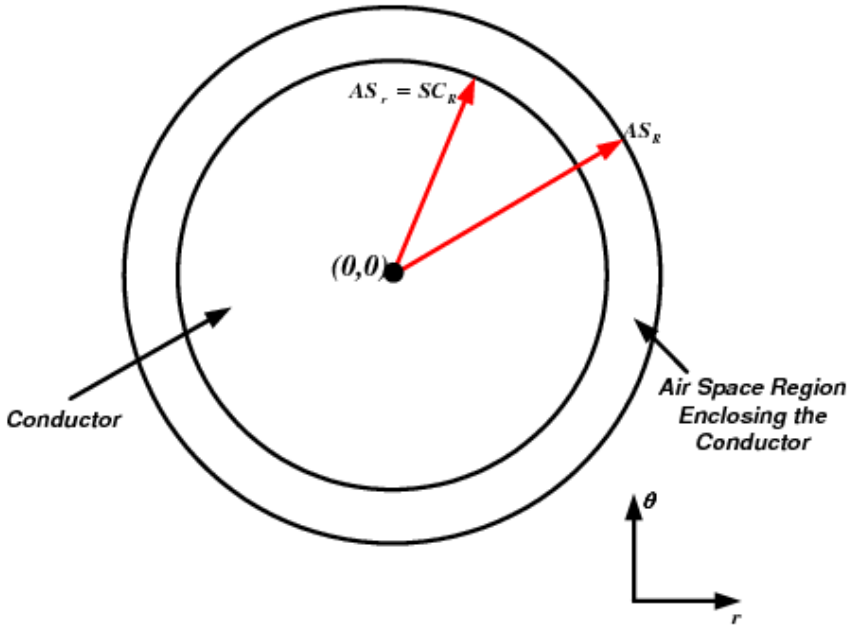

(b)

Figure 8.14: Geometry of the Problem Configuration

Sub-figure 8.14a illustrates the solid cylinder surrounded by a time-varying harmonic magnetic field. In sub-figure 8.14b, the domain consists of: a solid conductor region and an air space region which which encloses the solid conductor region. AS_R-Outer radius of the air space region, AS_r-Inner radius of the air space region. SC_R-Radius of the solid cylinder, where $AS_r = SC_R$. The polar coordinate system is used for reference due to the circular geometry of the domain.

Problem Setup

The problem involves a solid cylinder made of conducting material which is surrounded by a region of air space. This solid cylinder comes into contact with a time-varying magnetic field given by Equation (3.21) that exists within the air space as illustrated in sub-figure 8.14a. The time-varying magnetic field is repeated here for the readers convenience:

$$\vec{B}(t) = B_0 cos(\omega t)\hat{k}$$

The geometry of the domain space of this problem can be idealised as a two-dimensional planar problem where the solution will be simulated on the $r-\theta$ plane. The dimension

of the solid conductor region is approximately $0 \leq r \leq 1.6$m and the dimension of the air space region is approximately $1.6\text{m} \leq r \leq 1.8\text{m}$. The magnetic field exists across the air space region $(AS_r \leq r \leq AS_R)$ that encloses the solid conductor region $(0 \leq r \leq SC_R)$ as illustrated in sub-figure 8.14b. This magnetic field according to Faraday's Law creates a circulating/rotating electric field given by Equation (3.29) in phasor form as shown in sub-section 3.3.1. Equation (3.29) is repeated here for the readers convenience:

$$\tilde{E}_S = \frac{1}{2} j\omega B_0 \left(y\hat{i} - x\hat{j}\right)$$

and the current density of Equation (3.29) is [5, 9, 19]:

$$\tilde{J}_S = \frac{1}{2}\sigma j\omega B_0 \left(y\hat{i} - x\hat{j}\right) \tag{8.8}$$

Equations (3.29) and (8.13) can be written in polar coordinates as:

$$\tilde{E}_S = \frac{1}{2} j\omega B_0 r\hat{\theta} \tag{8.9}$$

and

$$\tilde{J}_S = \frac{1}{2}\sigma j\omega B_0 r\hat{\theta} \tag{8.10}$$

where $\omega = 2\pi f$. This rotating $\tilde{E}_S$-field of Equations (3.29) and (8.9) forms the BC of this eddy current configuration and is specified on the entire air space region $(AS_r \leq r \leq AS_R)$ of the domain as illustrated in sub-figure 8.14b (refer to Section 2.6). This imposed BC given by Equation (3.29), becomes the excitation force, as shown in sub-section 7.4.1.1, that induces an electric field solution $\vec{E}_E$ within the domain of the solid cylinder $(0 \leq r < SC_R)$. The electric field solution $\vec{E}_E$, then creates eddy currents $\vec{J}_E$, within the conducting regions of the domain [19, 16, 17]. Figure 8.15 shows the FE mesh of the problem.

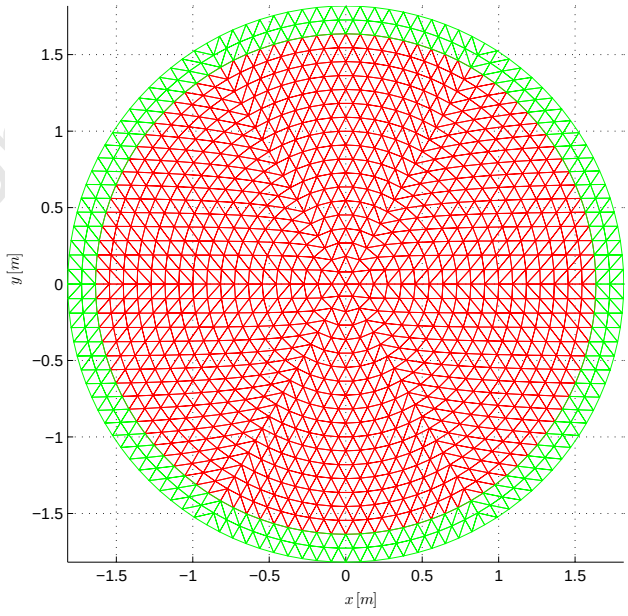

Figure 8.15: Finite Element Mesh of the Domain

The mesh consists of approximately 2400 triangular elements. The domain consists of two different material types, an air space region and a conductor region. The two material regions are indicated by the different colours of the mesh. RED-conductor region. GREEN-air space region.

The FE algorithm (as shown in Step 9 and 10 of Section 7.7) collects the computed vector components *of each FE in the domain* and so will display a *total vector field solution* over the entire domain of $(0 \leq r \leq AS_R)$ Thus, the total/overall electric vector field solution can be expressed as:

$$\vec{E_T} = \vec{E}_E + \vec{E}_S \tag{8.11}$$

which consisting of $\vec{E}_E$ over the region $(0 \leq r < SC_R)$ and $\vec{E}_S$ over the region $(AS_r \leq r \leq AS_R)$. Similarly, the total/overall current density vector field solution can be expressed as:

$$\vec{J_T} = \vec{J_E} + \vec{J_S} \tag{8.12}$$

which consisting of $\vec{J_E}$ over the region $(0 \leq r < SC_R)$.

8.3.2.1 FEM Simulated Solutions

The FE algorithm was used to generate vector field solutions to the eddy current configuration of sub-section 8.3.3. The FE solutions were simulated at: a permittivity value of $\mu = 0.25\left[\frac{\mathrm{H}}{\mathrm{m}}\right]$ across the conductor region; a permittivity value of $\mu = \mu_0\mu_r = \left(4\pi \times 10^{-7}\right)(1.00000037) \simeq \left(4\pi \times 10^{-7}\right)(1) = 4\pi \times 10^{-7}\left[\frac{\mathrm{H}}{\mathrm{m}}\right]$ across the air space region; time of $t = 0$s; a single conductivity value of $\sigma = 4\pi \backsimeq 12.566$ $[\frac{S}{m}]$ across the conductor region; a single conductivity value of $\sigma \backsimeq 1 \times 10^{-4}$ $[\frac{S}{m}]$ across the air space region; but at varying frequency values of $f = 0.5$Hz, $f = 1$Hz, $f = 5$Hz, and $f = 20$Hz, in order to illustrate the concept of skin effect behaviour [16, 17]. The computational time of the FE algorithm for this problem is 19.609s.

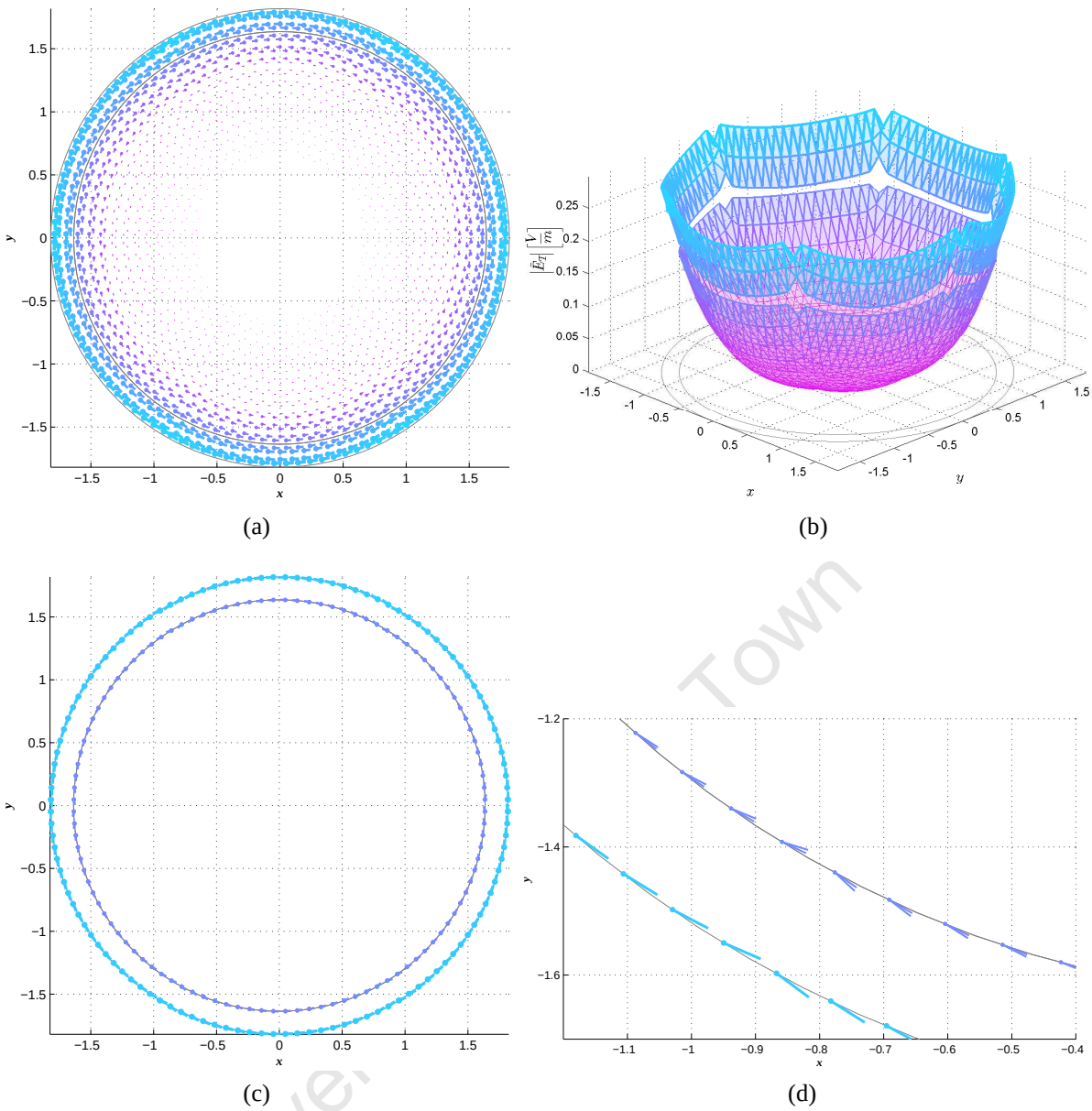

Figure 8.16: Solution Vector Field $\vec{E}_T$ Simulated at a frequency of $f = 0.5$Hz

Sub-figure 8.16a, illustrates the electric field $\vec{E}_E$, that would be induced in the region $0 \leq r \leq SC_R$ at a frequency value of $f = 0.5$Hz, the region $AS_r \leq r \leq AS_R$ contains the source electric field $\vec{E}_S$. Sub-figure 8.16b illustrates in the form of a meshed graph: $\left|\vec{E}_E\right|$(the magnitude of the vector field $\vec{E}_E$), across the region of $0 \leq r \leq SC_R$ of the domain and $\left|\vec{E}_S\right|$ (the magnitude of the vector field $\vec{E}_S$) across the region $AS_r \leq r \leq AS_R$ of the domain. In sub-figure 8.16b, $\left|\vec{E}_E\right|$ across the region $0 \leq r \leq SC_R$ suggests an attenuation of $\vec{E}_E$, over this same region. The weak attenuation behaviour of $\left|\vec{E}_E\right|$ across the region $0 \leq r \leq SC_R$, verifies that $\vec{E}_E$ penetrates deeply into the conductor at this frequency. Sub-figure 8.16c, shows the vectors of $\vec{E}_T$ located on the material interface. To view the behaviour of these vectors better, a region of this figure was enlarged which is shown in sub-figure 8.16d. Sub-figure 8.16d, clearly illustrates the discontinuous behaviour of $\vec{E}_T$ across the material interface located at the position $r = SC_R = AS_r$ and this discontinuity of $\vec{E}_T$ is verified by the "gap" found between different material regions of the meshed graph as seen in sub-figure 8.16b.

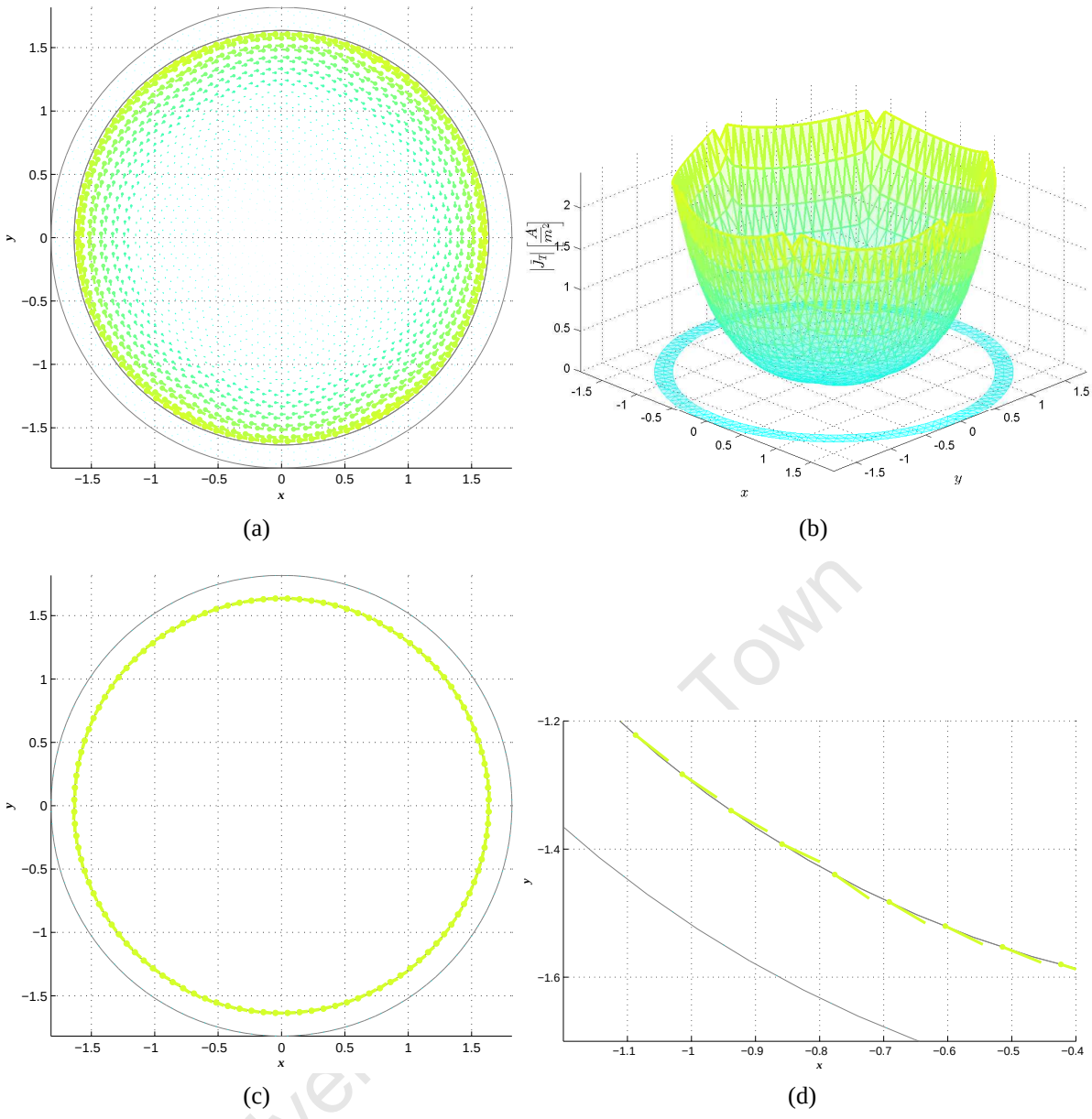

Figure 8.17: Solution Vector Field $\vec{J_T}$ Simulated at a frequency of $f = 0.5$Hz

Sub-figure 8.17a, illustrates the electric current density/eddy currents $\vec{J_E}$, that would be induced in the region $0 \leq r \leq SC_R$ at a frequency value of $f = 0.5$Hz and there are no $\vec{J_S}$ present in the air space region $AS_r \leq r \leq AS_R$, since air cannot conduct current density [8, 5, 10]. Sub-figure 8.17b illustrates in the form of a meshed graph: $\left|\vec{J_E}\right|$ (the magnitude of the vector field $\vec{J_E}$), across the region of $0 \leq r \leq SC_R$ and $\left|\vec{J_S}\right| = 0$ across the region $0 \leq r \leq SC_R$. In sub-figure 8.17b $\left|\vec{J_E}\right|$ across the region $HC_r \leq r \leq HC_R$ suggests an attenuation of $\vec{J_E}$ over this same region and in the region $AS_r \leq r \leq AS_R$, $\left|\vec{J_E}\right| = 0$ demonstrating that no $\vec{J_E}$ is present over this same region. In the region $AS_r \leq r \leq AS_R$. The weak attenuation behaviour of $\left|\vec{J_E}\right|$ across the region $0 \leq r \leq SC_R$, verifies that $\vec{J_E}$ has penetrated deeply into the conductor at this frequency. Sub-figure 8.17c, shows the vectors of $\vec{J_T}$ located on the material interface located at the position $r = SC_R = AS_r$. To view the behaviour of these vectors better, a region of this figure was enlarged which is shown in sub-figure 8.17d. In sub-figure 8.17d, only the vector field $\vec{J_E}$ (belonging to the conductor regions of the domain) is present on the material interface because $\vec{J_S}$ cannot exists in the air space region of the domain [8, 5, 10].

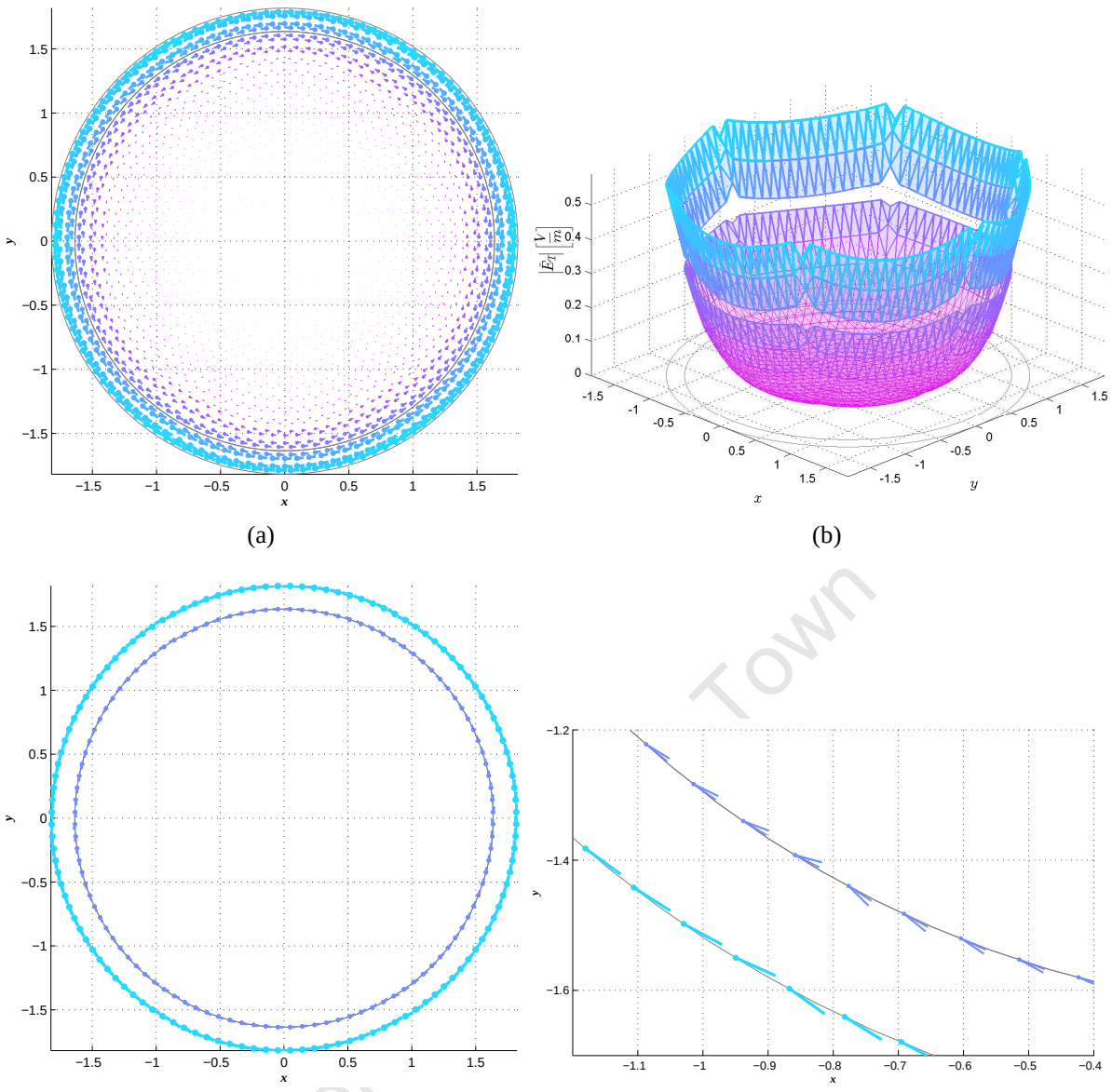

Figure 8.18: Solution Vector Field $\vec{E}_T$ Simulated at a frequency of $f = 1\text{Hz}$

Sub-figure 8.18a, illustrates the electric field $\vec{E}_E$, that would be induced in the region $0 \leq r \leq SC_R$ at a frequency value of $f = 1\text{Hz}$, the region $AS_r \leq r \leq AS_R$ contains the source electric field $\vec{E}_S$. Sub-figure 8.18b illustrates in the form of a meshed graph: $\left|\vec{E}_E\right|$(the magnitude of the vector field $\vec{E}_E$), across the region of $0 \leq r \leq SC_R$ of the domain and $\left|\vec{E}_S\right|$ (the magnitude of the vector field $\vec{E}_S$) across the region $AS_r \leq r \leq AS_R$ of the domain. In sub-figure 8.18b, $\left|\vec{E}_E\right|$ across the region $0 \leq r \leq SC_R$ suggests an attenuation of $\vec{E}_E$, over this same region. The weak attenuation behaviour of $\left|\vec{E}_E\right|$ across the region $0 \leq r \leq SC_R$, verifies that $\vec{E}_E$ penetrates deeply into the conductor at this frequency. Sub-figure 8.18c, shows the vectors of $\vec{E}_T$ located on the material interface. To view the behaviour of these vectors better, a region of this figure was enlarged which is shown in sub-figure 8.18d. Sub-figure 8.18d, clearly illustrates the discontinuous behaviour of $\vec{E}_T$ across the material interface located at the position $r = SC_R = AS_r$ and this discontinuity of $\vec{E}_T$ is verified by the "gap" found between different material regions of the meshed graph as seen in sub-figure 8.18b.

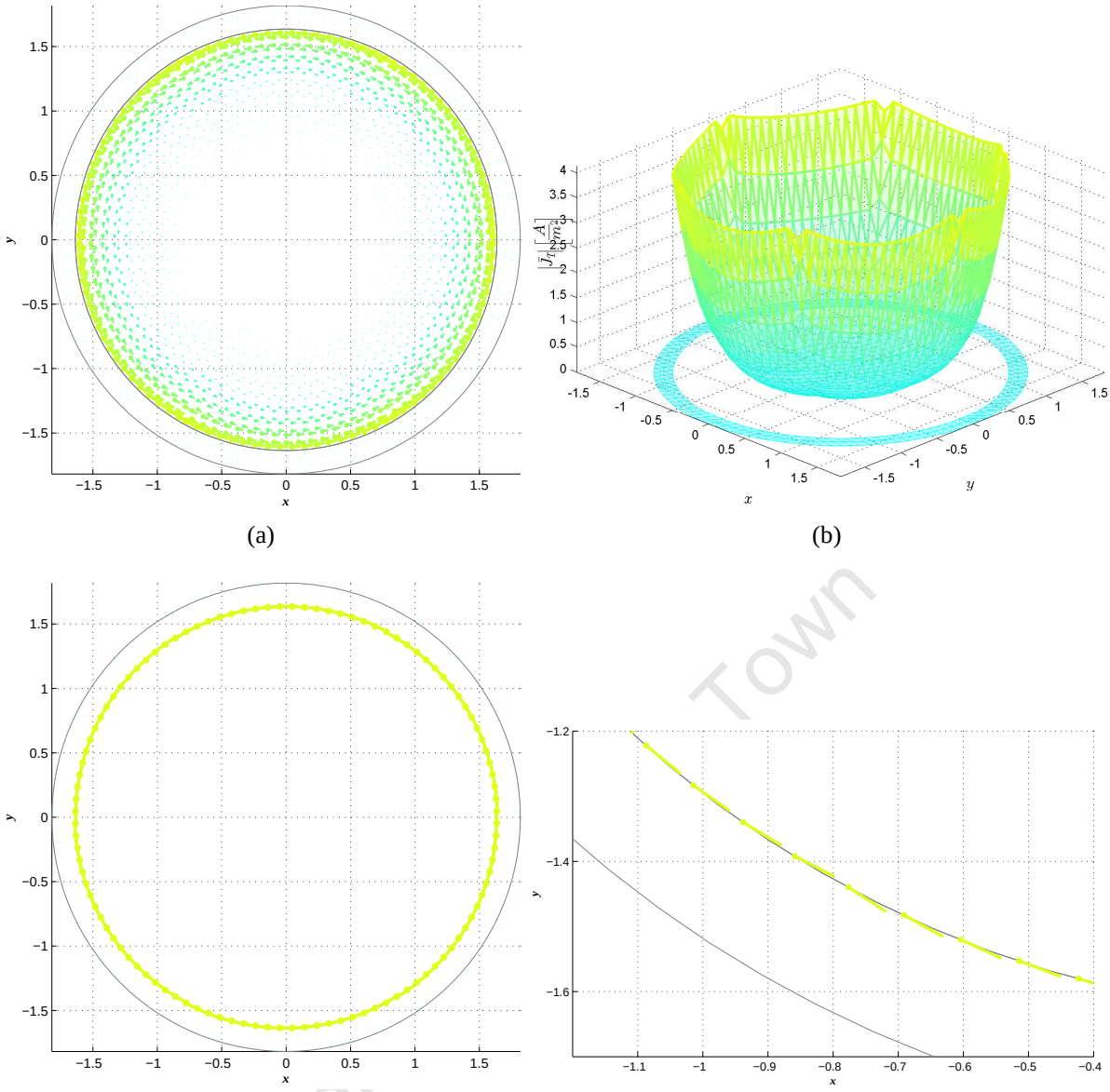

Figure 8.19: Solution Vector Field $\vec{J}_T$ Simulated at a frequency of $f = 1\text{Hz}$

Sub-figure 8.19a, illustrates the electric current density/eddy currents $\vec{J}_E$, that would be induced in the region $0 \leq r \leq SC_R$ at a frequency value of $f = 1\text{Hz}$ and there are no $\vec{J}_S$ present in the air space region $AS_r \leq r \leq AS_R$, since air cannot conduct current density [8, 5, 10]. Sub-figure 8.19b illustrates in the form of a meshed graph: $\left|\vec{J}_E\right|$ (the magnitude of the vector field $\vec{J}_E$), across the region of $0 \leq r \leq SC_R$ and $\left|\vec{J}_S\right| = 0$ across the region $0 \leq r \leq SC_R$. In sub-figure 8.19b $\left|\vec{J}_E\right|$ across the region $HC_r \leq r \leq HC_R$ suggests an attenuation of $\vec{J}_E$ over this same region and in the region $AS_r \leq r \leq AS_R$, $\left|\vec{J}_E\right| = 0$ demonstrating that no $\vec{J}_E$ is present over this same region. In the region $AS_r \leq r \leq AS_R$. The weak attenuation behaviour of $\left|\vec{J}_E\right|$ across the region $0 \leq r \leq SC_R$, verifies that $\vec{J}_E$ has penetrated deeply into the conductor at this frequency. Sub-figure 8.19c, shows the vectors of $\vec{J}_T$ located on the material interface located at the position $r = SC_R = AS_r$. To view the behaviour of these vectors better, a region of this figure was enlarged which is shown in sub-figure 8.19d. In sub-figure 8.19d, only the vector field $\vec{J}_E$ (belonging to the conductor regions of the domain) is present on the material interface because $\vec{J}_S$ cannot exists in the air space region of the domain [8, 5, 10].

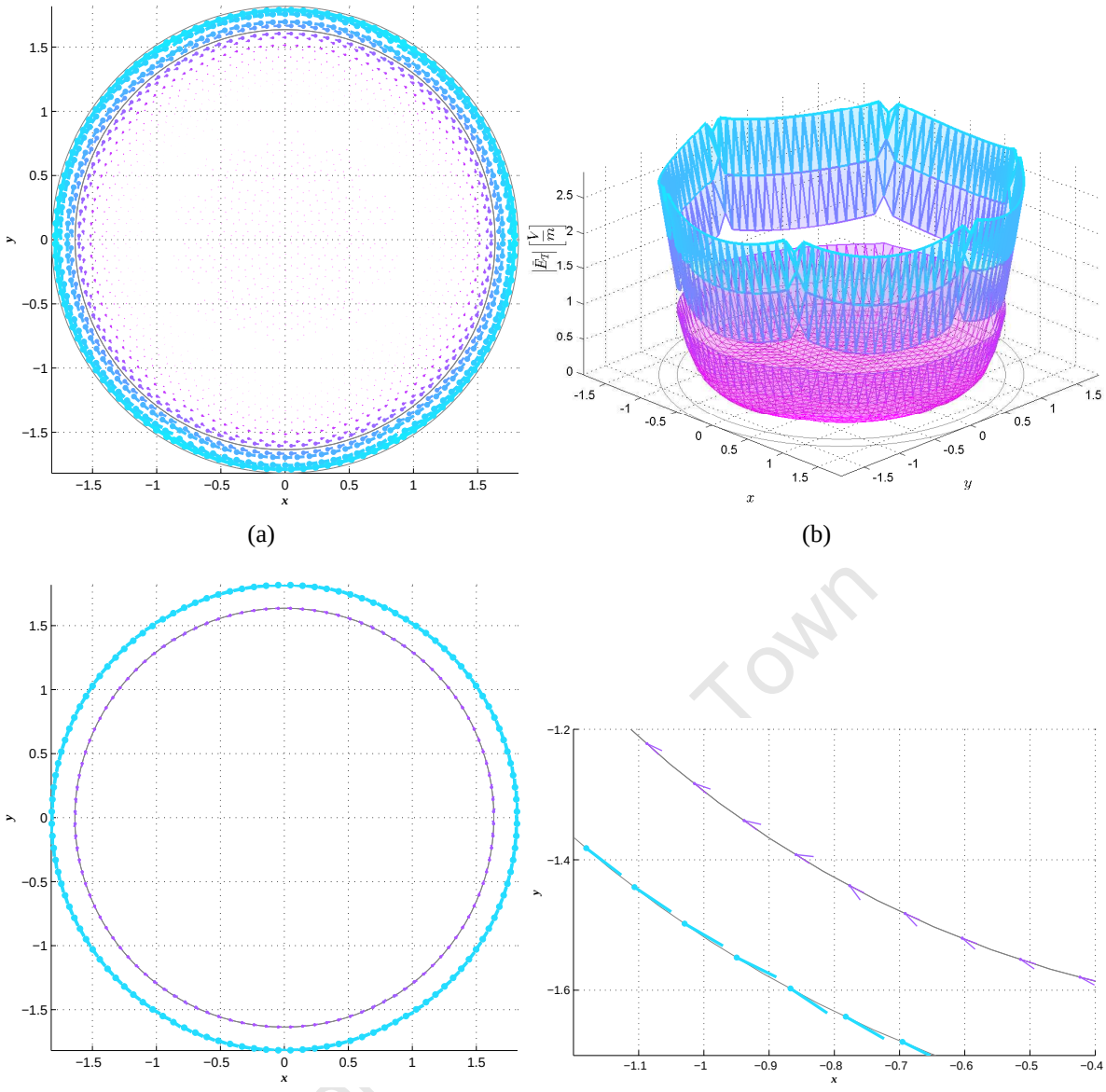

Figure 8.20: Solution Vector Field $\vec{E}_T$ Simulated at a frequency of $f = 5\text{Hz}$

Sub-figure 8.20a, illustrates the electric field $\vec{E}_E$, that would be induced in the region $0 \leq r \leq SC_R$ at a frequency value of $f = 5\text{Hz}$, the region $AS_r \leq r \leq AS_R$ contains the source electric field $\vec{E}_S$. Sub-figure 8.20b illustrates in the form of a meshed graph: $\left|\vec{E}_E\right|$(the magnitude of the vector field $\vec{E}_E$), across the region of $0 \leq r \leq SC_R$ of the domain and $\left|\vec{E}_S\right|$ (the magnitude of the vector field $\vec{E}_S$) across the region $AS_r \leq r \leq AS_R$ of the domain. In sub-figure 8.20b, $\left|\vec{E}_E\right|$ across the region $0 \leq r \leq SC_R$ suggests an attenuation of $\vec{E}_E$, over this same region. The moderate attenuation behaviour of $\left|\vec{E}_E\right|$ across the region $0 \leq r \leq SC_R$, verifies that $\vec{E}_E$ penetrates moderately into the conductor at this frequency. Sub-figure 8.20c, shows the vectors of $\vec{E}_T$ located on the material interface. To view the behaviour of these vectors better, a region of this figure was enlarged which is shown in sub-figure 8.20d. Sub-figure 8.20d, clearly illustrates the discontinuous behaviour of $\vec{E}_T$ across the material interface located at the position $r = SC_R = AS_r$ and this discontinuity of $\vec{E}_T$ is verified by the "gap" found between different material regions of the meshed graph as seen in sub-figure 8.20b.

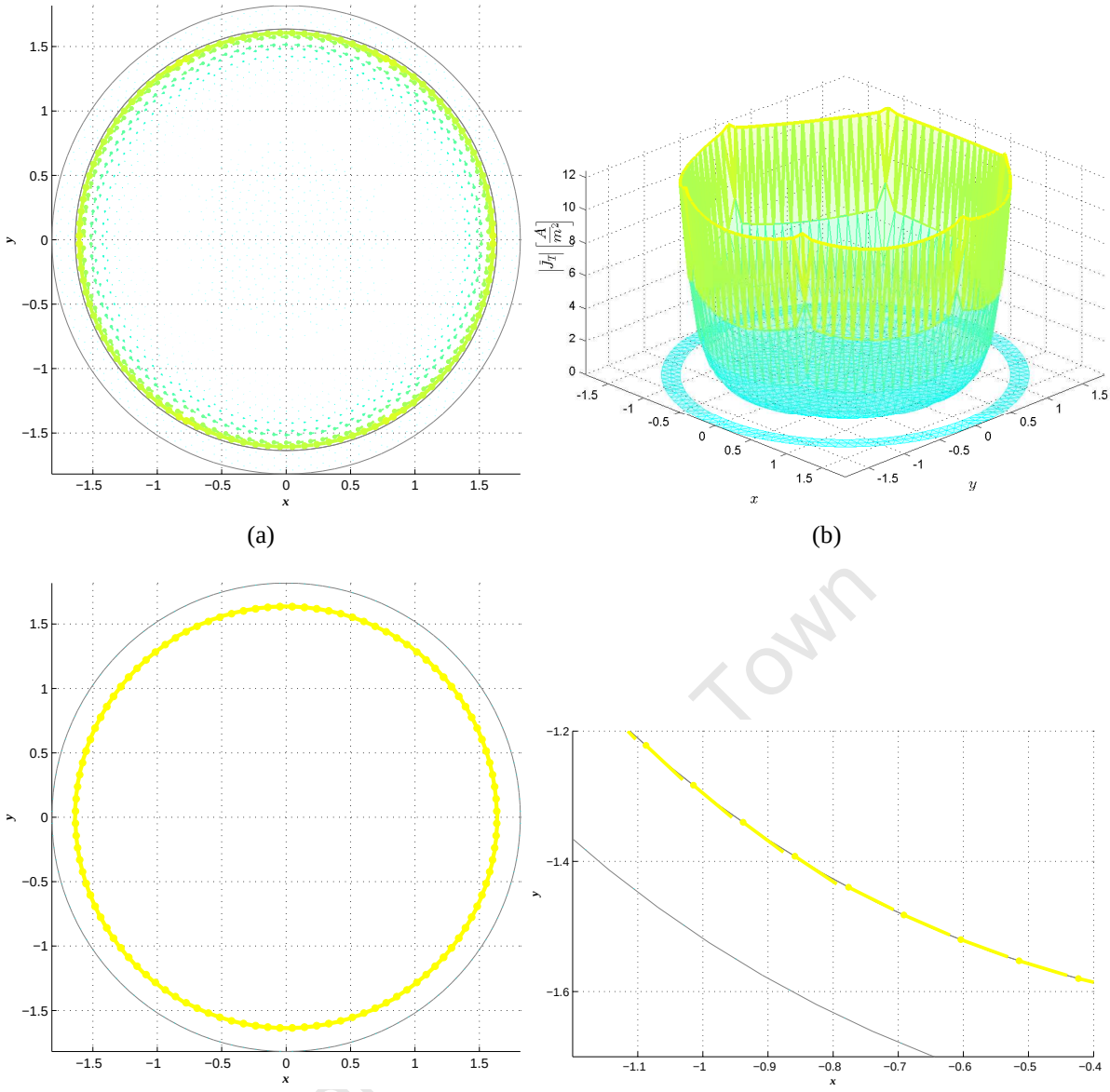

Figure 8.21: Solution Vector Field $\vec{J_T}$ Simulated at a frequency of $f = 5\text{Hz}$

Sub-figure 8.21a, illustrates the electric current density/eddy currents $\vec{J_E}$, that would be induced in the region $0 \leq r \leq SC_R$ at a frequency value of $f = 5\text{Hz}$ and there are no $\vec{J_S}$ present in the air space region $AS_r \leq r \leq AS_R$, since air cannot conduct current density [8, 5, 10]. Sub-figure 8.21b illustrates in the form of a meshed graph: $\left|\vec{J_E}\right|$(the magnitude of the vector field $\vec{J_E}$), across the region of $0 \leq r \leq SC_R$ and $\left|\vec{J_S}\right| = 0$ across the region $0 \leq r \leq SC_R$. In sub-figure 8.21b $\left|\vec{J_E}\right|$ across the region $HC_r \leq r \leq HC_R$ suggests an attenuation of $\vec{J_E}$ over this same region and in the region $AS_r \leq r \leq AS_R$, $\left|\vec{J_E}\right| = 0$ demonstrating that no $\vec{J_E}$ is present over this same region. In the region $AS_r \leq r \leq AS_R$. The moderate attenuation behaviour of $\left|\vec{J_E}\right|$ across the region $0 \leq r \leq SC_R$, verifies that $\vec{J_E}$ has penetrated moderately into the conductor at this frequency. Sub-figure 8.21c, shows the vectors of $\vec{J_T}$ located on the material interface located at the position $r = SC_R = AS_r$. To view the behaviour of these vectors better, a region of this figure was enlarged which is shown in sub-figure 8.21d. In sub-figure 8.21d, only the vector field $\vec{J_E}$ (belonging to the conductor regions of the domain) is present on the material interface because $\vec{J_S}$ cannot exists in the air space region of the domain [8, 5, 10].

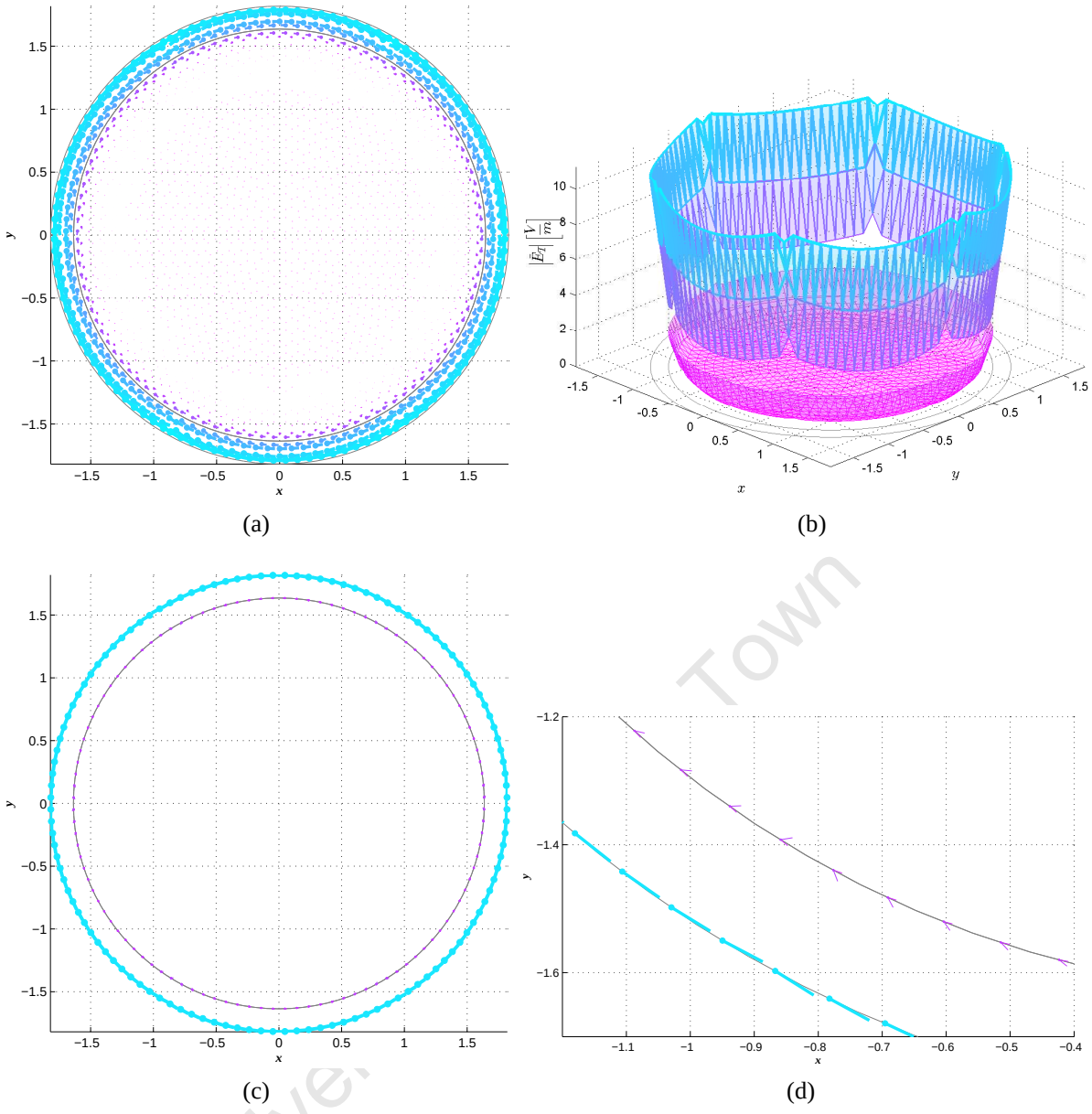

Figure 8.22: Solution Vector Field $\vec{E}_T$ Simulated at a frequency of $f = 20$Hz

Sub-figure 8.22a, illustrates the electric field $\vec{E}_E$, that would be induced in the region $0 \leq r \leq SC_R$ at a frequency value of $f = 20$Hz, the region $AS_r \leq r \leq AS_R$ contains the source electric field $\vec{E}_S$. Sub-figure 8.22b illustrates in the form of a meshed graph: $\left|\vec{E}_E\right|$(the magnitude of the vector field $\vec{E}_E$), across the region of $0 \leq r \leq SC_R$ of the domain and $\left|\vec{E}_S\right|$ (the magnitude of the vector field $\vec{E}_S$) across the region $AS_r \leq r \leq AS_R$ of the domain. In sub-figure 8.22b, $\left|\vec{E}_E\right|$ across the region $0 \leq r \leq SC_R$ suggests an attenuation of $\vec{E}_E$, over this same region. The sharp attenuation behaviour of $\left|\vec{E}_E\right|$ across the region $0 \leq r \leq SC_R$, verifies that $\vec{E}_E$ penetrates only slightly into the conductor at this frequency. Sub-figure 8.22c, shows the vectors of $\vec{E}_T$ located on the material interface. To view the behaviour of these vectors better, a region of this figure was enlarged which is shown in sub-figure 8.22d. Sub-figure 8.22d, clearly illustrates the discontinuous behaviour of $\vec{E}_T$ across the material interface located at the position $r = SC_R = AS_r$ and this discontinuity of $\vec{E}_T$ is verified by the "gap" found between different material regions of the meshed graph as seen in sub-figure 8.22b.

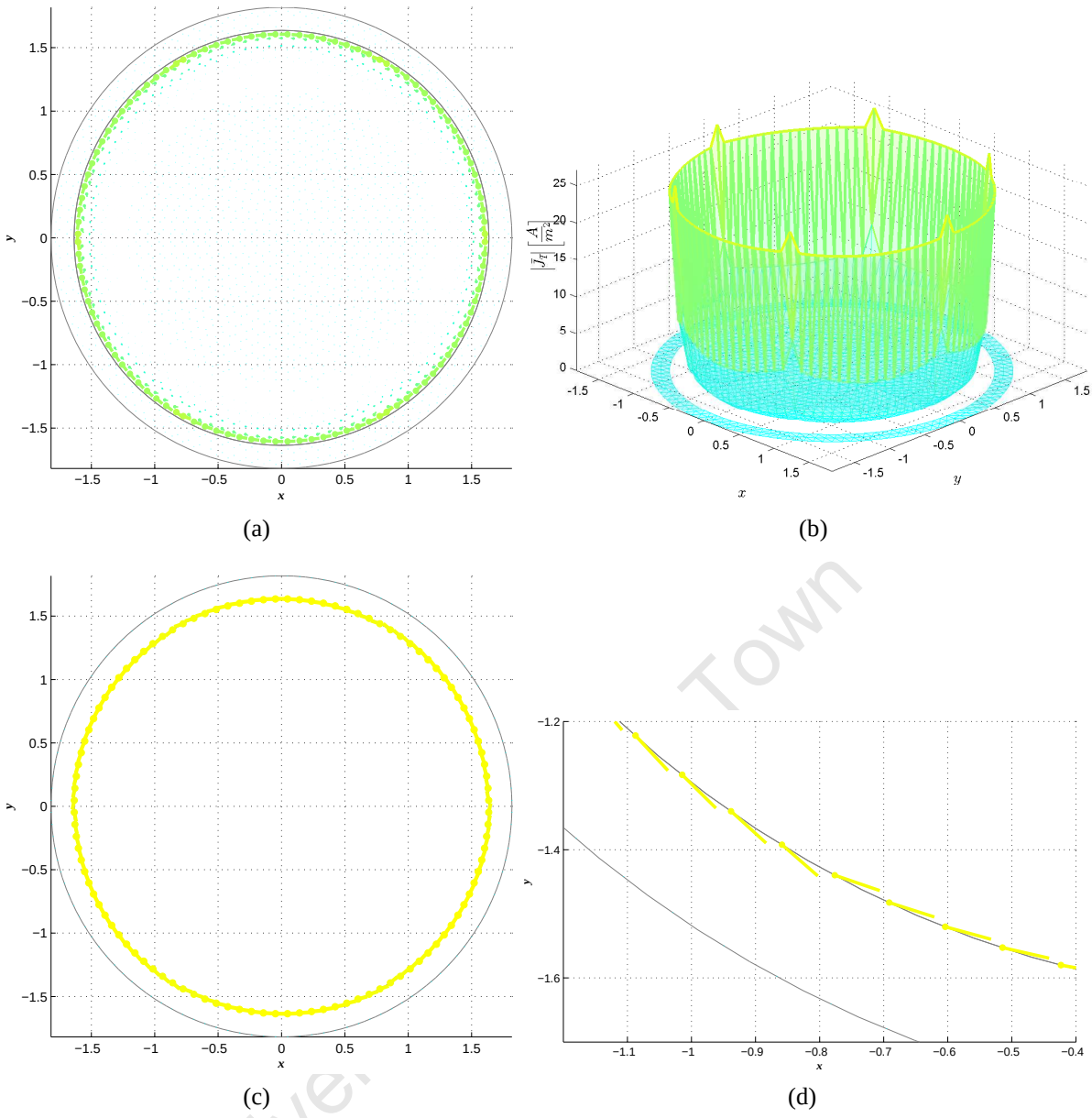

Figure 8.23: Solution Vector Field $\vec{J_T}$ Simulated at a frequency of $f = 20$Hz

Sub-figure 8.23a, illustrates the electric current density/eddy currents $\vec{J_E}$, that would be induced in the region $0 \leq r \leq SC_R$ at a frequency value of $f = 20$Hz and there are no $\vec{J_S}$ present in the air space region $AS_r \leq r \leq AS_R$, since air cannot conduct current density [8, 5, 10]. Sub-figure 8.23b illustrates in the form of a meshed graph: $\left|\vec{J_E}\right|$ (the magnitude of the vector field $\vec{J_E}$), across the region of $0 \leq r \leq SC_R$ and $\left|\vec{J_S}\right| = 0$ across the region $0 \leq r \leq SC_R$. In sub-figure 8.23b $\left|\vec{J_E}\right|$ across the region $HC_r \leq r \leq HC_R$ suggests an attenuation of $\vec{J_E}$ over this same region and in the region $AS_r \leq r \leq AS_R$, $\left|\vec{J_E}\right| = 0$ demonstrating that no $\vec{J_E}$ is present over this same region. In the region $AS_r \leq r \leq AS_R$. The sharp attenuation behaviour of $\left|\vec{J_E}\right|$ across the region $0 \leq r \leq SC_R$, verifies that $\vec{J_E}$ has penetrated only slightly into the conductor at this frequency. Sub-figure 8.23c, shows the vectors of $\vec{J_T}$ located on the material interface located at the position $r = SC_R = AS_r$. To view the behaviour of these vectors better, a region of this figure was enlarged which is shown in sub-figure 8.23d. In sub-figure 8.23d, only the vector field $\vec{J_E}$ (belonging to the conductor regions of the domain) is present on the material interface because $\vec{J_S}$ cannot exists in the air space region of the domain [8, 5, 10].

8.3.2.2 Observations of FE Generated Solutions

The following observations were made concerning all the FEM simulations of sub-section 8.3.2.1:

1. In sub-figures 8.16a, 8.18a, 8.20a,8.22a and sub-figures 8.17a, 8.19a, 8.21a,8.23a, no wave propagation can be observed across the solid cylinder region of $0 \leq r \leq$

SC_R.

2. The solution vector fields $\vec{E}_E$ and $\vec{J}_E$ across the solid conductor region of $0 \leq r \leq SC_R$ are polarised in the $\hat{\theta} - direction$ which is perpendicular to the direction of "travel" of these vector fields ($\vec{E}_E$ and $\vec{J}_E$) which is in the $\hat{r} - direction$ [10, 9] as shown in sub-figures 8.16a, 8.18a, 8.20a, 8.22a and sub-figures 8.17a, 8.19a, 8.21a, 8.23a.

3. In sub-figures 8.16a, 8.18a, 8.20a, 8.22a and sub-figures 8.17a, 8.19a, 8.21a, 8.23a the following was observed concerning the behaviour of $\vec{E}_E$ and $\vec{J}_E$ in relation to the radius r, of the domain:

   (a) With an increase in frequency f, the vector fields $\vec{E}_E$ and $\vec{J}_E$ appear to penetrate less into the solid conductor region of $0 \leq r \leq SC_R$.

4. *The meshed graphs of sub-figures 8.16b, 8.18b, 8.20b, 8.22b and sub-figures 8.17b, 8.19b, 8.21b, 8.23b seem to expose certain physical behaviour patterns of the vector fields $\vec{E}_E$ and $\vec{J}_E$ across the domain, more clearly that the vector fields of sub-figures 8.16a, 8.18a, 8.20a, 8.22a and sub-figures 8.17a, 8.19a, 8.21a, 8.23a.* The following was observed concerning the behaviour of $\left|\vec{E}_E\right|$ and $\left|\vec{J}_E\right|$ with relation to the radius r, of the domain:

   (a) Across the solid conductor region located at position $0 \leq r \leq SC_R$ of the domain, $\left|\vec{E}_E\right|$ and $\left|\vec{J}_E\right|$decays rapidly along the radial axis from position $r = SC_R$, towards the centre of the domain located at $r = 0$.
   (b) The decay of $\left|\vec{E}_E\right|$ and $\left|\vec{J}_E\right|$ across the solid conductor region $0 \leq r \leq SC_R$ becomes sharper as the frequency f, is increased.

5. In sub-figures 8.16a, 8.18a, 8.20a, 8.22a and sub-figures 8.17a, 8.19a, 8.21a, 8.23a the following was observed concerning the behaviour of $\vec{E}_S$ and $\vec{J}_S$ in relation to the radius r, of the domain:

   (a) Across the air space region located at $AS_r \leq r \leq AS_R$, $\vec{E}_S$ seems to decrease in strength and the vector field $\vec{J}_S$, across this same region does not exist.

6. In sub-figures 8.16b, 8.18b, 8.20b, 8.22b and sub-figures 8.17b, 8.19b, 8.21b, 8.23b, the following was observed concerning the behaviour of $\left|\vec{E}_S\right|$ and $\left|\vec{J}_S\right|$ in relation to the radius r, of the domain:

   (a) Across the air space region located at $AS_r \leq r \leq AS_R$, $\left|\vec{E}_S\right|$ decreases linearly and $\left|\vec{J}_S\right|$ does not exist.
   (b) $\left|\vec{E}_S\right|$ and $\left|\vec{J}_S\right|$ increases as the value of the frequency f, is set higher.

7. In sub-figures 8.16d, 8.18d, 8.20d and 8.22d the following was observed concerning the behaviour of $\vec{E}_T$, on the material interface located at position $r = SC_R = AS_r$ (refer to figure 8.14b):

   (a) The vector field $\vec{E}_T$, has two vectors originating from the same coordinate point located on the material interface.

8.3.2.3 Analysis of FE Generated Solutions

Previous research knowledge of Section 3.1 and sub-sections 8.2.3, 8.3.1.3 indicated that the vector fields solutions of $\vec{E}_E$ and $\vec{J}_E$ would attenuate across the solid conductor region $0 \leq r \leq SC_R$. Such a behaviour pattern of the vector fields solutions is expected because all the examples investigated in Sections 3.1, 8.2 and sub-section 8.3.1 and including this example was solved using the *same PDE given by Equation* (2.39), which governs the physical behaviour of eddy currents within a conductor and therefore there should be *some similarity in the physical behaviour of the vector field solutions* across their respective domains, although each example contained different BC's and geometry configurations.

The following analysis of the FE simulations has been made according to the observations found in sub-section 8.3.2.2:

1. The wavelengths λ, of the simulated solutions are probably too large for the dimension of the solid cylinder located at position $0 \leq r \leq SC_R$ of the domain, therefore no wave pattern "appeared" to be observed within this region. Refer to section 8.3.1 where a similar analysis occurred.

2. The circular domain geometry of this eddy current configuration (as shown in sub-figure 8.14b) produced vector field solutions $\vec{E}_E$ and $\vec{J}_E$ across the solid conductor region of $0 \leq r \leq SC_R$ that are polarised in the $\hat{\theta} - direction$ and the direction of "travel" of these vector fields ($\vec{E}_E$ and $\vec{J}_E$) are in the $\hat{r} - direction$ [10, 9] as shown in sub-figures 8.16a, 8.18a, 8.20a, 8.22a and sub-figures 8.17a, 8.19a, 8.21a, 8.23a.

3. According to sub-figures 8.16a, 8.18a, 8.20a, 8.22a and sub-figures 8.17a, 8.19a, 8.21a, 8.23a the following analysis is made concerning the behaviour of $\vec{E}_E$ and $\vec{J}_E$ in relation to the radius r, of the domain:

   (a) The attenuation of the vector fields $\vec{E}_E$ and $\vec{J}_E$ becomes stronger with an increase in frequency f, along the radial axis of the domain from position $r = SC_R$, towards the centre of the domain located at $r = 0$, thus the stronger the attenuation, the less the electric field $\vec{E}_E$ penetrates into the conducting body. As the frequency is increased the electric field $\vec{E}_E$, becomes situated closer and closer towards the boundary of the solid cylinder located at position $r = SC_R$ of the domain as shown in sub-figures 8.16a, 8.18a, 8.20a, 8.22a. This behaviour pattern is a clear indication of skin effect phenomena (refer to sub-section 3.1.3) which is an important characteristic of eddy current problems [16, 17]. The electric field $\vec{E}_E$, causes the motion of the free electrons within the conducting body, so producing an electric current density at the positions where the electric field penetrates the conducting body [10, 9, 19, 20] as seen in sub-figures 8.17a, 8.19a, 8.21a, 8.23a. It is this current density that is referred to as eddy currents, $\vec{J}_E$ [16, 17].

4. According to sub-figures 8.16b, 8.18b, 8.20b, 8.22b and sub-figures 8.17b, 8.19b, 8.21b, 8.23b the following analysis is made concerning the behaviour of $\left|\vec{E}_E\right|$ and $\left|\vec{J}_E\right|$ in relation to the radius r, of the domain:

   (a) $\left|\vec{E}_E\right|$ and $\left|\vec{J}_E\right|$decays rapidly along the radial axis from position $r = SC_R$, towards the centre of the domain located at $r = 0$. The attenuation "seems" to resemble some type of exponential "decaying" function with relation to the $r - axis$ which begins at the boundary of $r = SC_R$ of the solid conductor.

(b) The exponential "decaying" function (attenuation of $\left|\vec{E}_E\right|$ and $\left|\vec{J}_E\right|$) along the radial axis from position $r = SC_R$, towards the centre of the domain located at $r = 0$, becomes steeper as the frequency f is increased, which is another indication of skin effect phenomena (refer to sub-section 3.1.3).

5. According to sub-figures 8.16a, 8.18a, 8.20a, 8.22a and sub-figures 8.17a, 8.19a, 8.21a, 8.23a the following analysis is made concerning the behaviour of $\vec{E}_S$ and $\vec{J}_S$ in relation to the radius r, of the domain:

   (a) $\vec{E}_S$ becomes slightly weaker in strength along the radial axis from position $r = AS_R$ towards the inner position of $r = AS_r$ on the domain and so agrees with Equation (8.9), which defines this vector field $\vec{E}_S$ across this air space region of $AS_r \leq r \leq AS_R$,.

   (b) The air space region cannot support electric current density $\vec{J}_S$ (where $\vec{J}_S = \sigma\vec{E}_S$), due to the air having a conductivity value of approximately zero, that is $\sigma \backsimeq 0$ [9, 10, 19].

6. According to sub-figures 8.16b, 8.18b, 8.20b, 8.22b and sub-figures 8.17b, 8.19b, 8.21b, 8.23b the following analysis is made concerning the behaviour of $\left|\vec{E}_S\right|$ and $\left|\vec{J}_S\right|$ in relation to the radius r, of the domain:

   (a) Across the air space region $AS_r \leq r \leq AS_R$, $\left|\vec{E}_S\right|$ decreases linearly by a factor of r with relation to the radial axis from position of $r = AS_R$ to a position of $r = AS_r$ on the domain. Thus, the behaviour of $\left|\vec{E}_S\right|$ is in agreement with Equation (8.9).

   (b) As the frequency value f is increased, there is an increase in strength of $\left|\vec{E}_S\right|$ across the region $AS_r \leq r \leq AS_R$ (which is shown by the increase in "height" of these meshed graphs). The behaviour of these graphs is in agreement with Equation (8.9) which forms the excitation force (refer to sub-section 8.3.2) across the air space region $AS_r \leq r \leq AS_R$ within the domain of this eddy current configuration.

   (c) Across the air space region $AS_r \leq r \leq AS_R$, $\left|\vec{J}_S\right| = 0$ due to the air having a conductivity value of approximately zero, that is $\sigma \backsimeq 0$ [9, 10, 19].

7. In sub-figures 8.16d, 8.18d, 8.20d, 8.22d, the following analysis is made concerning the behaviour of $\vec{E}_T$ on the material interface located at position $r = SC_R = AS_r$ (refer to figure 8.24b):

   (a) The vector field $\vec{E}_T$, is discontinuous on the material interfaces of the domain and this discontinuity is indicated by two vectors originating from the same coordinate point located on the material interface. Refer to Section 5.1.3 and sub-section 5.3.3 where a comprehensive explanation concerning vector field discontinuity across a material interface is given.

   (b) In sub-figures 8.16b, 8.18b, 8.20b and 8.22b there are visible "gaps" present within the meshed graphs of $\left|\vec{E}_T\right|$, which also emphasises the discontinuity of the vector field $\vec{E}_T$, on the material interfaces as well.

Discontinuity of the Mesh Graphs

The mesh graphs of sub-figures 8.16b, 8.18b, 8.20b and 8.22b illustrates graphically (the magnitude of the vector field $\vec{E}_T$) $\left|\vec{E}_T\right|$ across each element within the entire domain. Each element within the domain is plotted individually using the MATLAB function called `patch`.

A discontinuity of the vector field $\vec{E}_T$, exists across the material interface and the discontinuity is recognised by two vectors which originate from a single coordinate point situated on the material interface. Each of the two vectors possess different magnitude values and direction (refer to sub-section 5.3.3) and therefore, *a single coordinate point located on the material interface will possess two different magnitude values* which corresponds to each vector. It is these different magnitude values of $\left|\vec{E}_T\right|$, located on the same coordinate point (on the material interface) of the domain of the mesh graphs that creates the discontinuity, which is visible seen as a "gap" present within the mesh graphs $\left|\vec{E}_T\right|$) when the function `patch` is used.

8.3.2.4 Summary

The FE algorithm is able to model and simulate:

- the physical behaviour of the total electric vector field $\vec{E}_T$, and total electric current density/eddy currents $\vec{J}_T$, across different material regions of the overall domain $(0 \leq r \leq AS_R)$.
- the discontinuity of the vector fields $\vec{E}_T$ across different material interface.
- the attenuation behaviour of the vector fields $\vec{E}_E$ and $\vec{J}_E$ (over the conductor region, $0 \leq r \leq SC_R$) at different frequencies thereby demonstrating the skin effect phenomena, which is an important behaviour effect found in eddy current problems [19, 16, 17].

Improvements to the accuracy of the solution vector field approximations and the simulations visually could be achieved through the used of higher-order vector elements and a self-adaptive mesh refinement technique. The reader is referred to sub-section 8.3.1 where these subjects were discussed.

8.3.3 FEM Solution of a Force Driven Eddy Current Configuration

This example considers eddy currents induced in a hollow cylinder made of conducting material. A time-varying harmonic magnetic field is passed through a solid cylinder made from conducting material. as shown in sub-figure 8.24a. The magnetic field induces an electric field within *another* cylinder which is hollow and made from the same type of conducting material. This induced electric field causes eddy currents to be produced within the hollow cylinder as shown in Section 2.3. The geometry of the eddy current configuration is pictured below in sub-figure 8.24a and sub-figure8.24b illustrates the structure of the domain space of this eddy current configuration.

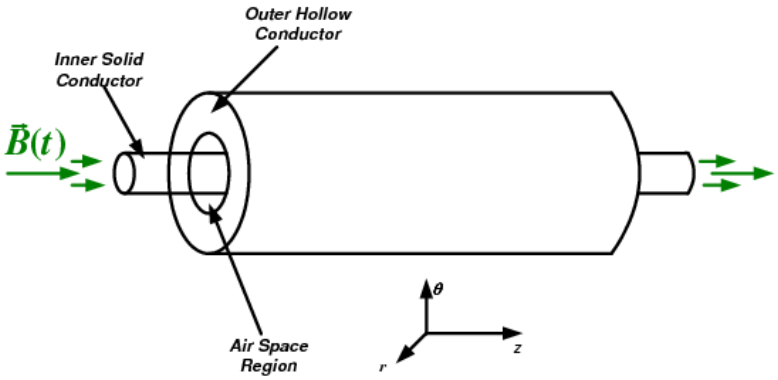

(a)

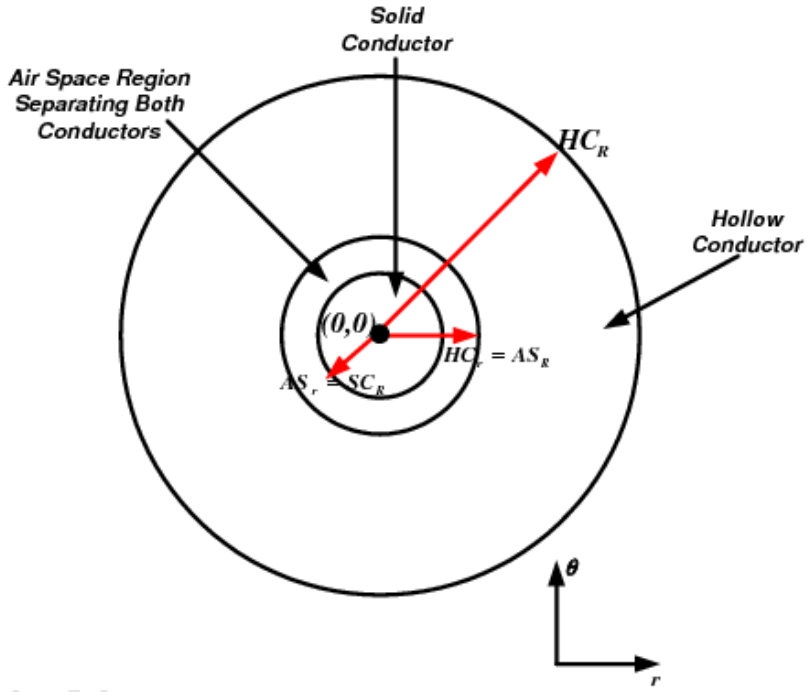

(b)

Figure 8.24: Geometry of the Problem Configuration

Sub-figure 8.24a illustrates the hollow cylinder containing the solid cylinder running through its centre. There is a small air gap located between the two cylinders and separates both cylinders. In sub-figure 8.24b, the domain consists of: a hollow conductor region, a solid conductor region and a air space region which separates the two conducting regions. HC_R-Outer radius of the hollow cylinder, HC_r-Inner radius of the hollow cylinder. AS_R-Outer radius of the air space region, AS_r-Inner radius of the air space region. SC_R-Radius of the solid cylinder, where $HC_r = AS_R$ and $AS_r = SC_R$. The polar coordinate system is used for reference due to the circular geometry of the domain.

Problem Setup

A time-varying magnetic field given by Equation (3.21) passes through the solid cylinder made from conducting material. The time-varying magnetic field is repeated here for the readers convenience:

$$\vec{B}(t) = B_0 cos(\omega t)\hat{k}$$

The geometry of the domain space of this problem can be idealised as a two-dimensional planar problem as shown in Figure 8.24b where the solution will be simulated on the $r-\theta$ plane. The dimension of the solid cylinder region is approximately $0 \leq r \leq 0.4$m, and the dimension of the air space region is approximately $0.4\text{m} \leq r \leq 0.7\text{m}$ and the dimension of the hollow conductor region is approximately $0.7\text{m} \leq r \leq 1.8\text{m}$. The magnetic field according to Faraday's Law creates a circulating/rotating electric field given by Equation (3.29) in phasor form, refer to sub-section 3.3.1. Equation (3.29) is repeated here for the readers convenience:

$$\tilde{E}_S = \frac{1}{2} j\omega B_0 \left(y\hat{i} - x\hat{j}\right)$$

and the current density of Equation (3.29) is [5, 9, 19]:

$$\tilde{J}_S = \frac{1}{2}\sigma j\omega B_0 \left(y\hat{i} - x\hat{j}\right) \tag{8.13}$$

where $\omega = 2\pi f$ in Equations (3.29) and (8.13). This rotating $\tilde{E_S}$-field given by Equation (3.29) forms the *excitation force* of this problem, as discussed in sub-sections 2.6, 3.2 and 7.4.1.2, and is specified on the entire region of the solid cylinder $(0 \leq r \leq SC_R)$. The solid cylinder is located inside another cylinder located at position $(HC_r \leq r \leq HC_R)$ of the domain, this cylinder is hollow and made from the same conducting material as the solid cylinder. The two cylinders are separated by an air gap region $(AS_r \leq r \leq AS_R)$. *The rotating $\tilde{E_S}$-field given by Equation* (3.29) *causes an electric vector field $\vec{E}_E$ to be produced within this hollow cylinder and the air gap*. The presence of the this electric vector field $\vec{E}_E$ within the hollow conductor causes an electric current density/eddy currents $\vec{J}_E$ to be produced [19]. The electric current density/eddy currents $\vec{J}_E$ produced within the hollow cylinder is the result of the response of the system to the excitation force given by Equation (3.29) (refer to Section 3.2 and sub-section 7.4.1.2). The problem is referred to as force-driven due to the presence of an excitation force as discussed in Section 2.6. Figure 8.25 shows the FE mesh of the problem.

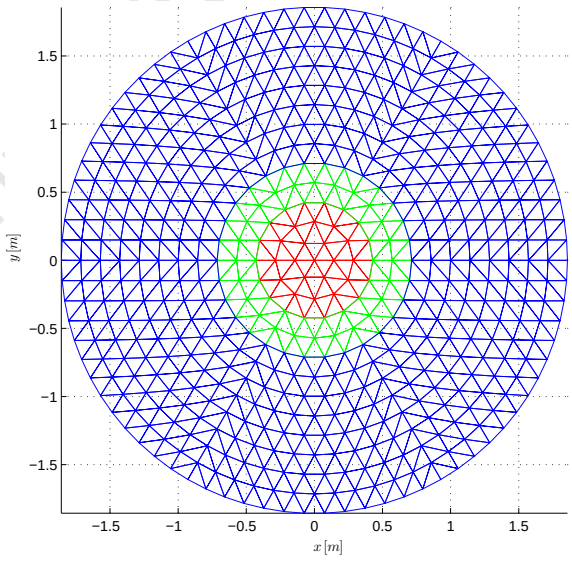

Figure 8.25: Finite Element Mesh of the Domain

The mesh consists of approximately 1014 triangular elements. The domain consists of three material types, an air space region and two conductor regions. The three material regions are indicated by the different colours of the mesh: RED-solid conductor region. GREEN-air space region. BLUE-hollow conductor region.

The FE algorithm (as shown in Step 9 and 10 of Section 7.7) collects the computed vector components *of each FE in the domain* and so will display a *total vector field solution* over

the entire domain of $(0 \leq r \leq HC_R)$ Thus, the total/overall electric vector field solution can be expressed as:

$$\vec{E_T} = \vec{E}_E + \vec{E}_S \tag{8.14}$$

which consisting of $\vec{E}_E$ over the regions $(AS_r \leq r \leq AS_R)$ and $(HC_r \leq r \leq HC_R)$ and $\vec{E}_S$ over the region $(0 \leq r < SC_R)$. Similarly, the total/overall current density vector field solution can be expressed as:

$$\vec{J_T} = \vec{J_E} + \vec{J_S} \tag{8.15}$$

which consisting of $\vec{J_E}$ over the region $(HC_r \leq r \leq HC_R)$ and $\vec{J_S}$ over the region $(0 \leq r < SC_R)$. Whether the eddy current configuration is boundary-driven or force-driven, BC's need to be specified on the domain of the problem so that the FEM will be able to solve the linear system of equations given by Equation (6.57), as shown in sub-section 7.4.1. Due to the behaviour of skin depth phenomena of conducting bodies as seen in sub-section 3.1.4 of section 3.2, it can accurately be assumed that the electric field solution $\vec{E}_E$, produced cannot reach or penetrate the boundary of the outer hollow cylinder located at position of $r = HC_R$, therefore all edges located on the boundary, $r = HC_R$ has its values set equal to zero as shown in Equation (8.16). The edge values are set to zero on the boundary of $r = HC_R$, that is the BC for this problem configuration is as follows:

$$Edges\,|_{HC_R} = 0 \tag{8.16}$$

where $HC_R = 1.8$m as can be seen in Figure (8.25).

8.3.3.1 FEM Simulated Solutions

The FE algorithm was used to generate vector field solutions to the eddy current configuration of sub-section 8.3.3. The FE solutions were simulated at: a permittivity value of $\mu = 0.25\left[\frac{\mathrm{H}}{\mathrm{m}}\right]$ across the conductor regions; a permittivity value of $\mu = \mu_0\mu_r = \left(4\pi \times 10^{-7}\right)(1.00000037) \simeq \left(4\pi \times 10^{-7}\right)(1) = 4\pi \times 10^{-7}\left[\frac{\mathrm{H}}{\mathrm{m}}\right]$ across the air space region; time of $t = 0$s; a single conductivity value of $\sigma = 4\pi \backsimeq 12.566$ $[\frac{S}{m}]$ across the conductor regions; a single conductivity value of $\sigma \backsimeq 1 \times 10^{-4}$ $[\frac{S}{m}]$ across the air space region; but at varying frequency values of $f = 0.5$Hz, $f = 1$Hz, $f = 5$Hz, $f = 20$Hz and $f = 50$Hz, in order to illustrate the concept of skin effect behaviour [16, 17]. The computational time of the FE algorithm for this problem is 9.99s.

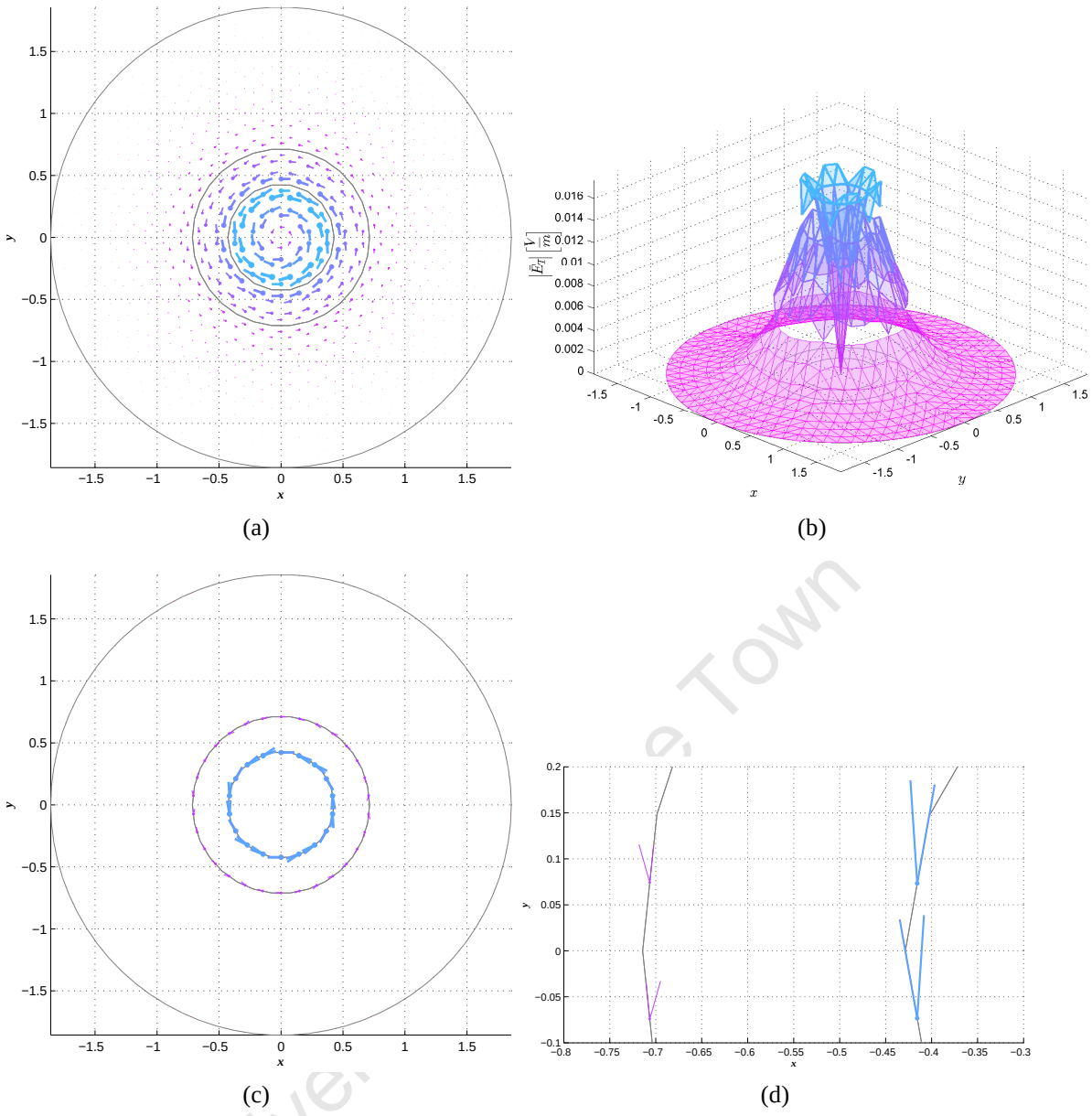

Figure 8.26: Solution Vector Field $\vec{E}_T$ Simulated at a frequency of $f = 0.5$Hz

Sub-figure 8.26a, illustrates the electric field $\vec{E}_E$, that would be induced in the regions $HC_r \leq r \leq HC_R$ and $AS_r \leq r \leq AS_R$ at a frequency value of $f = 0.5$Hz, the region $0 \leq r \leq SC_R$ contains the source electric field $\vec{E}_S$. Sub-figure 8.26b illustrates in the form of a meshed graph: $\left|\vec{E}_E\right|$ (the magnitude of the vector field $\vec{E}_E$), across the regions of $HC_r \leq r \leq HC_R$ and $AS_r \leq r \leq AS_R$ of the domain and $\left|\vec{E}_S\right|$ (the magnitude of the vector field $\vec{E}_S$) across the region $0 \leq r \leq SC_R$ of the domain. In sub-figure 8.26b, $\left|\vec{E}_E\right|$ across the region $HC_r \leq r \leq HC_R$ suggests an attenuation of $\vec{E}_E$, over this same region and $\left|\vec{E}_E\right|$ across the region $AS_r \leq r \leq AS_R$, demonstrates that $\vec{E}_E$ decreases over this same region. In the region $0 \leq r \leq SC_R$, $\left|\vec{E}_S\right|$ demonstrates that $\vec{E}_S$ increases linearly over this region and at the boundary of $r = SC_R$ $\left|\vec{E}_S\right|$ is at its "highest" value indicating that at this position of the domain $\vec{E}_S$ is at its strongest intensity. The weak attenuation behaviour of $\left|\vec{E}_E\right|$ across the region $HC_r \leq r \leq HC_R$, verifies that $\vec{E}_E$ penetrates deeply into the hollow conductor at this frequency. Sub-figure 8.26c, shows the vectors of $\vec{E}_T$ located on the material interface. To view the behaviour of these vectors better, a region of this figure was enlarged which is shown in sub-figure 8.26d. Sub-figure 8.26d, clearly illustrates the discontinuous behaviour of $\vec{E}_T$ across a material interface and this discontinuity of $\vec{E}_T$ is verified by the "gap" found between different material regions of the meshed graph as seen in sub-figure 8.26b.

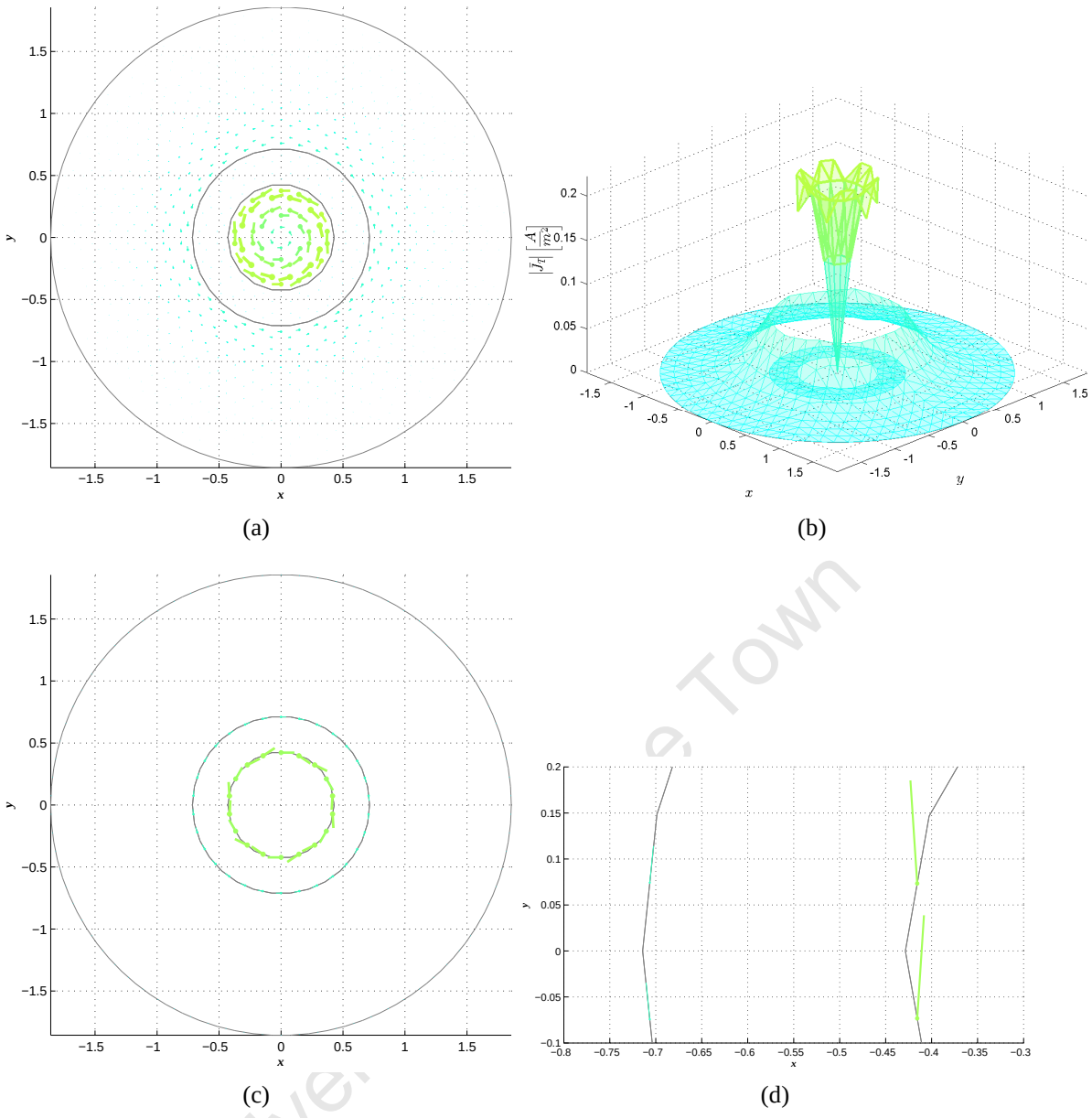

Figure 8.27: Solution Vector Field $\vec{J_T}$ Simulated at a frequency of $f = 0.5$Hz

Sub-figure 8.27a, illustrates the electric current density/eddy currents $\vec{J_E}$, that would be induced in the region $HC_r \leq r \leq HC_R$ at a frequency value of $f = 0.5$Hz, the region $0 \leq r \leq SC_R$ contains the source current density $\vec{J_S}$, and there are no $\vec{J_E}$ present in the air space region ($AS_r \leq r \leq AS_R$), since air cannot conduct current density [8, 5, 10]. Sub-figure 8.27b illustrates in the form of a meshed graph: $\left|\vec{J_E}\right|$(the magnitude of the vector field $\vec{J_E}$), across the region of $HC_r \leq r \leq HC_R$ and $\left|\vec{J_S}\right|$ (the magnitude of the vector field $\vec{J_S}$), across the region $0 \leq r \leq SC_R$. In sub-figure 8.27b $\left|\vec{J_E}\right|$ across the region $HC_r \leq r \leq HC_R$ suggests an attenuation of $\vec{J_E}$ over this same region and in the region $AS_r \leq r \leq AS_R$, $\left|\vec{J_E}\right| = 0$ demonstrating that no $\vec{J_E}$ is present over this same region. In the region $0 \leq r \leq SC_R$, $\left|\vec{J_S}\right|$ demonstrates that $\vec{J_S}$ increases linearly and at the boundary of $r = SC_R$ $\left|\vec{J_S}\right|$ is at its "highest" value indicating that at this position of the domain $\vec{J_S}$ is at its strongest intensity. The weak attenuation behaviour of $\left|\vec{J_E}\right|$ across the region $HC_r \leq r \leq HC_R$, verifies that $\vec{J_E}$ has penetrated deeply into the hollow conductor at this frequency. Sub-figure 8.27c, shows the vectors of $\vec{J_T}$ located on the material interface boundaries located at positions $r = SC_R = AS_r$ and $r = AS_R = HC_r$. To view the behaviour of these vectors better, a region of this figure was enlarged which is shown in sub-figure 8.27d. In sub-figure 8.27d, only the vector fields $\vec{J_E}$ and $\vec{J_S}$ (belonging to the conductor regions of the domain) is present on the material interface boundaries because $\vec{J_E}$ cannot exists in the air space region of the domain [8, 5, 10].

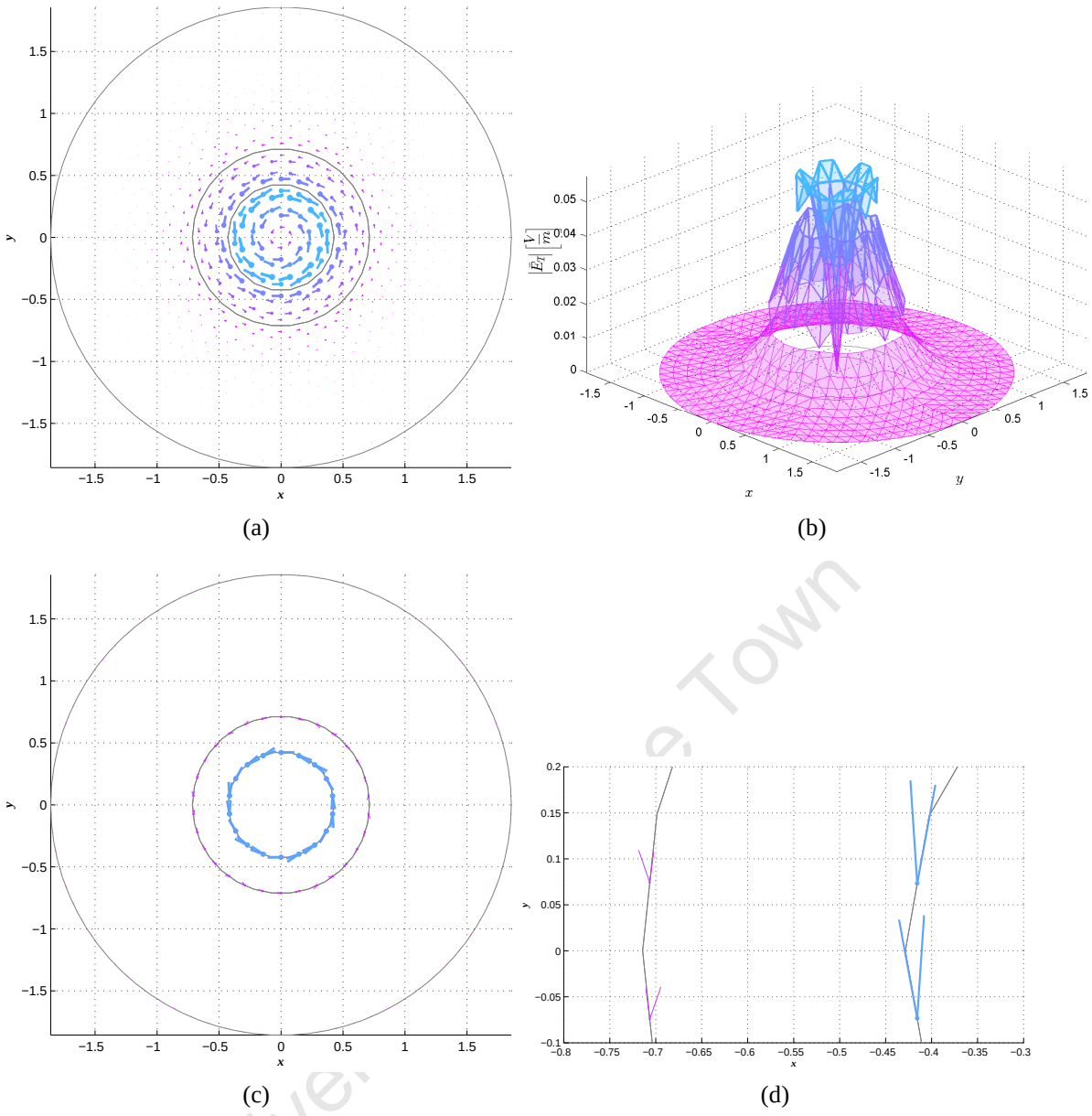

Figure 8.28: Solution Vector Field $\vec{E}_T$ Simulated at a frequency of $f = 1\text{Hz}$

Sub-figure 8.28a, illustrates the electric field $\vec{E}_E$, that would be induced in the regions $HC_r \leq r \leq HC_R$ and $AS_r \leq r \leq AS_R$ at a frequency value of $f = 1\text{Hz}$, the region $0 \leq r \leq SC_R$ contains the source electric field $\vec{E}_S$. Sub-figure 8.28b illustrates in the form of a meshed graph: $\left|\vec{E}_E\right|$ (the magnitude of the vector field $\vec{E}_E$), across the regions of $HC_r \leq r \leq HC_R$ and $AS_r \leq r \leq AS_R$ of the domain and $\left|\vec{E}_S\right|$ (the magnitude of the vector field $\vec{E}_S$) across the region $0 \leq r \leq SC_R$ of the domain. In sub-figure 8.28b $\left|\vec{E}_E\right|$ across the region $HC_r \leq r \leq HC_R$ suggests an attenuation of $\vec{E}_E$ over this same region and across the region $AS_r \leq r \leq AS_R$, $\left|\vec{E}_E\right|$ demonstrates that $\vec{E}_E$ decreases over this same region. In the region $0 \leq r \leq SC_R$, $\left|\vec{E}_S\right|$ demonstrates that $\vec{E}_E$ increases linearly and at the boundary of $r = SC_R$ $\left|\vec{E}_S\right|$ is at its "highest" value indicating that at this position of the domain $\vec{E}_S$ is at its strongest intensity. The weak attenuation behaviour of $\left|\vec{E}_E\right|$ across the region $HC_r \leq r \leq HC_R$, verifies that $\vec{E}_E$ has penetrated deeply into the hollow conductor at this frequency. Sub-figure 8.28c, shows the vectors of $\vec{E}_T$ located on the material interface. To view the behaviour of these vectors better, a region of this figure was enlarged which is shown in sub-figure 8.28d. Sub-figure 8.28d, clearly illustrates the discontinuous behaviour of $\vec{E}_T$ across a material interface and this discontinuity of $\vec{E}_T$ is verified by the "gap" found between different material regions of the meshed graph as seen in sub-figure 8.28b.

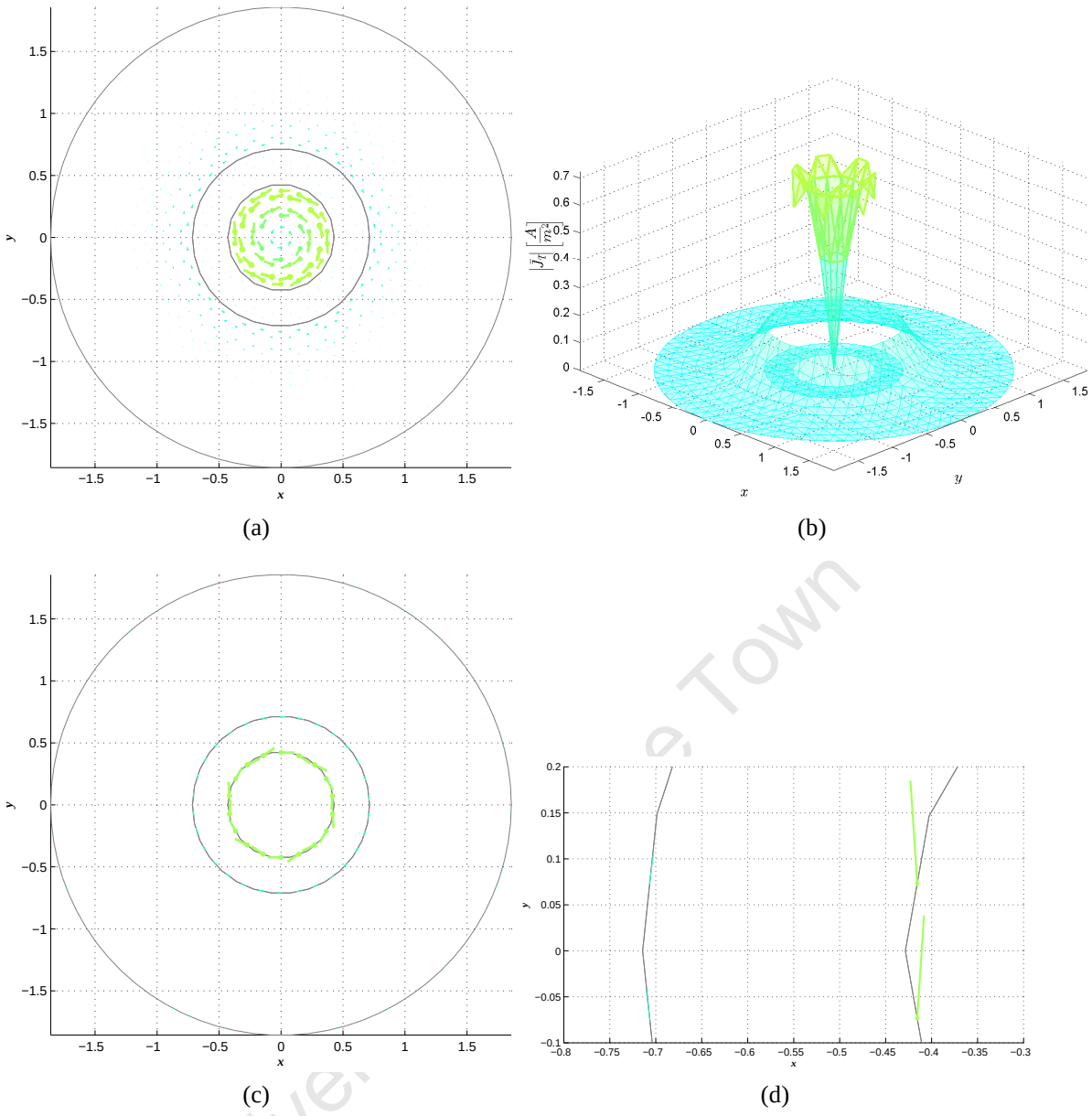

Figure 8.29: Solution Vector Field $\vec{J}_T$ Simulated at a frequency of $f = 1\text{Hz}$

Sub-figure 8.29a, illustrates the electric current density/eddy currents $\vec{J}_E$, that would be induced in the region $HC_r \leq r \leq HC_R$ at a frequency value of $f = 1\text{Hz}$, the region $0 \leq r \leq SC_R$ contains the source current density $\vec{J}_S$ and there are no $\vec{J}_E$ present in the air space region ($AS_r \leq r \leq AS_R$), since air cannot conduct current density [8, 5, 10]. Sub-figure 8.29b illustrates in the form of a meshed graph: $\left|\vec{J}_E\right|$(the magnitude of the vector field $\vec{J}_E$), across the region of $HC_r \leq r \leq HC_R$ and $\left|\vec{J}_S\right|$ (the magnitude of the vector field $\vec{J}_S$), across the region $0 \leq r \leq SC_R$. In sub-figure 8.29b $\left|\vec{J}_E\right|$ across the region $HC_r \leq r \leq HC_R$ suggests an attenuation of $\vec{J}_E$ over this same region and in the region $AS_r \leq r \leq AS_R$, $\left|\vec{J}_E\right| = 0$, demonstrating that no $\vec{J}_E$ is present over this same region. In the region $0 \leq r \leq SC_R$, $\left|\vec{J}_S\right|$ demonstrates that $\vec{J}_S$ increases linearly and at the boundary of $r = SC_R$ $\left|\vec{J}_S\right|$ is at its "highest" value indicating that at this position of the domain $\vec{J}_S$ is at its strongest intensity. The weak attenuation behaviour of $\left|\vec{J}_E\right|$ across the region $HC_r \leq r \leq HC_R$, verifies that $\vec{J}_E$ has penetrated deeply into the hollow conductor at this frequency.Sub-figure 8.29c, shows the vectors of $\vec{J}_T$ located on the material interface boundaries located at positions $r = SC_R = AS_r$ and $r = AS_R = HC_r$. To view the behaviour of these vectors better, a region of this figure was enlarged which is shown in sub-figure 8.29d. In sub-figure 8.29d, only the vector fields $\vec{J}_E$ and $\vec{J}_S$ (belonging to the conductor regions of the domain) is present on the material interface boundaries because $\vec{J}_E$ cannot exists in the air space region of the domain [8, 5, 10].

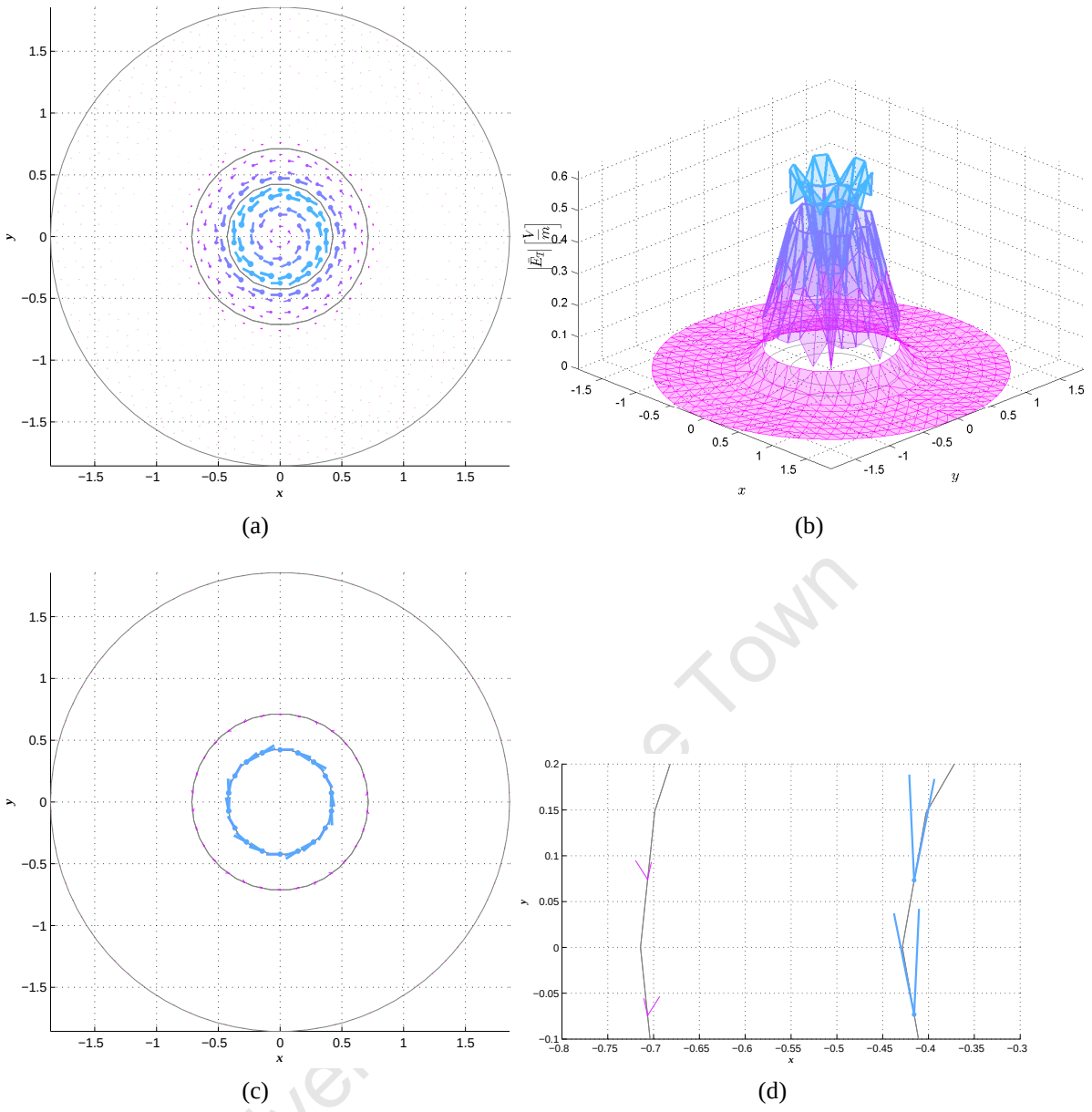

Figure 8.30: Solution Vector Field $\vec{E}_T$ Simulated at a frequency of $f = 5\text{Hz}$

Sub-figure 8.30a, illustrates the electric field $\vec{E}_E$, that would be induced in the regions $HC_r \leq r \leq HC_R$ and $AS_r \leq r \leq AS_R$ at a frequency value of $f = 5\text{Hz}$, the region $0 \leq r \leq SC_R$ contains the source electric field $\vec{E}_S$. Sub-figure 8.30b illustrates in the form of a meshed graph: $\left|\vec{E}_E\right|$ (the magnitude of the vector field $\vec{E}_E$), across the regions of $HC_r \leq r \leq HC_R$ and $AS_r \leq r \leq AS_R$ of the domain and $\left|\vec{E}_S\right|$ (the magnitude of the vector field $\vec{E}_S$) across the region $0 \leq r \leq SC_R$ of the domain. In sub-figure 8.30b $\left|\vec{E}_E\right|$ across the region $HC_r \leq r \leq HC_R$ suggests an attenuation of $\vec{E}_E$ over this same region and across the region $AS_r \leq r \leq AS_R$, $\left|\vec{E}_E\right|$ demonstrates that $\vec{E}_E$ decreases linearly over this same region. In the region $0 \leq r \leq SC_R$, $\left|\vec{E}_S\right|$ demonstrates that $\vec{E}_E$ increases linearly and at the boundary of $r = SC_R$ $\left|\vec{E}_S\right|$ is at its "highest" value indicating that at this position of the domain $\vec{E}_S$ is at its strongest intensity. The moderate attenuation behaviour of $\left|\vec{E}_E\right|$ across the region $HC_r \leq r \leq HC_R$, verifies that $\vec{E}_E$ has penetrated moderately into the hollow conductor at this frequency. Sub-figure 8.30c, shows the vectors of $\vec{E}_T$ located on the material interface. To view the behaviour of these vectors better, a region of this figure was enlarged which is shown in sub-figure 8.30d. Sub-figure 8.30d, clearly illustrates the discontinuous behaviour of $\vec{E}_T$ across a material interface and this discontinuity of $\vec{E}_T$ is verified by the "gap" found between different material regions of the meshed graph as seen in sub-figure 8.30b.

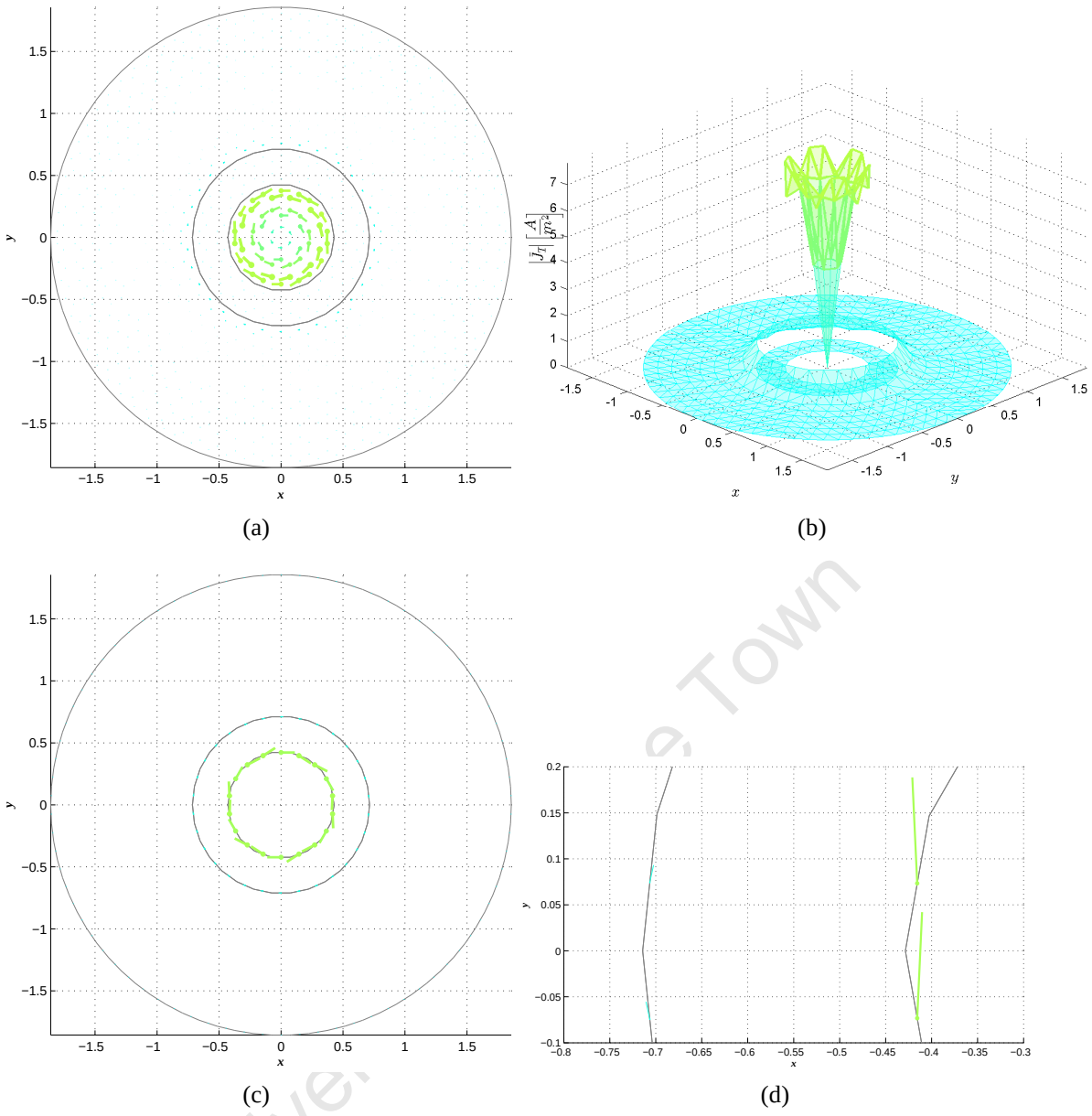

Figure 8.31: Solution Vector Field $\vec{J}_T$ Simulated at a frequency of $f = 5\text{Hz}$

Sub-figure 8.31a, illustrates the electric current density/eddy currents $\vec{J}_E$, that would be induced in the region $HC_r \leq r \leq HC_R$ at a frequency value of $f = 5\text{Hz}$, the region $0 \leq r \leq SC_R$ contains the source current density $\vec{J}_S$ and there are no $\vec{J}_E$ present in the air space region ($AS_r \leq r \leq AS_R$), since air cannot conduct current density [8, 5, 10]. Sub-figure 8.31b illustrates in the form of a meshed graph: $\left|\vec{J}_E\right|$(the magnitude of the vector field $\vec{J}_E$), across the region of $HC_r \leq r \leq HC_R$ and $\left|\vec{J}_S\right|$ (the magnitude of the vector field $\vec{J}_S$), across the region $0 \leq r \leq SC_R$. In sub-figure 8.31b $\left|\vec{J}_E\right|$ across the region $HC_r \leq r \leq HC_R$ suggests an attenuation of $\vec{J}_E$ over this same region and in the region $AS_r \leq r \leq AS_R$, $\left|\vec{J}_E\right| = 0$, demonstrating that no $\vec{J}_E$ is present over this same region. In the region $0 \leq r \leq SC_R$, $\left|\vec{J}_S\right|$ demonstrates that $\vec{J}_S$ increases linearly and at the boundary of $r = SC_R$ $\left|\vec{J}_S\right|$ is at its "highest" value indicating that at this position of the domain $\vec{J}_S$ is at its strongest intensity. The moderate attenuation behaviour of $\left|\vec{J}_E\right|$ across the region $HC_r \leq r \leq HC_R$, verifies that $\vec{J}_E$ has penetrated moderately into the hollow conductor at this frequency. Sub-figure 8.31c, shows the vectors of $\vec{J}_T$ located on the material interface boundaries located at positions $r = SC_R = AS_r$ and $r = AS_R = HC_r$. To view the behaviour of these vectors better, a region of this figure was enlarged which is shown in sub-figure 8.31d. In sub-figure 8.31d, only the vector fields $\vec{J}_E$ and $\vec{J}_S$ (belonging to the conductor regions of the domain) is present on the material interface boundaries because $\vec{J}_E$ cannot exists in the air space region of the domain [8, 5, 10].

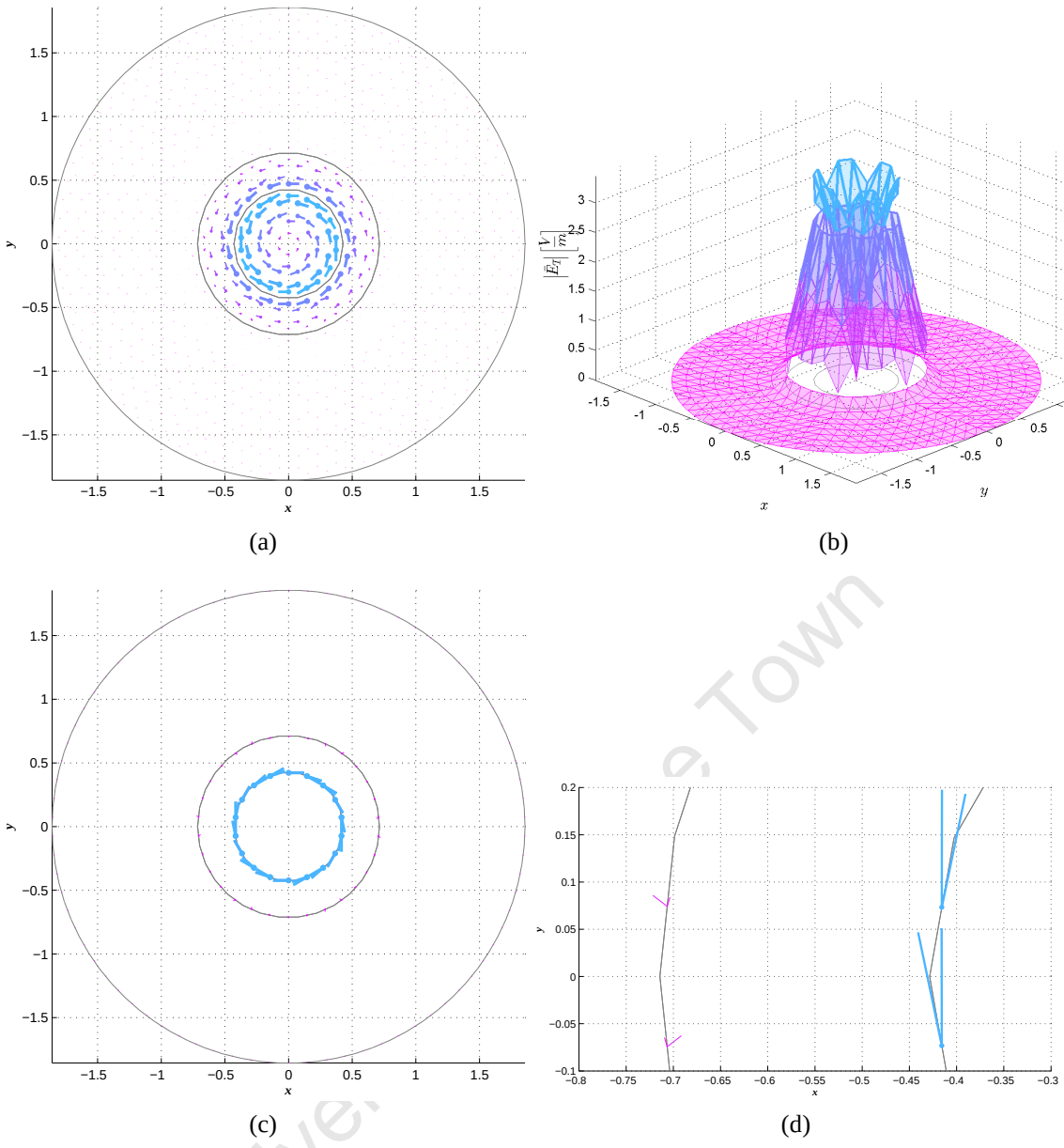

Figure 8.32: Solution Vector Field $\vec{E}_T$ Simulated at a frequency of $f = 20\text{Hz}$

Sub-figure 8.32a, illustrates the electric field $\vec{E}_E$, that would be induced in the regions $HC_r \leq r \leq HC_R$ and $AS_r \leq r \leq AS_R$ at a frequency value of $f = 20\text{Hz}$, the region $0 \leq r \leq SC_R$ contains the source electric field $\vec{E}_S$. Sub-figure 8.32b illustrates in the form of a meshed graph: $\left|\vec{E}_E\right|$ (the magnitude of the vector field $\vec{E}_E$), across the regions of $HC_r \leq r \leq HC_R$ and $AS_r \leq r \leq AS_R$ of the domain and $\left|\vec{E}_S\right|$ (the magnitude of the vector field $\vec{E}_S$) across the region $0 \leq r \leq SC_R$ of the domain. In sub-figure 8.32b $\left|\vec{E}_E\right|$ across the region $HC_r \leq r \leq HC_R$ suggests an attenuation of $\vec{E}_E$ over this same region and across the region $AS_r \leq r \leq AS_R$, $\left|\vec{E}_E\right|$ demonstrates that $\vec{E}_E$ decreases linearly over this same region. In the region $0 \leq r \leq SC_R$, $\left|\vec{E}_S\right|$ demonstrates that $\vec{E}_E$ increases linearly and at the boundary of $r = SC_R$ $\left|\vec{E}_S\right|$ is at its "highest" value indicating that at this position of the domain $\vec{E}_S$ is at its strongest intensity. The sharp attenuation behaviour of $\left|\vec{E}_E\right|$ across the region $HC_r \leq r \leq HC_R$, verifies that $\vec{E}_E$ has penetrated slightly into the hollow conductor at this frequency. Sub-figure 8.32c, shows the vectors of $\vec{E}_T$ located on the material interface. To view the behaviour of these vectors better, a region of this figure was enlarged which is shown in sub-figure 8.32d. Sub-figure 8.32d, clearly illustrates the discontinuous behaviour of $\vec{E}_T$ across a material interface and this discontinuity of $\vec{E}_T$ is verified by the "gap" found between different material regions of the meshed graph as seen in sub-figure 8.32b.

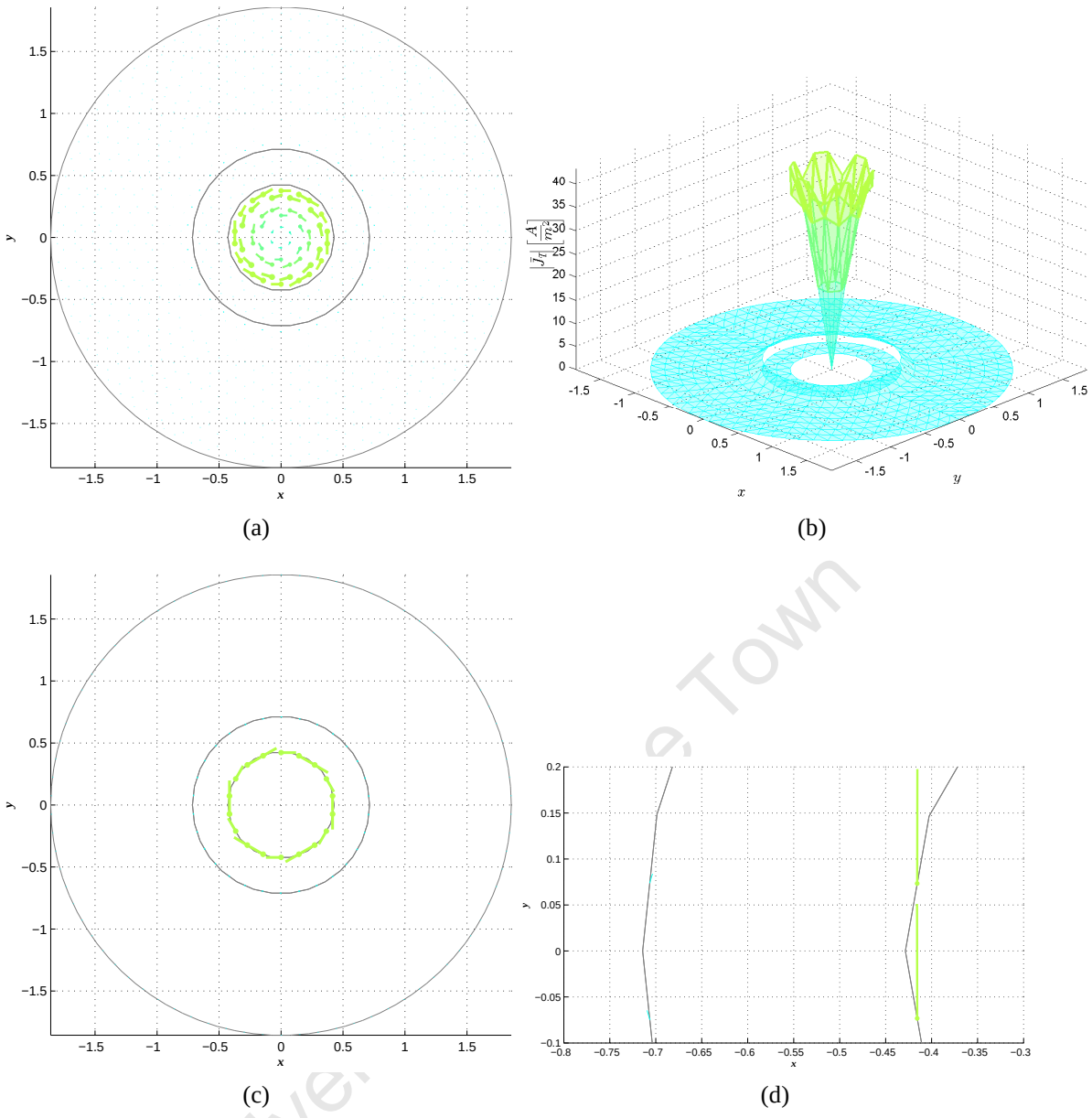

Figure 8.33: Solution Vector Field $\vec{J_T}$ Simulated at a frequency of $f = 20$Hz

Sub-figure 8.33a, illustrates the electric current density/eddy currents $\vec{J_E}$, that would be induced in the region $HC_r \leq r \leq HC_R$ at a frequency value of $f = 20$Hz, the region $0 \leq r \leq SC_R$ contains the source current density $\vec{J_S}$ and there are no $\vec{J_E}$ present in the air space region ($AS_r \leq r \leq AS_R$), since air cannot conduct current density [8, 5, 10]. Sub-figure 8.33b illustrates in the form of a meshed graph: $\left|\vec{J_E}\right|$(the magnitude of the vector field $\vec{J_E}$), across the region of $HC_r \leq r \leq HC_R$ and $\left|\vec{J_S}\right|$ (the magnitude of the vector field $\vec{J_S}$), across the region $0 \leq r \leq SC_R$. In sub-figure 8.33b $\left|\vec{J_E}\right|$ across the region $HC_r \leq r \leq HC_R$ suggests an attenuation of $\vec{J_E}$ over this same region and in the region $AS_r \leq r \leq AS_R$, $\left|\vec{J_E}\right| = 0$, demonstrating that no $\vec{J_E}$ is present over this same region. In the region $0 \leq r \leq SC_R$, $\left|\vec{J_S}\right|$ demonstrates that $\vec{J_S}$ increases linearly and at the boundary of $r = SC_R$ $\left|\vec{J_S}\right|$ is at its "highest" value indicating that at this position of the domain $\vec{J_S}$ is at its strongest intensity. The sharp attenuation behaviour of $\left|\vec{J_E}\right|$ across the region $HC_r \leq r \leq HC_R$, verifies that $\vec{J_E}$ has penetrated slightly into the hollow conductor at this frequency. Sub-figure 8.33c, shows the vectors of $\vec{J_T}$ located on the material interface boundaries located at positions $r = SC_R = AS_r$ and $r = AS_R = HC_r$. To view the behaviour of these vectors better, a region of this figure was enlarged which is shown in sub-figure 8.33d. In sub-figure 8.33d, only the vector fields $\vec{J_E}$ and $\vec{J_S}$ (belonging to the conductor regions of the domain) is present on the material interface boundaries because $\vec{J_E}$ cannot exists in the air space region of the domain [8, 5, 10].

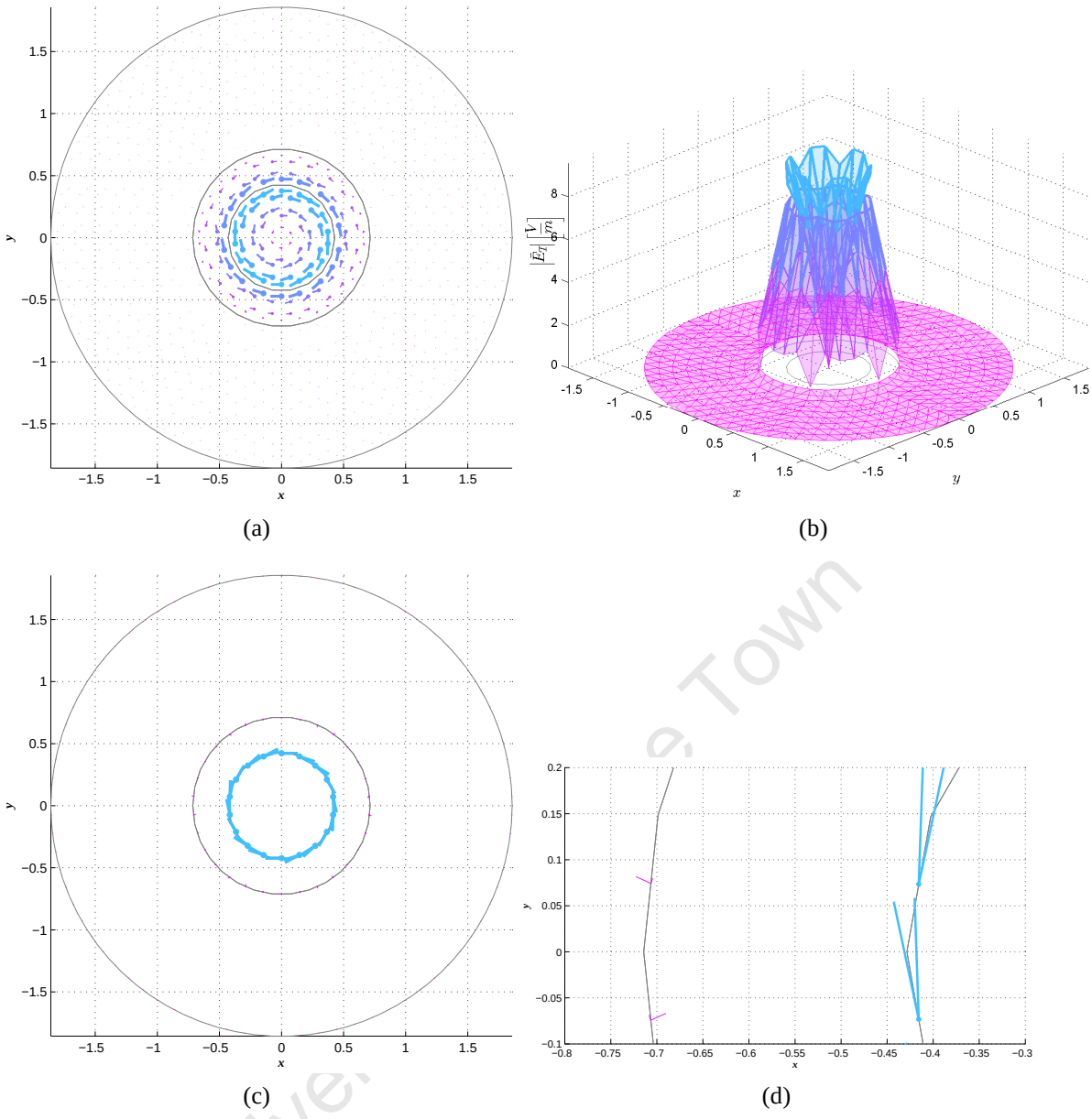

Figure 8.34: Solution Vector Field $\vec{E}_T$ Simulated at a frequency of $f = 50\text{Hz}$

Sub-figure 8.34a, illustrates the electric field $\vec{E}_E$, that would be induced in the regions $HC_r \leq r \leq HC_R$ and $AS_r \leq r \leq AS_R$ at a frequency value of $f = 50\text{Hz}$, the region $0 \leq r \leq SC_R$ contains the source electric field $\vec{E}_S$. Sub-figure 8.34b illustrates in the form of a meshed graph: $\left|\vec{E}_E\right|$ (the magnitude of the vector field $\vec{E}_E$), across the regions of $HC_r \leq r \leq HC_R$ and $AS_r \leq r \leq AS_R$ of the domain and $\left|\vec{E}_S\right|$ (the magnitude of the vector field $\vec{E}_S$) across the region $0 \leq r \leq SC_R$ of the domain. In sub-figure 8.34b $\left|\vec{E}_E\right|$ across the region $HC_r \leq r \leq HC_R$ suggests an attenuation of $\vec{E}_E$ over this same region and across the region $AS_r \leq r \leq AS_R$, $\left|\vec{E}_E\right|$ demonstrates that $\vec{E}_E$ decreases linearly over this same region. In the region $0 \leq r \leq SC_R$, $\left|\vec{E}_S\right|$ demonstrates that $\vec{E}_E$ increases linearly and at the boundary of $r = SC_R$ $\left|\vec{E}_S\right|$ is at its "highest" value indicating that at this position of the domain $\vec{E}_S$ is at its strongest intensity. The very sharp attenuation behaviour of $\left|\vec{E}_E\right|$ across the region $HC_r \leq r \leq HC_R$, verifies that $\vec{E}_E$ has hardly penetrated into the hollow conductor at this frequency. Sub-figure 8.34c, shows the vectors of $\vec{E}_T$ located on the material interface. To view the behaviour of these vectors better, a region of this figure was enlarged which is shown in sub-figure 8.34d. Sub-figure 8.32d, clearly illustrates the discontinuous behaviour of $\vec{E}_T$ across a material interface and this discontinuity of $\vec{E}_T$ is verified by the "gap" found between different material regions of the meshed graph as seen in sub-figure 8.34b.

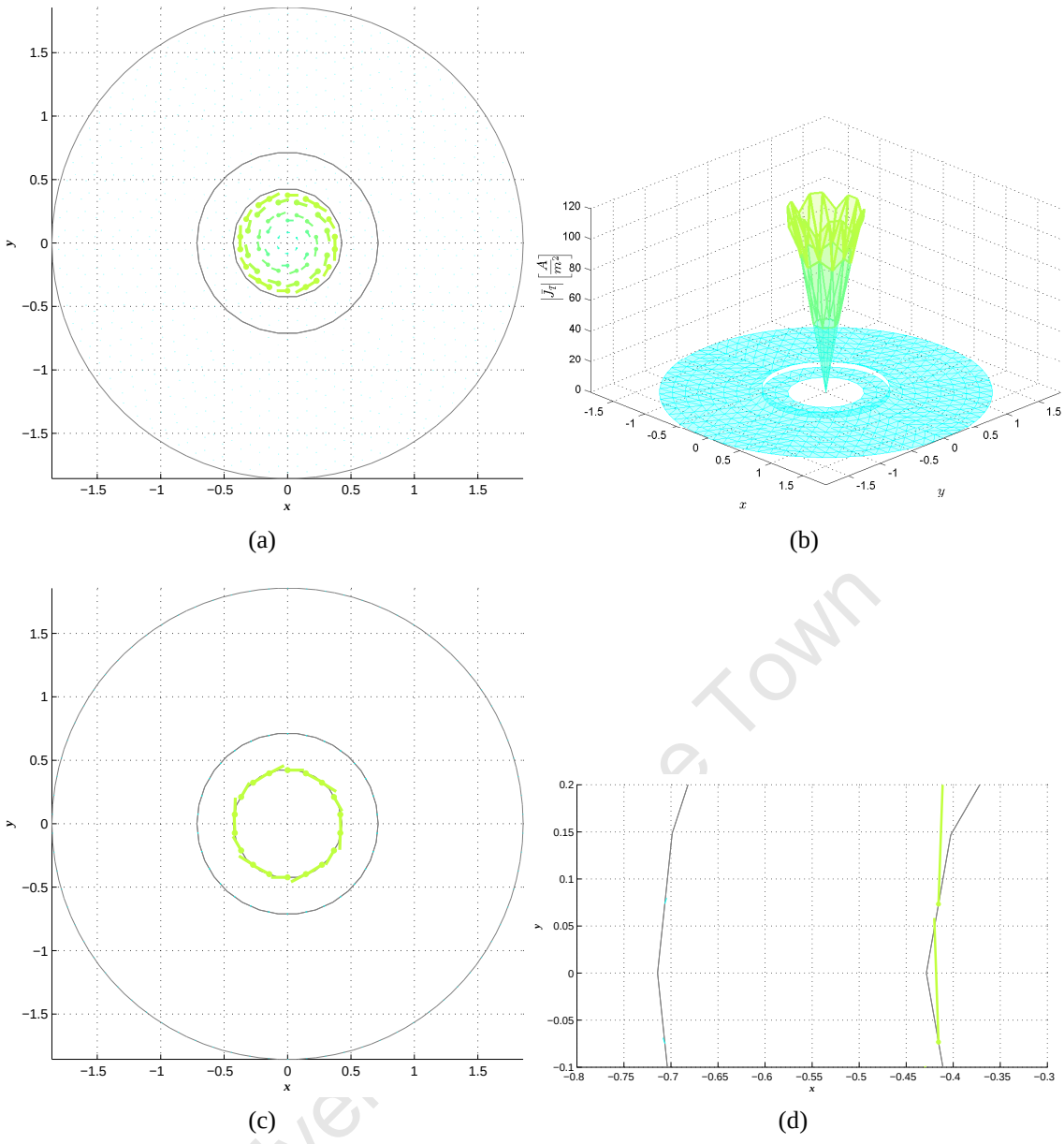

Figure 8.35: Solution Vector Field $\vec{J_T}$ Simulated at a frequency of $f = 50$Hz

Sub-figure 8.35a, illustrates the electric current density/eddy currents $\vec{J_E}$ that would be induced in the region $HC_r \leq r \leq HC_R$ at a frequency value of $f = 50$Hz, the region $0 \leq r \leq SC_R$ contains the source current density $\vec{J_S}$ and there are no $\vec{J_E}$ present in the air space region ($AS_r \leq r \leq AS_R$), since air cannot conduct current density [8, 5, 10]. Sub-figure 8.35b illustrates in the form of a meshed graph: $\left|\vec{J_E}\right|$(the magnitude of the vector field $\vec{J_E}$), across the region of $HC_r \leq r \leq HC_R$ and $\left|\vec{J_S}\right|$ (the magnitude of the vector field $\vec{J_S}$), across the region $0 \leq r \leq SC_R$. In sub-figure 8.35b $\left|\vec{J_E}\right|$ across the region $HC_r \leq r \leq HC_R$ suggests an attenuation of $\vec{J_E}$ over this same region and in the region $AS_r \leq r \leq AS_R$, $\left|\vec{J_E}\right| = 0$, demonstrating that no $\vec{J_E}$ is present over this same region. In the region $0 \leq r \leq SC_R$, $\left|\vec{J_S}\right|$ demonstrates that $\vec{J_S}$ increases linearly and at the boundary of $r = SC_R$ $\left|\vec{J_S}\right|$ is at its "highest" value indicating that at this position of the domain $\vec{J_S}$ is at its strongest intensity. The very sharp attenuation behaviour of $\left|\vec{J_E}\right|$ across the region $HC_r \leq r \leq HC_R$, verifies that there is hardly $\vec{J_E}$ present within the hollow conductor at this frequency. Sub-figure 8.35c, shows the vectors of $\vec{J_T}$ located on the material interface boundaries located at positions $r = SC_R = AS_r$ and $r = AS_R = HC_r$. To view the behaviour of these vectors better, a region of this figure was enlarged which is shown in sub-figure 8.35d. In sub-figure 8.35d, only the vector fields $\vec{J_E}$ and $\vec{J_S}$ (belonging to the conductor regions of the domain) is present on the material interface boundaries because $\vec{J_E}$ cannot exists in the air space region of the domain [8, 5, 10].

8.3.3.2 Observations of FE Generated Solutions

The following observations were made concerning all the FEM simulation of sub-section 8.3.3.1:

1. In sub-figures 8.26a, 8.28a, 8.30a, 8.32a, 8.34a and sub-figures 8.27a, 8.29a, 8.31a, 8.33a, 8.35a no wave propagation "seems" to be observed within the hollow cylinder region of $HC_r \leq r \leq HC_R$.

2. The vector fields solutions of $\vec{E}_T$ and $\vec{J}_T$ are polarised in the $\hat{\theta} - direction$ which is perpendicular to the direction of "travel" of the vector fields $\vec{E}_T$ and $\vec{J}_T$ which is in the $\hat{r} - direction$ [10, 9].

3. In sub-figures 8.26a, 8.28a, 8.30a, 8.32a, 8.34a and sub-figures 8.27a, 8.29a, 8.31a, 8.33a, 8.35a the following was observed concerning the behaviour of $\vec{E}_E$ and $\vec{J}_E$ in relation to the radius r, of the domain:

   (a) Across the air space region located at $AS_r \leq r \leq AS_R$, $\vec{E}_E$ seems to decrease in strength and the vector field $\vec{J}_E$, across this same region does not exist.

   (b) With an increase in frequency f, the vector fields $\vec{E}_E$ and $\vec{J}_E$ appear to penetrate less into the hollow conductor region of $HC_r \leq r \leq HC_R$.

4. *The meshed graphs of sub-figures 8.26b, 8.28b, 8.30b, 8.32b, 8.34b and sub-figures 8.27b, 8.29b, 8.31b, 8.33b, 8.35b seem to expose certain physical behaviour patterns of the vector fields $\vec{E}_E$ and $\vec{J}_E$ across the different material regions of the domain, more clearly that the vector fields of sub-figures 8.26a, 8.28a, 8.30a, 8.32a, 8.34a and sub-figures 8.27a, 8.29a, 8.31a, 8.33a, 8.35a.* The following was observed concerning the behaviour of $\left|\vec{E}_E\right|$ and $\left|\vec{J}_E\right|$ with relation to the radius r, of the domain:

   (a) Across the air space region located at $AS_r \leq r \leq AS_R$, $\left|\vec{E}_E\right|$ decreases linearly and $\left|\vec{J}_E\right|$ does not exist.

   (b) Across the hollow conductor region located at position $HC_r \leq r \leq HC_R$ of the domain, $\left|\vec{E}_E\right|$ and $\left|\vec{J}_E\right|$decays rapidly along the radial axis from position $r = HC_r$, towards the boundary of the domain located at $r = HC_R$.

5. In sub-figures 8.26a, 8.28a, 8.30a, 8.32a, 8.34a and sub-figures 8.27a, 8.29a, 8.31a, 8.33a, 8.35a the following was observed concerning the behaviour of $\vec{E}_S$ and $\vec{J}_S$ in relation to the radius r, of the domain:

   (a) Across the solid cylinder region located at $0 \leq r \leq SC_R$, $\vec{E}_S$ and $\vec{J}_S$ increases in strength.

6. In sub-figures 8.26b, 8.28b, 8.30b, 8.32b, 8.34b and sub-figures 8.27b, 8.29b, 8.31b, 8.33b, 8.35b, the following was observed concerning the behaviour of $\left|\vec{E}_S\right|$ and $\left|\vec{J}_S\right|$ in relation to the radius r, of the domain:

   (a) Across the solid cylinder region located at $0 \leq r \leq SC_R$, $\left|\vec{E}_S\right|$ and $\left|\vec{J}_S\right|$ increases linearly.

(b) $\left|\vec{E}_S\right|$ and $\left|\vec{J}_S\right|$ increases as the value of the frequency f, is set higher.

7. In sub-figures 8.26d, 8.28d, 8.30d, 8.32d, 8.34d the following was observed concerning the behaviour of $\vec{E}_T$ on the different material interfaces located at positions $r = SC_R = AS_r$ and $r = AS_R = HC_r$ (refer to figure 8.24b):

   (a) The vector field $\vec{E}_T$, has two vectors originating from the same coordinate point located on the material interface.

8.3.3.3 Analysis of FE Generated Solutions

Previous research knowledge of Section 3.1 and sub-sections 8.2.3, 8.3.1.3 indicated that the vector fields solutions of $\vec{E}_E$ and $\vec{J}_E$ would attenuate across the hollow conductor region $HC_r \leq r \leq HC_R$. Such a behaviour pattern of the vector fields solutions is expected because all the examples investigated in Sections 3.1, 8.2 and sub-section 8.3.1 and including this example was solved using the *same PDE given by Equation* (2.39), which governs the physical behaviour of eddy currents within a conductor and therefore there should be *some similarity in the physical behaviour of the vector field solutions* across their respective domains, although each example contained different BC's and geometry configurations.

According to [24], the field theory that approximately describes the solution to this problem can be derived from the integral form of Faraday's Law:

$$\begin{aligned} \oint \vec{E} \cdot \overrightarrow{dl} &= -\frac{d}{dt}\int_s \vec{B} \cdot \overrightarrow{ds} \\ &= -\int_s \frac{d\vec{B}}{dt} \cdot \overrightarrow{ds} \end{aligned} \tag{8.17}$$

Converting the magnetic field $\vec{B}(t)$, to phasor form [24]:

$$\vec{B} \Rightarrow B_0 e^{j\omega t}\hat{k} \tag{8.18}$$

therefore [24]:

$$\frac{d\vec{B}}{dt} \Rightarrow j\omega B_0 e^{j\omega t}\hat{k} \tag{8.19}$$

Case 1: for $r < SC_R$, Equation (8.17) becomes [24]:

$$\tilde{E}_\theta 2\pi r = \frac{dB_z}{dt}\pi r^2 \tag{8.20}$$

Simplifying Equation (8.20) produces [24]:

$$\tilde{E}_\theta = \frac{1}{2} r \frac{dB_z}{dt} \tag{8.21}$$

Substituting Equation (8.19) into Equation (8.21), gives [24]:

$$\tilde{E}_\theta(r,t) = \frac{1}{2} r j\omega B_0 e^{j\omega t} \tag{8.22}$$

Equation (8.22), describes an electric field polarised in the $\theta - direction$, and this field increases in strength by a factor of approximately r, in relation to the $r - axis$ of the domain [24]. Thus, the magnitude $|E_\theta|$can be described as increasing linearly across the solid conductor region of $0 \leq r \leq SC_R$ along the radial axis ($r - axis$ of the domain) [24].

The solid conductor region of $0 \leq r \leq SC_R$, forms the excitation region of the domain for this particular eddy current problem (refer to sub-section 8.3.3). The angular frequency is defined as follows:

$$\omega = 2\pi f \tag{8.23}$$

where f, is the frequency value. Through Equation (8.23), the frequency f, has a direct effect the field $\tilde{E}_\theta(r,t)$ given by Equation (8.22), by causing the field $\tilde{E}_\theta(r,t)$, to increase in strength as the frequency value f is increased.

Case 2: for $r > SC_R$, Equation (8.17) becomes [24]:

$$\tilde{E}_\theta 2\pi r = \frac{dB_z}{dt}\pi SC_R^2 \tag{8.24}$$

Simplifying Equation (8.24) produces [24]:

$$\tilde{E}_\theta = \frac{1}{2}SC_R^2\frac{1}{r}\frac{dB_z}{dt} \tag{8.25}$$

Substituting Equation (8.19) into Equation (8.25) gives [24]:

$$\tilde{E}_\theta(r,t) = \frac{1}{2}\frac{1}{r}SC_R^2 j\omega B_0 e^{j\omega t} \tag{8.26}$$

Equation (8.26), describes an electric field polarised in the $\theta - direction$, and this field decays in strength by a factor of approximately $\frac{1}{r}$, in relation to the $r - axis$ of the domain [24]. Thus, the magnitude $|E_\theta|$can be described as attenuating across the hollow conductor region of $HC_r \leq r \leq HC_R$ and the air space region of $AS_r \leq r \leq AS_R$, along the radial axis ($r - axis$ of the domain) by approximately a factor of $\frac{1}{r}$ in relation to the $r - axis$ of the domain [24]. Through Equation (8.23), the frequency f, has a direct effect the field $\tilde{E}_\theta(r,t)$ given by Equation (8.26), by causing the field $\tilde{E}_\theta(r,t)$, to decay more rapidly as the frequency value f is increased, thus the depth of penetration of the field $\tilde{E}_\theta(r,t)$ into this conductor region along the radial axis ($r - axis$ of the domain) would decrease [24].

The following analysis of the FE simulations has been made according to the observations found in sub-section 8.3.3.2:

1. The wavelengths λ, of the simulated solutions are probably too large for the dimension of the hollow cylinder located at position $HC_r \leq r \leq HC_R$ of the domain, therefore no wave pattern "appeared" to be observed within this region. Refer to section 8.3.1 where a similar analysis occurred.

2. The vector fields $\vec{E}_T$ and $\vec{J}_T$ are polarised in the $\theta - direction$, as indicated by the direction of the vectors, which corresponds to the vector field solutions of Equations (8.22) and (8.26).

3. According to sub-figures 8.26a, 8.28a, 8.30a, 8.32a, 8.34a and sub-figures 8.27a, 8.29a, 8.31a, 8.33a, 8.35a the following analysis is made concerning the behaviour of $\vec{E}_E$ and $\vec{J}_E$ in relation to the radius r, of the domain:

   (a) Across the air space region $AS_r \leq r \leq AS_R$, $\vec{E}_E$ physically becomes weak in strength along the radial axis from position $r = SC_R = AS_r$ towards the position of $r = AS_R$ on the domain and so agrees with Equation (8.26). The air space region cannot support electric current density/eddy currents $\vec{J}_E$ due to the air having a conductivity value of approximately zero, that is $\sigma \backsimeq 0$ [9, 10, 19].

(b) The attenuation of the vector fields $\vec{E}_E$ and $\vec{J}_E$ increases with an increase in frequency f, along the radial axis of the domain across the region $HC_r \leq r \leq HC_R$ and so also agrees with Equation (8.26).

(c) As the frequency is increased the electric field $\vec{E}_E$, becomes situated closer and closer towards the interior boundary of the hollow cylinder located at position $r = HC_r$ of the domain as shown in sub-figures 8.26a, 8.28a, 8.30a, 8.32a, 8.34a. This behaviour pattern is a clear indication of skin effect phenomena which is an important characteristic of eddy current problems [16, 17]. The electric field $\vec{E}_E$, causes the motion of the free electrons within the conducting body, so producing an electric current density at the positions where the electric field penetrates the conducting body [10, 9, 19, 20] (refer to section 2.3) as seen in sub-figures 8.27a, 8.29a, 8.31a, 8.33a, 8.35a. It is this current density that is referred to as eddy currents, $\vec{J}_E$ [16, 17].

4. According to sub-figures 8.26b, 8.28b, 8.30b, 8.32b, 8.34b and sub-figures 8.27b, 8.29b, 8.31b, 8.33b, 8.35b the following analysis is made concerning the behaviour of $\left|\vec{E}_E\right|$ and $\left|\vec{J}_E\right|$ in relation to the radius r, of the domain:

   (a) Across the air space region located at $AS_r \leq r \leq AS_R$, $\left|\vec{E}_E\right|$ "seems" to decreases linearly. The air space region is relatively small in comparison to the two conductor regions as seen in Figure 8.25, therefore the $\left|\vec{E}_E\right|$ "might seem" to decreases linearly across this region, however in reality, the $\left|\vec{E}_E\right|$ actually also decays across this region as described by Equation (8.26). Figure 8.36 shows a larger air space region, where the behaviour of $\left|\vec{E}_E\right|$ obeys Equation (8.26).

   (b) Across the air space region located at $AS_r \leq r \leq AS_R$, $\left|\vec{J}_E\right| = 0$ due to the air having a conductivity value of approximately zero, that is $\sigma \backsimeq 0$ [9, 10, 19].

   (c) $\left|\vec{E}_E\right|$ and $\left|\vec{J}_E\right|$decays rapidly along the radial axis from position $r = HC_r$, towards the boundary of the domain located at $r = HC_R$. There appears to be a $\frac{1}{r}$ decay of $\left|\vec{E}_E\right|$ and $\left|\vec{J}_E\right|$ in relation to the $r - axis$ of the domain across the region $HC_r \leq r \leq HC_R$ thus, these simulations seem to be in agreement with Equation (8.26).

5. According to sub-figures 8.26a, 8.28a, 8.30a, 8.32a, 8.34a and sub-figures 8.27a, 8.29a, 8.31a, 8.33a, 8.35a the following analysis is made concerning the behaviour of $\vec{E}_S$ and $\vec{J}_S$ in relation to the radius r, of the domain:

   (a) Across the solid cylinder region located at $0 \leq r \leq SC_R$, the vector fields $\vec{E}_S$ and $\vec{J}_S$ increases in strength along the radial axis ($r - axis$) and so is in agreement with Equation (8.22).

6. According to sub-figures 8.26a, 8.28a, 8.30a, 8.32a, 8.34a and sub-figures 8.27a, 8.29a, 8.31a, 8.33a, 8.35a the following analysis is made concerning the behaviour of $\left|\vec{E}_S\right|$ and $\left|\vec{J}_S\right|$ in relation to the radius r, of the domain:

   (a) Across the solid cylinder region located at $0 \leq r \leq SC_R$, $\left|\vec{E}_S\right|$ and $\left|\vec{J}_S\right|$ increases linearly long the radial axis ($r - axis$), which is in agreement with Equation (8.22).

(b) As the frequency value f is increased, there is an increase in strength of $\left|\vec{E}_S\right|$ and $\left|\vec{J}_S\right|$ across the region $0 \leq r \leq SC_R$ (which is shown by the increase in "height" of these meshed graphs). The behaviour of these graphs is in agreement with Equation (8.22) which forms the excitation force (refer to sub-section 8.3.3) across the region of the solid cylinder located at position $0 \leq r \leq SC_R$ within the domain of this eddy current configuration.

7. In sub-figures 8.26d, 8.28d, 8.30d, 8.32d, 8.34d the following analysis is made concerning the behaviour of $\vec{E}_T$ on the different material interfaces located at positions $r = SC_R = AS_r$ and $r = AS_R = HC_r$ (refer to sub-figure 8.24b):

   (a) The vector field $\vec{E}_T$, is discontinuous on the material interfaces of the domain and this discontinuity is indicated by two vectors originating from the same coordinate point located on the material interface. Refer to sub-sections 5.1.3 and 5.3.3 where a comprehensive explanation concerning vector field discontinuity across a material interface is given.

   (b) In sub-figures 8.26b, 8.28b, 8.30b, 8.32b, 8.34b, there are visible "gaps" present within the meshed graphs of $\left|\vec{E}_T\right|$, which also emphasises the discontinuity of the vector field $\vec{E}_T$, on the material interfaces as well (refer to point number 7 of sub-section 8.3.2.3).

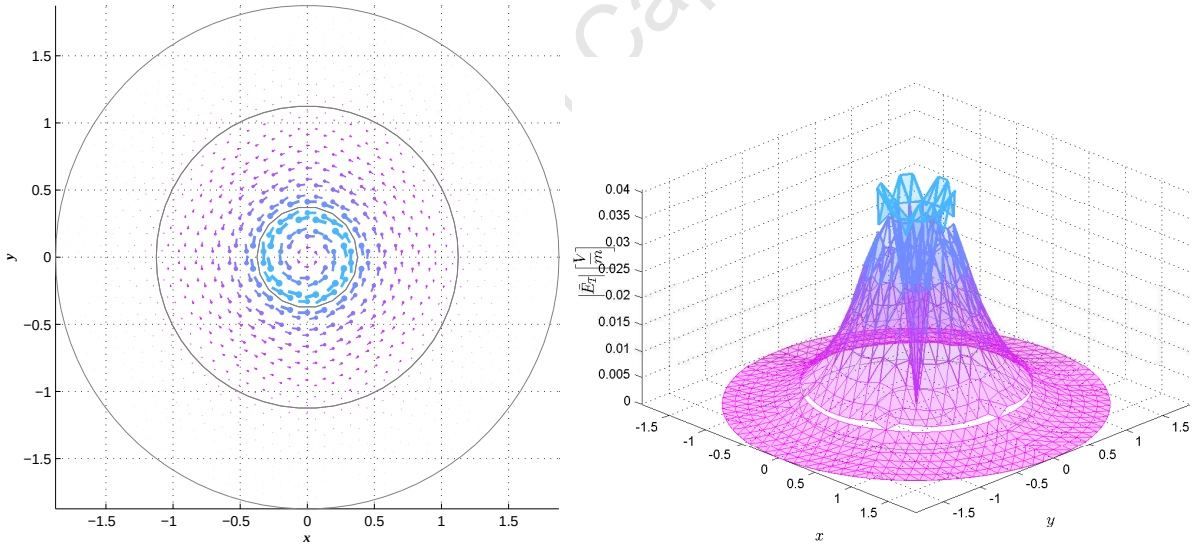

(a) (b)

Figure 8.36: Solution Vector Field $\vec{E}_T$ Simulated at a frequency of $f = 1$Hz

Sub-figure 8.36a, illustrates the electric field $\vec{E}_E$, that would be induced in the regions $HC_r \leq r \leq HC_R$ and $AS_r \leq r \leq AS_R$ at a frequency value of $f = 1$Hz, the region $0 \leq r \leq SC_R$ contains the source electric field $\vec{E}_S$. Sub-figure 8.36b illustrates in the form of a meshed graph: $\left|\vec{E}_E\right|$ (the magnitude of the vector field $\vec{E}_E$), across the regions of $HC_r \leq r \leq HC_R$ and $AS_r \leq r \leq AS_R$ of the domain and $\left|\vec{E}_S\right|$ (the magnitude of the vector field $\vec{E}_S$) across the region $0 \leq r \leq SC_R$ of the domain. In sub-figure [24] $\left|\vec{E}_E\right|$ across the region $HC_r \leq r \leq HC_R$ suggests an attenuation of $\vec{E}_E$, by a factor of approximately $\frac{1}{r}$ (in relation to the $r-axis$ [24]) over this same region and across the region $AS_r \leq r \leq AS_R$, $\left|\vec{E}_E\right|$ demonstrates that $\vec{E}_E$, also decays by a factor of approximately $\frac{1}{r}$ (in relation to the $r-axis$ [24]) over this same region. In the region $0 \leq r \leq SC_R$, $\left|\vec{E}_S\right|$ demonstrates that $\vec{E}_E$ increases linearly and at the boundary of $r = SC_R$, $\left|\vec{E}_S\right|$ is at its "highest" value indicating that at this position of the domain $\vec{E}_S$, is at its strongest intensity.

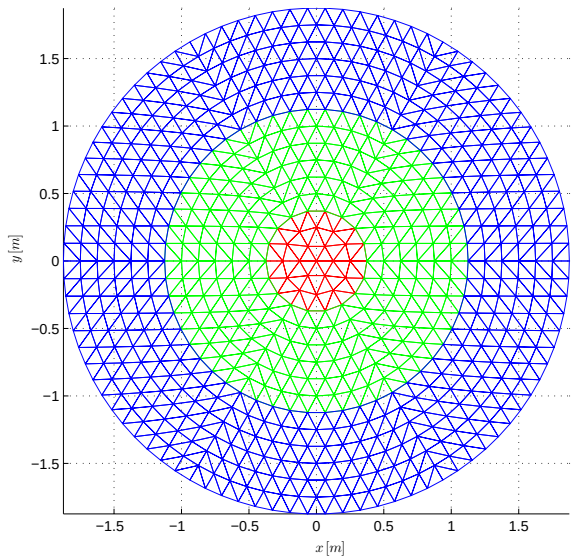

Figure 8.37: Finite Element Mesh

Finite element mesh used to simulate the vector field solution shown in Figure 8.36. This mesh shows a larger air space region in relation to the two conductor regions of the domain. The three material regions are indicated by the different colours of the mesh: RED-solid conductor region. GREEN-air space region. BLUE-hollow conductor region.

8.3.3.4 Summary

The FE algorithm is able to model and simulate:

- the physical behaviour of the total electric vector field $\vec{E}_T$, and total electric current density/eddy currents $\vec{J}_T$, across different material regions of the overall domain.
- the discontinuity of the vector fields $\vec{E}_T$ across different material regions of the domain.
- the attenuation behaviour of the vector fields $\vec{E}_E$ and $\vec{J}_E$ (over the conductor region, $HC_r \leq r \leq HC_R$) at different frequencies thereby demonstrating the skin effect phenomena, which is an important behaviour effect found in eddy current problems [19, 16, 17].

Improvements to the accuracy of the solution vector field approximations and the simulations visually could be achieved through the used of higher-order vector elements and a self-adaptive mesh refinement technique. The reader is referred to sub-section 8.3.1 where these subjects were discussed.

Chapter 9

Conclusion

An FE algorithm was developed in order to approximate and simulate vector field solutions to equation (2.39), which is the vector PDE under investigation that governs eddy current behaviour [16, 17]. Eddy current phenomena is classified as a particular branch of EM theory [16, 17] and therefore the vector field solutions to equation (2.39) possesses EM properties.

EM vector fields possess certain properties that makes them fundamentally different to other types of vector fields such as those encountered in structural mechanics [2, 3, 12]. The approximation of solution vector fields of EM problems using the FEM, thus promoted the need to be able to accommodate these different properties and therefore the vector finite element was developed [7, 2].

The FE algorithm made use of the vector finite element to graphically construct the solution vector fields of the eddy current problems in Chapter 8. In Chapter 5, an investigation was done to compare the functional capability of the vector element and the functional capability of the node-based vector element with regard to approximating EM vector fields. The investigation revealed that the vector element due to its "design structure" is more suitable for the use of EM problems than the conventional node-based vector element [7, 2] because it was proved particularly in sub-sections 5.3.3 and 5.3.1, that the vector element possessed unique properties which favoured EM behaviour and thus worked very well in visually exposing certain EM properties of the solution vector fields of the eddy current problems in Chapter 8.

The FE algorithm was applied to theoretical eddy current problems and the vector field solutions of these problems are visually shown in Chapter 8. The eddy current problem of sub-section 8.2.1 serves as a verification of the successful implementation of the FE algorithm, because of good physical and behavioural similarities between the simulation of the FE solution and the simulation of the analytical solution of the same problem found in Section 3.1. Due to Section 8.2, solutions to arbitrary eddy current problems were then simulated in Section 8.3. In sub-sections 8.3.2 and 8.3.3 the behaviour of the electric field solutions $\vec{E}_T$ and the eddy current solutions $\vec{J}_T$ are also shown across different material regions and these visual results corresponds to the EM field theory concerning discontinuity of EM vector fields across different material interfaces shown in Section 5.1.3 of Chapter 5.

9.1 Chapter Summary

Chapter 2 developed an eddy current model using Maxwell's equations [16, 17] and this model was used for derivation of the PDE represented by Equation (2.39), which gov-

erns eddy current behaviour. The eddy current model explored how eddy currents are physically formed [19, 20] in a conducting medium and the physical interpretation of Equation (2.39) revealed that this equation is capable of supporting both boundary-driven and force-driven eddy current problems [6, 15].

Chapter 3 focused on finding analytical solutions to certain theoretical fundamental eddy current problems. The analytical solutions helped to gain and develop insight and understanding into behaviour patterns of eddy current phenomena [16, 17, 21] which is governed by Equation (2.39) [16, 17]. The eddy current problem of Section 3.1 also served as a verification that the FE algorithm was implemented correctly.

Chapter 4 explains important concepts such as coordinate transformation between two triangular systems and shape functions that are used in the construction of nodal finite elements [1, 3, 12]. These concepts are also used for the construction of the vector finite element in Chapter 5 [7, 3, 2, 12]. The nodal element is only able to approximate scalar fields [1, 3, 12, 5].

Chapter 5 compares two different types of vector elements that are used to approximate EM vector fields [7, 12, 3], which are the node-based vector element and the vector element. Analysis of both the elements revealed that the vector element is better adapted to approximating EM vector fields in comparison to node-based vector element [7, 12, 3], thus making the vector finite element highly desirable to use for eddy current problems which is classified as a particular branch of EM problems [16, 17].

Chapter 6 outlined the procedure of the FEM and how the vector shape functions are incorporated into the Galerkin method in order to fully descretize Equation (2.39) and produce a system of linear equations consisting of FEM matrices [1, 3, 16, 17]. To check whether the FEM matrices were descretized correctly the FEM matrices were derived symbolically as well. The importance of element connectivity information is addressed concerning the assembly procedure of the FEM [1, 2, 23]. The assembly procedure is highly dependent on this data information in order for the FEM to be able to approximate a solution to Equation (2.39) across the entire domain through the global system of linear equations which is created through the assembly process [1, 2, 23].

In Chapter 7, addressed certain issues concerning the implementation of the FE algorithm. Important issues which affected certain processes of the FE algorithm were discussed, such as the creation of element connectivity information [1, 2, 23], the implementation of boundary-driven and force-driven problems [6, 15] and the construction of the solution vector field using the vector finite elements [2, 7, 3, 12]. Section 7.7 briefly outlined the processes involved in the FE algorithm where each process made use of concepts, knowledge and findings which was covered throughout this research.

Chapter 8 shows the simulated vector field solutions of theoretical eddy current problems where these problems are analyzed and certain conclusion are drawn which relates to concepts and research theory involving eddy current phenomena and vector finite elements that were covered in the previous chapters. Important behaviour patterns observed within the simulated solutions are discussed such as the skin effect phenomena [16, 17, 21] and the physical behaviour of the $\vec{E}_E$-field and $\vec{J}_E$-field across different material regions within the same domain [9, 10, 19]. These results displayed by the simulated solutions were compared to research theory of chapters 2, 3, 5 and electromagnetic field theory from [24] and it was concluded that the simulated solutions are in good agreement with the research theory and the field theory, thereby indicating that the FE algorithm was implemented successfully.

9.2 Future Work

This dissertation represents a first attempt at implementing a FE algorithm using vector finite elements at UCT. The FE algorithm can be upgraded in the following ways to achieve more accurate results and simulations concerning the vector field solutions of Equation (2.39):

- The meshing procedure used in this dissertation is primitive, and the development of a self-adaptive meshing algorithm would greatly enhance the simulation of the solution vector fields [17]. The nature of the skin effect behaviour present within eddy current problems requires that mesh is able to "physically adapt"; that is, refine itself only at the particular areas of the domain where the solution vector field is most prevalent, thereby avoiding unnecessary computational time [17].
- More accurate solutions can also be simulated by using more advanced vector elements which would consists of shape functions of higher-order [2, 13, 3, 11]. The higher-order vector elements would be better adapted to approximating the attenuation behaviour of the vector field solutions due to the non-linear nature of attenuation of the solution vector fields observed across the domain of a problem.

Appendix A

Analytical Solutions

Full derivation of the analytical solutions found in Chapter 3 are provided.

A.1 Derivation of the Analytical Solution Found in Section 3.1.

Assume that the electric vector field component $\tilde{E_E}$, is polarised in the $x-direction$ and travels in the $z-direction$ [8]. Equation (3.2) will then take on the following form [8]:

$$\frac{\partial^2 \tilde{E}_x}{\partial z^2} - \tilde{k}^2 \tilde{E}_x = 0 \tag{A.1}$$

Equation (A.1) is subjected to the following boundary conditions [8]:

$$\tilde{E}_x(0) = E_{S_0} \tag{A.2}$$

$$\tilde{E}_x(\infty) = 0 \tag{A.3}$$

According to [8, 10, 6], the analytical solution of Equation (A.1) takes the form :

$$\tilde{E}_x(z) = c_1 e^{\tilde{k}z} + c_2 e^{-\tilde{k}z} \tag{A.4}$$

Applying boundary condition Equation (A.2) to Equation (A.1) [8]:

$$\begin{aligned} 0 &= c_1 e^{\tilde{k}\infty} + c_2 e^{-\tilde{k}\infty} \\ 0 &= c_1 e^{\tilde{k}\infty} \end{aligned} \tag{A.5}$$

the term $e^{\tilde{k}\infty} \neq 0, \therefore \Rightarrow c_1 = 0$. Equation (A.4) becomes [8]:

$$\tilde{E}_x(z) = c_2 e^{-\tilde{k}z} \tag{A.6}$$

Applying boundary condition Equation (A.3) to Equation (A.4) [8]:

$$E_{S_0} = c_2 e^{-\tilde{k}0} \tag{A.7}$$

the term $e^{-\tilde{k}0} = 1, \therefore \Rightarrow c_2 = E_{S_0}$. Equation (A.2) becomes [8]:

$$\begin{aligned} \tilde{E}_x(z) &= E_{S_0} e^{-\tilde{k}z} \\ &= E_{S_0} e^{-\beta(1+j)z} \\ &= E_{S_0} e^{-\beta z} e^{-j\beta z} \end{aligned} \tag{A.8}$$

where $\tilde{k} = \beta(1+j)$ according to Equation (3.4). To recover the time varying solution of Equation (A.8) [10, 15, 9]:

$$\begin{aligned} \vec{E}_x(z,t) &= \mathbb{R}e\left(\tilde{E}_x(z)\,e^{j\omega t}\right) \\ &= \mathbb{R}e\left(E_{S_0}e^{-\beta z}e^{j(\omega t-\beta z)}\right) \end{aligned} \tag{A.9}$$

taking the real part of Equation (A.9) yields [8, 10, 5]:

$$\vec{E}_x(z,t) = E_{S_0}e^{-\beta z}\cos(\omega t-\beta z)\,\hat{i} \tag{A.10}$$

A.2 Derivation of the Analytical Solution Found in Section 3.2.

Assume that the, $\tilde{E_E}$-field is polarised in the $\hat{i}-direction$ and travels in the $\hat{k}-direction$ ($z-axis$). Equation (3.2) will then take on the following form:

$$\frac{\partial^2\tilde{E_x}}{\partial z^2} - \tilde{k^2}\tilde{E_x} = 0 \tag{A.11}$$

Equation (A.11) is subjected to the following forced condition:

$$\tilde{E_x}(0) = E_{s0} \tag{A.12}$$

The analytical solution of Equation (A.11) takes the form [8, 10]:

$$\tilde{E_x}(z) = c_1e^{\tilde{k}z} + c_2e^{-\tilde{k}z} \tag{A.13}$$

Applying boundary condition Equation (A.12) to Equation (A.11):

$$\begin{aligned} E_{s0} &= c_1e^{\tilde{k}0} + c_2e^{-\tilde{k}0} \\ &= c_1 + c_2 \end{aligned} \tag{A.14}$$

Equation (A.14) $\therefore\Rightarrow c_1 = c_2 = \frac{1}{2}E_{s0}$. After substituting Equation (A.14) into Equation (3.17), Equation (3.17) is analysed as follows:

$$\tilde{E_x}(z) = \begin{cases} \frac{E_{s0}}{2}e^{\tilde{k}z} & for \quad z<0 \\ \frac{E_{s0}}{2}e^{-\tilde{k}z} & for \quad z\geq 0 \end{cases} \tag{A.15}$$

Substituting Equation (3.4) into Equation (A.15) produces:

$$\tilde{E_x}(z) = \begin{cases} \frac{E_{s0}}{2}e^{\beta(1+j)z} & for \quad z<0 \\ \frac{E_{s0}}{2}e^{-\beta(1+j)z} & for \quad z\geq 0 \end{cases} \tag{A.16}$$

where $\beta = \sqrt{\pi f\mu\sigma}$ according to Equation (3.3). To recover the time varying solution of Equation (A.16):

$$\begin{aligned} \vec{E}_x(z,t) &= \mathbb{R}e\left(\tilde{E_x}(z)\,e^{j\omega t}\right) \\ &= \begin{cases} \mathbb{R}e\left(\frac{E_{s0}}{2}e^{\beta(1+j)z}\right)e^{j\omega t} & for \quad z<0 \\ \mathbb{R}e\left(\frac{E_{s0}}{2}e^{-\beta(1+j)z}\right)e^{j\omega t} & for \quad z\geq 0 \end{cases} \\ &= \begin{cases} \mathbb{R}e\frac{E_{s0}}{2}\left(e^{\beta z}e^{j\beta z}\right)e^{j\omega t} & for \quad z<0 \\ \mathbb{R}e\frac{E_{s0}}{2}\left(e^{-\beta z}e^{-j\beta z}\right)e^{j\omega t} & for \quad z\geq 0 \end{cases} \\ &= \begin{cases} \mathbb{R}e\frac{E_{s0}}{2}\left(e^{\beta z}e^{j(\omega t+\beta z)}\right) & for \quad z<0 \\ \mathbb{R}e\frac{E_{s0}}{2}\left(e^{-\beta z}e^{-j(\omega t-\beta z)}\right) & for \quad z\geq 0 \end{cases} \end{aligned} \tag{A.17}$$

taking the real part of Equation (A.17) yields:

$$\begin{aligned}\vec{E}_x(z,t) &= \begin{cases} \frac{E_{s0}}{2}e^{\beta z}\cos(\omega t+\beta z) & for \quad z<0 \\ \frac{E_{s0}}{2}e^{-\beta z}\cos(\omega t-\beta z) & for \quad z\geq 0 \end{cases} \\ &= \frac{E_{s0}}{2}e^{-\beta|z|}cos(\omega t-\beta|z|) \end{aligned} \tag{A.18}$$

A.3 Derivation of the Analytical Solution Found in Section 3.3.

Assume that the, $\tilde{E_E}$-field is polarised in the $\hat{i}-direction$ and $\hat{j}-direction$ and travels in the $\hat{k}-direction$ ($z-axis$). Equation (3.2) is repeated here for the readers convenience:

$$\vec{\nabla}^2\tilde{E_E}-\tilde{k}^2\tilde{E_E}=0$$

will then take on the following forms when decomposed into it's vector components:

$$\frac{\partial^2\tilde{E_x}}{\partial z^2}-\tilde{k}^2\tilde{E_x}=0 \tag{A.19}$$

in the $\hat{i}-direction$ and

$$\frac{\partial^2\tilde{E_y}}{\partial z^2}-\tilde{k}^2\tilde{E_y}=0 \tag{A.20}$$

in the $\hat{j}-direction$.

Vector Component in $\hat{i}-direction$. Beginning with Equation (3.30):

$$\frac{\partial^2\tilde{E_x}}{\partial z^2}-\tilde{k}^2\tilde{E_x}=0$$

in the $\hat{i}-direction$ and. Equation (3.30) is subjected to the following boundary conditions:

$$\tilde{E_x}(0)=\frac{1}{2}yj\omega B_0 \tag{A.21}$$

$$\tilde{E_x}(\infty)=0 \tag{A.22}$$

The analytical solution of Equation (3.30) takes the form [8, 10]:

$$\tilde{E_x}(z)=c_1e^{\tilde{k}z}+c_2e^{-\tilde{k}z} \tag{A.23}$$

Applying boundary condition Equation (3.33) to Equation (A.23):

$$\begin{aligned} 0 &= c_1e^{\tilde{k}\infty}+c_2e^{-\tilde{k}\infty} \\ 0 &= c_1e^{\tilde{k}\infty} \end{aligned} \tag{A.24}$$

the term $e^{\tilde{k}\infty}\neq 0, \therefore\Rightarrow c_1=0$. Equation (A.23) becomes:

$$\tilde{E_x}(z)=c_2e^{-\tilde{k}z} \tag{A.25}$$

Applying boundary condition Equation (3.32) to Equation (A.34):

$$\frac{1}{2}yj\omega B_0=c_2e^{-\tilde{k}0} \tag{A.26}$$

the term $e^{-\tilde{k}0} = 1, \therefore \Rightarrow c_2 = \frac{1}{2} y j\omega B_0$. Equation (A.34) becomes:

$$\begin{aligned} \tilde{E_x}(z) &= \frac{1}{2} y j\omega B_0 e^{-\tilde{k}z} \\ &= \frac{1}{2} y j\omega B_0 e^{-\beta(1+j)z} \\ &= \frac{1}{2} y j\omega B_0 e^{-\beta z} e^{-j\beta z} \end{aligned} \tag{A.27}$$

where $\tilde{k} = \beta(1+j)$ according to Equation (3.4). To recover the time varying solution of Equation (A.36):

$$\begin{aligned} E_x(z,t) &= \mathbb{R}e\left(\tilde{E_x}(z)\, e^{j\omega t}\right) \\ &= \mathbb{R}e\left(\frac{1}{2} y j\omega B_0 e^{-\beta z} e^{j(\omega t - \beta z)}\right) \end{aligned} \tag{A.28}$$

taking the real part of Equation (A.37) yields:

$$\begin{aligned} E_x(z,t) &= \frac{1}{2} y j\omega B_0 e^{-\beta z}\left[\cos(\omega t - \beta z) - j\sin(\omega t - \beta z)\right] \\ &= -\frac{1}{2} y\omega B_0 e^{-\beta z} \sin(\omega t - \beta z) \end{aligned} \tag{A.29}$$

where $\beta = \sqrt{\omega\mu\sigma}$.

Vector Component in $\hat{j} - direction$. Beginning with Equation (3.31):

$$\frac{\partial^2 \tilde{E_y}}{\partial z^2} - \tilde{k}^2 \tilde{E_y} = 0$$

in the $\hat{j} - direction$. Equation (3.31) is subjected to the following boundary conditions:

$$\tilde{E_y}(0) = E_{s0} \tag{A.30}$$

$$\tilde{E_y}(\infty) = 0 \tag{A.31}$$

The analytical solution of Equation (3.31) takes the form [8, 10]:

$$\tilde{E_y}(z) = c_1 e^{\tilde{k}z} + c_2 e^{-\tilde{k}z} \tag{A.32}$$

Applying boundary condition Equation (3.36) to Equation (A.32):

$$\begin{aligned} 0 &= c_1 e^{\tilde{k}\infty} + c_2 e^{-\tilde{k}\infty} \\ 0 &= c_1 e^{\tilde{k}\infty} \end{aligned} \tag{A.33}$$

the term $e^{\tilde{k}\infty} \neq 0, \therefore \Rightarrow c_1 = 0$. Equation (A.32) becomes:

$$\tilde{E_y}(z) = c_2 e^{-\tilde{k}z} \tag{A.34}$$

Applying boundary condition Equation (3.35) to Equation (A.34):

$$-\frac{1}{2} x j\omega B_0 = c_2 e^{-\tilde{k}0} \tag{A.35}$$

the term $e^{-\tilde{k}0} = 1, \therefore \Rightarrow c_2 = -\frac{1}{2} x j\omega B_0$. Equation (A.34) becomes:

$$\begin{aligned} \tilde{E_y}(z) &= -\frac{1}{2} x j\omega B_0 e^{-\tilde{k}z} \\ &= -\frac{1}{2} x j\omega B_0 e^{-\beta(1+j)z} \\ &= -\frac{1}{2} x j\omega B_0 e^{-\beta z} e^{-j\beta z} \end{aligned} \tag{A.36}$$

where $\tilde{k} = \beta(1+j)$ according to Equation (3.4). To recover the time varying solution of Equation (A.36):

$$\begin{aligned} E_y(z,t) &= \mathbb{R}e\left(\tilde{E}_y(z)\,e^{j\omega t}\right) \\ &= \mathbb{R}e\left(-\frac{1}{2}xj\omega B_0 e^{-\beta z}e^{j(\omega t-\beta z)}\right) \end{aligned} \tag{A.37}$$

taking the real part of Equation (A.37) yields:

$$\begin{aligned} E_y(z,t) &= -\frac{1}{2}xj\omega B_0 e^{-\beta z}\left[cos(\omega t-\beta z) - jsin(\omega t-\beta z)\right] \\ &= \frac{1}{2}x\omega B_0 e^{-\beta z}\sin(\omega t-\beta z) \end{aligned} \tag{A.38}$$

where $\beta = \sqrt{\omega\mu\sigma}$.

$$\begin{aligned} \vec{E}_E(x,y,z) &= E_x(y,z,t)\,\hat{i} + E_y(x,z,t)\,\hat{j} \\ &= -\frac{1}{2}y\omega B_0 e^{-\beta z}\sin(\omega t-\beta z)\,\hat{i} + \frac{1}{2}xj\omega B_0 e^{-\beta z}\sin(\omega t-\beta z)\,\hat{j} \\ &= \left(-\frac{1}{2}y\omega B_0\hat{i} + \frac{1}{2}x\omega B_0\hat{j}\right)e^{-\beta z}\sin(\omega t-\beta z) \\ &= \frac{1}{2}\omega B_0\left(-y\hat{i}+x\hat{j}\right)e^{-\beta z}\sin(\omega t-\beta z) \end{aligned} \tag{A.39}$$

A.3.1 Analytical Calculation of the Current Density or Eddy Currents

The actual values of the current density also referred to as eddy currents $\vec{J_E}$ can be calculated using Equation (2.20) and (3.38) as follows:

$$\begin{aligned} \vec{J_E} &= \sigma\vec{E}(x,y,z) \\ &= \sigma E_x(y,z,t)\,\hat{i} + E_y(x,z,t)\,\hat{j} \\ &= J_x\hat{i} + J_y\hat{j} \end{aligned} \tag{A.40}$$

$$\begin{aligned} \vec{J_E}(x,y,z) &= \sigma\frac{1}{2}\omega B_0\left(-y\hat{i}+x\hat{j}\right)e^{-\beta z}\sin(\omega t-\beta z) \\ &= \left(-y\hat{i}+x\hat{j}\right)\sigma\frac{1}{2}\omega B_0 e^{-\beta z}\sin(\omega t-\beta z) \end{aligned} \tag{A.41}$$

Convert vector part of Equation (A.41) to polar co-ordinates [5]:

$$\begin{aligned} \vec{J_E}(r,\theta) &= \left(-y\hat{i}+x\hat{j}\right) \\ &= \left(-r\sin(\theta)\hat{i} + r\cos(\theta)\hat{j}\right) \end{aligned} \tag{A.42}$$

where

$$\hat{i} = \cos(\theta)\hat{r} - \sin(\theta)\hat{\theta} \tag{A.43}$$

and

$$\hat{j} = \sin(\theta)\hat{r} + \cos(\theta)\hat{\theta} \tag{A.44}$$

$$\begin{aligned}
\vec{J_E}(r,\theta) &= -r\sin(\theta)\left(\cos(\theta)\hat{r}-\sin(\theta)\hat{\theta}\right)+r\cos(\theta)\left(\sin(\theta)\hat{r}+\cos(\theta)\hat{\theta}\right) \\
&= \left(-r\sin(\theta)\cos(\theta)+r\sin(\theta)\cos(\theta)\right)\hat{r}+\left(r\sin(\theta)sin(\theta)+r\cos(\theta)\cos(\theta)\right)\hat{\theta} \\
&= 0+r\left(\sin^2(\theta)+\cos^2(\theta)\right)\hat{\theta} \\
&= r\hat{\theta} \qquad \text{(A.45)}
\end{aligned}$$

Equation (A.41) is represented in polar co-ordinates as:

$$\begin{aligned}
\vec{J_E}(r,\theta,z) &= \sigma\frac{1}{2}\omega B_0\left(r\hat{\theta}\right)e^{-\beta z}\sin\left(\omega t-\beta z\right) \\
&= \sigma\frac{1}{2}\omega B_0 re^{-\beta z}\sin\left(\omega t-\beta z\right)\hat{\theta} \qquad \text{(A.46)}
\end{aligned}$$

Bibliography

[1] A.C.Polycarpou, Introduction to the Finite Element Method in Electromagnetics, Morgan and Claypool, 2006

[2] D.B.Davidson, Computational Electromagnetics for RF and Microwave Engineering, Cambridge University Press, 2005

[3] P.P.Silvester and R.L Ferrari, Finite Element for Electrical Engineers, Third edition, Cambridge University Press, 1993

[4] J.Stewart, Calculus (Concepts and Contexts), Brooks/Cole Publishing Company, 1998

[5] K.E.Lonngren, S.V.Savov and R.J.Jost, Fundamentals of Electromagnetics with MATLAB, Second Edition, Scitech Publishing, Inc. 2007

[6] D.G.Zill and M.R.Cullen, Advanced Engineering Mathematics, PWS Publishing Company, 1992

[7] J.P.Webb, "Edge elements and What They can do for You", IEEE Trans. Magn., vol. 29, no. 2, March 1993

[8] G.M.Tattersfield, Electromagnetic Field Theory (A Student's Manual), UCT, 1998

[9] D.Halliday, R.Resnick and J.Walker, Fundamentals of Physics Extended, Fourth Edition, John Wiley and Sons, Inc., Canada, 1993

[10] D.J.Griffiths, Introduction to Electrodynamics, Third Edition, Prentice-Hall, Inc., 1999

[11] J.P.Webb, "Hierarchal Vector Basis Functions of Arbitrary Order for Triangular and Tetrahedral Finite Elements", IEEE Trans. Antennas and Propagation, vol. 47, no. 8, August 1999

[12] J.Jin, The Finite Element Method in Electromagnetics, Second edition, John Wiley and Sons, Inc., New York, 2002

[13] D.B.Davidson, "An Evaluation of Mixed-Order Versus Full-Order Vector Finite Elements", IEEE Trans. Antennas and Propagation, vol. 51, no. 9, September 2003

[14] N.Morison, Introduction to Fourier Analysis, John Wiley and Sons, Inc., 1994

[15] R.Harberman, Elementary Applied Partial Differential Equations, Third Edition, Prentice-Hall, Inc., 1998

[16] N.A.Golias, C.S. Antonopoulus, T.D.Tsiboukis and E.E.Kriezis, “3D Eddy Current Computation with Edge Elements in Terms of Electric Intensity”, COMPEL-\the International Journal for Computation and Mathematics in Electrical and Electronic Engineering, vol. 17, no. 5, June 1998

[17] N.A.Golias, T.D.Tsiboukis, “3D Eddy Current Computation with a Self-Adaptive Refinement Technique”, IEEE Trans. Magnetics, vol. 31, no. 3, May 1995

[18] P.C.Sen, Principles of Electric Machines and Power Electronics, Second Edition, John Wiley and Sons, Inc., 1997

[19] S.Young and Z,Freedman, University Physics, Tenth Edition, Addison Wesley Longman, Inc., 2000

[20] W.D.Callister, Materials Science and Engineering an Introduction, Sixth Edition, John Wiley and Sons, Inc., 2003

[21] J.A.Edminister, Schaum’s Outline Series, Theory and Problems of Electromagnetics, Magraw-Hill Book Company

[22] A.L.Garcia, Probability and Random Process for Electrical Engineers, Second Edition, Addison-Wesley Publishing Company, Inc., 1994

[23] D.B.Davidson, “Implementation Issues for Three Dimensional Vector FEM Programs”, IEEE Trans. Antennas and Propagation, vol. 42, no. 6, December 2000

[24] A.J.Wilkinson, Personal Consultation with Supervisor, University of Cape Town, February 2011